INTERFACE DYNAMICS IN INKJET DEPOSITION

A Thesis
Presented to
The Academic Faculty

By

Wenchao Zhou

In Partial Fulfillment
Of the Requirements for the Degree
Doctor of Philosophy in the
School of Mechanical Engineering

Georgia Institute of Technology
May 2014

INTERFACE DYNAMICS IN INKJET DEPOSITION

Approved by:

Dr. David W. Rosen, Advisor
School of Mechanical Engineering
Georgia Institute of Technology

Dr. Andrei G. Fedorov, Co-Advisor
School of Mechanical Engineering
Georgia Institute of Technology

Dr. F. Levent Degertekin
School of Mechanical Engineering
Georgia Institute of Technology

Dr. Martha Grover
School of School of Chemical & Biomolecular Engineering
Georgia Institute of Technology

Dr. Wallace W. Carr
School of Materials Science and Engineering
Georgia Institute of Technology

Date Approved: [October 23, 2013]

献给我的父母

ACKNOWLEDGEMENTS

Major accomplishments always come with great support and help. This work is no exception. I am grateful to a number of people who have provided their generous help during the course of this work.

First and foremost, I would first like to thank my advisor, Dr. David W. Rosen, for guiding me to learn and inspiring me to grow throughout my entire graduate career with his encouragements, timely feedback, and valuable inputs and suggestions. His enthusiasm in research and education makes him a great role model for me to learn from.

I have also been fortunate to work in a team with Drs. Andrei G. Fedorov and F Levent Degertekin, who are also my thesis committee members. Dr. Fedorov has been extremely helpful with my research with inspiring questions, timely feedback, and constructive suggestions and criticisms. His depth of knowledge and high energy always inspire me to learn more and work harder. I am also deeply grateful to Dr. Degertekin for his time and numerous comments and suggestions during our biweekly meetings throughout most of my graduate career. I would also like to thank Drs. Martha A. Grover and Wallace W. Carr for agreeing to serve on my committee and their helpful comments on my research.

I am indebted to Drs. J. Mark Meacham and Thomas P. Forbes for their help with the nozzle fabrication in the beginning of my research and for answering my questions. I would also like to thank Steven Sheffield for sacrificing his time and letting me use his high speed camera. I am also grateful to Dr. Hongming Dong for providing the original experimental data. I am indebted to Dr. Jeffrey A. Donnell for his help on editing my thesis.

Many thanks go to Drs. Chad Duty and Frederick A. List III for mentoring me and helping me out with experiments when I was working at Oak Ridge National Lab as an intern. I would specially like to thank Dr. Rich Combes for his mentoring and personal support and encouragements during the past two years. I would also like to thank National Science Foundation through grant DMI-0900322 for their generous funding of my research. I would also like to thank Drew Loney for working together with me on the same project.

I am very thankful for the support from friends and lab members who have made my years at Georgia Tech a pleasant experience. Discussions, trips, and sports with Chad Hume, Amit Jariwala, Jane Kang, Namin Jeong, Patrick Chang, Jason Nguyen, Sangin Park, Harrison Jones, Dazhong Wu, and Toby Xu have been great and enjoyable.

Last but certainly not least, I owe my family immense gratitude for their unconditional love and support that have helped me go through the most difficult times. Without their support and sacrifice, I would not have gone so far.

TABLE OF CONTENTS

LIST OF TABLES

LIST OF FIGURES

LIST OF SYMBOLS AND ABBREVIATIONS

β	spread factor	—
$\delta_{\alpha\beta}$	Kronecker delta	—
δt	time increment in LB unit	—
δx	space increment in LB unit	—
ϵ	Knudsen number	—
η	dynamic viscosity	$\mathrm{Pa \cdot s}$
θ	contact angle	°
κ	surface tension parameter	N
λ	relaxation time	s
μ	chemical potential	Pa
ν	kinematic viscosity	$\mathrm{m^2/s}$
ξ	interface thickness	m
ρ	density	kg/m^3
σ	surface tension	$\mathrm{N/m}$
τ	dimensionless relaxation time	—
τ_{spr}	spreading timescale	s
τ_{osc}	oscillation timescale	s
τ_{vis}	viscous timescale	s
φ	level-set function	—
χ	tuning parameter for mobility	$\mathrm{m \cdot s/kg}$
ψ	polynomial function	—
$\mathbf{\Pi}$	momentum flux tensor	—
Ψ	particle interaction potential function	—

Ω	particle collision operator	—
c_s	lattice sound speed	—
C	composition variable	—
C_l, C_h	composition for gas and liquid	—
d	distance along droplet contour	m
D_0	droplet diameter	m
$\mathbf{e}$	microscopic velocity	m/s
E	free energy function	—
E_0	bulk free energy function	—
f	particle distribution function for density	$\mathrm{kg/m^3}$
f^{eq}	equilibrium particle distribution function for density	$\mathrm{kg/m^3}$
f_0, f_1	characteristic functions for droplet and the desired shape	—
f_0^*, f_1^*	characteristic matrices for droplet and the desired shape	—
$\mathbf{F}$	external force	N
$\mathbf{F}_\mathrm{p}$	inertial force	N
$\mathbf{F}_\sigma$	surface tension force	N
$\mathbf{F}_\mathrm{vis}$	viscous force	N
Fr	Froude number	—
g_i	particle distribution function for pressure	Pa
g_i^{eq}	equilibrium particle distribution function for pressure	Pa
G	constant for particle interaction potential	—
h_i	particle distribution function for composition	—
h_i^{eq}	equilibrium particle distribution function for composition	—
h	dimensionless droplet height	—

H	droplet height	m
H^*	dimensionless droplet height	—
i, j	index	—
$\mathbf{I}$	identity matrix	—
k	curvature	m
K	Sommerfeld parameter	—
l	mean free path	m
L	characteristic length scale	m
L_a	latitudinal distance	—
L_o	longitudinal distance	—
m	mass	kg
M	mobility	$\mathrm{m^3 \cdot s/kg}$
$\mathbf{n}$	normal vector	—
$\mathbf{n}_\mathrm{s}$	normal vector of the interface	—
nd	normalized distance	—
N	total number of points	—
N_s	number of sampling points	—
Oh	Ohnesorge number	—
p	pressure	Pa
$\mathbf{P}$	pressure tensor	Pa
Pe	Peclet number	—
r	centroid distance function	—
r_d, r_r	characteristic vectors for droplet and desired shape	—
R	gas constant	$\mathrm{J \cdot mol/K}$

R_0	droplet radius	m
R_d, R_r	Fourier characteristic vectors for droplet and desired shape	—
Re	Reynolds number	—
S	dimension of space	—
S_c	shape coefficient	—
t	time	s
t^*	dimensionless time	—
t_i	weight coefficient	—
T	temperature	°C
$\mathbf{u}$	macroscopic velocity vector	m/s
$\mathbf{u}'$	modified velocity	m/s
U	initial impact velocity (characteristic velocity)	m/s
VF	volume fraction function	—
We	Weber number	—
$\mathbf{x}$	particle coordinates vector	—
x_c, y_c, z_c	coordinates of the droplet centroid	—

SUMMARY

Ink-jet deposition is an emerging technology that provides a more efficient, economic, scalable method of manufacturing than other traditional additive techniques by laying down droplets layer by layer to build up 3-D objects. The focus of this thesis is to investigate the material interface evolution during the droplet deposition process, which holds the key to understanding the material joining process. Droplet deposition is a complicated process and can be broken down into droplet impingement dynamics and droplet hardening. This research focuses on the study of the interface dynamics of droplet impingement. In order to study the interface dynamics, a novel metric is developed to quantify the evolving geometry of the droplet interface in both 2-D and 3-D for single and multiple droplets respectively, by measuring the similarity between the evolving droplet geometry and a desired shape. With the developed shape metric, the underlying physics of the interface evolution for single droplet impingement are examined with simulations using an experimentally validated numerical model. Results show that the Weber number determines the best achievable shape and its timing during the droplet impingement when Ohnesorge number is smaller than 1, while the Reynolds number is the determining factor when Ohnesorge number is larger than 1. A regime map is constructed with the results and an empirical splash criterion to guide the choice of process parameters for given fluid properties in order to achieve the best shape without splash for single droplet impingement. In order to study the interface dynamics for multiple droplet interaction, which is computationally prohibitive for commercial software packages, an efficient numerical model is developed based on the Lattice Boltzmann (LB) method. A new LB formulation equivalent to the phase-field model is

developed with consistent boundary conditions through a multiscale analysis. The numerical model is validated by comparing its simulation results with that of commercial software COMSOL and experimental data. Results show our LB model not only has significant improvement of computational speed over COMSOL but is also more accurate. Finally, the developed numerical solver is used to study the interface evolution of multiple droplet interaction with the aid of the 3-D shape metric proposed before. Simulations are performed on a wide range of impingement conditions for two-droplet, a-line-of-droplet, and an-array-of-droplet interactions. The underlying physics of the interface coalescence and breakup coupling with the impingement dynamics are examined. For line-droplet interaction, the strategy for achieving the equilibrium shape in the shortest time is studied. An important issue is discovered for array-droplet interaction, which is the air bubble formation during the droplet interaction. The mechanism for the air bubble formation is investigated and the strategy to avoid this undesirable effect is also suggested. This thesis has largely reduced the gap between basic science of studying droplet impingement dynamics and engineering application in inkjet deposition and provided preliminary insights on the material joining process for additive manufacturing.

CHAPTER ONE

INTRODUCTION

Manufacturing is the process of converting raw materials into functional tools to serve various human activities via mechanical, chemical, thermal, electrical and biological means. The raw materials we can process symbolize the level of civilization, from the Stone Age, the Bronze Age, the Iron Age, to the composite age. Material processing techniques have evolved over the entire human history from simple cutting to the recent buzz "3-D printing". Yet we are still far away from complete freedom with material processing -- the capability of manipulating single atoms and building objects atom by atom in a parallel way, as described in many science fictions. Although the number of processable materials has exploded and the manufacturing techniques have become astoundingly sophisticated, we are still an elementary civilization in terms of manufacturing in the sense that a full understanding of the physical processes of various manufacturing techniques is still far beyond our grasp, which significantly limits our ability to control manufacturing processes.

1.1 Manufacturing Processes

As we know, there exists an interface between any two different material species or states when they are put together. Manufacturing can be conceptually considered as a material patterning technique that defines material interfaces to form various geometrical and physical patterns. There are three different approaches to define the material interface, including creating new material interface by removing materials, known as subtractive manufacturing, deforming an existing material interface, and reducing the material

interface by combining materials together, known as additive manufacturing. The outcome of manufacturing is a combination of different raw materials processed into desired geometry with certain physical properties (e.g., material strength) that meet the requirements for specific applications. A unified view of manufacturing can therefore be established by categorizing the various manufacturing processes by the approach of defining material interfaces that determines both geometrical and physical aspects of manufacturing outcome. Therefore, studying the material interface evolution on different scales during manufacturing processes can provide an avenue to advance our understanding of the physical processes of manufacturing, and that may lift our limits in controlling manufacturing process.

1.1.1 Subtractive manufacturing

Subtractive manufacturing, which has dominated the history of manufacturing, is based on the simple idea of removing unneeded materials from a workpiece. We have made significant advances from rock cutting to sophisticated computer-numerical-control (CNC) machining techniques that provide powerful and effective tools to process various important engineering materials and serve as the foundation of our modern civilization. Yet, subtractive manufacturing suffers from many fundamental drawbacks. From a microscopic view, subtractive manufacturing is to knock out atoms or molecules by breaking the bonds between them with externally supplied energy. To pursue speed, a large number of bonds are usually broken at the same time with intensive energy supply. With part of the supplied energy converted into interface energy, a large portion of the energy is dissipated into heat, which changes the local structures and causes inhomogeneity and manufacturing flaws. The removed materials are also typically

wasted. In addition to considerable waste of energy and materials, subtractive manufacturing is fundamentally limited by the complexity of the geometry it can make. The more intricate the designed structure is, the more time it takes to remove unneeded materials and the more costly the manufacturing is. In addition, some common geometries (e.g., a hollow ball) are beyond the capability of subtractive manufacturing due to the physical limitations of the cutting tool, which significantly constraints design.

1.1.2 Deformative manufacturing

Deformative manufacturing can be broadly defined as a process of rearranging atoms to change the number of the atoms at the material interface with external energy input under certain environmental conditions. There are two different approaches to rearrange atoms: one is to reduce the bond energy between atoms by raising temperature so that the atoms can be easily rearranged globally (e.g., melting the materials), as in casting and molding; the other approach is to apply intensive local energy to rearrange atoms locally with or without the assist of high temperature, as in forging. Casting is among the oldest deformative manufacturing methods that can be traced back to 4000BC [1] and is usually used for making complex geometries that would be otherwise challenging or uneconomical to make by other methods [2]. Rearranging atoms in a large space at the same time will inevitably cause uneven distribution of energy and thus inhomogeneity and manufacturing defects. Although casting is a long-evolved technique, it remains a challenging task to produce castings that are free of defects. A different approach is to apply localized force to change the local shape of the workpiece, as in forging. Forging is another deformative manufacturing method with a long history that dates back to 5000BC [1]. While localized change in the forging process makes it relatively easier to control the

defects, it significantly limits the complexity of the geometries that can be achieved. Most of the deformative manufacturing methods involve a die or a mold that serves as the geometric constraints. Using a die, on the one hand, significantly reduces the cost for mass production, on the other hand, leads to high upfront capital investment and tooling cost, long design-to-production cycle, and less flexibility for changing production.

1.1.3 Additive manufacturing

The idea of joining materials together to build more complicated objects comes quite naturally to our human beings. Throughout human history, we can find various forms of practices of joining materials together, such as building a house brick by brick, use of adhesives to glue things together since 5200 years ago [3], and welding. Many of our ancestors put their efforts and intelligence into figuring out the fundamental building blocks of matter because we have long realized we will have no limits in building objects if we know the fundamental building blocks and how they can be combined. Additive manufacturing (AM) is based on such a powerful idea that is meant to unleash unprecedented flexibility for manufacturing. In 1986, Chuck Hull [4] invented the first commercial AM machine that used a computer-controlled concentrated light beam to selectively polymerize liquid photopolymer and built the object layer by layer. The powerful capability and promising outlook of the new technology led to a round of investments in the early 1990s, and many other forms of AM technologies were born [5], including powder bed fusion processes (e.g., selective laser sintering (SLS)), extrusion-based systems (e.g., fused deposition modeling (FDM)), printing-based processes (e.g., inkjet deposition), sheet lamination processes (e.g., Laminated Object Manufacturing (LOM)), beam deposition processes (e.g., Laser Engineered Net Shaping (LENS)), etc.

However, many of the venture-backed startups went under because many of the technologies were pre-mature for market applications to support their growth.

Although the various intuitive ideas of combining materials together paint a promising picture, the fundamental understanding of how materials are combined is still elusive, which prevents the technologies from maturing. From a microscopic perspective, new bonds are formed between atoms, and the number of atoms at the interface decreases (i.e., material interface reduces) when materials are combined. While a detailed account of how bonds are formed during the material joining process is mind-boggling, a study of the material interface evolution on different scales may provide insights into how the material joining process affects the manufacturing results, because the material interface determines the geometry of the manufactured part and also affects the distribution of energy in the materials on which the material properties depend.

1.2 Inkjet Deposition

While the idea of joining material units together trivializes the geometrical complexity for manufacturing, it suffers from long building time that leads to high manufacturing cost. Among many AM technologies, inkjet deposition holds the great promise to bring down the manufacturing time and cost by selectively depositing droplets onto a substrate in parallel using a scalable array of nozzles. This, also significantly reduces the complexity of the manufacturing system. In addition, inkjet AM machines can deliver the highest resolution among all current commercial AM machines on the market. The parts made with inkjet AM machines also typically have very good surface finish. More importantly, multiple material deposition can be naturally integrated into inkjet systems,

which opens up the possibility for material composition to be designed to optimize the material distribution in the manufactured parts for desired functions and thus generate great economic benefits.

Although the idea of distributing materials in liquid form can be traced back to very early stages of human history (e.g., use of syringe), the concept of inkjet was only first explored by Lord Kelvin in 1867 and the first commercial inkjet device was not introduced until 1951 by Siemens [6]. In the late 1970s, inkjet found its use in the desktop printing industry when the personal computer came along. As a material distributing technique, inkjet was quickly adopted as a manufacturing method in the AM industry in the 1990s. A historical development of inkjet deposition for manufacturing can be found in [5]. To differentiate from its successful counterpart "inkjet printing" for two-dimensional printing, the term "inkjet deposition" is used here to represent three-dimensional inkjet printing as a manufacturing method. Inkjet deposition can be generally divided into two parts: droplet generation and droplet deposition.

1.2.1 Droplet generation

A millimeter-scale droplet can be generated simply by letting a fluid flow through a small hole such that the fluid breaks off from the aperture surface when the fluid mass accumulated on the surface exceeds the surface tension force that holds the fluid onto the surface, as we see from a leaking faucet. In order to produce micron-scale droplets for inkjet, the fluid must be supplied with enough kinetic energy per unit volume so that it can overcome the interfacial energy between the fluid and the aperture surface and create the increased fluid interface when a droplet breaks off. Historically two conceptually

different approaches have been developed: continuous inkjet and drop-on-demand (DOD) inkjet.

1.2.1.1 Continuous inkjet

In a continuous inkjet system, a high pressure is applied to a fluid reservoir to produce a continuous fluid jet of approximately the diameter of the nozzle, which breaks into droplets after leaving the nozzle due to Plateau-Rayleigh instability. An acoustic wave can be used to excite the ejector to break up the droplets at regular intervals. The diameter of the droplets are typically twice as big as that of the nozzle. The typical droplet generation frequency ranges from tens to hundreds of kHz, and up to MHz at the expense of increased hydraulic complexity. The typical droplet diameter range is from 6μm to 1mm [5]. The operating pressures are usually from 5 to 50 psi and the ejection speed typically ranges from 2 to 50 m/s [7]. The continuous inkjet typically operates at a higher frequency than DOD inkjet but requires a much higher minimum-operating-fluid-volume.

1.2.1.2 Drop-on-Demand inkjet

In contrast to continuous inkjet that breaks a continuous jet into droplets, DOD inkjet creates a short-duration jet that condenses into a single droplet of the desired diameter. Many different approaches have been explored for DOD inkjets, including thermal jet (a.k.a. bubble jet), piezoelectric jet, focused ultrasonic jet, liquid spark jet, electro-hydrodynamic jet, etc [7]. Thermal jet [8], which applies electrical pulses to heating elements in order to vaporize a small amount of liquid to produce bubbles in the fluid that create pressure pulses to eject droplets, is commonly used in consumer desktop inkjet

printers including those from Canon, Hewlett-Packard, and Lexmark. Thermal jets have a simple drive-mechanism (a resistor) that can be easily integrated into a dense array of inkjet print head, but suffers from low operating frequency and the requirement of special ink that can generate bubbles upon heating.

The piezoelectric jet [9] is another widely used inkjet technique, used in Epson printers. Unlike the thermal jet that uses a heating element to generate bubbles to create pressure pulse, piezoelectric jet relies on the mechanical deformation of a piezoelectric element to produce the needed pressure pulse. The big advantage is that the pressure pulse can be accurately tuned due to the properties of the piezoelectric element and the operation does not chemically change the composition of the fluid as does the thermal jet. The drawback to the piezoelectric jet is that it is difficult to integrate the large-area piezoelectric elements into a dense array of micro-machined nozzles so that each nozzle can be individually controlled. Thermal jet and piezoelectric jet both suffer from the incapability of ejecting high viscosity fluids (<40cP) and the clogging issue, especially for small aperture size.

An acoustic resonance jetting technique that uses focused ultrasonic beams to generate a high pressure gradient at the tip of the nozzle, invented by Xerox PARC, holds promise to raise the viscosity upper limit and to alleviate the clogging issue [10]. An inexpensive ultrasonic droplet generator was developed based on the same idea by Meacham et al. [11]. The acoustic resonance jet has the potential to significantly raise the upper viscosity limit of printable fluids and the operating frequency to MHz, but such systems have the same issue to integrate the drive-mechanism (piezoelectric transducer that requires large area) into a dense array of nozzles, which limits the number of nozzles on a print head.

There are also many other droplet generation techniques for various applications. An overview of these methods is given by Lee [7].

1.2.2 Droplet deposition

Droplet deposition refers to the process from the time droplets exit the nozzles to the time all droplets harden on the substrate. This complicated process can be broken down into several interacting sub-processes, including droplets in flight, interaction between droplets and the substrate, and the droplet hardening process.

1.2.2.1 Droplets in flight

There is a substantial difference in controlling the droplets in flight between continuous inkjets and DOD inkjets. For continuous inkjet, the droplets first enter a charging field to become electrically charged and then pass through a deflection field that directs the charged droplets to their desired destinations—either a location on the substrate or a container of material to be recycled or disposed [12]. It is much simpler for the DOD inkjet, in which the droplets travel in straight lines after detaching from the nozzles and arrive at their desired location on the substrate by controlling the relative positions between the print head and the substrate. Due to the lack of control of the droplets in the flight, a short distance between the print head and the substrate (typically ~1mm) is needed to ensure the positioning accuracy of droplets on the substrate, because irregular velocity of the droplet (not always vertical) gained in the droplet generation process and the random collision with air molecules in the flight may significantly deflect the droplets from their desired destinations [13]. In addition, the air resistance will significantly reduce droplet momentum for the droplet size and ejection velocity of interest, because

the drag force is proportional to the droplet velocity or the droplet velocity squared for low Reynolds number and high Reynolds number respectively. Therefore, the DOD inkjets typically require a very short distance between the print head to the substrate, which may limit many industrial applications. In contrast, continuous inkjets allow for a relatively long distance between print head and substrate due to its high ejection velocity (up to 50m/s) and flight control of the droplets.

1.2.2.2 Droplet impingement

There are several different possible outcomes when a droplet comes down to a solid substrate with an initial velocity, including spreading, rebound, and splash. The outcome is determined by the fluid properties of the droplet, the impact velocity, droplet size, the surrounding gas, and the wettability of the solid surface. One popular approach to quantify the wettability of the solid surface is by the equilibrium contact angle θ, which is defined as the angle between liquid-vapor interface and the solid surface as shown in Figure 1-1. The contact line is defined as the intersection of all three phases.

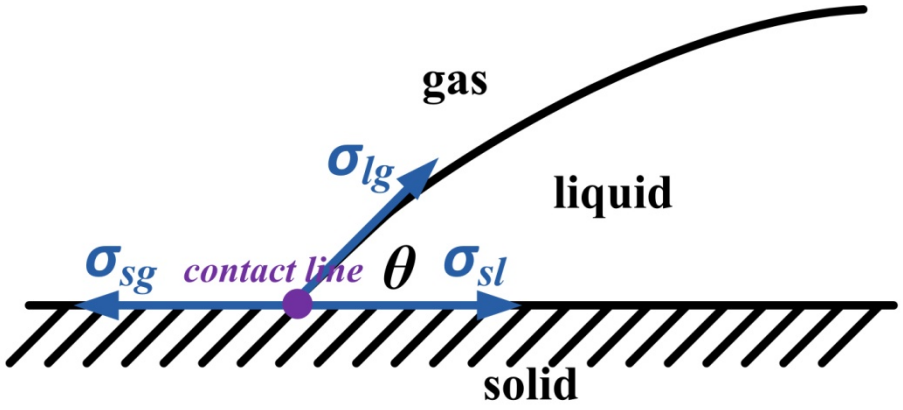

Figure 1-1. Illustration of the equilibrium contact angle on a planar geometry.

By considering the force balance when the droplet is in equilibrium, the well-known Young's Equation can be derived [14]:

$$\sigma_{sg} = \sigma_{sl} + \sigma_{lg}\cos\theta \quad (1\text{-}1)$$

where σ_{sg}, σ_{sl}, and σ_{lg} are the surface tension between solid-gas, solid-liquid, and liquid-gas respectively.

The Young's Equation assumes a flat, rigid, perfectly smooth, and chemically homogeneous surface. In many cases, the real surfaces are far from being ideal, which results in a phenomenon called contact-angle hysteresis [15], which refers to the difference between the advancing contact angle θ_A and the receding contact angle θ_R. The contact-angle hysteresis occurs because there are many different thermodynamically stable contact angles (i.e., meta-stable states) on a non-ideal solid surface [16] due to surface inhomogeneity, surface roughness, and impurities on the surface [17]. When a droplet hits on a solid surface with an initial velocity U, it will first spread, recede, oscillate and come to equilibrium in the end as shown in Figure 1-2. Previous experimental study [18] has found the time evolution of the impact process can be divided into four distinct phases: the kinematic phase, the spreading phase, the relaxation phase, and the wetting equilibrium phase.

In the kinematic phase, the droplet deforms like a solid sphere upon impact on the surface and exhibits the shape of a truncated sphere. The time duration of this phase is usually very short, and the spreading diameter changes with time in a power law relationship. In this phase, the impact behavior is mostly determined by the impact velocity and droplet size and the contact line motion is mainly determined by geometric considerations.

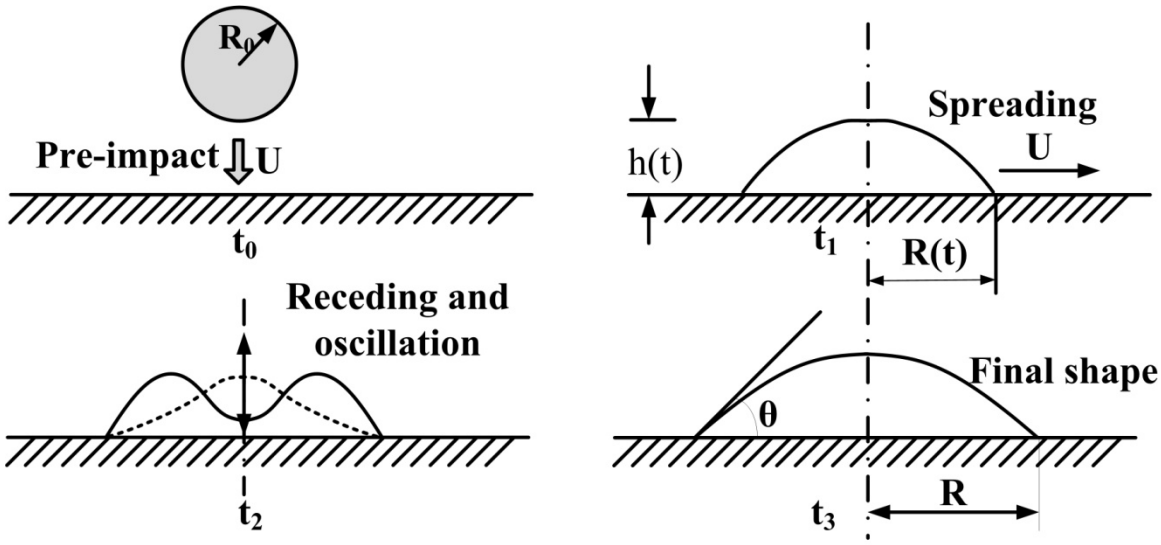

Figure 1-2. Illustration of droplet spreading, receding, oscillating, and achieving equilibrium upon impinging on a solid surface.

The kinematic phase ends and the spreading phase starts when the material points at the base of the droplet start to move radially and not mainly vertically, which corresponds to the generation of a spreading lamella radially expanding film bounded by a rim. The surface tension and viscosity effects start to play a role in this phase. According to [18], increasing the impact velocity and droplet size will lead to faster spreading and increasing the surface tension and viscosity will lead to slower expansion.

After the spreading diameter reaches maximum, the drop may begin to recede depending on the impact conditions. The receding contact angle plays an important role in this phase. It comes to the wetting equilibrium phase when all the kinetic energy is dissipated by viscosity. When the initial impact velocity is large enough and the solid surface is hydrophobic (i.e., $\theta > 90°$), the droplet may rebound or partially rebound from the surface. Common experience tells us that increasing the impact velocity to a certain point will lead to splash, as also experimentally suggested by Worthington [19]. Splash has been

extensively studied, and three different causes have been identified: the surrounding gas [20-21], the surface roughness [21-23], and the compliance of the solid substrate [24]. The splash caused by surrounding gas is referred as "corona splash" and the splash caused by the surface properties is referred as "prompt splash". When a drop impacts on a substrate, a spreading lamella will be generated during the spreading phase and the front edge of the lamella will be perturbed by the external environment, either surrounding gas or substrate, and the lamella will be destabilized.

Previous experiments have shown that the splashing threshold follows the empirical relation: $WeRe^{1/2}=K$, where K is a constant that depends on the external parameters, such as surrounding gas pressure, surface roughness [22, 25], etc. Here We is the Weber number defined as $We=\rho U^2 D_0/\sigma$ and Re is the Reynolds number defined as $Re= \rho U D_0/\eta$, where ρ is the liquid density, U is the impact velocity, D_0 is the droplet diameter, σ is the surface tension and η is the viscosity. Under a given condition, K is a constant number. For inkjet deposition, the impact conditions that lead to rebound or splash should be avoided.

1.2.2.3 Droplet hardening

Generally materials can be prepared in liquid form in different ways. Metals can be melted into liquid, a suspension can be made with fine metal or ceramic particles dispersed in a liquid, and liquid monomer solutions can be used to make polymers. Correspondingly, there are three different approaches to turn the droplet into solid for different materials, including solidification by cooling, drying of suspension solution, and polymerization of monomers.

For solidification, the droplet can be cooled through the heat conduction to the substrate or the fluid convection to the surroundings. The heat transfer mode can be very different at different stages of droplet impact: at early stage of the impact the heat conduction to the substrate is dominant and at later stages the convection in the fluid and the conduction in both fluid and solid along the spreading direction can be prevailing. The thermal contact resistance between droplet and substrate [26] and the impact velocity [27] are identified as two key factors that influence the cooling rate of the droplet. The time scales of the droplet impingement dynamics and the heat transfer and phase change are critical in determining the coupling effects between them, which is important for controlling the final shape of the droplet.

Drying of suspension is another popular approach to obtain solids. Many commercial inks for inkjet deposition are made with nano-particles with aqueous or non-aqueous based solutions, such as the inks produced by Novacentrix or Cabot for printed electronics applications. The effects of the surface temperature on the dynamics of the heat transfer and evaporation of the droplet have been extensively studied [28]. Four different regimes have been identified, including film evaporation, nucleate boiling, transition boiling, and film boiling. In the regime of film evaporation, the surface temperature is relatively low, and the droplet spreads and evaporates slowly. In addition, the droplet is in total contact with the surface, and conduction is the dominant mechanism inside the droplet. When the surface temperature goes slightly higher and vapor bubbles start to arise in the droplet, it enters the nucleate boiling regime, in which the momentum transport around the droplet is significantly increased and the contact between the droplet and the surface becomes partial and intermittent. In the transitional boiling regime with

an even higher surface temperature, the frequency of contact between the droplet and the surface decreases, and an unstable vapor film forms between the droplet and the surface. When the temperature goes above the Leidenfrost point in the film boiling regime, a thin and stable vapor film is formed and there is no contact between the droplet and the surface, which is known as the Leidenfrost effect.

Another challenge for the drying process is that the evaporation flow will bring the solid particles to the surface of the droplet and form a solid crust that prevents the droplet from further drying [29]. A porous substrate may provide additional fluid flow channel for the mass transfer during the drying process to prevent the crust formation [30]. The segregation of the solid particles after the drying process is completed raises another challenge for inkjet deposition, which may significantly deteriorate the material properties. The particle segregation is found to be caused by the capillary flow induced by the differential evaporation rates across the drop, which is known as the "coffee ring" effect [31]. Many researchers have come up with different approaches to reduce the "coffee ring" effect [32-34] to improve the materials properties for inkjet deposition.

Polymerization is another approach widely used in stereolithography, inkjet, and other commercial AM machines to make a liquid droplet become solid. Usually a mixture of monomer solution and initiators is prepared in liquid form, and the polymerization process is initiated by light or heat. Polymers can be generally categorized by their functional behavior into elastomers and plastics. Elastomers are flexible and " rubbery" materials that can be readily deformed and rapidly return to almost their original shape and plastics are materials which can be shaped or molded under appropriate conditions of temperature and pressure, and then hold their shape. Plastics can be further divided into

thermoplastics and thermosets, the essential difference of which is that thermoplastics remain permanently fusible and can soften and eventually melt under heat while cured thermoset polymers only char and break down at high temperatures. While stereolithography(SL) machines use primarily thermoset materials such as epoxy and acrylates, most of the polymers used in the commercial AM machines are thermoplastics, such as acrylonitrile-butadiene-styrene(ABS), polyamide(Nylon), polycarbonate (PC), and polyetherimide(Ultem).

In order to predict the outcome of the polymerization process, a reaction-diffusion model is often required [35]. The complexity arises when the polymerized monomers start to influence the diffusion rates of the chemical components, which will in turn affect the polymerization process. Depending on the reaction rates, the heat released from chemical reaction may causes bubbles and other issues and further complicate the problem. In addition, the shrinkage for the thermosets caused by the polymerization process results in difficulty of controlling the dimensional accuracy [5]. The effects of oxygen inhibition of the polymerization process add more uncertainty in predicting the results. As a result, understanding and controlling the polymerization process remain a challenge for manufacturing.

1.2.3 Applications

As an emerging AM technique that directly deposits materials onto a substrate, inkjet deposition provides a more flexible, efficient, economic, and scalable method of manufacturing than other AM techniques. It opens up numerous possibilities to the solutions of many grand challenges [36] we are facing today, such as fabricating thin films for economical solar cells, building up self-repairing and self-evolutionary

machines for infrastructure maintenance and improvement, and printing artificial organs. In addition, it has immediate utility for many important industrial applications, such as printed electronics [37], flexible electronics [38], thin films [39-40], surface coating [41], medical devices [42], optical devices [43], bio-printing [44], rapid prototyping [45], and many other emerging applications.

Printed electronics is one of the most active research fields for inkjet deposition in recent years. With different droplet hardening mechanisms, various conductive inks have been studied and successfully printed, such as molten metal [46-48], conductive polymers [49-50], organo-metallic compounds [51-52], metal precursors [53], and metallic nano-particle suspensions [33, 54-55]. For molten metal, the operating temperature is usually very high and thus limits the choice of the substrates and increases the cost of manufacturing. For organometallic compounds or metal precursors, additional heat treatment procedure is required for them to become metal and the organic residues after the heat treatment may reduce the electric conductivity of the manufactured part. In addition, the heat treatment procedure involves chemical reactions that complicate the control of the manufacturing process.

Metallic nano-particle suspension, however, is really promising and has attracted lots of attention [56-57] because it can avoid the extreme processing conditions required for standard lithographic fabrication and molten-metal-droplet deposition and the processing temperature (less than 300 $^{\circ}$C) is compatible with most of the substrates. Suspensions of silver, gold and copper nano-particles are the common choices, and these have all been successfully printed to form conductive lines [33, 57-58]. With the cost of gold nano-particles being prohibitive and the easy oxidization of copper nano-particles, silver nano-

particles have been the most popular choice among all the relevant studies. Printing conductive lines with nano-particle suspensions has been extensively studied by different research groups [56, 59-63] with varying particle, particle size, solvent, weight concentration, hardening condition, etc. and different results on line width, line thickness and conductivity have been obtained. Although significant progress has been made for printed electronics and many other applications, inkjet deposition is still missing a fundamental understanding, which boils down to how to break materials down into units and how to combine the unit materials back together.

1.3 Motivation for Study

Conceptually, the process of breaking down materials into units is the reverse of the process of joining unit materials back together. Understanding of one process may lead to breakthroughs in the other. In this study, we will investigate the material joining process, as it is the core idea of additive manufacturing, and it is relevant not only to inkjet deposition but also to many other AM techniques. Manufacturing can be viewed as an interface science, so studying the interface evolution on relevant scales during the manufacturing processes may advance our understanding of manufacturing processes and may provide new means for us to control the manufacturing processes as well as the manufacturing results. Consequently, we wish to study the material interface evolution of the material joining process. The material interfaces affect both the geometrical and the physical aspects of the manufacturing result, that is, the geometry and material properties of the manufactured part. It is because the geometry of the interfaces between the materials not only determines the shape of the manufactured part but also affects the

energy distribution in the space and thus the material properties. Therefore, studying the material interface evolution during the material joining process can help us predict the final manufacturing results. For inkjet deposition, one of the most important issues is the voids that are formed during the droplet deposition process due to the air trapped by the interaction of droplets and the substrate, which can significantly affect the material properties (e.g., mechanical strength or electrical conductivity). These voids are the extra material interfaces that are not reduced during the material joining process. In order to eliminate these extra material interfaces, an understanding of the dynamics of the interface evolution on the relevant scale will be crucial, which will also be beneficial to reduce the manufacturing time. The most relevant scale is the scale of the droplet size, and therefore we will focus on studying the droplet interface (i.e., the droplet shape) evolution during interaction between the droplets and the substrate.

1.4 Problem Formulation

The long-term goal of this research is to establish an understanding of how the droplet deposition process determines the manufacturing results (including both geometrical shape and material properties) by studying the droplet interface evolution. Although the interaction of drops with surfaces has been extensively and intensively investigated for over a century [19], the development of comprehensive, predictive models has been difficult due to the complexity of the process and the interactions among many physical phenomena, including fluid mechanics, heat transfer, chemical reactions, phase change, surface chemistry, etc. In order to achieve a better understanding of the complicated droplet deposition process, we can break it down to several sub-problems and build up

the understanding step by step. The structure of the problem can be shown in Figure 1-3. The boxes in solid lines show the scope of this study, while the boxes in dashed lines will be postponed for future research. Three research questions (RQ) have been raised concerning single-droplet and multiple-droplet impingement dynamics.

1.4.1 Single-droplet impingement

Droplet impingement is a century-old problem and most of previous research focuses on studying single-droplet impingement and how the spreading radius (or wetted area) changes during the impinging process. The spreading radius can sometimes provide important information for a variety of industrial applications, such as thermal spraying and inkjet printing, but it does not provide enough information for us to predict either geometrical or physical aspects of manufacturing results. In the context of manufacturing, studying the droplet shape evolution as mentioned before, however, can provide valuable information that can be used to predict manufacturing results.

A shift of focus from the change of spreading radius to shape evolution opens up a whole new domain for us to explore, which can be roughly broken down into smaller problems as shown in Figure 1-4. Shape is an abstract geometrical concept, and it is very difficult to track its change. In order to study shape evolution, a shape metric is thus required to characterize and quantify the droplet shape at different moments of the impinging process. From the perspective of design, the objective of manufacturing is to meet the design requirements and one of the most important design requirements is the geometry. It is therefore reasonable to define a shape metric by measuring the similarity between the droplet shape and the desired shape, which can also provide a means for optimization of the manufacturing process. As thin film is of interest to many industrial applications, a

uniform film is targeted as the desired shape for this study. This choice can also be justified because more complicated geometries can be built if we have the ability to build a regular geometric unit. Therefore, two research questions and their hypotheses can be formulated as the following.

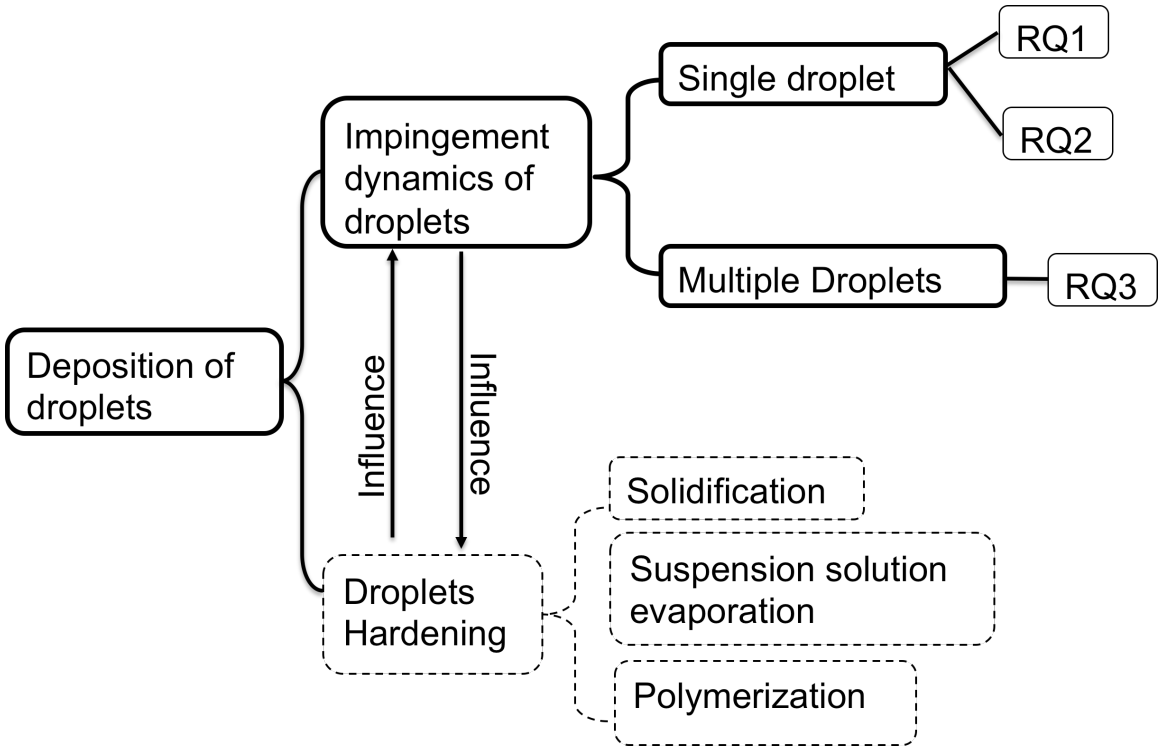

Figure 1-3. Breakdown of the droplet deposition process.

RQ1: How to characterize and quantify the droplet shape to enable the shape optimization of the droplet deposition process?

Hypothesis: A shape coefficient that is defined to measure the similarity between the droplet shape and the desired shape (a uniform film) can be used to characterize and quantify the droplet shape.

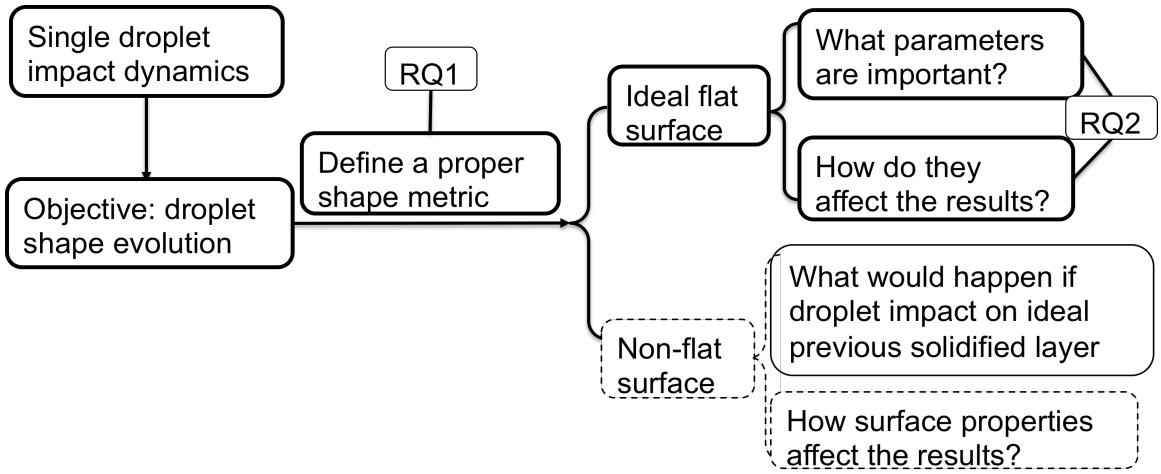

Figure 1-4. Breakdown of the problem of single-droplet impingement.

The proposed shape metric will provide us the ability to catch the moment when the droplet shape is closest to our desired shape during the shape evolution. As shown in previous research, the droplet impingement dynamics on a flat surface are governed by the Navier-Stokes equations with many physical parameters, including fluid density ρ, viscosity η, surface tension σ, droplet size D_0, impact velocity U, and contact angle θ. The number of influencing factors can be reduced to three dimensionless numbers through a standard dimensionless analysis of the Navier-Stokes equations, including the Weber number, the Reynolds number and the Froude number, which are used to characterize the ratios of different physical forces. The Weber number is the ratio of the inertial force to surface tension, the Reynolds number is the ratio of inertial force to viscous force, and the Froude number is the ratio of inertial force to gravity. As we intuitively understand that the inertial force drives the droplet into a uniform film, the surface tension holds the droplet together into a spherical shape, and the viscous force resists any shape change, we can formulate our second research question and hypothesis as below.

RQ2: How do the relevant dimensionless numbers affect the best-achievable shape (i.e., closest to a uniform film) and the timing of it for single-droplet impingement on an ideal flat surface?

Hypothesis: A larger Weber number can achieve a more uniform film when the viscous effects are small, and a larger Reynolds number leads to a better best-achievable shape when the viscous effects are large. The Froude number does not influence much of the shape evolution when the droplet size is sub-millimeter.

The shape evolution of single-droplet impinging onto a non-flat surface is left for future study.

1.4.2 Multiple-droplet impingement

A similar approach can be taken to study the more complicated droplet shape evolution for multiple-droplet impingement. However, multiple-droplet impingement is rarely studied in previous research due to the lack of a proper research tool. The computational cost for simulating three-dimensional (3-D) droplet impingement is prohibitive with traditional computational fluid dynamics (CFD) algorithms. In order to overcome this hurdle, we first need to develop an efficient numerical solver to enable 3-D simulation of droplet impingement so that we can study multiple-droplet impingement. A breakdown of the problem is shown in Figure 1-5. The computational cost of traditional CFD algorithms comes from solving the non-linear Navier-Stokes equations for the velocity field and the Poisson equation for the pressure field. A particle-based numerical method lattice Boltzmann method (LBM) has recently grabbed a lot of attention for its efficiency in simulating fluid dynamics with a set of evolution equations for particle population dynamics. Therefore, the third research question and hypothesis can be stated as below.

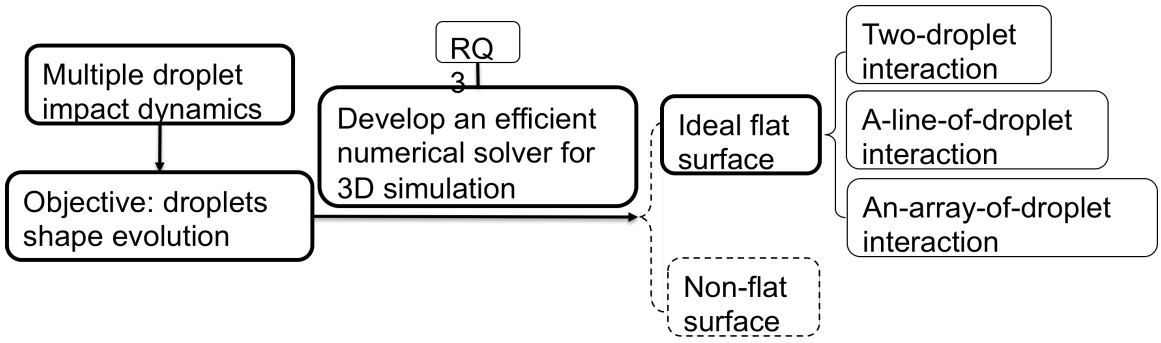

Figure 1-5. Breakdown of the problem of multiple-droplet impingement.

RQ3: How to build a numerical model that can simulate the droplet impingement dynamics more efficiently than the traditional commercial software packages with certain accuracy to enable 3-D simulation of the droplet impingement dynamics and make it possible to study the multiple-droplet interaction dynamics?

Hypothesis: A lattice Boltzmann model can be used to simulate 3-D droplet impingement dynamics more efficiently than the commercial software packages that use the traditional macroscopic methods within certain range of accuracy and reliability.

Answering the three research questions and testing the hypotheses will be the main research activities that will be conducted in this project. The research topics presented in the boxes in the dashed line as in Figure 1-3, Figure 1-4, and Figure 1-5 will be left for future exploration.

1.5 Summary

This research focuses on studying the interface dynamics in inkjet deposition, which may hold the key to understanding material joining process and advancing the manufacturing technology to next stage. The thesis is organized as follows. In Chapter 2, a detailed literature survey on the topics related to the three research questions is presented,

including shape characterization, multi-phase flow modeling, and lattice Boltzmann method. Chapter 3 presents the development of a novel shape metric to characterize the droplet shape in both 2-D and 3-D. In Chapter 4, a detailed study of the shape evolution of single-droplet impinging on a solid surface is conducted. First, a 2-D numerical model is developed and validated. The effects of relevant dimensionless numbers on the shape evolution of the droplet are then studied using the numerical model. A regime map is then constructed to indicate the impingement conditions that lead to a shape closest to the desired shape. Chapter 5 presents a new lattice Boltzmann (LB) formulation that can simulate droplet impingement dynamics in 3-D very efficiently. The simulation results are then compared with the predictions of the commercial software COMSOL, previous LB models, and experimental data. Results show the proposed LB simulation approach yields not only a significant speed improvement over COMSOL, but that it also has better accuracy than both COMSOL and the previously reported LB technique. Chapter 6 demonstrates the capability of the developed LB solver with simulations of multiple-droplet impingement in 3-D. The shape evolutions of multiple-droplet impingement, including two-droplet, a-line-of-droplet, and an-array-of-droplet, are investigated with varying impact conditions. Chapter 7 gives conclusions and future work recommendations based on the work presented here.

CHAPTER TWO

LITERATURE SURVEY

The droplet deposition process is very complicated as it involves many complex physical phenomena and crosses into a wide range of subjects. As this research targets to answer three critical research questions as presented in Chapter 1, it is beneficial to survey the literature to understand the state of the art on the relevant subjects. In order to provide a sufficient background for the three research questions we raised, three subjects need to be reviewed, including shape representation, multiphase flow modeling, and the lattice Boltzmann method.

2.1 Shape Representation

Shape, as a geometrical concept, is our perception and visual representation of the geometry of various objects in the real world. We humans have developed sophisticated mathematical tools for analysis of various models in our life, including many regular geometrical models. However, it is still not easy for us to comprehend arbitrary shapes due to the difficulty of representing them mathematically. Entering the digital age, more and more digital images are produced and there is a growing interest in shape representation for multimedia searching and image retrieval in computer graphics, computer vision, computational geometry, computer-aided-design (CAD) and related fields. Extensive research has been conducted on shape representation techniques for both 2-D and 3-D shapes during the past decades [64-66], but very little research has been reported on studying the physics of shape change. Therefore, we will present a survey of the shape characterization techniques that are developed for image searching and retrieval

purposes, for both 2-D and 3-D shapes. There are two different approaches to represent a shape. One is to use a feature vector to represent the geometrical feature or some derived feature of the entire shape, and the other is to break the shape down into small segments called primitives and then represent the shape by the sequence of the primitives, which is also known as structural representation.

2.1.1 Feature vector-based shape representation

Feature vector has long been used as a standard approach for multimedia retrieval [67] when it is difficult to compare two objects directly. The similarity between shapes can be measured using a distance-based metric in the vector space. A feature vector can be constructed with many different aspects of the geometrical information of the shape, including statistical, boundary (contour/surface for 2-D/3-D shapes respectively), and bulk (region/volume for 2-D/3-D shapes respectively) information. The boundary and bulk information can be represented in either the spatial or the frequency domain.

2.1.1.1 Statistical representation

The simplest statistics of a shape include bounding area/volume, object orientation, ratio of principle axis for both 2-D and 3-D shapes. Paquet et al. [68] reviewed several possible simple statistical shape descriptors. Peura et al. [69] also proposed some other simple descriptors such as convexity and elliptic variance. To capture more detailed information on the shapes, some parameterized statistics [70] are employed, such as the moment of inertia of boundary points, the average distance of the boundary points from the principle axis, and the variance of the distance. Geometric moments have been adopted in multiple studies with different sampling schemes of boundary points [68, 71].

More complicated statistics intended to capture more details are investigated utilizing different shape distribution functions, such as the distribution of angles between three random points on the boundary, the Euclidean distances between one fixed point and random points on the boundary, the angles between chords and principle axes [68, 71-72].

2.1.1.2 Boundary representation

It is appropriate to use the boundary to represent a shape when most of the effective information of the shape are on the boundary. There are numerous ways to approximate or represent the information on a shape boundary. Some common geometrical features (often called shape signatures) [59, 66, 73] can serve as the foundation to construct feature vectors, including, centroidal profile, complex coordinates of the boundary points, centroid distance, tangent angle, cumulative angle, curvature, boundary normal, area, chord-length, etc. Typically the shape-signature vectors have very high dimensionalities in order to sample enough information on the boundary. The dimensionality can be reduced by transforming the feature vectors in the spatial domain into the frequency domain and picking only the relevant frequency components while ignoring the high-frequency components. This method can also help overcome the problem of noise sensitivity and boundary variations. A large set of methods are built on such an idea, including Fourier descriptor (FD) [64, 73-74] based on Fourier transform, wavelet descriptor (WD) [75] based on wavelet transform, spherical descriptor based on spherical harmonics for 3-D shapes [71, 76], scale space method based on continuous Gaussian filtering to obtain shape components on different scale [77]. Although wavelet descriptor has the advantage of multi-resolution in both the spatial and the frequency domains, Fourier descriptor has gained wide popularity over other methods for several reasons: 1)

Fourier theory is well-developed and well-understood; 2) it is simple to compute the Fourier descriptors; 3) each descriptor has specific physical meaning; 4) normalization is easy; 5) both global and local features can be well captured. There are also some other methods that approximate the boundary shape with a base shape (e.g., a second-order spline curve) plus a small perturbation [78]. The coefficients of the perturbations can construct a feature vector to describe the shape. This method is often used for specific applications.

2.1.1.3 Bulk representation

A different approach to represent the shape is to use all the information in the bulk (region/volume for 2-D/3-D respectively). One of the most intuitive ways to do this is to use a grid-based method [79], which scans the shape in the space and builds a "bitmap" with 1 meaning the cell is occupied by the shape and 0 otherwise. A binary vector can then be constructed to represent the shape, and the similarity between shapes can be measured by the binary Hamming distance. Instead of sampling on a regular grid, the circular/spherical sampling schemes have also been used for 2-D/3-D shapes [80-81], in which a polar raster of concentric circles/spheres and radial lines is overlaid in the center of the mass, and a shape matrix can then be built with the sampling. The spherical harmonics can be applied to the sampled information to construct a feature vector [81]. Statistical methods have also been used to describe the shapes as histograms of point fractions that fall into partitions of the enclosing object space with different partitioning models [82]. A comprehensive comparison of various feature-vector based shape representation methods for 3-D shapes is presented in [83], which shows that the performance of different methods varies greatly with different shape characteristics, and

the overall effectiveness increases with the dimensionality of the feature vector first and then plateaus after the dimensions reach certain point.

2.1.2 Structural shape representation

Structural shape representation breaks shapes down into primitives using polygonal approximation, curvature decomposition, curving fitting, etc [84]. The common primitives can be polygon, a quadratic arc, a spline, etc. The result of the structural decomposition is a string of letters that represents the sequence of the primitives, and the similarity of shapes can be measured with the edit distance of two string sequences. One early-introduced structural shape representation technique is the chain code representation [85], in which an arbitrary curve shape is represented by a sequence of small unit vectors with a limited set of possible directions. The author argues this method can be extended to encode arbitrary geometric configurations. Instead of using unit vectors, the shapes can also be decomposed into polygons [86] and smooth curves [87], and similar approaches can be used to compare shapes as in the chain code representation method. It is also possible to describe the shapes with their topology and to compare the shapes by their topological structure [88]. A similar approach is to first obtain thin skeletons of the shapes using a suitable skeletonization algorithm and then to compare the topological structures of the skeletons of the shapes [89]. The structural shape representation techniques are usually tailored to specific shape recognition problems, while their applicability to general problems still needs further exploration in terms of both effectiveness and efficiency.

2.2 Multiphase Flow Modeling

The droplet impingement dynamics falls into the category of multiphase flow problems within fluid dynamics and it has presented a challenging task in both physical modeling and numerical computation. Both kinds of challenges arise from the existence of the moving interface between phases. It is physically difficult to model the physical transfer processes (mass, momentum, energy, etc.) across the interface because the geometry of the interface is not known as a priori but requires to be calculated during the process. The numerical challenges come from the discontinuities of the physical quantities across the interface. When it comes to droplet impingement on a solid surface in the air, two fluid phases are involved, the air and the droplet, and the large deformation of the droplet shape (i.e. the interface between the two phases) makes the problem become very difficult. It becomes even more challenging due to the high density, viscosity, and speed ratios. Among the numerous computational methods for the multiphase flow problem, they can be generally divided into the macroscopic method that is based on continuum assumption of the fluids, the microscopic method that tracks the individual molecules or atoms with Newton's equations of motion or statistical mechanics, and the mesoscopic method that falls in between of microscopic and macroscopic methods by modeling a group of fluid molecules as a fluid particle and ignoring all the molecular details within the particle.

2.2.1 Macroscopic methods

It is often enough to model a problem on its relevant scale. The macroscopic method models the fluid as a continuous medium and the governing equations of the fluid motion —the Navier-Stokes equations—can be derived from Newton's second law with certain assumptions on the stress tensors. Based on different treatments of the interfaces between

phases in a multiphase flow problem, a variety of models have been proposed and can be generally divided into Euler-Euler, Euler-Lagrange and direct interface resolving approaches.

2.2.1.1 Euler-Euler approach

In a multiphase flow, the continuous phase is often modeled in an Eulerian reference, and the dispersed phases can be treated in either Eulerian or Lagrangian reference. In the Euler-Euler approach, all the phases are treated mathematically as interpenetrating continua, and the conservation equations are derived for each phase in the same way. Two common approaches have been used for different applications with different assumptions and simplifications.

1) Mixture model

The mixture model takes the single-fluid approach that treats all the phases as a mixture and solves one set of conservation equations for the mixture and volume fraction equations for the secondary phases [90]. These equations are closed by prescribing algebraic expressions of the relative velocities to the mixture for each phase with the assumption that a local equilibrium between the phases should be reached over short spatial length scale, in which the coupling effects between the phases are incorporated. If all the relative velocities are set to zero, the mixture model reduces to a homogeneous multiphase model. The continuous phase can be either liquid or gas, and the dispersed phases can be solid particles, drops, or bubbles. Due to the largely simplified modeling of the inter-phase phenomena, the mixture model is typically applied to problems with low volume fraction of dispersed phases, such as particle-laden flows with low loading and bubbly flows with low gas volume fraction [91].

2) Eulerian model

Unlike the mixture model, the Eulerian model solves a set of conservation equations for each phase [92]. Constitutive relations are required for interfacial transport to complete the overall model. The constitutive relations are often derived from kinetic theory or experiments depending on different flow patterns and types of phases involved. The advantage of this approach is that the interfacial transport process can be rigorously defined while the flip side is it often requires a great depth of understanding and experimental data of the phenomena being modeled. The user-defined approach for the interfacial transport processes provides a flexible framework for a wide variety of applications, such as bubble columns [93] and fluidized beds [94]. The complexity of the model and the computational cost of solving multiple sets of governing equations, however, largely limit its applications.

2.2.1.2 Euler- Lagrange approach

If the dispersed phases are rather small in size compared to the grid resolution of the continuous phase, it is natural to adopt the Lagrangian representation to track the trajectories of the dispersed phases [95]. In this case, the dispersed phases can be simplified as particles, and the particle trajectories are determined individually by particle equation of motion at specified intervals during the fluid phase calculation. It is also possible for the particles to exchange mass, momentum, and energy with the fluid phase. A fundamental assumption for this approach is that the dispersed phases have a low volume of fraction, which makes it not suitable for modeling any interfacial phenomena.

2.2.1.3 Direct interface resolving approach

Unlike the previous models, a direct interface resolving approach calculates the topological evolution of the phase-interface between two fluids without any prior knowledge of the size and the shape of the phase-interface. It treats all the fluid phases as one single fluid field and solves one set of governing equations. An additional surface tension term is added to the governing equations to account for the effects of phase-interface on the fluid field. Various models have been developed to represent the phase-interface. Marker-and-cell is among the first of such methods that was initially developed for tracking the free surface of a fluid using marker particles that move with the local velocity of the fluid [96]. The idea of using a marker function for tracking the position of the fluid interface has inspired many successful methods for simulating multiphase flow, such as the volume-of-fluid (VOF) method [97], the level-set method [98], the phase-field method [99], and the front-tracking method [100]

1) Volume-of-fluid method

The VOF method uses a function of volume fraction *VF* to represent the fluid interface [97]. Assuming every "fluid particle" retains its identify (i.e., does not change phase), the material derivative of *VF* needs to be 0, which leads to the advection equation for *VF*:

$$\frac{\partial VF}{\partial t} + \mathbf{u} \cdot \nabla VF = 0 \tag{2-1}$$

where *t* is time, **u** is velocity, and *VF* is the volume fraction of one fluid ranging from 0 to 1, with 0 meaning the grid cell is filled with a different fluid. The choice of volume fraction as the interface marker function allows a sharp representation of the interface and accurate advection of the volume fraction so that the mass is conserved, which is the major advantage of the VOF method. However, it is rather difficult to use volume fractions to calculate accurate local curvature at the fluid interface, yet this is critical for

computing the surface tension term in the governing equations. Therefore, a geometric reconstruction of the fluid interface, as illustrated in Figure 2-1, is needed in order to calculate the curvatures [101]. If the reconstructed interface is not smooth enough, it often causes large variation of curvature at the interface and thus numerical errors and instability. The interface reconstruction also incurs extra complexity and great computational cost, especially for 3-D simulations. The VOF method has been adopted by many commercial and open source codes (e.g., ANSYS Fluent, STAR-CCM, Flow3D, Gerris Flow Solver, etc.) for simulating multiphase flow problems for its ability to handle large interface topology change and interface coalescence and breakup, which lends itself to simulation of droplet impingement dynamics by many research groups [102-103].

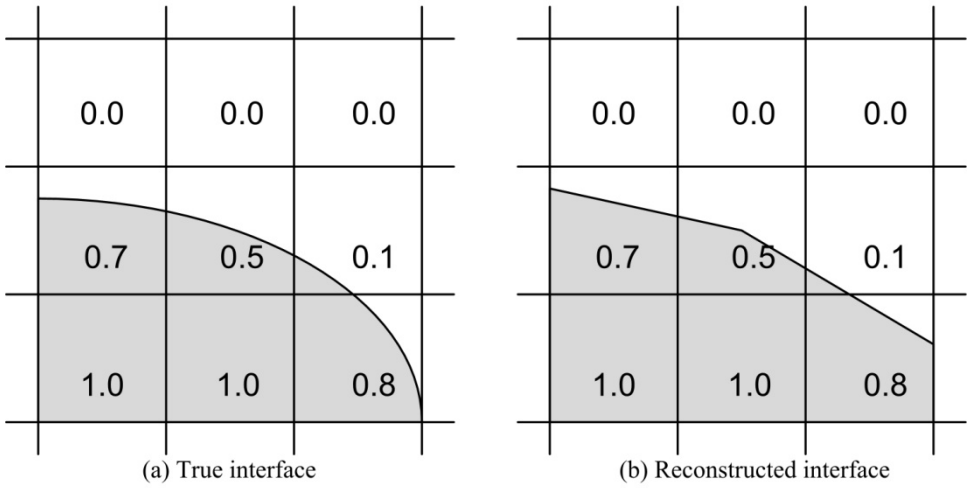

Figure 2-1. Illustration of the geometric reconstruction of the fluid interface from volume fractions.

2) Level-set method

In order to avoid the interface reconstruction operation that results from the discontinuous volume fraction function in the VOF method, a continuous smooth level-set function φ is

introduced in the level-set method so that the exact location of the fluid interface can be determined from the level-set function. The level-set function advects with the velocity field in the same way as the volume fraction in the VOF method as in Eq. (2-1). A typical level-set function adopts a signed distance to the fluid interface, with 0 being the location of the interface. The great advantage of using a smooth level-set function is the easiness of calculating the curvature of the interface. The unit normal vector **n** and the mean curvature k are simply:

$$\mathbf{n} = \frac{\nabla \varphi}{|\nabla \varphi|} \tag{2-2}$$

and

$$k = \nabla \cdot \frac{\nabla \varphi}{|\nabla \varphi|} \tag{2-3}$$

respectively. In spite of its apparent simplicity in calculating the curvature, the level-set function φ provides no intrinsic mechanism to ensure the mapping of φ to the location of the interface keeps the same way. That is, the relationship between φ and the distance to the interface may change as the interface thickness changes during the simulation, which makes the determination of the interface location inconsistent. To solve this problem, a re-initialization procedure is needed to reinitialize the level-set function φ at every time step. Although it is possible to conserve φ, the mass enclosed by the zero level-set is not conserved due to the artificial re-initialization procedure, especially when the interface undergoes severe stretching and tearing [104]. Many successors have tried to improve the level-set method, and many different approaches are attempted such as "hybrid VOF/level-set method" [105] and "ghost fluid method" [106]. The level-set method has

been used for studying various multiphase flow problems [107] and adopted by many commercial and open source codes, such as COMSOL.

3) Phase-field method

In contrast to the VOF and level-set methods that treat the material interface as an infinite thin or sharp boundary with generally discontinuous physical quantities across the interface, the phase-field method falls into the category of diffusive interface methods [108] that describe the interface as a finite-thick transitional region with continuous variations of an order parameter (e.g., density) from one material phase to another. Unlike the level-set method relying on an artificial level-set function, the order parameter of the phase-field method generally is a physical quantity governed by the physical laws, which provides a physical principle to maintain the material interface and eliminates the need for re-initialization of the level-set function as in the level-set method. In a multiphase flow, a typical order parameter is the composition of one fluid. The evolution of the composition variable C is driven by the gradient of chemical potential μ and governed by the Cahn-Hilliard equation [99]. The surface tension force can be derived as a body force with no need to calculate the curvature at the fluid interface. Due to the intrinsic incorporation of the interfacial dynamics, the phase-field method can find a wide variety of multiphase applications in droplet impingement dynamics [109], phase change [110], viscous fingering [111], etc. Since the thickness of the real material interface is generally on the scale of nanometers, it usually requires a finer mesh than the sharp interface models to numerically resolve the interface in order to achieve high accuracy. The phase-field method has also been implemented in several commercial and open source codes, such as COMSOL, OpenFOAM, and OpenPhase.

4) Front-tracking method

Unlike previous models that represent the interface using an interface marker function on a fixed grid, the front-tracking method introduces additional computational elements to keep track of the front. This approach considerably reduces the mesh density needed to maintain a sharp and numerically well-resolved interface. The higher accuracy for similar mesh density is at the expense of more complexity. The interface is typically represented by a connected set of particles that carry forces. The complexity arises from handling the interactions between the introduced particles and the fixed grid. The interface particles generally need restructuring as the calculation proceeds, which becomes more complicated in 3-D. The interface curvature can be obtained from the positions of the marker particles, and the surface tension term can thus be calculated. The front-tracking method is best suited for well-defined fronts that are easily identifiable in the initial conditions and is not suited for dealing with interface coalescence or breakup.

2.2.2 Microscopic methods

In principle, all the physical phenomena can be described by zooming into the molecular level and modeling the motion of the molecules and their interactions. There are two approaches to describe the behavior of the molecules: deterministic and stochastic. Correspondingly, two different methods have been developed to simulate various physical phenomena when quantum effects are not important: molecular dynamics (MD) [112] and Monte Carlo (MC) method [113].

2.2.2.1 Molecular dynamics

Molecular dynamics generally solves the trajectories of interacting atoms/molecules based on Newton's equation of motion where the forces between particles and potential energy are defined by molecular mechanics force fields. The macroscopic thermodynamic properties of the system can then be determined by statistical ensemble averages. Although in theory the MD method can simulate almost any kind of macroscopic dynamics as a "virtual microscope" with high temporal and spatial resolution, it suffers from three fundamental limitations. First, MD simulation minimizes the potential energy rather than the free energy of the system and thus neglects all entropic contribution to the system. Second, accurate integration of the motion equations require a time step to be short enough ($\sim 10^{-15}$s) to resolve atomic vibrations. In addition, it is limited to simulate systems in relatively small spatial and time scales by the huge computational cost and cumulative numerical errors. MD is often applied for studying chemical physics, materials science, and bio-molecules modeling. Most of the time the molecular-level details are not needed for modeling macroscopic fluid dynamics, but some phenomena are inherently multiscale, such as droplet impingement dynamics. The motion of the contact line usually occurs on a much smaller scale than the rest of the droplet. MD has been used for studying contact line dynamics to improve our understanding of contact line motion and dynamic contact angle [114]. The no-slip wall boundary condition is reported to break down around two-atom scale [115].

2.2.2.2 Monte Carlo method

The Monte Carlo method can be used to simulate a wide range of problems in the physical sciences, engineering, finance and business, and mathematics, especially when an analytical model is not available. In contrast to molecular dynamics, which tracks

molecules using a deterministic model for simulating physical systems, the Monte Carlo method relies on a stochastic procedure that generates random walks in the configuration space to determine the states of the system. The best-known MC method is the Metropolis algorithm [116]. It moves one atom at a time by a small random displacement generated in the configuration space from a probability distribution (often the classical Boltzmann distribution) to obtain thermodynamic properties or minimum-energy structures. However, this method can only simulate the equilibrium state of a physical system because there is no concept of time in the model. The kinetic Monte Carlo (KMC) method [117] is developed to simulate kinetics based on the idea of transition rates from state to state, which depends on the energy barrier between the states. The transition from state to state neglects all the trajectories of atoms between states and enables KMC to reach much longer time scale than MD, typically seconds and well beyond. The determination of the transition rates between states, however, can be challenging and critical to the accuracy of the simulation results. The MC method has also been used to study droplet spreading on a solid substrate [118] to test Tanner's law in nano scale, which shows the MC method can well bridge the gap between the timescales of the MD and macroscopic methods. The spatial scale that MC can reach is still largely limited by the computational cost for simulating large number of atoms.

2.2.3 Mesoscopic methods

In order to achieve a larger time and spatial scale than the microscopic methods while retaining their flexibility of modeling complex physical phenomena, a new class of methods known as the mesoscopic methods has emerged to bridge the gap between microscopic and macroscopic descriptions of various physical phenomena. Rather than

describing the materials as a continuous medium or as individual molecules, the mesoscopic methods treat them as discrete particles that consist of a group of molecules, and ignore all the molecular scale details within the particles. It is quite natural to use the idea of particle as it enjoys various benefits of the microscopic description of materials, such as simple description for very complex phenomena that would otherwise require explicit treatment for the macroscopic methods, rigorous conservation of mass and momentum, and relatively low coding effort in developing numerical tools. Neglect of the molecular-level details also enables the particle methods to reach a much larger spatial scale and longer time scale than the microscopic methods. A variety of mesoscopic methods have been developed during the past decades, such as Lattice Gas Automata (LGA) [119], the Lattice Boltzmann method (LBM) [120], Dissipative Particle Dynamics (DPD) [121], Smoothed Particle Hydrodynamics (SPH) [122], Fluid Particle Model [123], and Vortex Particle Method [124]. These methods are developed primarily for simulating complex gas and fluid dynamics, including multiphase flow. This section will give a brief review of dissipative particle dynamics and smooth particle hydrodynamics and the lattice Boltzmann method will be thoroughly reviewed in the next section.

2.2.3.1 Dissipative particle dynamics

Dissipative particle dynamics can be considered as a coarse-grained molecular dynamics model. The differences are DPD has a much larger particle size (a cluster of molecules) and softer interaction between particles. The particles interact with each other through three different forces: a conservative force that describes the repulsion between particles, a dissipative force that tries to reduce velocity differences between particles, and a

random force that describes the random and dissipative interactions between particles based on Fluctuation-Dissipation theorem [121]. The standard DPD model has only the repulsive force and is used primarily for gas dynamics. The random and dissipative forces are incorporated to characterize the fluctuating dissipative behavior of non-ideal fluids. The particle interaction ensures the conservation of mass and momentum, which provides DPD the ability to capture the hydrodynamics of a fluid at large scales. The conceptual framework allows DPD to model the behavior of various complex fluids, such as particle suspension, polymer solutions, emulsions, gels, and other complex fluids and soft condensed matter. Although the DPD method has received substantial theoretical support and experienced rapid development during the past decades [123], it still faces many issues. Numerous efforts have been put forward in developing thermodynamically consistent DPD models [125], and it still appears unclear what physical length and time scales are actually simulated [123]. A rule of thumb is that the DPD particle size should be no more than 10 to 100 times the molecule size and that DPD simulations are typically 10^5 times faster than MD simulations [126].

2.2.3.2 Smooth particle hydrodynamics

Smoothed Particle Hydrodynamics is a mesh free Lagrangian method that can be used to approximate numerical solutions of the equations of fluid dynamics by replacing the fluid with a set of particles. Although it was originally developed for the astrophysics community [122], it has been widely used in simulating various complex fluid problems. The fluid particles have a spatial influencing distance, known as "smoothing length," over which the fluid properties are smoothed with a "bell-shaped" kernel function based on the idea that a continuous field can be represented by superimposing many smooth "bell-

shaped" functions. The "smoothing length" can automatically adapt itself to the local density or other conditions and can thus achieve an equivalent effect of "adaptive mesh" as in grid-based methods. It also enjoys the benefits of particle-based methods, such as exact advection and trivial treatment for interface problems. SPH is a fast developing method and still faces many theoretical and numerical issues for various applications, and a comprehensive review of the progress can be found in [127].

2.3 Lattice Boltzmann Method

The Lattice Boltzmann (LB) method has experienced rapid development since its birth two decades ago [128] for its promising ability to simulate complex fluids, such as multiphase flow, particulate and suspension flows, and flows in porous media. Similar to previously introduced mesoscopic methods, LBM is also a particle based method that describes the probability of particle distribution in the space using a particle distribution function (PDF) rather than tracking the exact locations and momenta of individual particles as in molecular dynamics. Therefore, it enjoys the simplicity of modeling various complex macroscopic phenomena by modeling particle interactions, which follows the Boltzmann transport equation:

$$(\partial_t + \mathbf{e} \cdot \nabla_{\mathbf{x}} + \mathbf{F} \cdot \nabla_{\mathbf{e}}) f(\mathbf{x}, \mathbf{e}, t) = \Omega(f(\mathbf{x}, \mathbf{e}, t)) \tag{2-4}$$

where t is time, $\mathbf{x}$ is the particle coordinates in the physical space, $\mathbf{e}$ is the microscopic velocity of a particle, $\mathbf{F}$ is the external force exerted on the particle, and $f(\mathbf{x}, \mathbf{e}, t)$ is the number of particles that can be found at time t within a phase-space element $\mathrm{d}^3\mathbf{x} \cdot \mathrm{d}^3\mathbf{e}$. $\Omega(f(\mathbf{x}, \mathbf{e}, t))$ is a collision term that defines the particle behavior after collision with each

other, which can be derived by taking into account only binary collisions based on the assumption that the velocity of a particle is independent of its position in space.

Computational efficiency is another advertised advantage of LBM over traditional computational fluid dynamics (CFD) techniques. Although it largely depends on the specific implementation for specific problems, the LBM generally wins because it only updates the particle states using explicit equations rather than solving non-linear Navier-Stokes equations. In addition, the locality of the computation in LBM offers the opportunity for massive parallelization of the algorithms, which can significantly speed up the simulations.

2.3.1 Origin of lattice Boltzmann method

The lattice Boltzmann equation (LBE) can be derived in several different ways, but its direct precursor is the lattice gas automata method [119], which is derived from the concept of cellular automata [129], originally discovered by Stanislaw Ulam and John von Neumann and popularized by Conway's Game of Life. The basic idea of cellular automata is to have a grid of cells that can be set to a finite number of states (e.g., two states: on and off.), to update their states based on a fixed rule (e.g., if all the neighbors of a cell are on, the state of the cell is changed to off.), and to iterate from an initial state. It is found that some simple rules can evolve into very complex patterns from different initial states. The idea is then employed to simulate gas dynamics. On a lattice, the state of each site is purely Boolean; either there is or is not a particle moving in each direction (e.g., if there are 6 possible velocity directions, each site is represented by 6 Boolean variables). The iteration rule is divided into two steps: propagation and collision. In propagation, each state propagates on the lattice for one step in its direction. In collision,

a set of rules that conserve mass and momentum are established to determine how the particles change their states after collision under different collision situations. The LGA method suffers from lack of Galilean invariance and statistical noise [130]. The LBE is derived by replacing the Boolean states in the LGA equation with particle distribution function [128]:

$$f_i(\mathbf{x} + \mathbf{e}_i\delta t, t + \delta t) = f_i(\mathbf{x}, t) + \Omega_i(f_i(\mathbf{x}, t)) \tag{2-5}$$

where i = 0, 1 …, Q, represents the number of directions in a discretized phase space, $f_i(\mathbf{x}, t)$ is the particle distribution function in the i-th direction, Ω_i is the collision operator that defines the rules of collision, $\mathbf{e}_i$ is the unit microscopic velocity in the i-th direction, δt and δx are time and space increments respectively with $\delta x = |\mathbf{e}_i|\delta t$. The density ρ and the momentum density $\rho\mathbf{u}$ can be calculated from the moments of the distribution function:

$$\rho = \sum f_i \tag{2-6}$$

$$\rho\mathbf{u} = \sum f_i\mathbf{e}_i \tag{2-7}$$

where $\mathbf{u}$ is the macroscopic velocity. The collision operator is required to conserve mass and momentum at each lattice site, therefore,

$$\sum \Omega_i = 0 \tag{2-8}$$

$$\sum \Omega_i\mathbf{e}_i = 0 \tag{2-9}$$

In order to solve the equation, a significant simplification of the collision term is made by assuming that the local particle distribution relaxes back to an equilibrium state at a rate of λ, which can be expressed as the Bhatnagar-Gross-Krook (BGK) collision operator [131]:

$$\Omega(f(\mathbf{x}, \mathbf{e}, t)) = -\frac{f - f^{eq}}{\lambda} \tag{2-10}$$

where the equilibrium distribution f^{eq} can be expanded to the second order of $\mathbf{u}$ under the small Mach number assumption [132]:

$$f_i^{eq} = \rho[a_0 + a_1 \mathbf{e}_i \cdot \mathbf{u} + a_2 (\mathbf{e}_i \cdot \mathbf{u})^2 + a_3 \mathbf{u}^2] \tag{2-11}$$

where the coefficients a_0 to a_3 can be obtained analytically from the constraints Eqs. (2-8) and (2-9) [133]. The single relaxation time scheme (i.e., λ is a scalar) and the multiple relaxation time scheme (i.e., λ is a matrix) have both been explored extensively in the literature [120, 134]. The multiple-relaxation-time scheme can generally improve the numerical stability at the expense of increased computational cost. The effects of external body force acting on particles can be incorporated by modifying the macroscopic velocity $\mathbf{u}$:

$$\mathbf{u}' = \mathbf{u} + \Delta\mathbf{u} = \mathbf{u} + \frac{\lambda \mathbf{F}}{\rho} \tag{2-12}$$

where $\mathbf{u}'$ is the updated velocity after incorporating the effects of the external body force and $\Delta\mathbf{u}$ is the velocity change due to the act of external body force $\mathbf{F}$ during the relaxation time λ.

2.3.2 Discrete Boltzmann model

A different approach to derive the LBE is to view it as a discretization of the continuous Boltzmann equation, which is originally proposed by He et al. [135] and provides more theoretical foundation for the lattice Boltzmann method. The starting point is Eq. (2-4) with the BGK collision operator, where the equilibrium distribution function f^{eq} takes the form of the Maxwell-Boltzmann distribution function:

$$f^{eq} = \frac{\rho}{(2\pi RT)^{S/2}} \exp\left[-\frac{(\mathbf{e}-\mathbf{u})^2}{2RT}\right] \tag{2-13}$$

where R and T are the gas constant and the temperature, S is the dimension of the space, $\mathbf{e}$ and $\mathbf{u}$ are the microscopic and macroscopic velocity respectively. Since the derivative $\nabla_{\mathbf{e}} f$ in Eq. (2-4) cannot be calculated directly because the relationship between f and $\mathbf{e}$ is unknown, it is approximated using the leading order of f:

$$\nabla_{\mathbf{e}} f \approx \nabla_{\mathbf{e}} f^{eq} = -\frac{\mathbf{e}-\mathbf{u}}{RT} f^{eq} \tag{2-14}$$

Therefore, Eq. (2-4) becomes:

$$(\partial_t + \mathbf{e}\cdot\nabla_{\mathbf{x}}) f(\mathbf{x},\mathbf{e},t) = -\frac{f-f^{eq}}{\lambda} + \frac{\mathbf{F}\cdot(\mathbf{e}-\mathbf{u})}{RT} f^{eq} \tag{2-15}$$

The macroscopic quantities can be obtained by calculating the moments of the distribution function:

$$\rho = \int f \mathrm{d}\mathbf{e} \tag{2-16}$$

$$\rho\mathbf{u} = \int \mathbf{e} f \mathrm{d}\mathbf{e} \tag{2-17}$$

$$\frac{S}{2}\rho RT = \int (\mathbf{e}-\mathbf{u})^2 f \mathrm{d}\mathbf{e} \tag{2-18}$$

2.3.2.1 Lattice structures

In order to solve Eq. (2-15) numerically, the phase space needs to be discretized. The discretization needs to be done to make sure the necessary symmetries are retained and the integration of the distribution function moments (e.g., Eqs. (2-16) to (2-18)) can be preserved exactly using Gaussian quadrature:

$$\int \psi(\mathbf{e}) f \mathrm{d}\mathbf{e} \equiv \sum_i t_i \psi(\mathbf{e}_i) f_i \tag{2-19}$$

where $\psi(\mathbf{e})$ is a polynomial of $\mathbf{e}$ and t_i is the weight coefficient of the quadrature. In the process of recovering Navier-Stokes equations, up to the fourth order of the distribution function moments will be used and therefore need to be preserved by the Gaussian quadrature in Eq. (2-19). With the constraints of Eq. (2-19) and necessary symmetries, for a given lattice model one can obtain the weight coefficients and the following constraints [136]:

$$RT = c_s^2 \tag{2-20}$$

$$\sum t_i = 1;\ \sum t_i \mathbf{e}_i = 0;\ \sum t_i \mathbf{e}_i \mathbf{e}_i = c_s^2 \delta_{\alpha\beta};\ \sum t_i \mathbf{e}_i \mathbf{e}_i \mathbf{e}_i = 0; \tag{2-21}$$

$$\sum t_i \mathbf{e}_i \mathbf{e}_i \mathbf{e}_i \mathbf{e}_i = c_s^4 \left[\delta_{\alpha\beta}\delta_{\gamma\delta} + \delta_{\alpha\gamma}\delta_{\beta\delta} + \delta_{\alpha\delta}\delta_{\beta\gamma}\right];\ \sum t_i \mathbf{e}_i \mathbf{e}_i \mathbf{e}_i \mathbf{e}_i \mathbf{e}_i = 0$$

where $\delta_{\alpha\beta}$ is the Kronecker delta, $\alpha, \beta, \gamma, \delta$ are dimensions of the space, c_s is a lattice constant and often identified as the lattice "sound of speed" that depends on the lattice structure model, which is typically referred to as *d*-dimensional *b* velocity *DdQb* model. A typically used lattice model is *D3Q19*, which has:

$$c_s^2 = \frac{1}{3};\ t_0 = \frac{1}{3}; t_{1-6} = \frac{1}{18}; t_{7-18} = \frac{1}{36} \tag{2-22}$$

Other typical lattice models are summarized in Appendix A. The Maxwell-Boltzmann distribution function in Eq. (2-13) can be expanded retaining the terms up to O($\mathbf{u}^2$) under small Mach number assumption:

$$f_i^{eq} = t_i \rho \left[1 + \frac{\mathbf{e}_i \cdot \mathbf{u}}{c_s^2} + \frac{(\mathbf{e}_i \cdot \mathbf{u})^2}{2c_s^4} - \frac{\mathbf{u} \cdot \mathbf{u}}{2c_s^2}\right] \tag{2-23}$$

The same coefficients can also be derived for the lattice gas Boltzmann model as presented in the previous section. The discretized Boltzmann equation then becomes:

$$\frac{\partial f_i}{\partial t} + \mathbf{e}_i \cdot \nabla f_i = -\frac{f_i - f_i^{eq}}{\lambda} + \mathbf{F} \cdot \frac{\mathbf{e}_i - \mathbf{u}}{\rho c_s^2} f_i^{eq} \tag{2-24}$$

2.3.2.2 Chapman-Enskog multiscale analysis

In order to relate the discretized Boltzmann equation to the Navier-Stokes equations, it is necessary to separate physical phenomena occurring on different scales via the Chapman-Enskog multiscale expansion. The particle distribution function can be expanded around its equilibrium state as:

$$f_i = f_i^{eq} + \epsilon f_i^{(1)} + \epsilon^2 f_i^{(2)} + \mathrm{O}(\epsilon^3) \tag{2-25}$$

where ϵ is identified as the Knudsen number, which is defined as the ratio of the molecule mean free path l (i.e., average distance travelled by a moving molecule between successive collisions) to the characteristic scale of the system L:

$$\epsilon = \frac{l}{L} \tag{2-26}$$

When the Knudsen number is very small, the materials can be considered as a continuous medium. Therefore, the Knudsen number is introduced as a small number in the Chapman-Enskog theory to keep track of the scales. The time and spatial derivatives can be expanded in a similar way:

$$\frac{\partial}{\partial t} = \epsilon \frac{\partial}{\partial t_1} + \epsilon^2 \frac{\partial}{\partial t_2} + \mathrm{O}(\epsilon^3) \tag{2-27}$$

$$\nabla = \epsilon \nabla^{(1)} + \mathrm{O}(\epsilon^2) \tag{2-28}$$

where the spatial derivative is not expanded beyond its first order term. The higher order terms in the expansions represent the influences of a longer timescale and a larger spatial

scale. By assuming the external body force acts on a longer timescale and a larger spatial scale than particle collisions (i.e., $\mathbf{F}$ is treated as a second order term), equations on different scales can be obtained by expanding Eq. (2-24) with the expansions of particle distribution function and time and spatial derivatives:

$$\epsilon: \frac{\partial f_i^{eq}}{\partial t_1} + \mathbf{e}_i \cdot \nabla^{(1)} f_i^{eq} = -\frac{f_i^{(1)}}{\lambda} \tag{2-29}$$

$$\epsilon^2: \frac{\partial f_i^{eq}}{\partial t_2} + \left(\frac{\partial}{\partial t_1} + \mathbf{e}_i \cdot \nabla^{(1)}\right) f_i^{(1)} = -\frac{f_i^{(2)}}{\lambda} + \mathbf{F} \cdot \frac{\mathbf{e}_i - \mathbf{u}}{\rho c_s^2} f_i^{eq} \tag{2-30}$$

Eqs. (2-8), (2-9), and (2-10) lead to the following constraints:

$$\sum f_i^{(1)} = 0; \sum f_i^{(2)} = 0 \tag{2-31}$$

$$\sum f_i^{(1)} \mathbf{e}_\mathrm{i} = 0; \sum f_i^{(2)} \mathbf{e}_\mathrm{i} = 0 \tag{2-32}$$

Summing Eqs. (2-29) and (2-30) over *i* respectively then yields:

$$\frac{\partial \rho}{\partial t_1} + \nabla^{(1)} \cdot (\rho \mathbf{u}) = 0 \tag{2-33}$$

$$\frac{\partial \rho}{\partial t_2} = 0 \tag{2-34}$$

The mass conservation equation can be obtained by combining Eqs. (2-33) and (2-34):

$$\frac{\partial \rho}{\partial t} + \nabla \cdot (\rho \mathbf{u}) = 0 \tag{2-35}$$

Multiplying Eqs. (2-29) and (2-30) by $\mathbf{e}_\mathrm{i}$ and then summing them up over *i* lead to:

$$\frac{\partial \rho \mathbf{u}}{\partial t_1} + \nabla^{(1)} \cdot \mathbf{\Pi}^{(0)} = 0 \tag{2-36}$$

$$\frac{\partial \rho \mathbf{u}}{\partial t_2} + \nabla^{(1)} \cdot \mathbf{\Pi}^{(1)} = \mathbf{F} \tag{2-37}$$

where

$$\boldsymbol{\Pi}^{(0)} = \sum f_i^{eq} \mathbf{e}_i \mathbf{e}_i = \rho c_s^2 \mathbf{I} + \rho \mathbf{u}\mathbf{u} \tag{2-38}$$

$$\boldsymbol{\Pi}^{(1)} = \sum f_i^{(1)} \mathbf{e}_i \mathbf{e}_i = -\lambda c_s^2 (\nabla \rho \mathbf{u} + \rho \mathbf{u} \nabla) \tag{2-39}$$

where $f_i^{(1)}$ is obtained from Eq. (2-29):

$$f_i^{(1)} = -\frac{t_i \lambda}{c_s^2} \left[\mathbf{Q}_i : \nabla \rho \mathbf{u} - \mathbf{e}_i \nabla : \rho \mathbf{u}\mathbf{u} + \frac{1}{2c_s^2} (\mathbf{e}_i \cdot \nabla)(\mathbf{Q}_i : \rho \mathbf{u}\mathbf{u}) \right] \tag{2-40}$$

where $\mathbf{Q}_i = \mathbf{e}_i \mathbf{e}_i - c_s^2 \mathbf{I}$ and $\mathbf{I}$ is the identity matrix. It should be noted that the microscopic perspective of $f_i^{(1)}$ ($f_i^{(1)}$ is a first order gradient term) is consistent with the macroscopic perspective of $\boldsymbol{\Pi}^{(1)}$ ($\boldsymbol{\Pi}^{(1)}$depends on first order gradient of macroscopic velocity). Therefore, combining Eqs. (2-36) and (2-37) yields the momentum conservation equation:

$$\frac{\partial \rho \mathbf{u}}{\partial t} + \nabla \cdot (\rho \mathbf{u}\mathbf{u}) = -\nabla \rho c_s^2 + \nabla \cdot [\lambda c_s^2 (\nabla \rho \mathbf{u} + \rho \mathbf{u} \nabla)] + \mathbf{F} \tag{2-41}$$

where $\nu = \lambda c_s^2$ is identified as the kinematic viscosity and ρc_s^2 is the pressure of the ideal gas.

2.3.3 Boundary conditions

Implementation of boundary conditions for LBM is generally more complicated than for macroscopic methods because the degrees of freedom (DOFs) of the particle distribution functions are generally more than the boundary constraints that are typically given in terms of macroscopic quantities. Here we present a brief review of several elementary boundary conditions; more complex boundary conditions can be developed using the same principles.

2.3.3.1 Periodic boundary condition

The periodic boundary condition is one of the simplest boundary conditions for particle-based methods in terms of implementation and is designed to isolate the domain of consideration from boundary effects. Due to the particle nature of the lattice Boltzmann method, it can be simply implemented as when one particle distribution function is leaving the domain it enters the domain from the opposite side of the domain as illustrated in Figure 2-2. The periodic boundary condition is directly applied in the microscopic perspective rather than translated from the macroscopic boundary conditions, which makes it easy to implement.

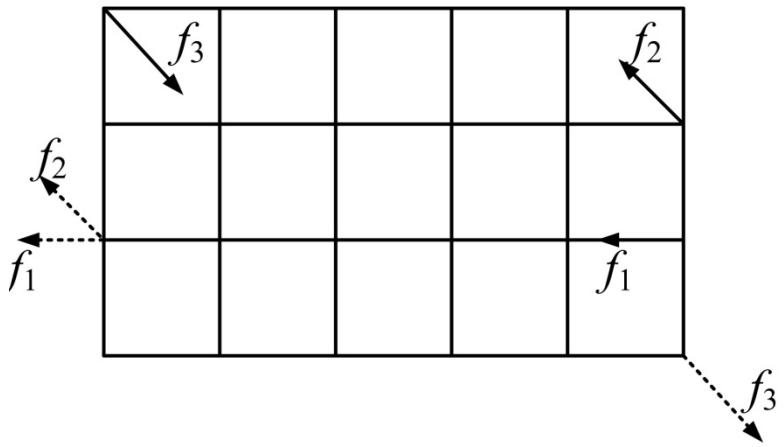

Figure 2-2. Illustration of periodic boundary condition

2.3.3.2 Symmetric boundary condition

The symmetric boundary condition is another simple boundary condition in terms of implementation. Since microscopic symmetry implies macroscopic symmetry, the symmetric boundary condition can be directly applied in the microscopic perspective as well. The symmetric boundary condition is equivalent to the free-slip boundary condition that is typically applied for smooth wall boundaries with negligible friction. The

boundary acts like a mirror that gives specular reflection to impinging particles, which does not transfer any momentum to the wall. As illustrated in Figure 2-3 on lattice site *a*, the incoming distribution function f_2 is unknown after the propagation step, and it is taken the value of f_1 as if it were reflected from f_1, which ensures the velocity component normal to the wall is zero according to Eq. (2-6). A different implementation is to build a symmetric buffer zone as illustrated in Figure 2-3 on lattice site *b*. Before the propagation step, the value of f_3 on lattice site *b* is copied to its symmetric site *b*' about the boundary in a symmetric way and then the propagation step is performed as normal.

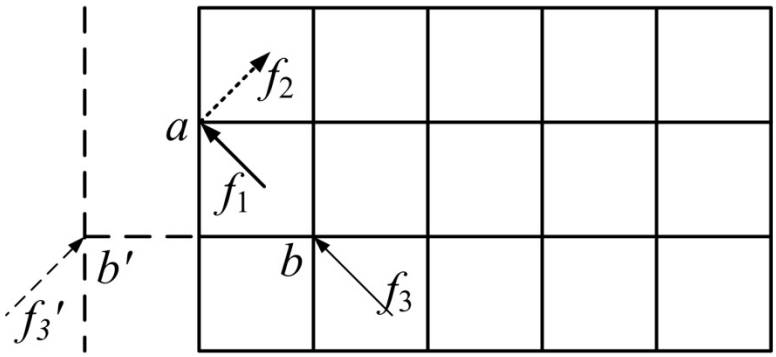

Figure 2-3. Illustration of symmetric boundary condition

2.3.3.3 No-slip boundary condition

The no-slip condition is a common macroscopic boundary condition that is often applied when zero fluid velocity is assumed at a solid wall. In order to apply it to the LBM scheme, the particle distribution functions on the boundary need to be determined to satisfy the zero-velocity constraints. It is apparent this is an under-constrained problem because the number of particle distribution functions that need to be determined are greater than the number of velocity constraints. Therefore, additional constraints need to

be introduced to fully determine the particle distribution functions. One of the most popular approaches is the so-called "bounce-back" scheme, where the particle distribution functions are sent back to where they come from. There were two types of implementation depending on whether the wall boundary lies on the lattice grid or half-way in between two lattice grids, which are often referred to as on-grid or mid-grid bounce-back respectively. Bouzidi et al. devised a more general bounce-back scheme no matter where the wall boundary is located in between of grids [137]. A different approach to implement the no-slip condition is the "wet node" approach, which treats the boundary nodes as part of the fluid and require a compliance with the Chapman-Enskog multiscale analysis. Various implementations have been proposed, such as the Inamuro boundary condition [138], Zou-He boundary condition [136], regularized boundary condition [139], etc. A complete review and comparison of the "wet node" methods can be found in [140] for simple straight wall boundaries.

2.3.4 Lattice Boltzmann models for multiphase flow

The LBM has been widely used to model multiphase flow and interface phenomena. A number of approaches for modeling inter-particle force have been proposed, of which three models have achieved significant success, including the "Shan-Chen" (SC) model [141-142] that mimics the intermolecular interactions with an empirical forcing "potential" function to correct the velocity field after each time step, the "free-energy-based" model [143-144] that incorporates the thermodynamic effects of complex fluids into a modified equilibrium distribution function resulting from a modified momentum flux tensor using the concept of free-energy functional, and the "He-Shan-Doolen" (HSD) model [135, 145] that provides a solid theoretical foundation for a transition from the

continuous Boltzmann equation to the lattice Boltzmann equation and a different perspective of viewing LBM as a special finite difference approximation of the Boltzmann equation.

2.3.4.1 Shan-Chen model

The Shan-Chen model is one of the earliest and probably most used LB multiphase models. It is based in the lattice gas Boltzmann framework introduced in section 2.3.1. The forcing term is expressed as the sum of the attractive force from its nearest neighbors:

$$\mathbf{F}(\mathbf{x},t) = -G\Psi(\mathbf{x},t)\sum t_i \Psi(\mathbf{x}+\mathbf{e}_i\delta t,t)\mathbf{e}_i \tag{2-42}$$

where $\Psi(\mathbf{x},t)$ is an empirical interaction "potential" function and G is the interaction strength between particles. This forcing term is then used to modify the velocity field using Eq. (2-12). The biggest advantage of this model is its simplicity, and it has been successfully used in simulating several fundamental interfacial phenomena, such as that Laplacian law for static droplets and oscillation of a capillary wave [120]. However, it is difficult to introduce temperature into the model with thermodynamically consistency, and the large spurious currents around the interface cause serious numerical instabilities [146], especially for large density and viscosity ratios. The lack of repulsive force between particles in the model also causes unphysical effects.

2.3.4.2 Free energy model

The free energy model was first introduced by Swift et al. [144]. The basic idea of this model is to replace the idea gas pressure in tensor $\mathbf{\Pi}^{(0)}$ as in Eq. (2-38) with a pressure tensor **P** that is derived from macroscopic interface models, such as the Carh-Hilliard model. Then the equilibrium distribution function f_i^{eq} is modified accordingly to satisfy

this constraint, which therefore ensures that the desired macroscopic equations will be recovered. The major advantage of this model is that the thermodynamics of the complex fluids are properly modeled, since it is derived from the thermodynamically consistent macroscopic models. However, it suffers from the lack of Galilean invariance and it does not take full advantage of the particle nature of the lattice Boltzmann method. The interfacial spurious currents are another major issue for high density and viscosity ratio fluids.

2.3.4.3 HSD model

The HSD model establishes the framework of the discrete Boltzmann model as presented in section 2.3.2 to transition from the continuous Boltzmann equation to the lattice Boltzmann equation. The inter-particle interaction force is not from imposed artificial rules as in the Shan-Chen model, but derived from the approximation of the Enskog's extension of the Boltzmann equation, including both attraction and repulsion [135]. The HSD model is thermodynamically consistent due to its roots in the Boltzmann equation, and it has been successfully applied to simulate the Rayleigh-Taylor instability problem [145]. Because of the density gradient term in the forcing term, the HSD model also suffers from interfacial spurious currents for high density ratio fluids.

2.4 Summary

This chapter has surveyed a wide range of subjects in the literature relevant to the objectives of this research. In order to characterize the geometry of the droplet interface, a wide variety of shape representation and characterization techniques are reviewed and categorized and their advantages and disadvantages are analyzed. It is shown that the

feature vector is an effective approach to characterize most of the geometries and the Fourier descriptor is of interest for characterization of various shapes due to its many unique advantages. To study droplet impingement dynamics, a comprehensive survey of the methods for multiphase flow modeling is presented, which are categorized based on the scales of the models, including macroscopic, microscopic and mesoscopic methods. The available commercial and open source codes for these methods are also examined. Compared to other macroscopic multiphase flow modeling techniques, the phase-field method provides great numerical capability and stability for handling complicated interfacial phenomena by treating the interface as a diffusive interface based on thermodynamic principles. The lattice Boltzmann method is thoroughly reviewed for its promising ability to handle multiple-droplet interaction in 3-D. Its origin from the lattice gas automata and its connection to Boltzmann equation are presented. Typical boundary conditions and the principles required to develop complex boundary conditions for the LBM have been examined. Three successful LB multiphase flow models have been briefly reviewed as well.

CHAPTER THREE

INTERFACE CHARACTERIZATION

An interface can be geometrically represented by a shape. Various shape descriptors have been proposed to characterize both 2-D and 3-D shapes for multimedia storage, searching and retrieval as introduced in section 2.1. Shape, as a geometric representation of objects in space, contains rich information about the physics of underlying phenomena. Yet, little research has been reported on connecting the shape representation to fundamental understanding of the physical phenomena to support a capability for the model-based rational design and control of complex processes. This chapter presents an integral metric —a shape coefficient—that is used for characterization of the droplet shape during impact in order to establish a foundation for side-by-side quantitative comparison of desired and physically-realizable shapes.

3.1 Droplet Interface Characterization in 2-D

For a single droplet impingement, droplet shape can be represented axi-symmetrically in 2-D. Methods of 2-D shape representation can be categorized generally into the contour-based and region-based methods [147]. The contour based method is chosen due to the relatively simple characteristics of droplet shape, wherein most of the droplet shape information is contained in the droplet boundary. Since the objective is to achieve a uniform film upon the impact of a single droplet (i.e., to flatten the droplet to a pancake like structure), the shape metric is defined by measuring the similarity between the actual droplet shape and the desired shape (i.e. a rectangle in 2-D cross-sectional space or a cylinder in 3-D).

3.1.1 Interface characteristic function

In order to study droplet shape evolution, the droplet image at each time instant can be obtained from the simulation, as representatively shown in Figure 3-1(a). Since the axis of rotation (the left-hand-side edge in Figure 3-1(a)) is not part of the droplet boundary and thus should not be included in the droplet contour, a mirror operation is performed on a half-space droplet representation shown in Figure 3-1(a), resulting in a full droplet cross section in Figure 3-1(b). The latter contour representation includes only physical interfaces of a droplet projected on a 2-D space which are then processed with a modified Moore-Neighbor tracing algorithm [84] to obtain the droplet contour as shown in Figure 3-1(c).

(a) (b) (c)

Figure 3-1. (a) Half of a droplet cross section (symmetric about the vertical axis of rotation at the left edge) at one time instant obtained directly from simulation; (b) Full cross section of a droplet by mirror imaging of the half-space image in (a) about the axis of rotation; (c) Droplet contour obtained with Moore-Neighbor tracing algorithm.

To characterize the droplet contour, the centroid distance is used as a shape signature [66]. Let the coordinates of the points on the contour obtained from image processing be ($x(j)$, $y(j)$, where j=1,2,...N and N is the total number of points). We can calculate the centroid of the droplet contour as:

$$x_c = \frac{1}{N}\sum_{j=1}^{N} x_j \; ; \; y_c = \frac{1}{N}\sum_{j=1}^{N} y_j \tag{3-1}$$

The normalized centroid distance can be defined as:

$$r(j) = \sqrt{(x(j) - x_c)^2 + (y(j) - y_c)^2}/D_0 \tag{3-2}$$

where D_0 is the droplet diameter. Note that the points on the contour acquired from image processing are not evenly distributed and are highly dependent on the specific image and the image processing algorithm and thus cannot be directly used to compare the droplet shape from different images. Although Eq. (3-2) shows that the centroid distance is a function of the coordinates (*x, y*), a closer look can show that it is a one-dimensional function that only varies with one independent variable, since *x* and *y* are related on the contour. A natural choice of the independent variable for the centroid distance would be the polar angle with respect to the centroid. However, during droplet impingement the droplet shape could sometimes be deformed significantly such that the centroid distance changes rapidly with the polar angle. According to the Nyquist–Shannon sampling theorem, a very high sampling frequency would be required to obtain sufficient information so that the droplet shape can be recovered from discretely sampled points, which leads to high computational cost and sensitivity to image noises. Therefore, we used the distance *d* along the contour with respect to a reference point (e.g., the starting point of the contour chosen to be the left bottom corner point) as the independent variable, so that the centroid distance will not change very fast with it no matter what the droplet shape looks like. Then we can plot the centroid distance of a droplet contour as a function of the normalized distance *nd* (defined as *d*/perimeter of the contour) as shown in Figure 3-2. So a droplet contour can be characterized by the function *r(nd)*. If a finite

number of points is taken on the contour, the characteristic function *r(nd)* becomes a characteristic vector for the droplet shape, which is rotationally and translationally invariant as long as the same reference point is used.

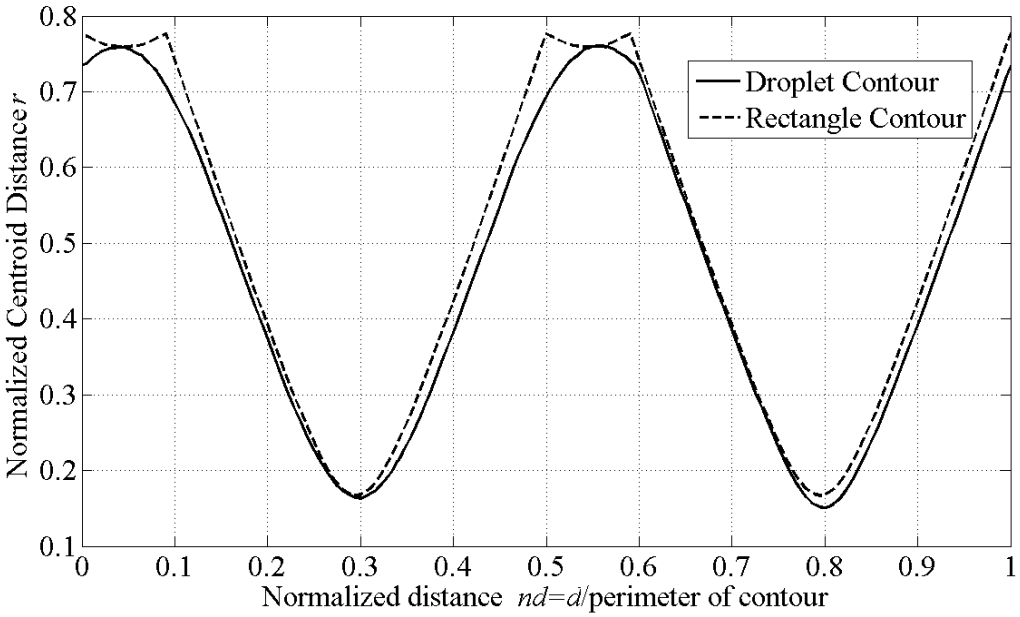

Figure 3-2. Centroid distance *r* as a function of normalized distance *nd* for droplet and rectangle contours.

The desired geometry is defined as a rectangle that circumscribes the droplet contour as shown in Figure 3-3; its characteristic function is plotted as the dashed line in Figure 3-2.

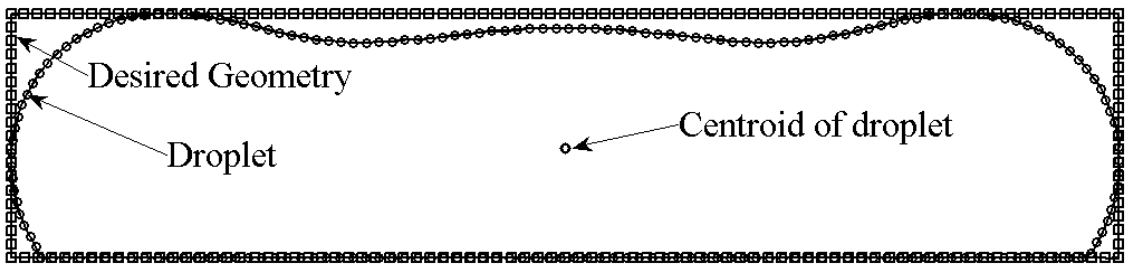

Figure 3-3. Uniform sampling of droplet contour and the contour of the desired geometry.

3.1.2 Interface quantification

Now, measurement of the similarity between two shapes becomes computation of the "distance" between the two functions defined in the same domain in Figure 3-2 using one of the possible metrics for the norm of the space. Since the contours are obtained numerically from discrete point image processing, we need to sample these two functions at the same normalized distance in order to turn these two functions into two vectors, and then measure the distance in the vector space. With the points obtained from the image processing algorithm, a piecewise cubic spline is used to fit the shape functions of $r(nd)$ and then N_s points are sampled at normalized distance $nd = i/N_s$ (where i = 0, 1...N_s) to obtain the characteristic vectors r_d and r_r for the droplet and a desired shape, respectively. To this point, we have developed an approach to measure the similarity between the two shapes in terms of a distance between the two characteristic vectors that parameterize the shape contours. But there are two reasons that we want to take a further step to measure the similarity between the shapes in the frequency domain by taking a Fourier transform of these two vectors. First, if there is a sharp spike somewhere on the droplet contour caused by noise in image processing or acquisition, it can be easily eliminated in the frequency domain using low pass filtering. Second, if the droplet is scaled differently during the image processing, the characteristic vectors will be scaled, as well as the distance between them, and it is relatively easier to normalize in frequency domain by the DC component of the shape due to its averaging characteristics.

Thus, a discrete Fourier transform of the characteristic vectors is computed by Eqns. (18) and (19):

$$R_d(k) = \left[\frac{1}{N_s}\sum_{j=1}^{N_s} r_d(j)\exp\left(\frac{2\pi i(j-1)(k-1)}{N_s}\right)\right] \Big/ R_d(1) \tag{3-3}$$

$$R_r(k) = \left[\frac{1}{N_s}\sum_{j=1}^{N_s} r_r(j)\exp\left(\frac{2\pi i(j-1)(k-1)}{N_s}\right)\right] \Big/ R_d(1) \tag{3-4}$$

where R_d and R_r are the Fourier characteristic vectors for droplet and rectangle, respectively, and $R_d(1)$ is the DC component of vector R_d. Normalizing both R_d and R_r by $R_d(1)$ eliminates the baseline scaling effect, but keeps the relative distance between the vectors unchanged. Note that no low pass filter needs to be applied to eliminate the high frequency image noises because N_s determines the high cutoff frequency since the fundamental frequency is determined by the length of the signal that is fixed at 1 as shown in Figure 3-2.

With the Fourier characteristic vectors, we can thus define a shape coefficient to measure the similarity between the simulated or experimentally observed droplet shape and the desired target shape by measuring the Euclidean distance between the two Fourier characteristic vectors:

$$S_C = 1 - \sqrt{\sum_{j=1}^{N_s} |R_d(j) - R_r(j)|^2} \Big/ \sqrt{\sum_{j=1}^{N_s} |R_r(j)|^2} \tag{3-5}$$

The shape coefficient S_C ranges from 0 to 1, with unity corresponding to the perfect match between the realized droplet shape and the desired geometry. With this definition of the shape coefficient, we also need to determine how to choose an appropriate N_s, which cannot be too small such that the approximation error is too large and cannot be too large such that high frequency noise is introduced. As shown in Figure 3-4, the shape

coefficient converges to a limiting value as N_s increases, and when N_s approaches 200, less than 0.1% relative error is observed for the specific case of droplet shapes considered in this study.

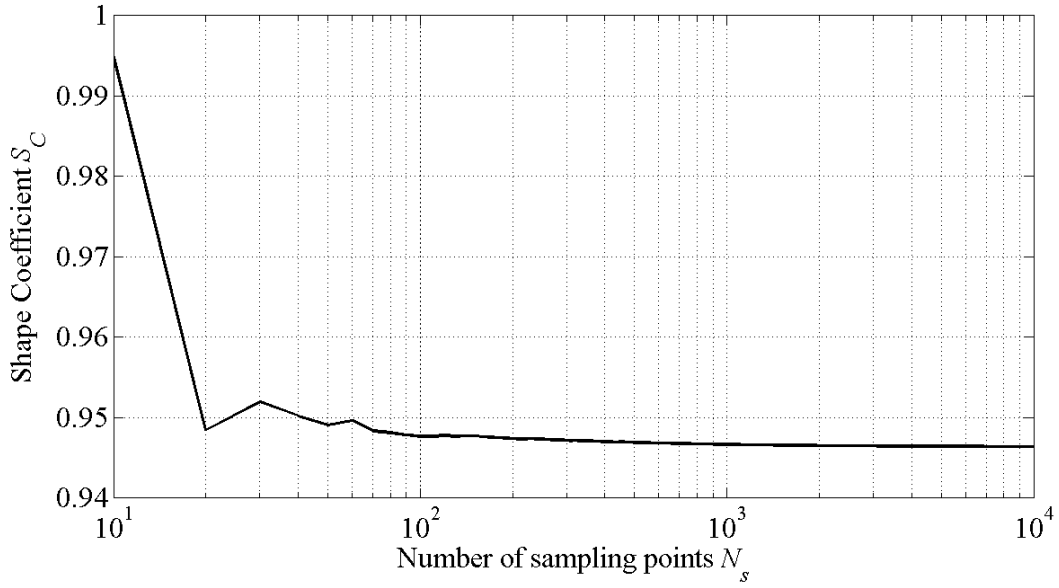

Figure 3-4. Shape coefficient change with number of sampling points.

3.1.3 Effectiveness verification

The effectiveness of the shape coefficient in capturing droplet shape upon impact is exemplified in Figure 3-5. Simulations were performed for a Weber number of 17.9, a Reynolds number of 49.77, and a Froude number of 50968. The shape coefficient, along with the realized and desired (rectangular) droplet shapes at three different time instants, is plotted as a function of time from the moment of impact until the final equilibrium is attained. As one can see from the inset figures, the similarity of droplet shapes is well captured by maximizing the shape coefficient. The change of the spread factor with time is also plotted for comparison. As we can see, the shape coefficient is able to capture more details of the droplet spreading than the spread factor. In the early stages of droplet

impact, the shape coefficient oscillates significantly, indicating significant changes in droplet shape. However, the spread factor hardly changes and provides much less insight into changes in droplet shape. In addition, the maximum shape coefficient occurs at a different time than the spread factor and usually occurs before the maximum spread factor as shown in Figure 3-5 and discussed in our previous work [148]. While this work focuses on shape evolution and on attaining an optimal shape upon impact of a single droplet, it would be of significant practical interest to consider a problem of the liquid film shape evolution upon impingement of multiple interacting droplets. While the physics of interacting droplets will obviously be more complex, the shape coefficient introduced in this section will still be a valid metric to use for assessing the behavior of the deposited liquid layer in respect to its similarity to a desired shape as dictated by the target application.

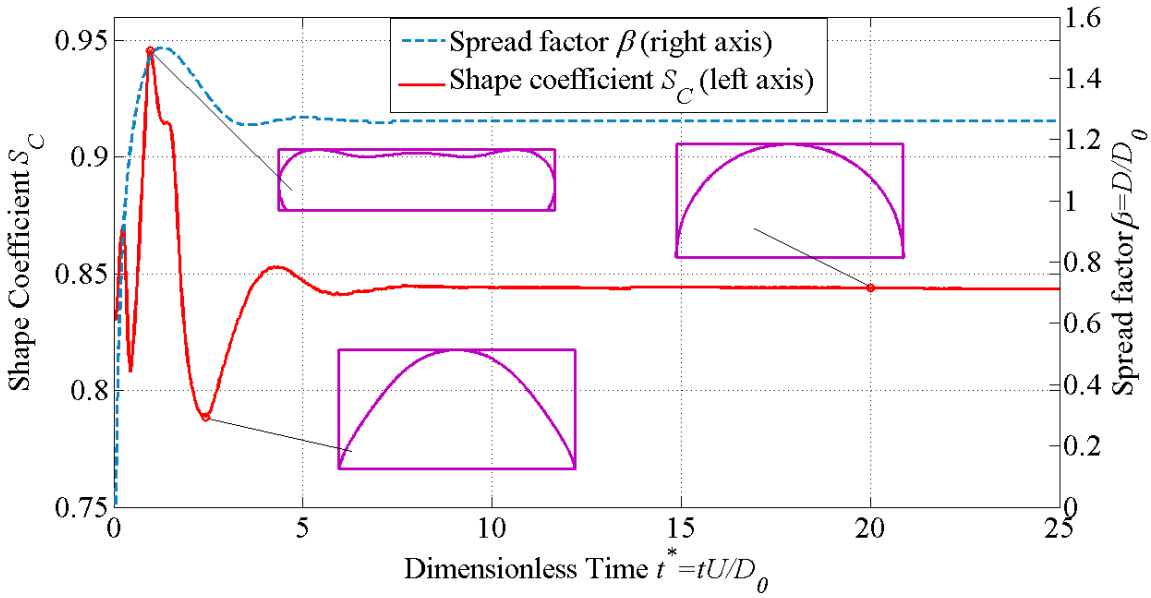

Figure 3-5. Change of shape coefficient and spread factor with time during the droplet impingement.

3.2 Droplet Interface Characterization in 3-D

Since 3-D simulations are needed for multiple droplet impingement, a 3-D shape metric is thus required to study the shape evolution. For 3-D shape characterization, there are volumetric representations, surface representations and view-based representations [83]. For the same reason we chose the contour based method in 2-D, the surface representation is chosen to characterize droplet in 3-D, and the same centroid distance idea is used. The desired shape for a thin film in 3-D can be either a cylinder or a cuboid and therefore two different definitions are proposed for cylindrical and cubic desired shapes respectively.

3.2.1 Cylindrical desired shape

We can readily extend the idea in the 2-D shape coefficient definition to 3-D for a cylindrical desired shape as explained in the following. First, the 3-D droplet shape data at each time point is obtained from our 3-D simulation as shown in Figure 3-6.

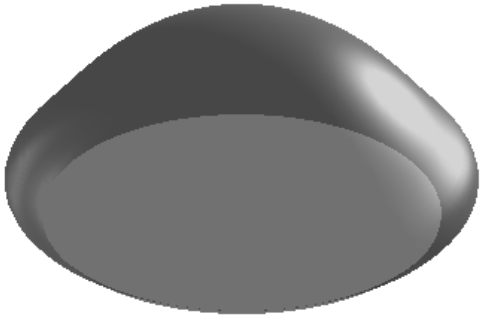

Figure 3-6. Three dimensional droplet shape at one time instant during the droplet impingement.

Due to the difficulty of tracing the surface boundary in 3-D, this step is delayed, and the centroid of the droplet can be calculated as (x_c, y_c, z_c) by taking average of the coordinates

of all the points in the droplet volume. Assuming the coordinates of the points on the droplet surface boundary are (x_b, y_b, z_b), the centroid distance can be calculated as:

$$r(x_b, y_b, z_b) = \sqrt{(x_b - x_c)^2 + (y_b - y_c)^2 + (z_b - z_c)^2}/D_0 \quad (3\text{-}6)$$

It can be found that there are only two independent variables for the function $r(x_b, y_b, z_b)$ since (x_b, y_b, z_b) are related by the droplet surface boundary. In order to uniformly sample the function $r(x_b, y_b, z_b)$, we need to choose two appropriate independent variables for the function. In other words, we need to find a way to map the droplet surface boundary to a plane. We chose the longitudinal coordinate and the latitudinal coordinate by treating the droplet like a sphere as shown in Figure 3-7. Unlike the earth using longitude and latitude as coordinates, we chose the normalized longitudinal distance L_o and latitudinal distance L_a, which are defined as the distances to the reference points along the longitudinal and latitudinal contour normalized by the perimeter of the contour respectively in the same way as the normalized distance *nd* is defined in 2-D. The "equator" is the horizontal cross section that passes the centroid of the droplet.

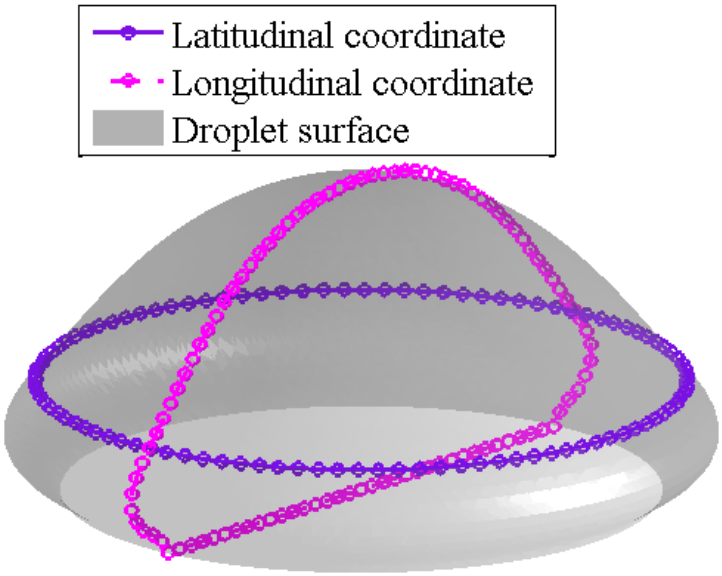

Figure 3-7. Longitudinal and latitudinal coordinate for droplet surface.

Therefore, the centroid distance function $r(x_b, y_b, z_b)$ becomes a two dimensional function $r(L_o, L_a)$ with both L_o and L_a varying from 0 to 1. The points on the surface boundary are then sampled at the coordinates $(L_o = i/N_{so},\ L_a = j/N_{sa})$ (where i, j are from 0 to N_{so}, and N_{sa} respectively) by taking cross sections of the droplet at the specified coordinates, and the imaging processing and sampling in 2-D are performed in the same way as described above. The desired geometry in 3-D is a cylinder that circumscribes the droplet and we can do the sampling on the desired geometry in the same way. The characteristic centroid distance matrices of both the droplet and the cylinder are plotted against L_a and L_o as shown in Figure 3-8.

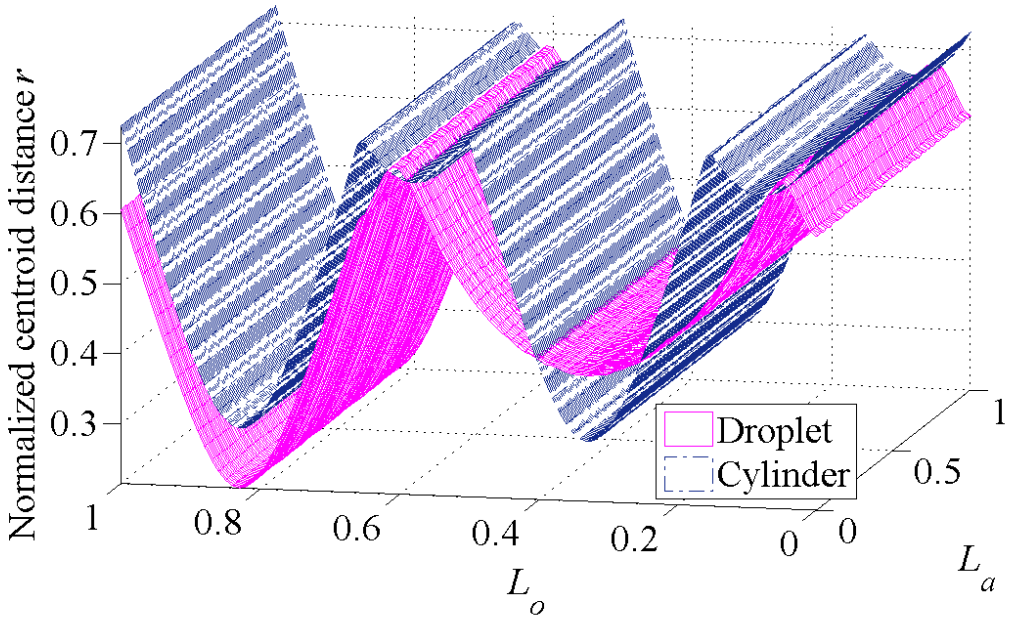

Figure 3-8. Centroid distance as a function of normalized longitudinal distance L_o and latitudinal distance L_a for both droplet and the desired geometry -- a cylinder that circumscribes the droplet.

It is worthwhile to point out that the mapping of the droplet surface to the L_a-L_o plane could introduce some errors. Gauss's Theorema Egregium has proven that the surface of a

sphere cannot be represented on a plane without distortion, and we also know that any genus zero surface can be conformally mapped to a sphere. Since the droplet surface remains as a genus zero surface during the impingement if there is no splashing, it would be difficult to map the droplet surface to a plane without distortion, which means we cannot get an uniform sampling on the droplet surface even if we sample the mapped plane uniformly. Therefore, an error will be inevitably introduced by the mapping. Our choice of longitudinal and latitudinal distances could reduce such an error.

With the characteristic centroid distance matrices for both droplet and the desired geometry cylinder, a 2-D discrete Fourier transform is applied to both matrices, and we can get the characteristic matrices R_{d3} and R_{r3} in the frequency domain for the droplet and the cylinder respectively. And the 3-D shape coefficient can be defined as:

$$S_{C3} = 1 - Norm_2(|R_{d3} - R_{r3}|)/Norm_2(|R_{r3}|) \tag{3-7}$$

where $Norm_2$ means the second norm of the matrix.

For 3-D shape coefficient, we can test its effectiveness by comparing its results with 2D shape coefficient results. A 3-D simulation of a single droplet impingement is conducted. The simulation results are processed with both the 2-D shape coefficient and the 3D shape coefficient to study the shape evolution of the droplet. The 2-D shape of the droplet is obtained by taking a cross section that passes through the axi-symmetrical axis of the droplet. The shape evolution of the droplet is plotted with both 2-D shape coefficient and 3-D shape coefficient as shown in Figure 3-9. As can be seen, the 3-D shape coefficient follows the 2-D shape coefficient very well. They both have the peak and valley at the same time and the trend of the change is about the same. However, there is a noticeable difference in terms of the magnitude of the shape coefficient. This result is expected due

to the uneven sampling of points on the droplet surface in the 3-D shape coefficient definition. Although we did a uniform sampling on the mapped L_a-L_o plane, the sampling was not uniform on the droplet surface due to the distortion of the mapping in the vicinity of the two poles. And the pole area is where the centroid distance of droplet has the smallest difference with the centroid distance of the desired shape – the cylinder. More sampling points around that area weigh toward a smaller difference between the droplet shape and the desired shape (i.e. a larger shape coefficient). Nonetheless, the proposed 3-D shape coefficient can effectively characterize the trend of the shape evolution for a single droplet impingement.

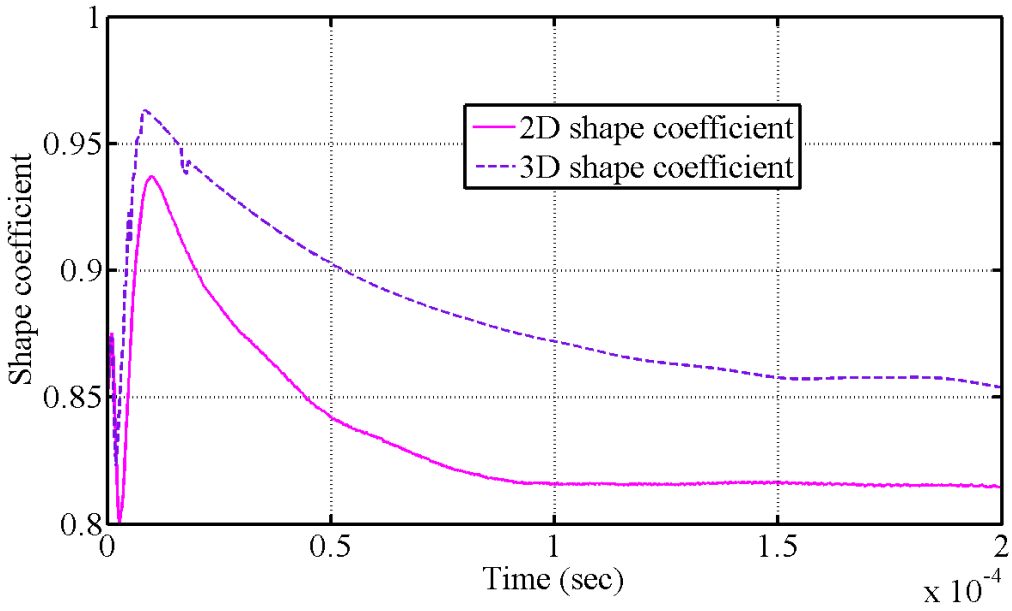

Figure 3-9. Results comparison between 2-D and 3-D shape coefficients for the same simulation of single droplet impingement.

3.2.2 Cuboid desired shape

In most cases a cuboid-shaped thin film is desired. This section presents a 3-D shape coefficient definition with a cuboid desired shape. Let the coordinates of the points on the

droplet surface be represented by (x_b, y_b, z_b). Since (x_b, y_b, z_b) are correlated on the droplet interface, we can reduce the dimension by replacing *(x_b, y_b, z_b)* with two independent variables, which can be understood as a mapping process from a 3-D surface to a 2-D plane. Here we have chosen *x* as one variable defined as $(x_b - x_c)/D_0$ and the normalized distance *nd* at different *x* cross section defined in the same way as in section 3.1 as the second variable, and thus the coordinates (x_b, y_b, z_b) become (x, nd). Next we need to define a characteristic function on the (x, nd) plane to characterize the shape of the droplets, which needs to keep all the coordinates information of the droplet shape. Therefore, we can simply define the characteristic function as:

$$f_0(x, nd) = [(y_b - y_c) + i * (z_b - z_c)]/D_0 \tag{3-8}$$

where y_b and z_b are the *y* and *z* coordinates of the point on the droplet interface at location (x, nd), y_c and z_c are the coordinates of the centroid of the shape, *i* is the imaginary unit, D_0 is the droplet diameter. With this characteristic function, we can readily recover all the information of the shape. A similar characteristic function $f_1(x, nd)$ can be defined for the desired shape. Then we can obtain corresponding characteristic matrices by uniformly sampling the characteristic functions of both the droplet and the desired shape in the (x, nd) plane as illustrated in Figure 3-10. The characteristic functions for the shapes in Figure 3-10(b) are plotted in Figure 3-11.

Following the same procedure as in section 3.2.1, we can define a 3-D shape coefficient by measuring the Euclidean distance of the characteristic matrices in the Fourier domain:

$$S_{C3} = 1 - Norm_2(|(\mathcal{F}(f_0^*) - \mathcal{F}(f_1^*))|)/Norm_2(|(\mathcal{F}(f_1^*))|) \tag{3-9}$$

where the symbol $\mathcal{F}$ means Fourier transform, f_0^* and f_1^* are the characteristic matrices for the droplet shape and the desired shape respectively.

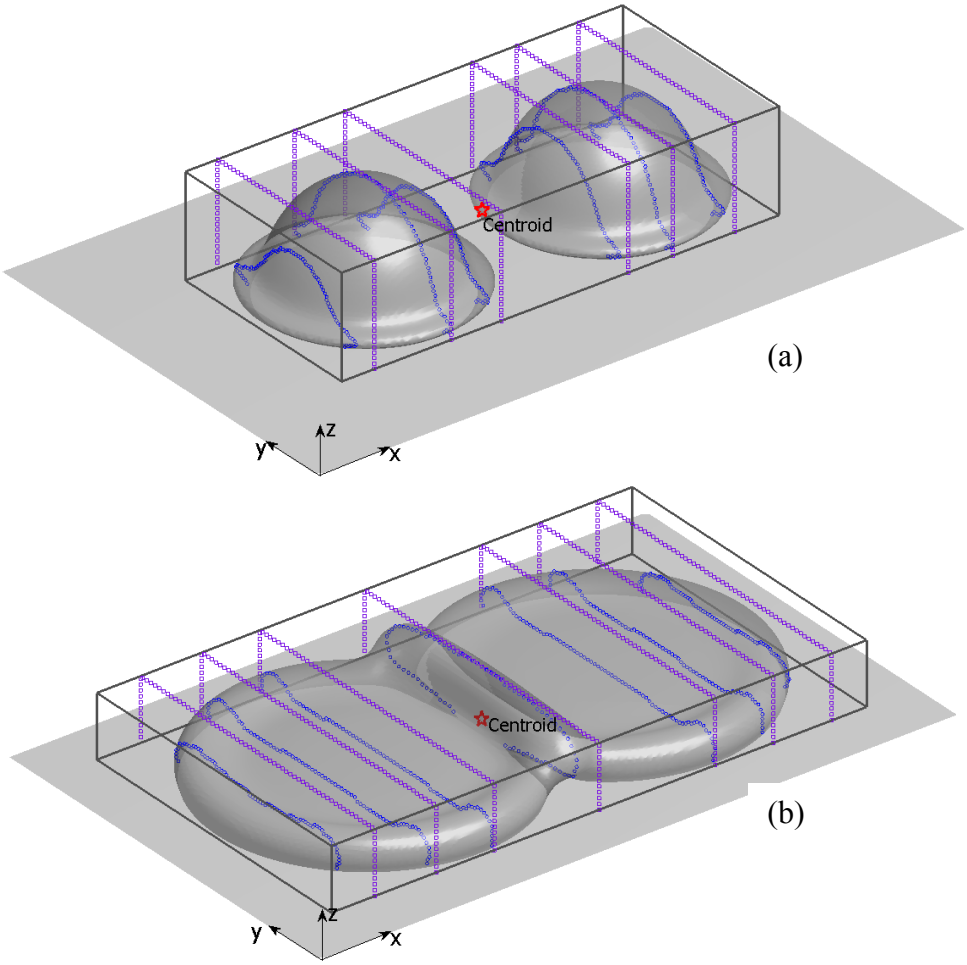

Figure 3-10. Three dimensional shape of multiple droplets at two different time instants during the droplet impingement, where the gray box represents the desired shape, blue circle marker indicates the points on the droplet interfaces, purple square marker symbols the desired shape at different cross sections.

With the defined shape coefficient, we can then test its effectiveness by studying two droplets interacting with each other upon impingement on a solid surface as shown in Figure 3-12. The defined shape coefficient characterizes the similarity between the shape of the droplets and the desired shape fairly effectively. Upon impingement, the two droplets first coalesce together and get closer to a uniform thin film and then relax back under surface tension to the equilibrium shape. To better see the effectiveness of the

shape coefficient, the shape evolution of an-array-of-droplet interacting is plotted in Figure 3-13. The droplets first spread on the surface and during the interface coalescence a thin film is formed at the very bottom of the surface, which results in the decrease of the shape coefficient as shown in the second inset graph of Figure 3-13. Then the droplet interfaces relax back driven by surface tension and form a nearly uniform thin film, the shape coefficient of which is very close to 1, which demonstrates the proposed shape coefficient can characterize very complex geometry effectively.

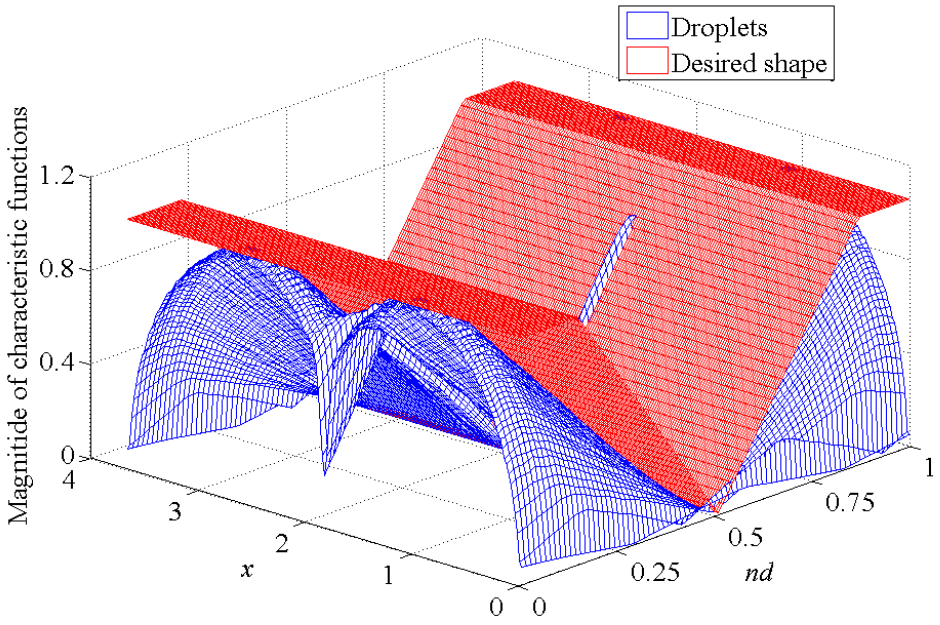

Figure 3-11. Magnitude of the characteristic function as a function of x (normalized by droplet diameter D_0) and normalized distance nd both droplet and the desired geometry -- a cuboid that circumscribes the droplet.

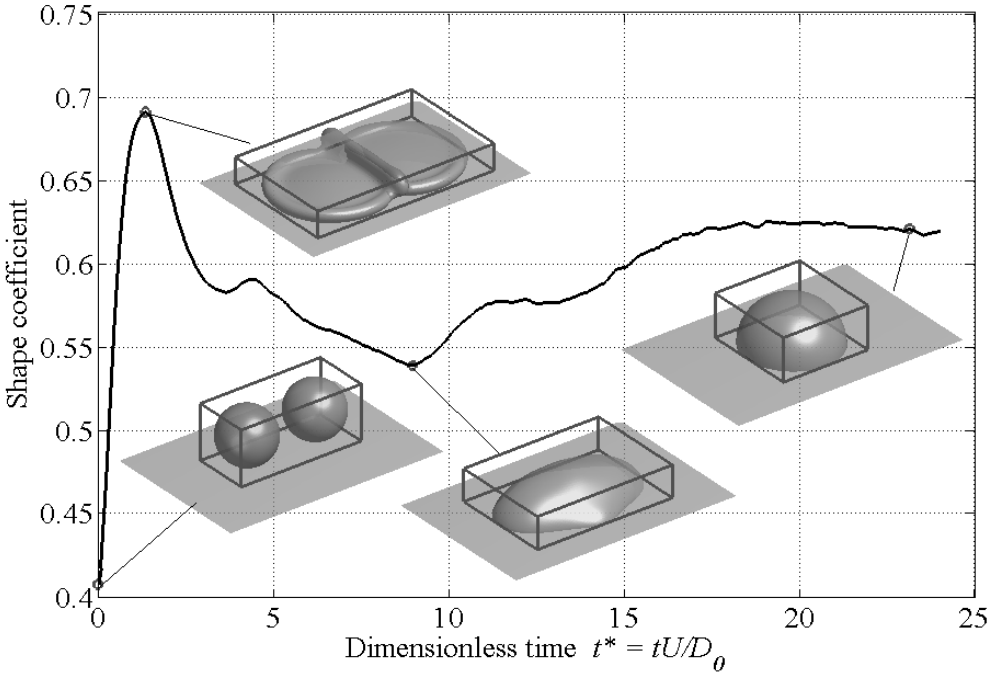

Figure 3-12. Shape evolution of two droplets interacting upon impinging on a solid surface

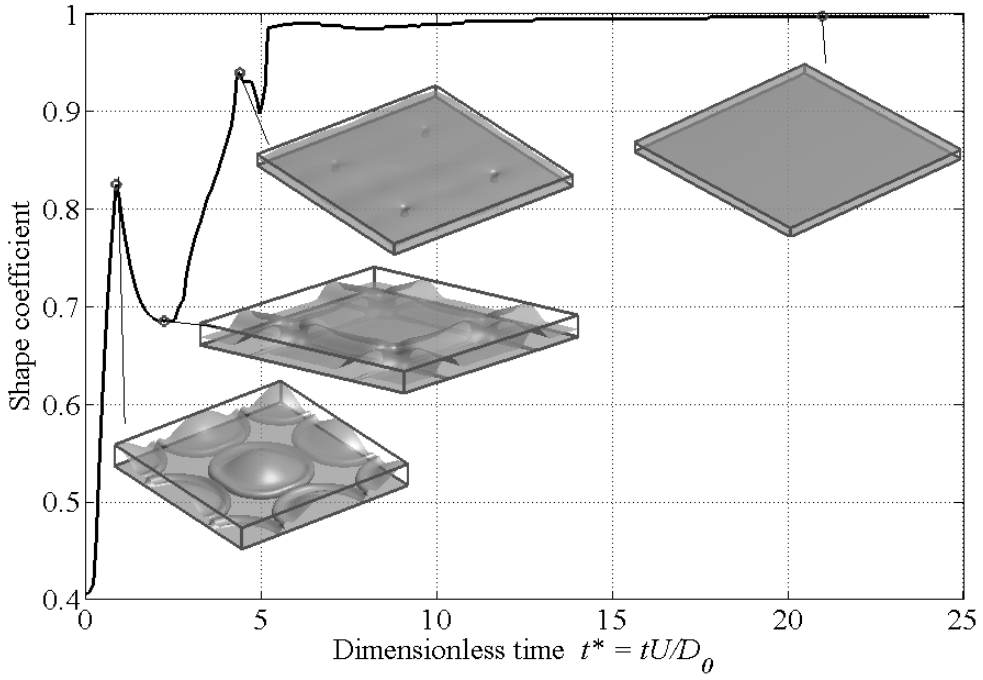

Figure 3-13. Shape evolution of an-array-of-droplet interacting upon impinging on a solid surface

3.3 Summary

The first research questions is studied and the hypothesis is validated that a shape coefficient measuring the similarity between the droplet shape and the desired shape (a uniform film) can effectively characterize and quantify the droplet shape. A 2-D shape coefficient is first defined to study the droplet shape evolution for ink-jet deposition. The procedure of calculating the 2-D shape coefficient and the reasoning behind the procedure are described in detail. The effectiveness of the 2-D shape coefficient is tested and validated. The droplet shape evolution under different impact conditions has been studied with the 2-D shape coefficient and the physical implications of the shape coefficient are revealed. It is found that the inertial force favors large shape coefficient values. The definition of the 2-D shape coefficient is then extended to 3-D. First, a mapping method of the droplet surface to a plane is proposed and analyzed for a desired shape as a cylinder. The effectiveness of the 3-D shape coefficient is tested by comparison with the 2-D shape coefficient. The trend of the shape change agrees well. The difference in the magnitude of the shape coefficient is due to the non-uniform sampling in the 3-D shape coefficient definition, which is caused by the distortion of the mapping from droplet surface to a plane. A different 3-D shape coefficient is then proposed to study multiple-droplet interaction with a desired shape as a cuboid. The effectiveness of the proposed shape coefficient is verified by studying the shape evolution of multiple-droplet interaction.

It should be noted that the proposed shape coefficient only captures the similarity between the evolving droplet shape and a target shape. The information contained in this integrated metric is the target shape combined with a sense of similarity to this target

shape while most of other detailed information on the evolving shape itself is lost. From a designer's perspective, different shape metrics can be defined in a similar way with different designed target shapes, which can then be used for design purposes. In our currently study, the target shape is chosen to be a uniform thin film, which is favored by the inertial force during the droplet impingement and thus connects the defined shape metric to the physical forces as well. Therefore, choosing an appropriate and meaningful target shape is of vital importance in defining a shape metric for studying other physical processes because most of the information of the shape metric is contained in the target shape.

CHAPTER FOUR

INTERFACE EVOLUTION OF SINGLE DROPLET

Numerical simulation has established itself in recent decades as a third approach in addition to physical experiments and theoretical modeling to understand complex systems in physical sciences by using computers to conduct inexpensive "virtual experiments" with properly validated numerical models. Droplet impingement is a century-old scientific problem that has been extensively studied. However, most previous research focuses on studying the change of the droplet spreading radius, which is only marginally relevant to manufacturing. In order to get one step closer to manufacturing, the goal of this chapter is to present an investigation of the underlying physics to improve our understanding of the interface evolution of single droplet impingement with the aid of numerical simulations and the proposed shape coefficient as defined in the previous chapter.

4.1 Numerical Modeling of Single Droplet Impingement

Because droplet impact could be very complicated in the most general case, several assumptions are made to simplify the analysis for the impact conditions of interest.

a) Since the impact velocities of interest are around 10m/s, which is much less than the speed of sound in the fluid, the fluid is assumed to be incompressible.
b) The shape of the droplet may oscillate from prolate to oblate during fall because of the effect of the surrounding atmosphere, which is negligible for droplet diameters less than about 280μm [149]. Since we are concerned with much smaller (10s of

micrometer in diameter) droplet, it is assumed to be spherical throughout the transit period and at impact.

c) The fluid flow is assumed to be Newtonian, and both liquid and gas flow are treated as laminar based on the magnitude of the Reynolds number. The viscosity and surface tension are assumed to be constant during the impact.

d) The droplet and substrate are assumed to be isothermal.

With the assumptions above, the equations of mass and momentum conservation are as follows:

$$\nabla \cdot \mathbf{u} = 0 \tag{4-1}$$

$$\rho \frac{\partial \mathbf{u}}{\partial t} + \rho \mathbf{u} \cdot \nabla \mathbf{u} = \nabla \cdot [-p\mathbf{I} + \eta(\nabla \mathbf{u} + (\nabla \mathbf{u})^T)] + \mathbf{F} \tag{4-2}$$

where ρ is the fluid's density (kg/m^3), **u** is the velocity vector (m/s), p is the pressure (Pa), η denotes the dynamic viscosity (Pa˙s), **F** is the body force and **I** is the identity matrix.

4.1.1 Phase-field model

The phase-field method [99] is adopted to track the movement and deformation of the interface between the liquid phase and gas phase on a fixed grid. Unlike the sharp interface models, such as VOF and level-set as reviewed in section 2.2.1.3, the phase-field method provides a way of modeling interfacial forces as continuum forces by treating the interface as a diffusive interface described by the Cahn-Hilliard equation [150], which ensures the correct dissipation of energy. The commercially available software COMSOL 3.5a is used to implement the model. A phase-field variable C ranging from C_l to C_h is introduced to represent different phases. COMSOL chooses C_l = -1 representing the gas phase, C_h = 1 for the liquid phase, and C_l to C_h across the

interface. The convective Cahn-Hilliard equation describes the evolution of the interface in terms of the phase-field variable,

$$\frac{\partial C}{\partial t} + \mathbf{u} \cdot \nabla C = \nabla \cdot M \nabla \mu \tag{4-3}$$

where M is the mobility (m^3s/kg) and μ is the chemical potential (Pa), which is the derivative of Gibbs free energy with respect to C at constant temperature and pressure. The free energy takes Ginzburg-Landau form for two-phase flow [151]:

$$E(C, \nabla C) = \beta (C - C_l)^2 (C - C_h)^2 + \frac{\kappa}{2} |\nabla C|^2 \tag{4-4}$$

where the first term on the right hand side is the bulk free energy E_0 that strives to separate the phases, and the second term is the gradient energy that tries to mix the phases together, β (Pa) is a constant relating to bulk free energy, κ (N) is a parameter related to surface tension σ (N/m). Minimizing the free energy of the system leads to a constant chemical potential from calculus of variation:

$$\mu = 4\beta (C - C_l)(C - C_m)(C - C_h) + \kappa \nabla^2 C \tag{4-5}$$

where $C_m = (C_l + C_h)/2$. For a plane interface under equilibrium, we can obtain a profile of the phase field variable across the interface from Eq. (4-5):

$$C(z) = \frac{C_h + C_l}{2} + \frac{C_h - C_l}{2} \tanh\left(\frac{2z}{\xi}\right) \tag{4-6}$$

where z is the coordinate normal to the interface, and ξ is the interface thickness, which is given by:

$$\xi = \frac{4}{C_h - C_l} \sqrt{\frac{\kappa}{2\beta}} \tag{4-7}$$

With the profile of the phase field variable, we can obtain the surface tension by integrating the free energy across the interface:

$$\sigma = \frac{(C_h - C_l)^3}{6}\sqrt{2\kappa\beta} \tag{4-8}$$

When the interface thickness ξ approaches 0, the asymptotic limit of the phase field model is the sharp interface model [99]. In this limit, the mobility M and the interface thickness ξ must reduce to 0 at the same time. Thus, a constraint is placed on M and ξ:

$$M = \chi\xi^2 \tag{4-9}$$

where χ ($\mathrm{m \cdot s/kg}$) is a tuning parameter.

Unlike the sharp interface models that have to deal with the discontinuities across the interface to calculate the interfacial force as a surface force from the interface curvatures, the phase-field model treats the interfacial force as a continuum body force $\mathbf{F}_{st}$ within the diffusive interface domain, which is calculated by:

$$\mathbf{F}_{st} = \mu\nabla C \tag{4-10}$$

Taking into account the gravity force $\mathbf{F}_g$, the total body force $\mathbf{F}$ in Eq. (4-2) becomes:

$$\mathbf{F} = \mathbf{F}_g + \mathbf{F}_{st} = \rho\mathbf{g} + \mu\nabla C \tag{4-11}$$

where $\mathbf{g}$ is the gravity vector.

The governing equations are non-dimensionalized based on the following scaling relationship:

$$\mathbf{x}^* = \frac{\mathbf{x}}{L} \quad \mathbf{u}^* = \frac{\mathbf{u}}{U} \quad t^* = \frac{tU}{L} \quad p^* = \frac{p}{\rho_0 U^2} \quad \mathbf{g}^* = \frac{\mathbf{g}}{g_0} \tag{4-12}$$

$$\rho^* = \frac{\rho}{\rho_0} \quad \eta^* = \frac{\eta}{\eta_0} \quad \sigma^* = \frac{\sigma}{\sigma_0} \quad \mu^* = \frac{\mu L}{\sigma_0} \tag{4-13}$$

where L is the characteristic length scale, U is the characteristic velocity, the subscript '0' is for reference values, and the superscript '*' stands for dimensionless. The non-

dimensional governing equations, in which the superscripts '*' are omitted for convenience, are:

$$\nabla \cdot \mathbf{u} = 0 \tag{4-14}$$

$$\rho \frac{\partial \mathbf{u}}{\partial t} + \rho \mathbf{u} \cdot \nabla \mathbf{u} = \nabla \cdot \left[-p\mathbf{I} + \frac{1}{Re}\eta(\nabla \mathbf{u} + (\nabla \mathbf{u})^T) \right] + \frac{1}{Fr}\rho \mathbf{g} + \frac{1}{We}\mu \nabla C \tag{4-15}$$

where *Re* is the Reynolds number, *We* is the Weber number, and *Fr* is the Froude number. The Ohnesorge number *Oh* can be obtained from the Reynolds and Weber numbers, as follows:

$$Re = \frac{\rho_0 U L}{\eta_0} \quad We = \frac{\rho_0 U^2 L}{\sigma_0} \quad Fr = \frac{U^2}{g_0 L} \quad Oh = \frac{\sqrt{We}}{Re} = \frac{\eta_0}{\rho_0 \sigma_0 L} \tag{4-16}$$

To non-dimensionalize the Cahn-Hilliard equation, the chemical potential μ is scaled with diffusion parameters to better reflect μ as the driving force of the diffusion process:

$$\mu^* = \frac{\mu \xi^2}{\kappa} \tag{4-17}$$

and then we can obtain:

$$\frac{\partial C}{\partial t} + \mathbf{u} \cdot \nabla C = \frac{1}{Pe}\nabla^2 \mu \tag{4-18}$$

where *Pe* is the Peclet number, which characterizes the ratio of advection rate to diffusive rate:

$$Pe = \frac{UL\xi^2}{M\kappa} \tag{4-19}$$

4.1.2 Model configuration

The numerical model is implemented using the commercially available software COMSOL 3.5a. A typical case is shown here to illustrate the implementation of the numerical model. Due to the problem symmetry, the droplet and the substrate can be

modeled in a half-domain, as shown in Figure 4-1, where the droplet falls down from a certain distance above the substrate with an initial velocity. The droplet travels downward due to inertia and gravity, impinges on the rigid horizontal wall and spreads. The boundary conditions are shown in Figure 4-1, and the equilibrium contact angle between the droplet and the substrate is set to $\pi/2$. Note that the wall boundary is set as no-slip and it requires no special treatment for the moving contact line with the Phase-Field method because the diffusive interface provides an effective slip length for the contact line to move [152]. The parameters of a typical simulation are listed in Table 4-1. To calculate the dimensionless numbers for droplet impact, the droplet diameter D_0 is taken to be the characteristic length scale and the impact velocity U is taken to be the reference velocity. The reference density and viscosity are set to be the density and viscosity of the liquid droplet. The reference surface tension is set to be the surface tension between the liquid and gas phases.

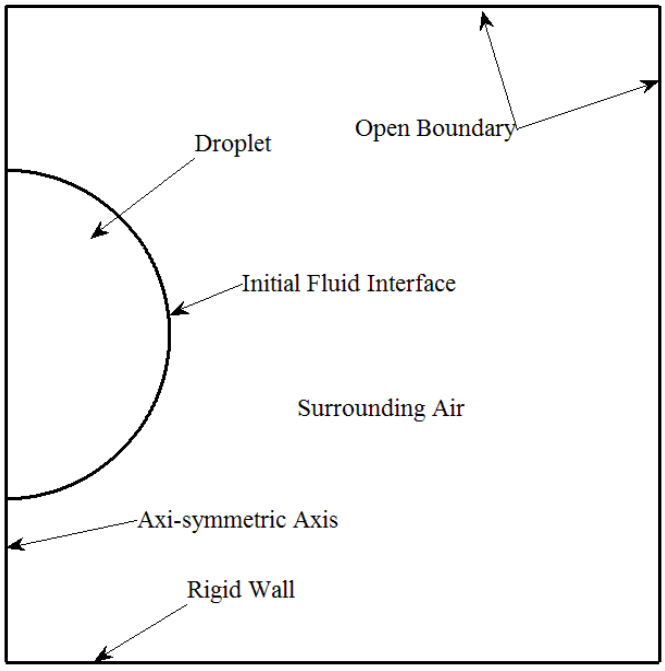

Figure 4-1. Numerical model configuration: geometry and boundary conditions.

Table 4-1. Parameters of a typical simulation.

Medium	Density	Dynamic Viscosity	Surface tension	Initial Velocity	Radius
Droplet	1000 kg/m^3	0.01 Pa·s	0.07 N/m	10 m/s	25 μm
Air	1.225 kg/m^3	1.789E-5 Pa·s			

4.1.3 Validation

In order to validate the numerical model developed, a study of grid independence is conducted first, which includes assessment of the influence of the simulation domain extent and the mesh size refinement. The results of several static and dynamic analytical models are compared with those of the simulations. Finally, the simulation results are compared to the experimental results from literature for the impact condition of interest to additive manufacturing.

4.1.3.1 Grid & domain independence

The "Open Boundary" condition is used in COMSOL to simulate an infinite domain, and we examined if this boundary condition has any effects on the simulation results with different simulation domain sizes. To this end, the boundary length (the length of the boundary marked as "open boundary" as Figure 4-1) was varied from 100μm to 300μm for the simulation parameters in Table 4-1, and the simulation results showed a negligibly small change upon this variation. Therefore, the boundary length of 100μm is sufficient to obtain accurate results for fluid flow simulations. The grid independence validation ensures that the simulation results do not change significantly with different mesh sizes. In our numerical experiments, the minimum grid size of the mesh was changed from 4μm to 2μm and the results show that the mesh size of 4μm can provide sufficient accuracy in predicting the spreading radius and mass conservation.

4.1.3.2 Validation against analytical models

1) Equilibrium factor

The spread factor is defined as the ratio of spreading radius to the initial radius of the droplet, and the equilibrium spread factor is the spread factor when the droplet stops spreading, which is very important to determine the final shape of the droplet. Two analytical models for the equilibrium spread factor are compared with our simulation results. The first model is the spherical model, which assumes that the droplet during spreading maintains a sphere cap shape [153].

$$\beta_{equil} = 2\left[\frac{sin^3\theta_e}{(4 - 6cos\theta_e + 2cos^3\theta)}\right]^{\frac{1}{3}} \tag{4-20}$$

where θ_e is the equilibrium contact angle. For the parameters listed in Table 4-1, the simulation gives the equilibrium spread factor of β_{se}=1.2160, while the analytical result is β_{equil}=1.2599, yielding the relative error $|\beta_{equil} - \beta_{se}|/\beta_{se}$=3.61%. The second analytical model is the cylindrical model, which assumes the droplet spreads as a self-similar cylinder [153]:

$$\beta_{equil} = 2\left[\frac{1}{(6(1 - cos\theta_e)}\right]^{\frac{1}{3}} \tag{4-21}$$

The equilibrium spread factor for this model is β_{equil}=1.1006, and the relative error as compared to simulations is s $|\beta_{equil} - \beta_{se}|/ \beta_{se}$=9.49%.

It can be seen that the simulation result is between that of the spherical and cylindrical models, where two extreme approximations are taken. The droplet shape under these impact conditions is neither a sphere cap nor a cylinder, but is more close to a sphere, which agrees well with results in the literature. Specifically, the results demonstrate that,

for viscous fluids impacting at low velocity, droplet shapes are close to spherical for the entire deposition process, while droplets of low viscosity fluids have a spherical shape after reaching equilibrium, but not during dynamic spreading [153].

2) Maximum spread factor

Maximum spread factor is defined as the ratio of the maximum spread radius of the droplet to its initial radius. The maximum spread factor dictates how the spacing between nozzles in the array needs to be arranged and how the neighbor droplets interact with each other. There are many empirical [154-155] or semi-empirical [156-157] models to predict the maximum spread factor, and the following empirical equation was shown to provide better predictions than other models [158]:

$$\left[0.2Oh^{0.33}We^{0.665} + \frac{1}{4}(1 - cos\theta_e)\right]\beta_{max}^2 + \frac{2}{3}\beta_{max}^{-1} = \frac{We}{12} + 1 \qquad (4\text{-}22)$$

where Oh is the Ohnesorge number, We is the Weber number, β_{max} is the maximum spread factor, and θ_e is the equilibrium contact angle. Two simulations were performed under different impact conditions and compared with the analytical model (Eq. (4-22)), as shown in Table 4-2. It can be seen the simulation results agree well with the analytical results.

Table 4-2. Max spread factor comparison between simulations and analytical model.

	Droplet Radius	Impact Velocity	Dynamic Viscosity	Surface Tension	Simulation Results	Analytical Results	Relative Error
Case1	25μm	10m/s	0.01Pa·s	0.07N/m	1.7632	1.7476	0.88%
Case2	30μm	15m/s	8.94e-4Pa·s	0.072N/m	3.0667	3	2.71%

3) Dynamic spreading

In this section, the results of three well-known 1-D models for dynamic evolution of the wetted area/height of the droplet are compared with those of our numerical simulations under certain impact conditions. The main challenge of the 1-D model lies in the assumed physics of viscous dissipation and in the lack of self-consistency between the description of kinetic energy and that of dissipation. Bechtel et al. [159] first proposed a 1-D model, referred to as the BBT model, to include the change in kinetic energy using a variational method:

$$\frac{1}{12}\frac{d}{dt}\left[\left(\frac{1+2h^3}{2h+h^4}\right)^2\left(\frac{1}{9}h^{-1}+\frac{11}{18}h^2+\frac{26}{45}h^5\right)\left(\frac{dh}{dt}\right)^2\right] \tag{4-23}$$

$$+\frac{d}{dt}\left[\frac{1}{3}[h^{-1}+2h^2-(h^{-1}-h^2)cos\theta_e]\right]$$

$$+\frac{\gamma}{18}Oh\frac{(h^3-1)^2(1+2h^3)^2}{h^4(2+h^3)^2}\left(\frac{dh}{dt}\right)^2=0$$

with the initial conditions:

$$h|_{t=0}=1;\ \frac{dh}{dt}|_{t=0}=-\sqrt{We} \tag{4-24}$$

where

$$h=\frac{H}{D_0};r=\frac{R}{D_0};\ r^2=\frac{1}{3}(h^{-1}-h^2);\ \gamma=\sqrt{\pi}Oh^{-1/2} \tag{4-25}$$

and the coefficient $\sqrt{\pi}$ in the parameter γ is adjustable to the boundary layer thickness [156-160]; H and R are the droplet height and the droplet radius during spreading, respectively; and D_0 is the initial droplet diameter. The comparison of results between the simulation and the BBT model is shown in Figure 4-2, from which we can see that the results agree very well when the coefficient-multiplier of γ goes to 40. It is noteworthy that there is no rigorous calculation of γ and only a rough estimation can be made here.

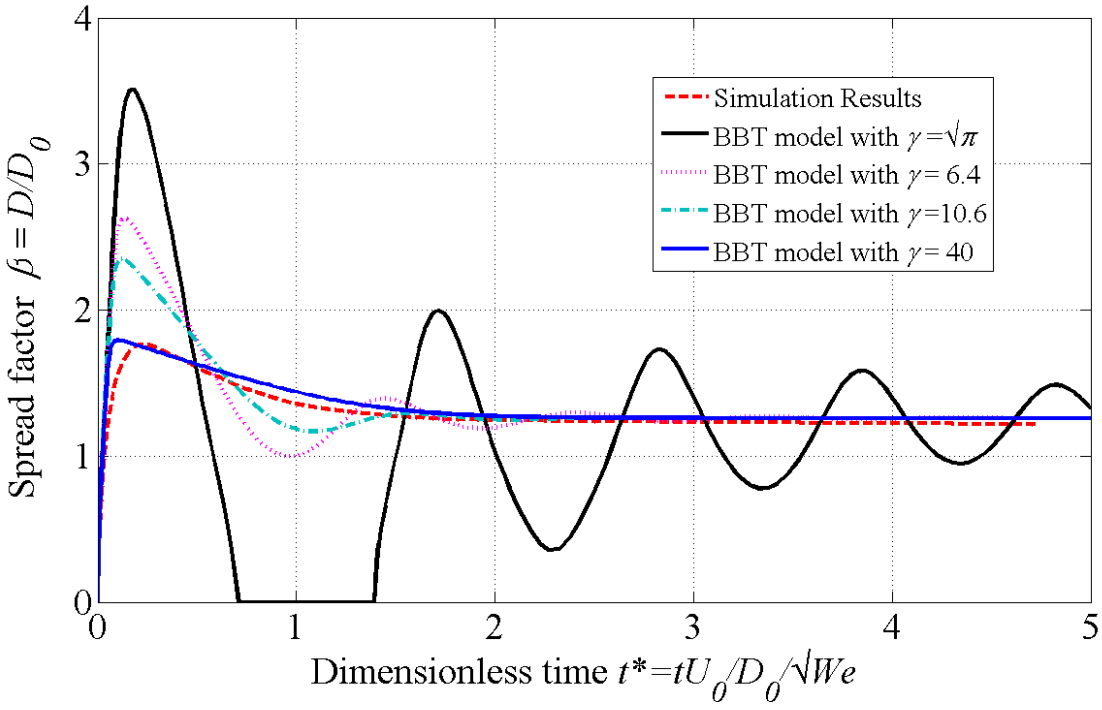

Figure 4-2. Comparison between simulation and the BBT model.

After that, various 1-D models have been proposed [154-158, 160-161]. Since the free surface of low viscosity droplets at its first maximum spreading is far from being spherical, the cylinder form was adopted by Kim et al. [160], which is referred to as the KC model:

$$\frac{1}{12}\frac{d}{dt}\left[\left(\frac{1}{2}+\frac{1}{27}\frac{1}{r^6}\right)\left(\frac{dr}{dt}\right)^2\right]+\frac{d}{dt}\left[r^2(1-cos\theta_e)+\frac{1}{3r}\right] \tag{4-26}$$

$$+\frac{\gamma}{2}Oh\, r^2\left(\frac{dr}{dt}\right)^2=0$$

with the initial conditions:

$$r_0^2(1-cos\theta_e)+\frac{1}{3r_0}=1;\ \frac{dr}{dt}|_{t=0}=\sqrt{We}\left(\frac{1}{2}+\frac{1}{27}\frac{1}{r^6}\right)^{-\frac{1}{2}} \tag{4-27}$$

where

$$r = \frac{R}{D_0};\ \gamma = \sqrt{\pi} Oh^{-1/2} \tag{4-28}$$

As in the BBT model, the coefficient $\sqrt{\pi}$ in the parameter γ is adjustable. The results are compared with simulation results as shown in Figure 4-3. When the coefficient-multiplier of γ goes to 20, the KC model corresponds with the simulation results.

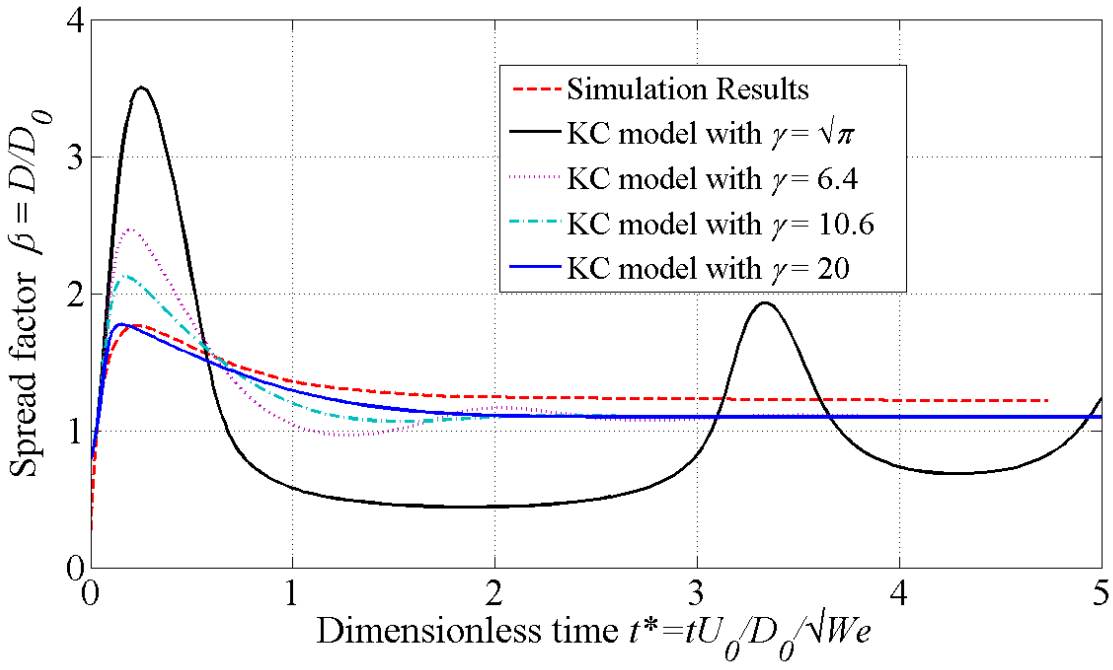

Figure 4-3. Comparison between simulation and the KC model.

Both BBT and KC models assume that the dissipation mainly occurs in the boundary layer. In contrast, Attane et al. [153] used a rimmed cylinder to approximate the shape of the droplet during spreading and further assumed that the rolling motion occurring in the rim promoted an additional dissipation mechanism. They proposed the AGM model:

$$\frac{1}{12}\frac{d}{dt}\left[\left(\frac{2}{3}+\frac{1}{45}\frac{1}{r^6}\right)\left(\frac{dr}{dt}\right)^2\right] + \frac{d}{dt}\left[r^2(1-cos\theta_e)+\frac{1}{3r}\right] \tag{4-29}$$

$$+ 4Oh\left(3r^4 + \frac{2}{3r^2} + sr\right)\left(\frac{dr}{dt}\right)^2 = 0$$

with the initial conditions:

$$[r_0^2(1-cos\theta_e)+\frac{1}{3r_0}]=1\ (\theta_e<109°);\ r_0=0.39\ (\theta_e>109°) \tag{4-30}$$

$$\frac{dr}{dt}|_{t=0}=\sqrt{We}\left(\frac{2}{3}+\frac{1}{45}\frac{1}{r^6}\right)^{-\frac{1}{2}} \tag{4-31}$$

where

$$r=\frac{R}{D_0};\ \ s=1.41Oh^{-\frac{2}{3}} \tag{4-32}$$

and the coefficient 1.41 in the parameter *s* is adjustable. The comparison is shown in Figure 4-4, which indicates that when the coefficient-multiplier goes to 0.45, the early stage of the spreading agrees well, and the long-term spreading dynamics predictions agree well with each other when *s* takes its default value.

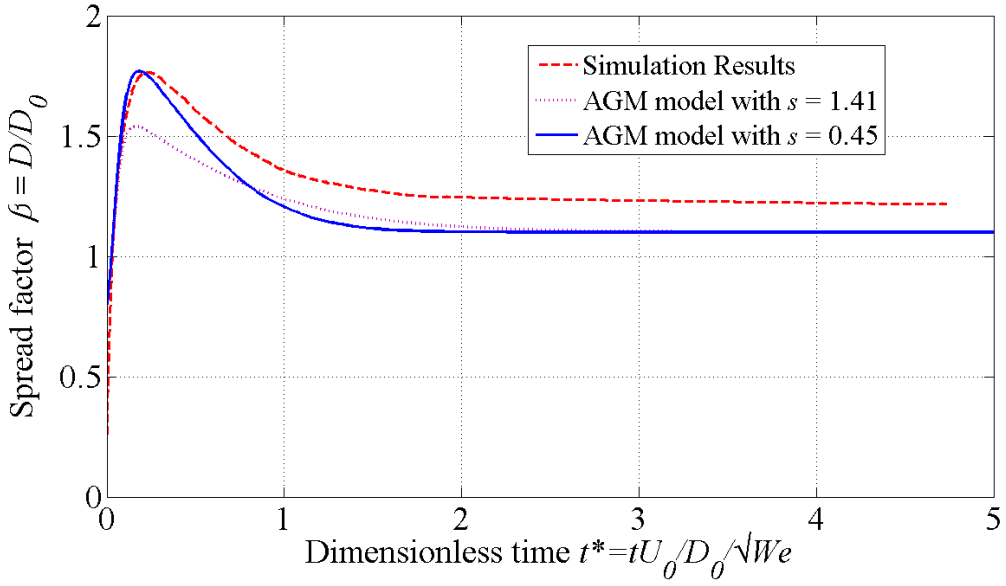

Figure 4-4. Comparison between simulation and the AGM model.

4.1.3.3 Experimental validation

To further validate the numerical model, experimental validation is necessary. Two sets of experimental data are selected from literature to compare with the simulation results.

One is a water droplet with a diameter of 2mm impacting on a steel substrate with Weber number of 27 and contact angle of $\pi/2$ [156]. The results are shown in Figure 4-5 and a good agreement is observed.

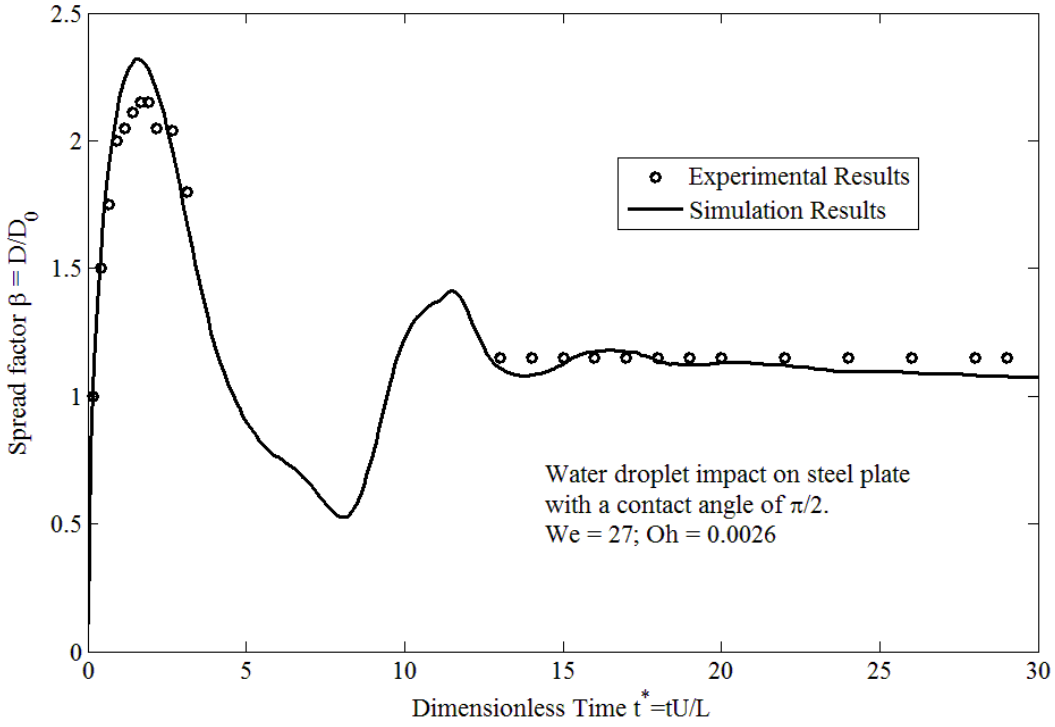

Figure 4-5. Comparison of the spread factor evolution of a water droplet impinging on a steel plate between experiment [103] and simulation.

In order to obtain similar droplet impact behavior to our interests, an experiment with a micron-sized droplet impact is chosen for comparison [162]. The droplet size is 48.8μm and the impact speed is 4.36m/s. The fluid properties of the liquid droplet and the surrounding gas are taken as the properties of water and air at 1 atm and 25°C. The results of the simulation and experiment are compared in Figure 4-6, which shows very good agreement.

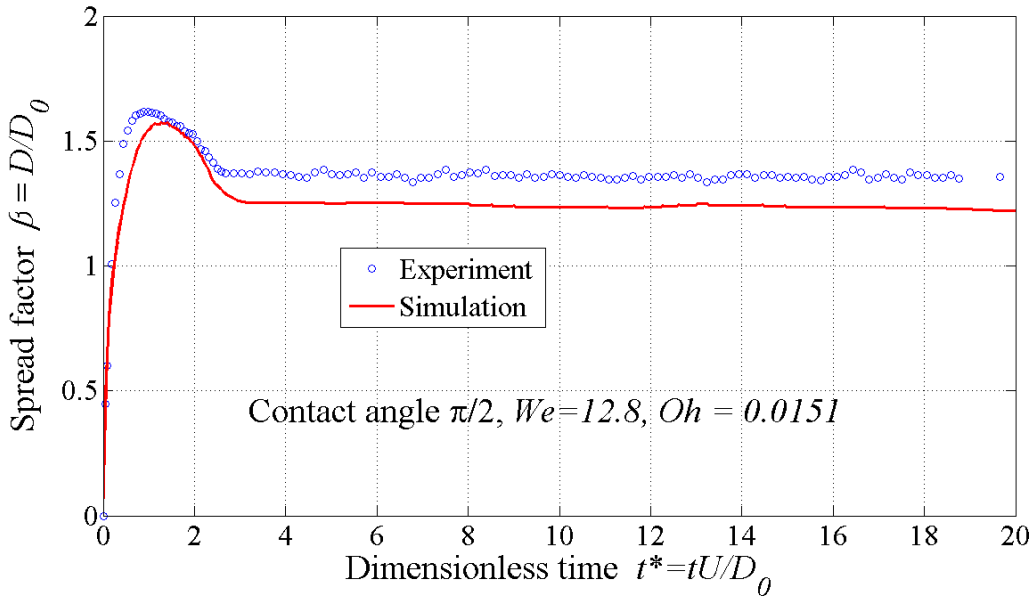

Figure 4-6. Comparison of the spread factor evolution of a micron-sized droplet impinging on a solid surface between experiment [162] and simulation.

4.1.4 Interface evolution under different impact conditions

Based on the dimensionless analysis presented in section 4.1.1, the solutions of the governing equations under different impact conditions will be the same as long as the four dimensionless numbers (i.e., Reynolds number *Re*, Weber number *We*, Froude number *Fr*, and Peclet number *Pe*) match with each other (the contact angle between droplet and solid surface is limited to π/2 in this study unless otherwise specified). The Peclet number *Pe* is a dimensionless number that characterizes the ratio of advection rate to diffusive rate, which should be balanced to avoid thinning or thickening of the fluid interface [99] in the numerical simulations. Therefore, the Peclet number has become a numerical parameter that is used to fine tune the numerical simulations in order to maintain a constant thickness interface. Hence, we will investigate the effects of the rest of the three dimensionless numbers. This section is devoted to studying the droplet

impact behavior under different impact conditions, i.e. different combinations of the dimensionless numbers, so that we can know how to control the impact conditions to make the droplet shape closer to the desired shape. According to [163], the droplet impact behavior is mainly determined by the driving force and the resisting force of the impact and can be divided into four different impact regimes as shown in Figure 4-7. The Weber number can be used to characterize the driving force and the Ohnesorge number, obtained from the rearrangement of Reynolds number and Weber number ($Oh=(We)^{1/2}/Re$), can be used to characterize the resisting force.

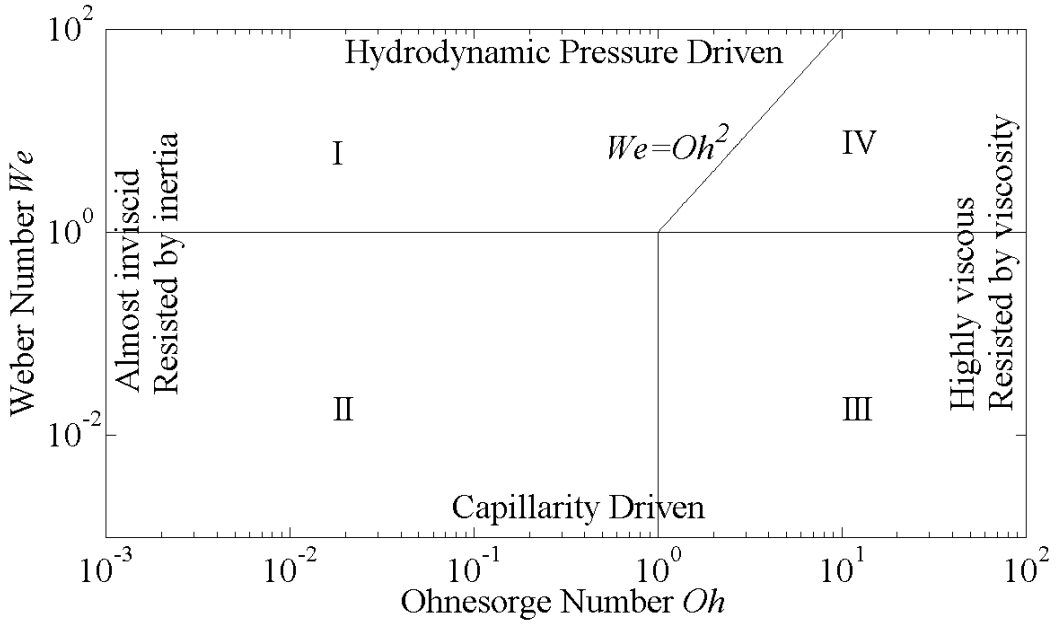

Figure 4-7. Regime map for the spreading (redrawn based on [163])

A different way to define the Weber and Ohnesorge numbers is to define them as a ratio of different timescales. There are three different timescales during droplet impingement: spreading timescale τ_{spr} , oscillation timescale τ_{osc} and viscous timescale τ_{vis}:

$$\tau_{spr} = D_0/U\,;\ \tau_{osc} = \sqrt{\rho D_0^3/\sigma}\,;\ \tau_{vis} = \rho D_0^2/\eta \tag{4-33}$$

The Weber number can be defined as a ratio of oscillation timescale to spreading timescale, while the Ohnesorge number can be defined as a ratio of oscillation timescale to viscous timescale:

$$We = \left(\tau_{osc}/\tau_{spr}\right)^2; Oh = \tau_{osc}/\tau_{vis} \tag{4-34}$$

The impact behaviors are simulated in the four different regimes. In regime I, spreading is driven by the impact pressure and resisted by inertia. In the simulation, the Weber number and the Ohnesorge number are 100 and 0.01 respectively. The change of spreading radius and the shape coefficient with time are plotted as shown in Figure 4-8. As can be seen, the aspect ratio of the optimal droplet shape is very low, which would result in a manufacturing resolution lower than the droplet size. In addition, oscillation is expected due to the small Ohnesorge number (i.e. oscillation timescale is smaller than viscous timescale), and oscillations are across one dimensionless time unit because the Weber number is larger than 1 (i.e. oscillation timescale is larger than spreading timescale).

Another important observation that can be made is that the maximum shape coefficient is achieved before the droplet achieves its maximum spreading radius, as shown in Figure 4-8. This relationship holds true for all the regimes as verified in the following. One possible reason is as follows. Upon impact, the droplet goes away from its equilibrium shape (i.e. sphere-like cap or sphere) after it hits the substrate, and the spreading is driven by the hydrodynamic pressure (which is defined as the pressure difference in Bernoulli's equation) and spreading starts to decelerate due to the resistance of viscous and capillarity forces. Before the speed of the contact line reaches 0 (i.e. the maximum spreading radius), the capillarity force outweighs the hydrodynamic pressure and

dominates the spreading and thus starts to restore the droplet shape back to its equilibrium shape. This is true since usually the maximum shape coefficient is achieved when the droplet is furthest away from its equilibrium shape.

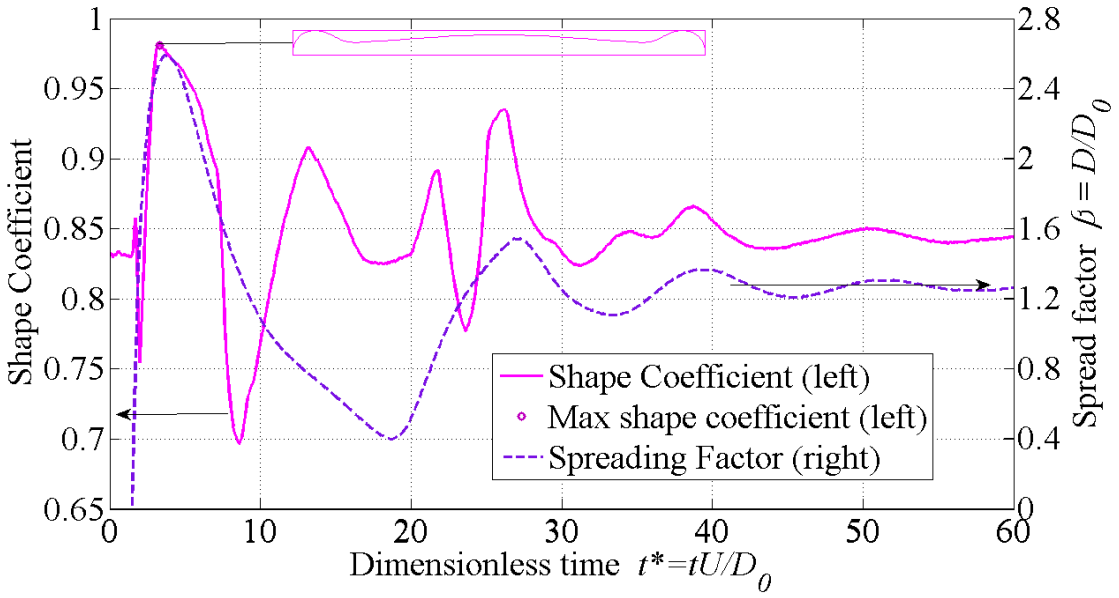

Figure 4-8. Change of spread factor and shape coefficient with time in Regime I.

In the second regime, spreading is mainly driven by the capillarity force imbalance at the contact line, since the impact velocity is so slow that its effects can be neglected. Inertia resists spreading, which is followed by under-damped oscillation. In the simulation, the Weber and Ohnesorge numbers are 0.01 and 0.01 respectively, and the results are shown in Figure 4-9. As can be seen, the aspect ratio of the optimal droplet shape is relatively large, which could lead to a better manufacturing resolution than in the first regime, although the maximum achievable shape coefficient is smaller than that in the first regime. Besides, oscillation exists because the Ohnesorge number is smaller than 1, and oscillations disappeared after one dimensionless time unit because the Weber number is smaller than 1. In addition, the relationship whereby the maximum shape coefficient comes before maximum spreading radius still holds true as shown in Figure 4-9 although

in this regime the two points are very close to each other because the Weber number is so small that the capillarity force dominates the spreading from the beginning.

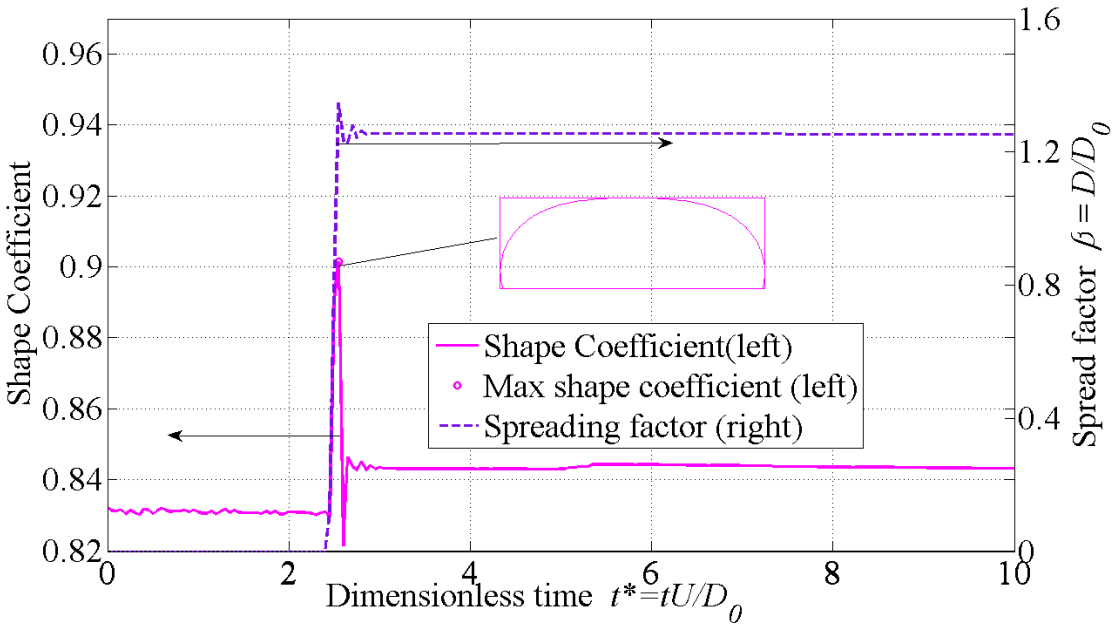

Figure 4-9. Change of spread factor and shape coefficient with time in Regime II.

In the third regime, spreading is driven by the capillarity force and is over-damped by the viscous force so that the inertial oscillations are absent. We simulated droplet impingement with a Weber number of 1 and an Ohnesorge number of 10. The results are shown in Figure 4-10. As can be seen, the droplet shape starts to change once it hits the substrate, while the spreading radius does not change much until a much later stage. Once again, this confirms that the shape coefficient can show smaller and more detailed change during the impingement process. In addition, the optimal droplet shape does not go very far away from its equilibrium shape due to high viscous force. Furthermore, the sphere-like shape is likely to cause voids in the parts during the manufacturing process and thus is not a desirable shape; and the impingement process also goes much slower which would lead to longer manufacturing time. Besides, the viscous timescale is smaller than

the oscillation timescale (Ohnesorge number is larger than 1) and thus the oscillation is damped out. As the same as before, the maximum shape coefficient comes before the maximum spreading radius, as shown in Figure 4-10.

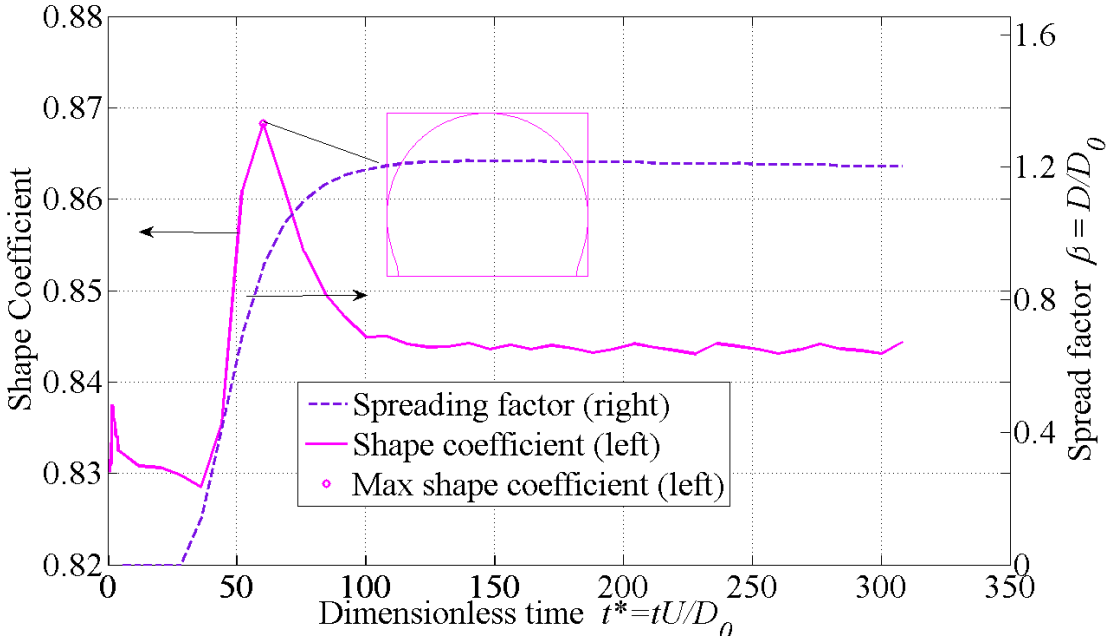

Figure 4-10. Change of spread factor and shape coefficient with time in Regime III.

In the fourth regime, the impact pressure drives the spreading, and the viscous force over-damps the spreading so that no oscillation happens. Setting the Weber and Ohnesorge numbers to 100, the simulation results are shown in Figure 4-11. Similar to regime III, the high viscous force and the low inertial energy significantly increase the spreading time and thus the manufacturing time. This regime also gives the same relationship between shape coefficient and maximum spreading radius. From the above simulation results, we can see that the spreading factor gives us less related information about the droplet shape for manufacturing purposes, while the shape coefficient can better characterize the droplet shape and give us more information about how to get the desired shape by controlling the impact conditions.

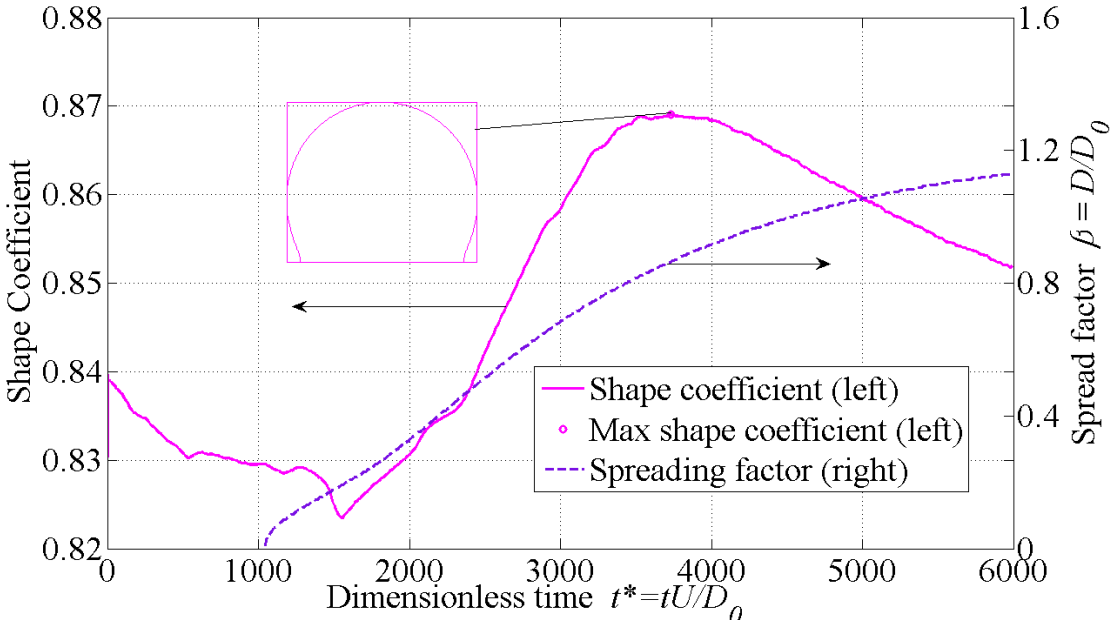

Figure 4-11. Change of spread factor and shape coefficient with time in Regime IV.

In the regime map in Figure 4-7, the Froude number derived from the dimensionless analysis was not included. Therefore, a set of simulations was conducted with various Froude numbers and the same Weber and Reynolds numbers to see the effects of the Froude number on droplet impact behavior. Our interested material is SR351 resin (a photopolymer with fast cure response and numerous applications) [164], and the material properties at 25ºC are listed in Table 4-3.

Table 4-3. Material properties of the simulation.

Medium	Density	Dynamic Viscosity	Surface Tension
SR351	1.109e3 kg/m^3	0.106 Pa·s	0.0361 N/m
Air	1.1839 kg/m^3	1.8616E-5 Pa·s	

We are interested in the impact behavior of SR351 droplets at the micro-scale for potential ink-jet printing application. The Weber and Ohnesorge numbers are set to be 153.6 and 2.37 respectively. The deposition temperature is assumed to be 25ºC so the

material properties are as listed in Table 4-3, and the droplet diameter is 50μm. The Weber and Ohnesorge numbers are matched up when the droplet size is scaled up to 200μm, 600μm and 1mm by changing the impact velocity and material viscosity correspondingly as shown in Table 4-4. The simulation results are compared as shown in Figure 4-12 and Figure 4-13.

Table 4-4. Impact conditions with different droplet size.

Droplet diameter	Corresponding impact velocity	Corresponding viscosity
50μm	10m/s	0.1060 Pa·s
200μm	5m/s	0.2120 Pa·s
600μm	2.8868m/s	0.3672 Pa·s
1mm	2.2361m/s	0.4740 Pa·s

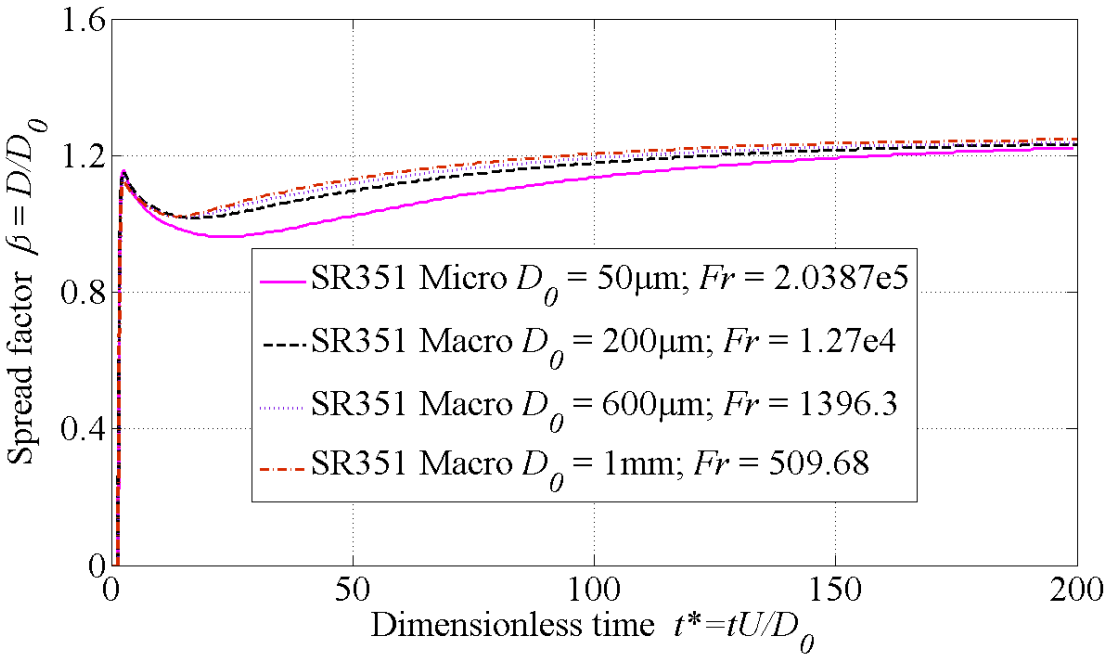

Figure 4-12. Spread factor change with time for different Froude numbers.

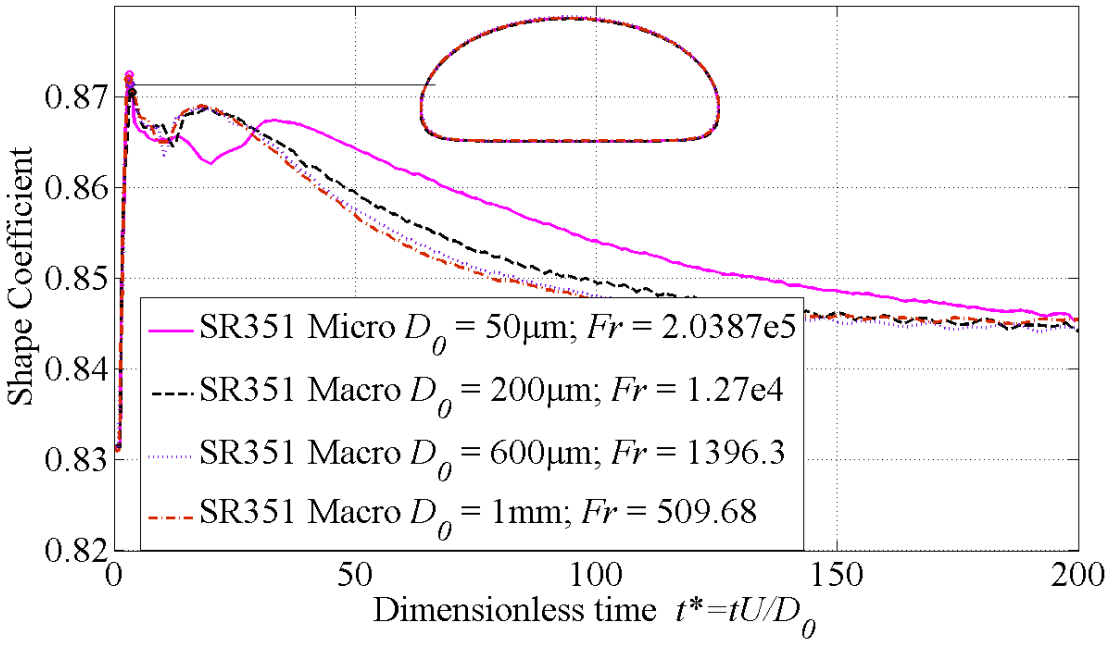

Figure 4-13. Shape coefficient change with time for different Froude numbers.

As shown in the figures, the Froude number does not affect the droplet impact behavior much at early stages of impingement when the maximum shape coefficient is achieved. This can be further confirmed by comparing the Froude number with the Weber and Ohnesorge numbers. We can see that in the above simulated impact conditions, the Froude number is over 500 (for droplet size of 1mm), which is much higher than the Weber (153.6) and Ohnesorge numbers (2.37). Referring back to the dimensionless analysis in section 4.1.1 (Eq. (4-15)), the contribution of the Froude number is much less than that of the Weber and Ohnesorge numbers.

4.1.5 Successive droplet impact

Besides studying single droplet impact behavior on the regime map, we can also explore the impact behaviors of multiple droplets that fall on top of each other. In this section, an ideal situation of successive droplets impact is investigated. The ideal situation is where

the first droplet impinges on the substrate and is frozen instantly at the moment when its shape is closest to the desired shape. Then the next droplet hits on top of the previous frozen droplet and is frozen instantly. This process is repeated for successive droplets. The impact conditions are set to be Weber number equal to 71.42 and Ohnesorge number equal to 0.169 (or Reynolds number equal to 50) and the Froude number equal to 2.0387E5. The first droplet impingement is shown in Figure 4-14 and is frozen instantly when its shape coefficient reaches maximum.

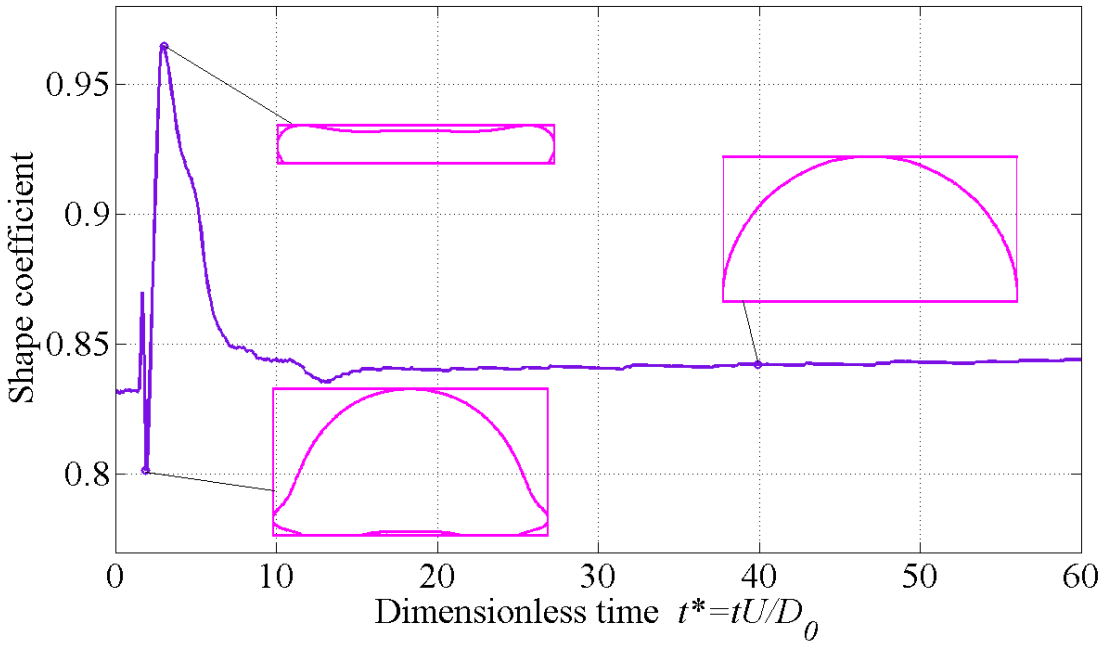

Figure 4-14. Shape coefficient change with time of the first droplet.

The second droplet impingement on top of the first frozen droplet is plotted in Figure 4-15. Comparing Figure 4-15 with Figure 4-14, we find that the best achievable shape is improved (i.e. the maximum shape coefficient for two successive droplets impact is larger than that of the single droplet impact).

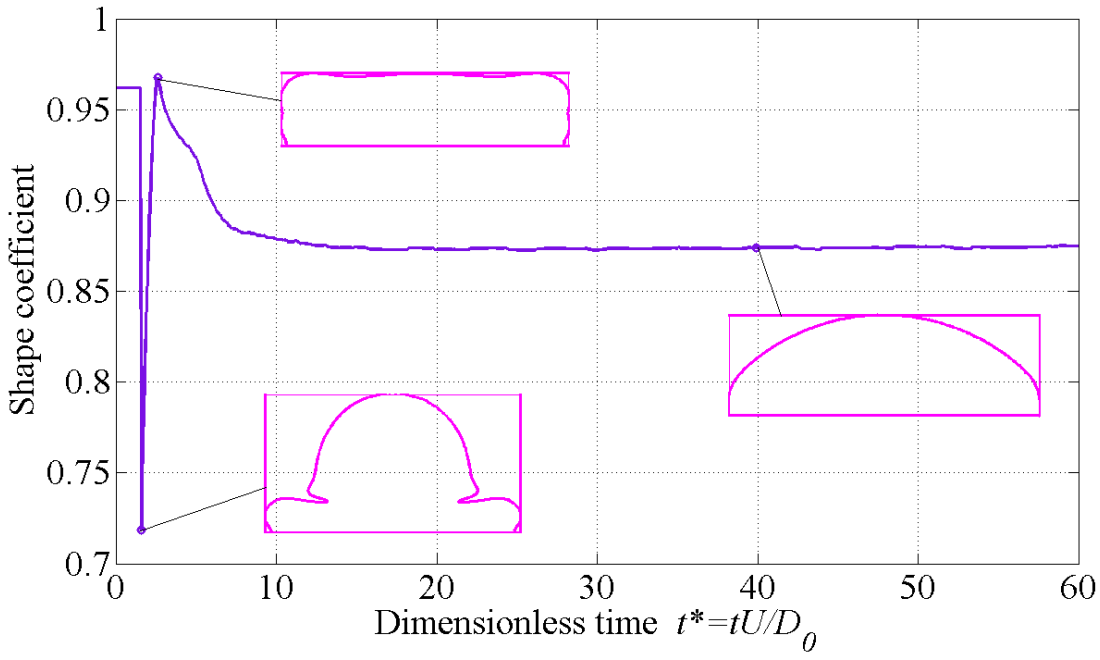

Figure 4-15. Change of shape coefficient with time for two successive droplets impact.

To further test this idea, multiple successive droplet impact simulations are conducted and the shape coefficient is plotted against the number of droplets, as shown in Figure 4-16. As can be seen, the resultant shapes get closer and closer to the desired shape as the number of droplets increases. Furthermore, the time required to achieve the maximum shape coefficient reduces, which suggests it is possible to optimize the manufacturing process by controlling the droplet deposition and solidification processes to reduce the manufacturing time. There are two reasons for the improvement of the shape with successive droplets impingement. First, the contact angle changes. When the first droplet solidifies, the substrate becomes the solidified droplet fluid and thus the contact angle becomes smaller when the second droplet hits on it. Second the shape of the substrate changed since the previous solidified droplets serve as the substrate for the next droplet as shown in Figure 4-16. Since the previous droplet is solidified at the best

achievable shape, the shape of the substrate approaches the desired shape for every additional droplet. The results suggest that it is possible to obtain a closer shape to the desired shape by changing the contact angle of the substrate and/or changing the shape of the substrate.

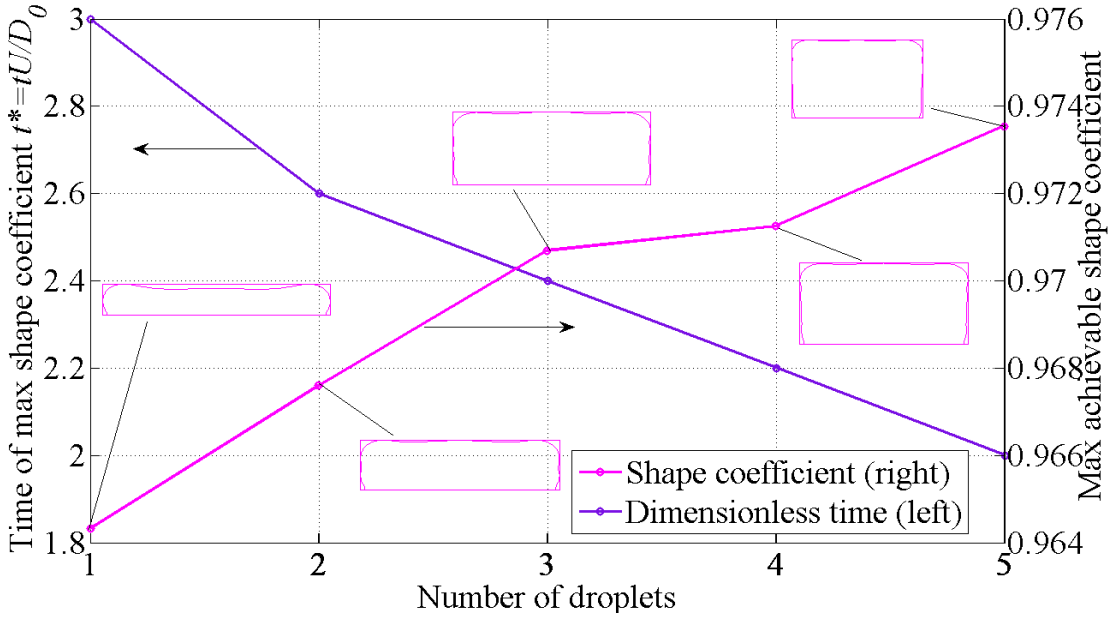

Figure 4-16. Change of best achievable shape coefficient with number of droplets.

4.2 Effects of Dimensionless Numbers on Droplet Interface Evolution

This section is devoted to investigating how the Ohnesorge number and Weber number affect the shape evolution of a single droplet, which includes the shape evolution pattern and the time point when the maximum shape coefficient is achieved. Timing control is very important for manufacturing and can help reduce the manufacturing time and thus the manufacturing cost while potentially improving part quality.

4.2.1 Effects of Weber number

In order to study the effects of the Weber number on droplet shape evolution, several simulations were conducted using the parameters listed in Table 4-5. All the parameters are kept constant except the impact velocity, which is varied from 0.5m/s to 20m/s. To avoid the influence of the viscous force (i.e. to make the viscous force small enough so that the role of Weber number in the shape evolution can be studied), the Ohnesorge number is kept at 0.0813 while the Weber number changes from 0.23 to 369.59 that run across regime I and II.

Table 4-5. Simulation parameters for Weber number sweep.

ρ_{ink}	**1.1827E3 kg/m^3**	ρ_{air}	**1.225 kg/m^3**
η_{ink}	5E-3 Pa·s	η_{air}	1.7894E-5 Pa·s
σ	0.064 N/m	g	9.81 m/s^2
U	-[20, 15, 10, 8, 5, 3, 2.5, 1, 0.75, 0.5] m/s		
D_0	50 μm		

As mentioned above, there are three different forces playing roles in the spreading of the droplet, which are the inertial force, the surface tension and the viscous force, corresponding to the spreading time scale, oscillation time scale and viscous time scale. Therefore, the three different forces can be defined as below:

$$\mathbf{F}_p = \rho U^2 D_0^2;\ \mathbf{F}_\sigma = \sigma D_0;\ \mathbf{F}_{vis} = \eta U D_0 \tag{4-35}$$

where $\mathbf{F}_p$ is the inertial force, $\mathbf{F}_\sigma$ is the surface tension force, and $\mathbf{F}_{vis}$ is the viscous force. Inertial force comes from the kinetic energy, surface tension force comes from the surface tension energy while the viscous force dissipates energy. During the droplet spreading, the inertial force tries to deviate the droplet from the equilibrium shape and the surface tension force strives to restore the droplet shape to its equilibrium shape. Without

viscous force, the energy will be transferred between kinetic energy and surface energy and droplets will oscillate continuously. However, the viscous force will dissipate the kinetic energy and the droplet will come to equilibrium. So during droplet impact, if the inertial force is larger than the surface tension force, the droplet will deform and the kinetic energy will be transferred to surface energy and dissipated by the viscous force and therefore the inertial force will reduce until it becomes smaller than the surface tension force. Then, the droplet will be relaxed back to its equilibrium shape under the surface tension force and in the meantime the surface energy will be transferred to kinetic energy, which will result in inertial force, and if it is still larger than the surface tension force, this process will be repeated until the kinetic energy is dissipated. This process can be shown in Figure 4-17.

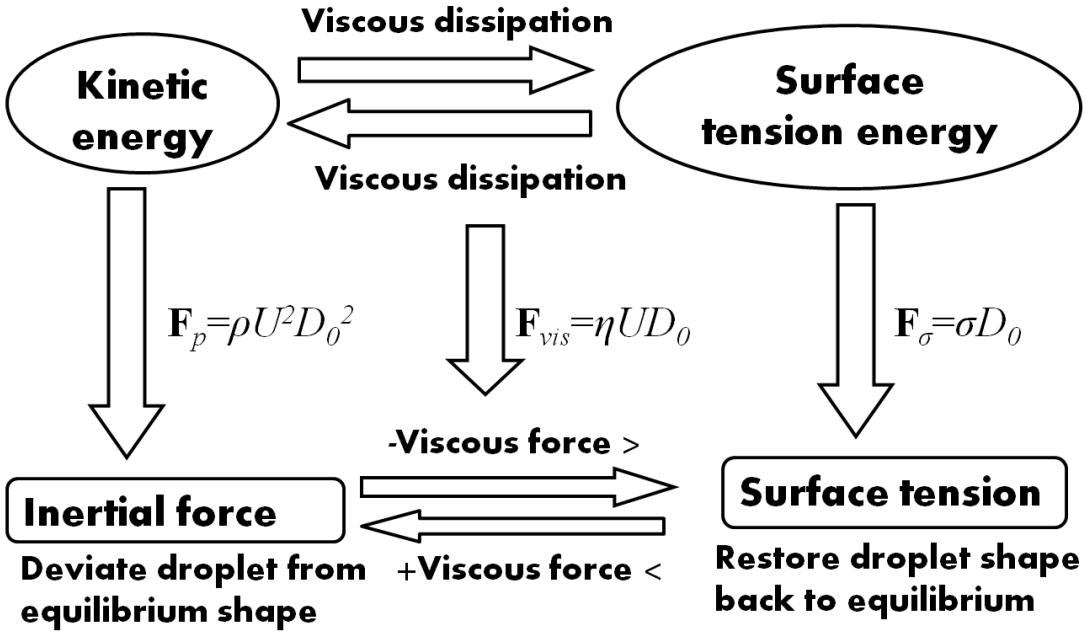

Figure 4-17. Physical interpretation of the droplet impingement dynamics.

With the droplet impact process in mind, we can define the dimensionless numbers in another way as the ratios of the three forces from Eq. (4-35):

$$We = \mathbf{F}_p/\mathbf{F}_\sigma\,;\;\; Re = \mathbf{F}_p/\mathbf{F}_{vis}\,;\;\; Oh = \sqrt{We}/Re \tag{4-36}$$

This definition gives more physical sense to the Weber number and therefore can help with the analysis of effects of the Weber number during droplet impact. A series of simulations was conducted for various Weber numbers between 0.23 and 369.59. The maximum shape coefficient and the time at which it occurs were tracked as a function of Weber number, as shown in Figure 4-18. The inset graphs show shape coefficient results as a function of time for several Weber numbers across regime I and II.

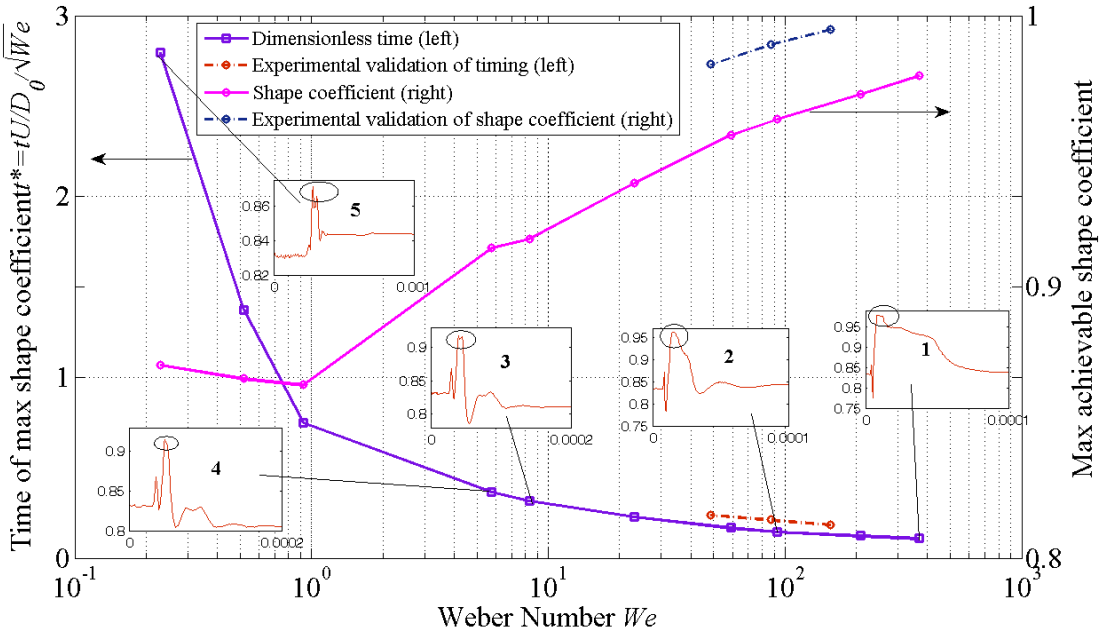

Figure 4-18. Max achievable shape coefficient and its corresponding time with different Weber numbers.

The results are partially validated by experiments from the literature. Since very little shape data of droplet impact exists in the literature, simulations were conducted with the same parameters as the experiments in the literature [165], and the spreading factors are compared as shown in Figure 4-19. With good agreement between the simulations and experiments in the early stage of droplet spreading, shape information from the simulated

experiments is compared with the previous analysis and plotted with dot-dashed curves in Figure 4-18. As can be seen, the results agree well and the slight discrepancy could be due to the effects of gravity, since in the experiments the droplet size was 2.7mm, which leads to Froude numbers that are comparable in magnitude to the Weber numbers and thus affects the results according to Eq. (4-15).

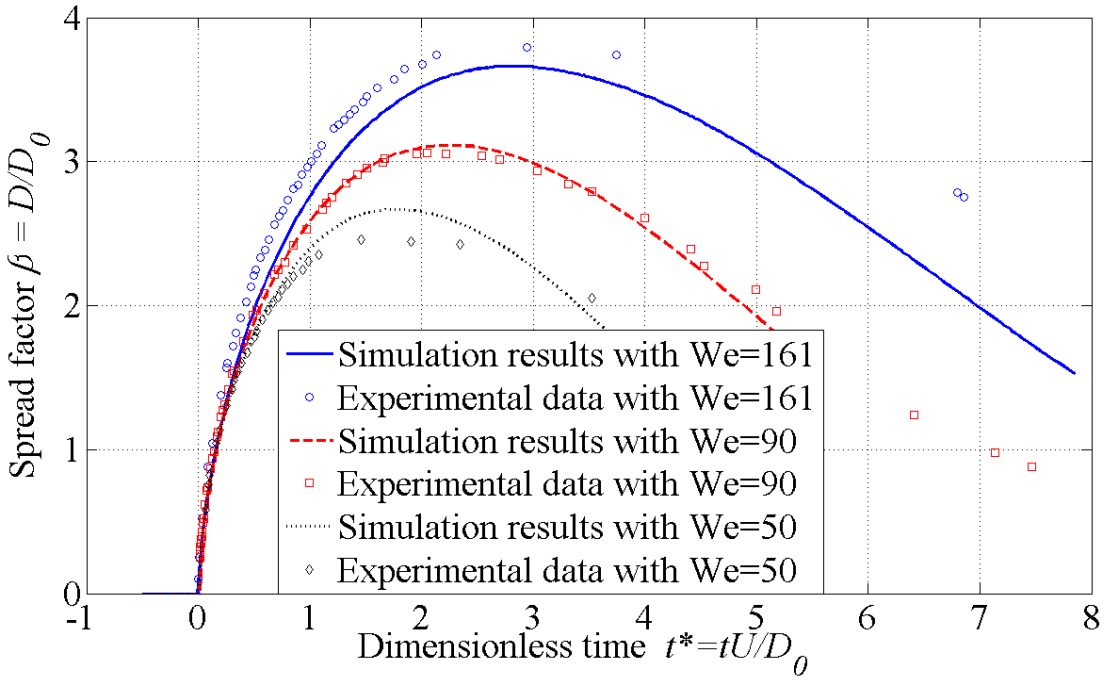

Figure 4-19. Comparison of spreading factor between simulations and experiments with different Weber numbers (experimental data comes from Figure 6 of [165]).

4.2.2 Effects of Ohnesorge number

To examine the effects of the Ohnesorge number on droplet shape evolution, a series of simulations was performed at the conditions listed in Table 4-6. As can be seen, all the physical parameters are kept constant except droplet viscosity, which was varied from 5e-4Pa*s to 5Pa*s uniformly on a log scale. The Weber number was kept at 100 while the Ohnesorge number ranged from 0.01 to 100 that run across regime I and IV.

Table 4-6. Simulation parameters for Ohnesorge number sweep across regime I and IV.

ρ_{ink}	**1000 kg/m^3**	ρ_{air}	**1.225 kg/m^3**
η_{ink}	$10^{\log_{10}(5e-4)+(i-1)*\log_{10}(5/5e-4)/50}$ Pa·s (i = 1, 2, ..., 50)		
η_{air}	1.7894E-5 Pa·s	g	9.81 m/s^2
U	-10 m/s	σ	0.05 N/m
D_0	50 μm		

The maximum shape coefficient and its time of occurrence are plotted against the Ohnesorge number as shown in Figure 4-20. The evolution of the shape coefficient with time for several representative time points is plotted in the inset graphs as well.

When the Ohnesorge number is small, the viscous force is relatively small compared with surface tension and inertial force and thus the viscous effect is negligible during the early stage of spreading. Since the maximum shape coefficient always occurs during early stages of spreading as shown before, the maximum shape coefficient time point is nearly constant (the slight variation was because different time resolutions were used) when the Ohnesorge number is small, as shown in subplots 1 to 5 in Figure 4-20. The maximum shape coefficient decreases in this range due to the increasing dissipation of the kinetic energy as the Ohnesorge number increases. As the Ohnesorge number increases, the damping effects get larger, and the maximum achievable shape coefficient in the first spreading cycle (i.e. before droplet reaches its maximum spreading radius) decreases until it becomes smaller than the second peak as can be seen from the transition from subplot 5 to subplot 6 and therefore the global maximum shifts from the first peak to the second peak. The timing of the second peak depends on the relaxing process. The

Ohnesorge number at which a transition in behavior occurs (i.e. the second peak replaces the first peak and become the global maximum) depends on the Weber number. Large Weber numbers require larger viscous forces to damp the droplet response and cause the first peak to lose the position as the global maximum. At Ohnesorge numbers larger than the transitional Ohnesorge number (i.e. after subplot 5), the spreading and relaxing process after the first peak is mainly driven by surface tension and therefore the maximum achievable shape coefficient does not change much.

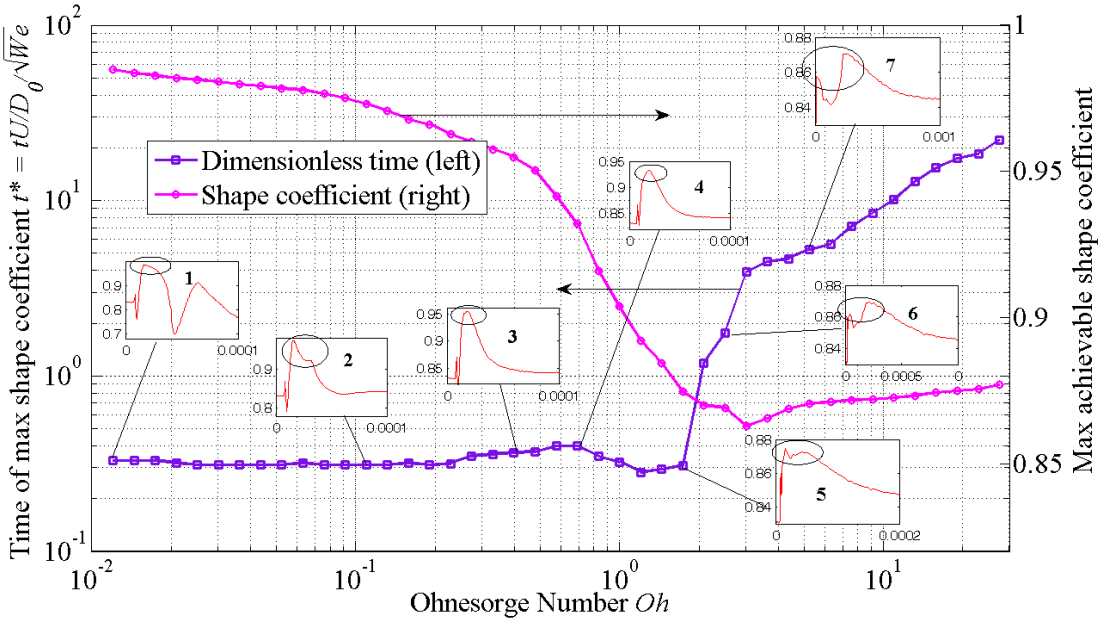

Figure 4-20. Max achievable shape coefficient and its corresponding time with different Ohnesorge numbers.

4.3 Regime Map for Interface Evolution of Single Droplet

During droplet impact, the inertia force drives the fluid to spread and possibly splash, while the surface tension force strives to hold the fluid together and viscous force always goes against the moving direction. If there is no surface tension, fluid will try to form a

thin film under gravity. If there is no inertia, the surface tension at the liquid-gas, liquid-solid and solid-gas interfaces will turn the droplet into a spherical cap with an appropriate contact angle, as determined from the Young equation. With this simple insight into droplet behavior in the limiting cases, it is possible to bring some physical meaning to the shape coefficient. With the link of competing forces to proposed shape coefficient in the limiting cases, we can examine the effects of the ratios of the competing forces on the shape evolution of a single droplet.

4.3.1 Effects of Weber number

A set of simulations is first conducted to study the effects of Weber and Ohnesorge numbers when the Ohnesorge number is small (i.e., much smaller than unity). A two dimensional sweep over a range of Weber and Ohnesorge numbers is performed, as shown in Table 4-7. The droplet diameter is fixed at 50μm to make the Froude number much larger than the corresponding Weber and Reynolds numbers, so that gravity has little influence on the droplet impact results. The results are plotted in Figure 4-21 and Figure 4-22.

Table 4-7. Combinations of Weber and Ohnesorge numbers in regime I and II.

	We = 0.714	We=17.9	We=45.7	We=71.4	We=121	We=183
Oh=0.085	(0.714, 0.085)	(17.9, 0.085)	(45.7, 0.085)	(71.4, 0.085)	(121, 0.085)	(183, 0.085)
Oh=0.1	(0.714, 0.1)	(17.9, 0.1)	(45.7, 0.1)	(71.4, 0.1)	(121, 0.1)	(183, 0.1)
Oh=0.129	(0.714, 0.129)	(17.9, 0.129)	(45.7, 0.129)	(71.4, 0.129)	(121, 0.129)	(183, 0.129)
Oh=0.224	(0.714, 0.224)	(17.9, 0.224)	(45.7, 0.224)	(71.4, 0.224)	(121, 0.224)	(183, 0.224)
Oh=0.338	(0.714, 0.338)	(17.9, 0.338)	(45.7, 0.338)	(71.4, 0.338)	(121, 0.338)	(183, 0.338)
Oh=0.4	(0.714, 0.4)	(17.9, 0.4)	(45.7, 0.4)	(71.4, 0.4)	(121, 0.4)	(183, 0.4)

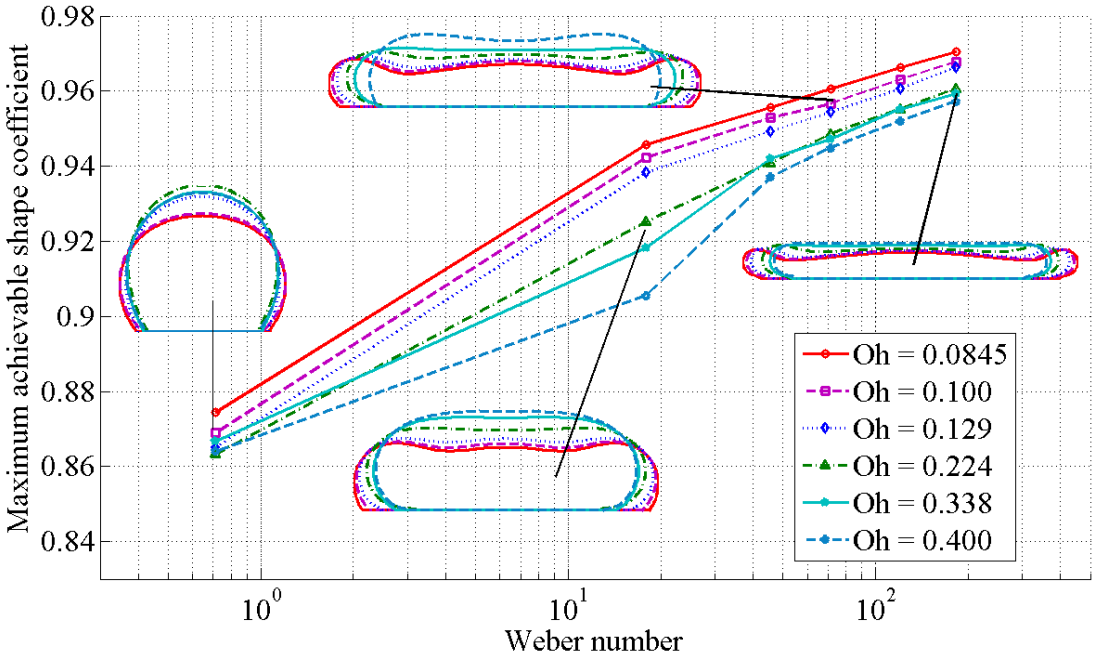

Figure 4-21. Maximum shape coefficient achieved for varying the Weber number (for low *Oh* number fluids).

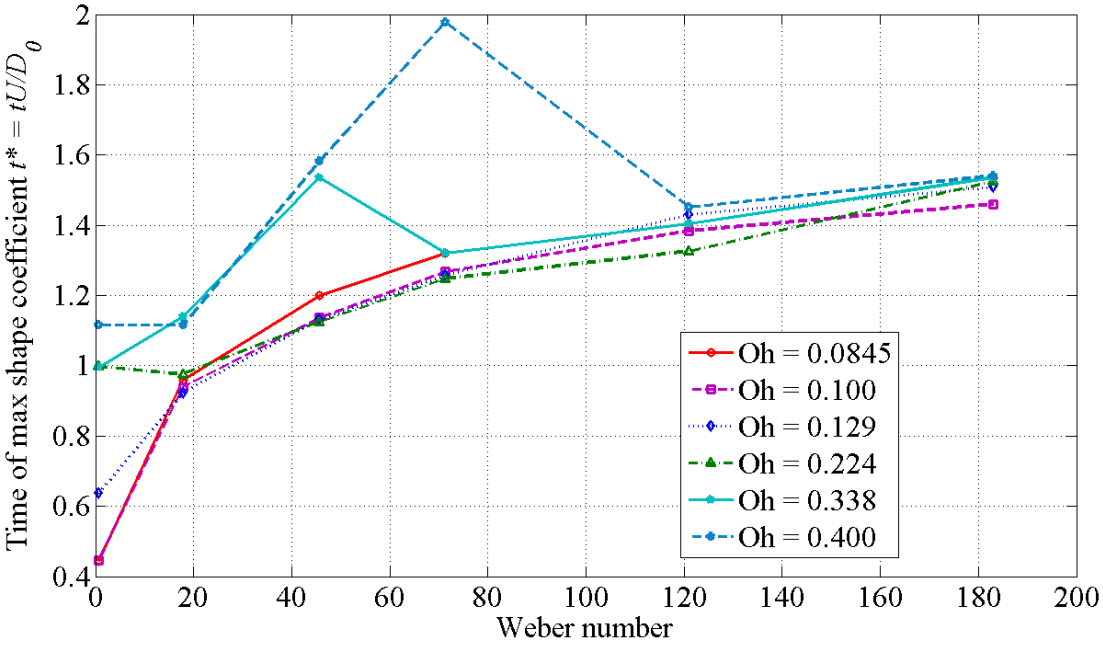

Figure 4-22. Time instant for achieving a maximum shape coefficient for different Weber numbers (for low *Oh* number fluids).

With the physics in mind, we can explain the results shown Figure 4-21 and Figure 4-22. Since an Ohnesorge number smaller than 1 implies the viscous force is smaller than surface tension, the latter will be the main resistance force that opposes flattening of the droplet shape upon impact. Additionally, the inertia force needs to overcome the surface tension to achieve a flat shape. Therefore, we need the inertia force to be larger than the surface tension (i.e., Weber number is large) for the large shape coefficient to result. In other words, the maximum achievable shape coefficient is primarily influenced by the Weber number, as shown in Figure 4-21, with little influence of the Ohnesorge number for fluids with relatively low viscosity, and smaller viscous forces as compared to both fluid inertia and surface tension, for which $Oh<<1$. However, as the Ohnesorge number is approaching unity, the effect of viscous forces on shape evolution becomes more pronounced (i.e., the curves begin to split in Figure 4-21) especially in the case when neither surface tension ($We<<1$) nor inertia ($We>>1$) dominate the shape evolution upon impact. That is when $We\sim(1\text{-}10)$ surface tension and inertia balance each other, giving a greater significance to the viscous stresses in defining how the interface will evolve during the impact. This does not change the overall trend of a monotonic increase in the shape coefficient with the Weber number, but introduces a minor suppression in the rate of this increase as the behavior transitions from surface tension to inertia dominated. In addition, the simulations indicate that when the Ohnesorge number is much smaller than 1 and the Weber number is much larger than 1, the maximum shape coefficient is achieved in the first spreading cycle (i.e. before the droplet reaches its maximum spreading radius)**;** however, when the Ohnesorge number is approaching unity the maximum shape coefficient does not always occur in the first spreading cycle, especially

for the moderately large Weber number cases [148]. It requires either a sufficiently large Weber number, bordering an onset of droplet splash, or a sufficiently small Ohnesorge number for the maximum shape coefficient to occur in the first spreading cycle. When the maximum shape coefficient does occur in the first spreading cycle, we can see from Figure 4-22 that the Ohnesorge number does not affect much of the dimensionless time (scaled by the inertia time scale) corresponding to the maximum shape coefficient. This is because the viscous forces have minimal effect on the droplet shape evolution during the first spreading cycle when the kinetic energy of the droplet is very high and inertia forces dominate the momentum transport. On the other hand, when droplet inertia is greater than surface tension, but not overly dominant in the first spreading cycle (i.e., relatively moderate Weber numbers between 10 and 100), the maximum shape coefficient does not necessarily occur in the first spreading cycle since the spreading and shape evolution is defined by the interplay between surface tension and viscous forces. Indeed, this is illustrated by an increased dispersion of the dimensionless time vs. We number curves in Figure 4-22 as the Ohnesorge number approaches unity. Interestingly, the local maxima are observed in the time required for droplets to reach their maximum shape coefficient, which becomes more pronounced for greater *Oh* number cases and shifts towards a greater critical We number at which the maximum occurs. The "location" of all maxima corresponds to approximately the same value of the Reynolds number ($Re = We^{1/2}/Oh$) for all cases, which is about 20 for our simulation resolution in terms of the Weber number. This suggests that there is a universal scaling in relative magnitude of inertia and viscous forces that is required to achieve the best match between the

physically realized and a desired, pancake-like droplet shape in the case of low surface tension fluid droplet impingement.

4.3.2 Effects of Reynolds number

To assess the effect of the viscous force, rather than surface tension, as a balancing force acting against the fluid inertia upon droplet impact, we performed another set of simulations with viscous force being the main resistance force (i.e. *Oh* >1). With the hypothesis that the ratio of the inertia force to the main resistance force is the determining factor for shape coefficient, we did a two-dimensional sweep of Reynolds (instead of the Weber number) and Ohnesorge numbers within the ranges shown in Table 4-8 (the corresponding Froude numbers for each case are listed in the last row). The results of the simulations are shown in Figure 4-23 and Figure 4-24.

Table 4-8. Combinations of Reynolds and Ohnesorge numbers in regime III and IV.

	Re = 0.5	Re = 2.5	Re = 4.0	Re = 5.0	Re = 6.5	Re = 8
Oh=1.01	(0.5, 1.01)	(2.5, 1.01)	(4, 1.01)	(5, 1.01)	(6.5, 1.01)	(8, 1.01)
Oh=1.2	(0.5, 1.2)	(2.5,1. 2)	(4, 1.2)	(5, 1.2)	(6.5, 1.2)	(8, 1.2)
Oh=1.34	(0.5, 1.34)	(2.5, 1.34)	(4, 1.34)	(5, 1.34)	(6.5, 1.34)	(8, 1.34)
Oh=1.55	(0.5, 1.55)	(2.5, 1.55)	(4, 1.55)	(5, 1.55)	(6.5, 1.55)	(8, 1.55)
Oh=1.69	(0.5, 1.69)	(2.5, 1.69)	(4, 1.69)	(5, 1.69)	(6.5, 1.69)	(8, 1.69)
Oh=2	(0.5, 2)	(2.5, 2)	(4, 2)	(5, 2)	(6.5, 2)	(8, 2)
Oh=2.58	(0.5, 2.58)	(2.5, 2.58)	(4, 2.58)	(5, 2.58)	(6.5, 2.58)	(8, 2.58)
Oh=4.47	(0.5, 4.47)	(2.5, 4.47)	(4, 4.47)	(5, 4.47)	(6.5, 4.47)	(8, 4.47)
Fr	2.04×10^3	5.09×10^4	1.30×10^5	2.04×10^5	3.45×10^5	5.22×10^5

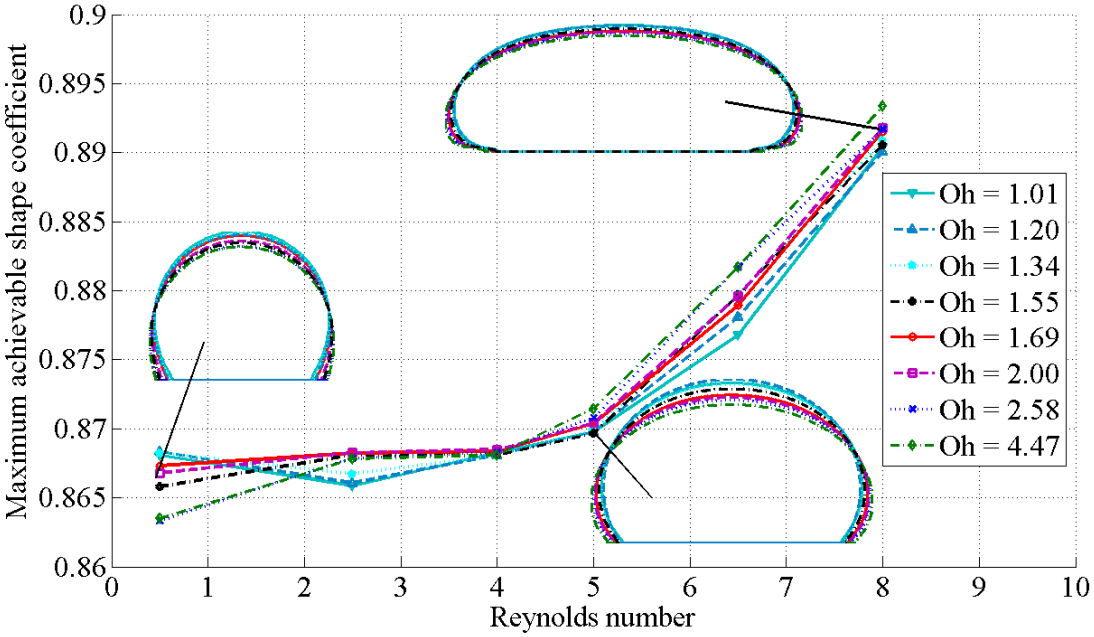

Figure 4-23. Max shape coefficient achieved for varying the Reynolds number (for high Oh number fluids)

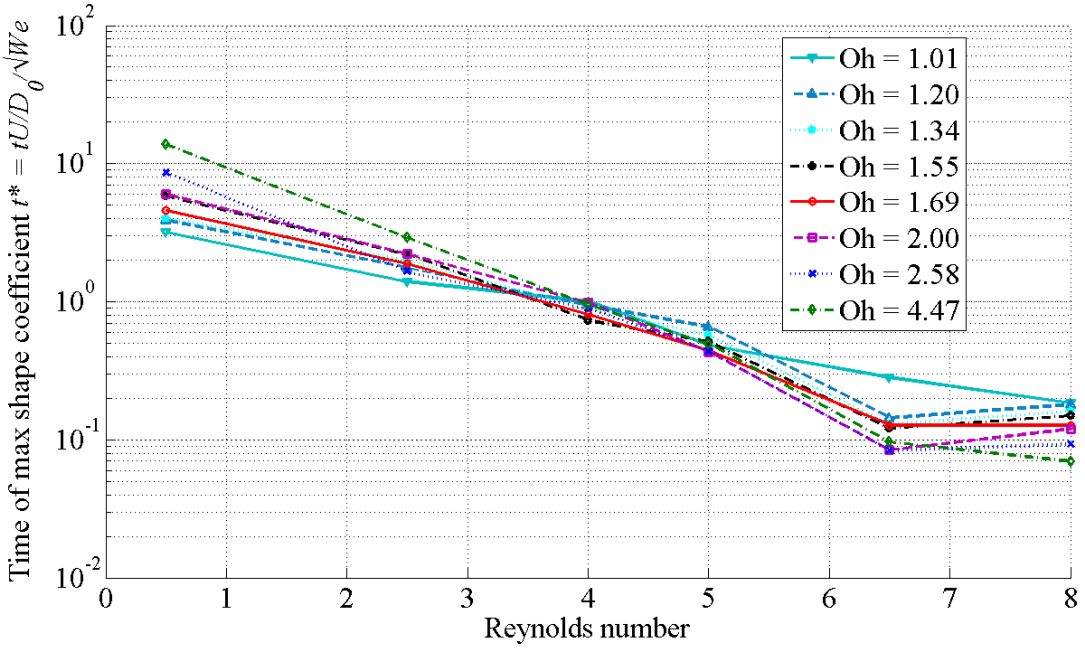

Figure 4-24. Time instant for achieving a maximum shape coefficient for different Reynolds numbers (for high *Oh* number fluids).

As expected, the curves of the maximum achievable shape coefficient with different Ohnesorge numbers collapse together when the Reynolds number is larger than unity, since the process is fully dominated by inertia and both the surface tension and viscous force are suppressed. The timing curves shown in Figure 4-24, depicting a dimensionless time to achieve the maximum shape coefficient, converge to the same value in the limit of small Reynolds number (*Re*~1 and below) and follow the same trend, with some spread but essentially parallel to each other, for larger Reynolds numbers. Note that the definition of the dimensionless time is modified in this case by an additional scaling with the square root of the Weber number to account for the strong effect the surface tension is expected to play in arresting the film spreading when the interface is highly curved near the advancing contact line. Interestingly, when the Reynolds number becomes very large (>10), the dimensionless time to achieve the maximum shape coefficient does not vary significantly.

4.3.3 Regime map for shape evolution

The results of the analysis presented in Figure 4-21 through Figure 4-24 can be placed on a regime map to define the region(s) in the space of relevant dimensionless numbers where we can obtain a desired pancake-like film with a maximum shape coefficient from an impinging droplet on a solid surface. Two equivalent regime maps can be generated with the Ohnesorge number as the abscissa and the Weber or Reynolds number as the ordinate as shown in Figure 4-25 and Figure 4-26, respectively. The Ohnesorge number depends only on physical properties and the size of the droplet and thus can be viewed as a property variable, whereas the Weber and Reynolds numbers can be viewed as process variables (i.e. they depend on the impingement velocity, which can be controlled

regardless of the droplet size and fluid properties). The regime maps are divided into four different domains and typical ranges of maximum achievable shape coefficient and maximum spread factor obtained from simulations in section 4.3.2 are also included.

Regimes I and II are where the large shape coefficients can be obtained and the droplet shape evolution is dominated by the inertia force. In regime I, the viscous effects are less important and surface tension is the main resistance force; thus, the maximum achievable shape coefficient is mainly determined by the Weber number. The larger the Weber number, the larger shape coefficient can be achieved. Therefore, on the lines that are above and parallel to We=1 (i.e., where We=const>1) in regime I, the maximum shape coefficient does not vary significantly, and the time needed to achieve the maximum shape coefficient is also approximately constant. In regime II, the viscous force becomes the main resistance force, as compared to surface tension, and the maximum achievable shape coefficient is mainly controlled by the magnitude of the Reynolds number. That is, the larger the Reynolds number is, the larger shape coefficient can be achieved. On the lines that are above and parallel to Re=1 (i.e., Re=constant>1) in regime II, the maximum achievable shape coefficient stays almost the same regardless of the magnitude of the Ohnesorge number, which is greater than 1 in regime II. The dimensionless time to reach the maximum shape coefficient does depend slightly on the Ohnesorge number, but follows the same trend (see Figure 4-24) and stops changing after Re>10.

In regime III, the inertia effects are weak, and the droplet does not deform much on impact. Its shape evolution is dominated by slow equilibration via the surface tension or viscous forces, depending on the magnitude of the Ohnesorge number. Regime IV is where the inertia is excessively large and splash happens. An empirical relation has been

established experimentally to predict when splash happens through the dimensionless number, the "Sommerfeld" parameter $K=We^{1/2}Re^{1/4}$ [25]. One can expect splash when K is greater than a critical threshold value of K_c (a reasonable estimate for K_c is ~ 50 although the exact value of K_c depends on the roughness of the solid surface and the surrounding gas [166]). The surface roughness and surrounding gas effects can be accounted for by choosing an appropriate critical threshold value for K_c which can be obtained empirically in different situations.

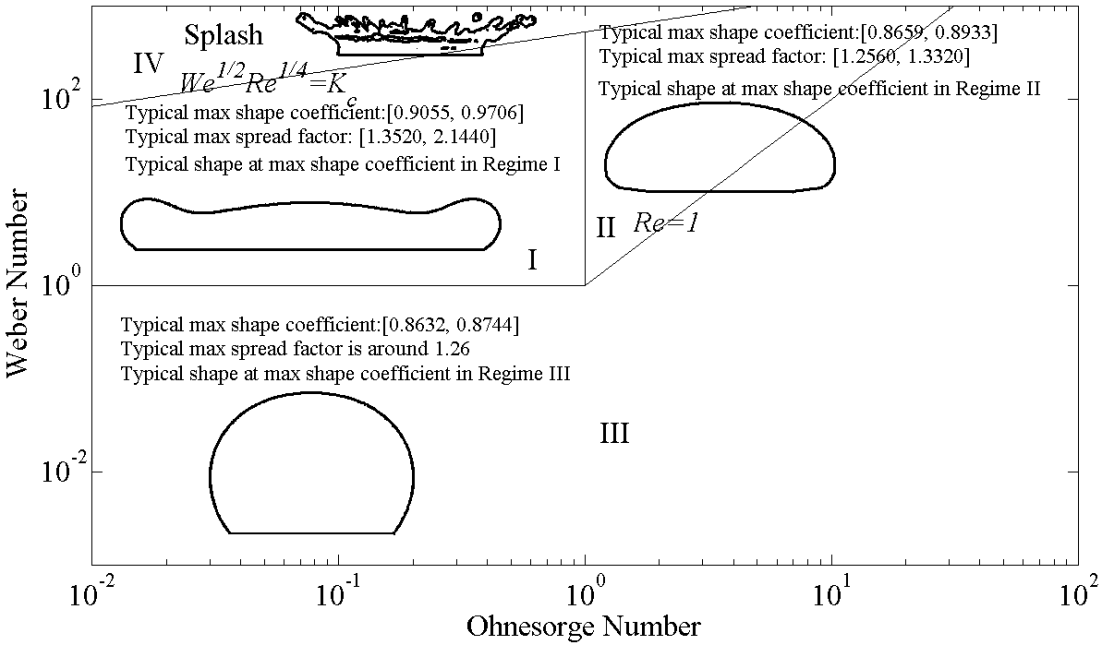

Figure 4-25. Regime map with the Weber number as the ordinate.

It is worth noting that when the Ohnesorge number is greater than K_c, there will never be a chance for the droplet to reach regime II before it splashes as shown in Figure 4-26. This result is expected because when $Oh > 50$ and $Re > 1$ the surface tension is so weak, as compared to the inertial force, that it cannot hold the droplet together (i.e., a droplet will breakup). That implies that for a highly viscous fluid, a desired pancake-like film

topology cannot be realized by a single droplet impact even with sufficiently large impingement speed. Another important observation for applications that one can deduce from the regime II in Figure 4-26 is that for more viscous fluids (i.e., featuring larger Ohnesorge numbers) there is a smaller limit on the maximum shape coefficient that one can achieve before splash occurs. The conclusion is opposite in regime I (Figure 4-25), which shows that for more viscous fluids we have a larger upper limit for the maximum achievable shape coefficient.

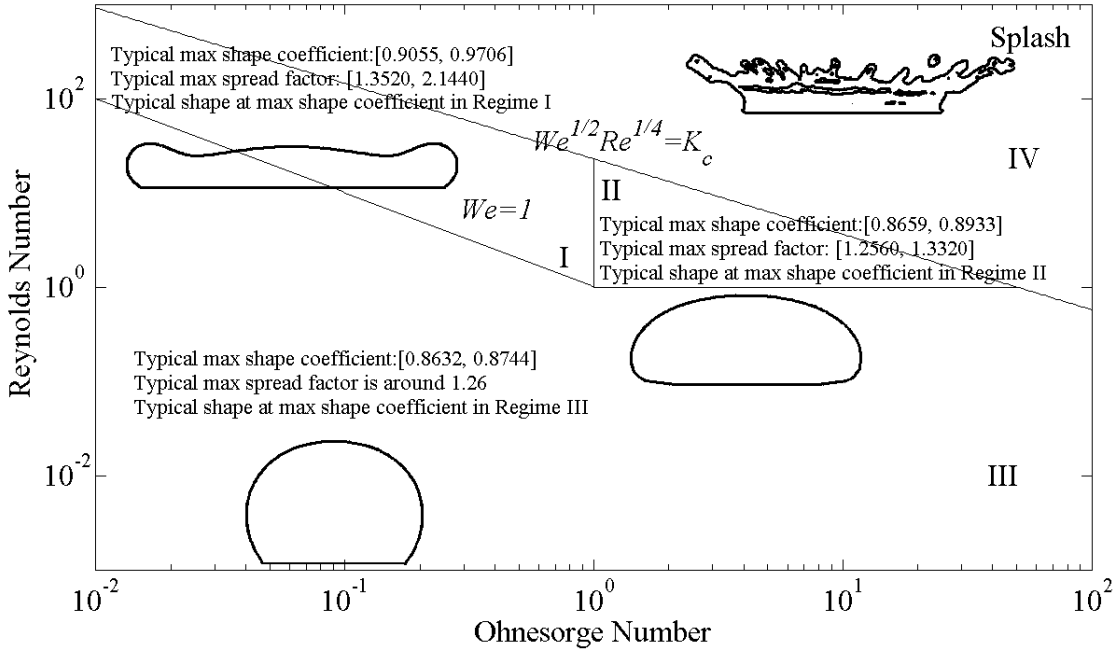

Figure 4-26. Regime map with the Reynolds number as the ordinate.

4.4 Summary

The second research question is studied in this chapter and the hypothesis is validated that a larger Weber number and Reynolds number can achieve a more uniform film when the viscous effects are small and large respectively while the Froude number does not influence much of the droplet shape evolution when the droplet size is sub-millimeter.

A numerical model for droplet impact is developed and extensively validated by comparison to various analytical models and experimental data from literature. A dimensionless analysis of the droplet impact is conducted and has revealed that three independent dimensionless numbers determine the droplet impact behavior. A wide range of impact conditions on a regime map that is composed of two of the three independent dimensionless numbers (i.e. the Weber number and the Ohnesorge number) have been simulated and provided more information of the droplet impact behavior in terms of the shape coefficient proposed in section 3.1.

The examination of the effects of the Froude number on the droplet impact behavior is performed, and it is shown that Froude number does not affect the droplet impact behavior very much under interested impact conditions, which makes it possible to conduct the droplet impact experiments in macro-scale to estimate the impact behavior in micro-scale. A close look at the effects of dimensionless numbers on the shape evolution of droplet impact reveals that the best shape can only be obtained in the early stage of the spreading, and different shape evolution patterns with different Weber number and Ohnesorge number are summarized and analyzed, which show that larger Weber number and smaller Ohnesorge number give better shape coefficients. Other than the investigation of the single droplet impact behavior on the regime map, the multiple droplets impact has also been explored. An ideal situation of successive droplets impingement is examined, which shows that the droplets shape can be improved toward the desired shape by increasing the number of droplets under this ideal situation.

Simulations are performed to further study the effects of the Weber number, Reynolds number and Ohnesorge number on the maximum achievable shape coefficient. It is found

that the maximum achievable shape coefficient is mainly determined by the Weber number when the Ohnesorge number is smaller than 1, and increasing the Weber number results in a larger shape coefficient. It has also been found that the Reynolds number is the main determining factor of the maximum achievable shape coefficient when Ohnesorge number is greater than 1. The physics behind the droplet impact was examined and used to explain the results. Using an insight obtained from parametric simulations of the limiting cases, a regime map was developed to indicate the regimes in the space of relevant dimensionless parameters where a desired pancake-like droplet shape can be obtained upon impact while avoiding a detrimental effect of splash. Important implications are derived on the processing conditions for practical applications involving drop-on-demand thin film deposition of high viscosity fluids with high degree of thickness uniformity through critical analysis of the impingement regime maps.

CHAPTER FIVE

LATTICE BOLTZMANN MODELING OF DROPLET IMPINGEMENT

In order to gain more insight into the material interface evolution during the inkjet deposition process, it is beneficial to study how the interface evolves for multiple-droplet interaction, which requires 3-D simulation of droplet impingement dynamics. However, most of the previous research has focused on studying single droplet impingement due to the prohibitive computational cost and complexity of simulating droplet impingement in three-dimensional settings. This chapter presents a novel numerical model based on the lattice Boltzmann method to simulate the interface dynamics during impingement and interaction of multiple droplets.

5.1 Introduction

5.1.1 Rationale of choosing lattice Boltzmann method

Droplet impingement falls into the category of the multiphase flow modeling in fluid mechanics. As reviewed in Chapter 2, there are many computational methods for multiphase flow modeling and mesoscopic methods can achieve a much larger time and spatial scale than the microscopic methods while enjoy the benefits of reduced modeling and computational complexity. Among many mesoscopic methods as reviewed in Chapter 2, the LBM is one of the most developed during the past two decades. Therefore, we decide to adopt the LBM for modeling of droplet impingement dynamics.

5.1.2 Challenges

In Chapter 2, we have reviewed the lattice Boltzmann method itself. However, there are also many challenges in applying the LBM to droplet impingement dynamics. One notable challenge is the numerical instability arising from the spurious flow around the interface between the droplet and the surrounding air due to the high density and/or viscosity ratio, which has been tackled by several different research groups [167-169].

Some representative studies on droplet impingement using the LBM are described in the following. Briant et al. developed free-energy based wetting boundary conditions to simulate contact line dynamics [170-171]. Yan et al. studied spontaneous water drop spreading on both homogeneous and heterogeneous partially wetting surfaces [169]. Although the equlibrium profiles of the spreading droplets matched well with predictions, the transient profiles were not compared with either experiments or theory. Lee and Liu [172] reported transient LBM simulation of droplet impingement and used a slightly different definition of the spreading factor from the experiments in order to match the experimental data. In spite of all these progresses, several challenges remain to be addressed in order to achieve satisficatory computational efficiency and accuracy, including modeling of the liquid-air interface and boundary conditions, which will be elaborated in the next section.

5.1.3 Objective and approaches

The objective of this chapter is to come up with a LB formulation that is fundamentally consistent with the well-established phase-field model in order to address the remaining challenges mentioned above. Although the LBM originated from a microscopic description of the fluid behavior, it could link to the macroscopic description through the

Chapman-Enskog multiscale analysis [173] and recover the Navier-Stokes equations. From this perspective, the LBM can be viewed as a special approach of solving the macroscopic Navier-Stokes equations. The phase-field model is a well established approach for simulating two-phase flows [99] and is included in the commercial software COMSOL [174]. Many previous results have shown successful application of the phase-field model in simulating droplet impingement dynamics [109, 148]. Therefore, in this chapter, we proposed a LB formulation equivalent to the phase-field model, which provides an alternative to solving the phase-field model equations.

Four primary contributions are made in this chapter regarding LB models of droplet impingement. First, we derived an inter-particle forcing term from the phase-field model as in section 5.2.2. Second, we showed the inconsistency between the existing LB schemes and the phase-field model in calculating the relaxation time around the phase interface and proposed a new quadratic scheme to ensure the consistency with the phase-field model as in section 5.2.4.1. Third, contrary to the popular surface energy formulation of the wetting boundary condition in the existing LB schemes [170-172], we proposed a geometric formulation of the wetting boundary condition to be consistent with the phase field model as in section 5.2.4.2. Results show the geometric formulation enforces the prescribed contact angle better than the surface energy formulation in both static and dynamic wetting. Fourth, we showed that the previously used "bounce-back" scheme [169-170, 175] and "equilibrium bounce-back" scheme [172] for the velocity boundary condition for the binary fluids LB scheme does not conserve momentum on the wall boundary, and proposed a modified scheme to ensure momentum conservation as in section 5.2.4.3. The proposed LB formulation is applied to simulating droplet

impingement dynamics in 3-D and the simulation results were compared with those predicted by COMSOL, previous reported LBM simulations [172], and with experimental data from literature [162]. Results show that, for simulating droplet impingement dynamics on the scale of our interest, our proposed LB simulation approach yields not only a significant speed improvement over COMSOL, but also better accuracy than both COMSOL and the previous reported LB technique. Finally, the case of multiple interacting droplets in 3D, including interfacial dynamics upon droplet impact, spreading, coalescence and relaxation, has been successfully simulated and used to demonstrate the new capabilities enabled by the proposed LBM simulation algorithm.

5.2 Lattice Boltzmann formulation

As reviewed in Section 2.3, the LBM solves macroscopic motion of a fluid by following the evolution of a lattice Boltzmann equation that governs the behavior of the single-particle distribution function as in Eq. (2-24). This section is to present a LB formulation consistent with the phase-field model based on Eq. (2-24).

5.2.1 Two-distribution-function formulation

In order to directly track the pressure field rather than using the equation of state (EOS), He et al. [145] first introduced a new distribution function using the following transformation:

$$g_i = f_i c_s^2 + \zeta(\rho)\Gamma_i(0) \tag{5-1}$$

$$g_i^{eq} = f_i^{eq} c_s^2 + \zeta(\rho)\Gamma_i(0) \tag{5-2}$$

where f_i and f_i^{eq} are defined in Eqs. (2-4) and (2-23) respectively,

$$\Gamma_i(\mathbf{u}) = \frac{f_i^{eq}}{\rho} = t_i\left[1 + \frac{\mathbf{e}_i \cdot \mathbf{u}}{c_s^2} + \frac{(\mathbf{e}_i \cdot \mathbf{u})^2}{2c_s^4} - \frac{\mathbf{u} \cdot \mathbf{u}}{2c_s^2}\right] \tag{5-3}$$

$$\zeta(\rho) = p - \rho c_s^2 \tag{5-4}$$

where p is the thermodynamic pressure, which is only a function of density ρ for a simple compressible substance under isothermal condition. Combining Eqs. (2-6), (2-7), (2-15), (2-21), (5-1), and (5-2) using algebraic manipulations, yields:

$$\frac{\partial g_i}{\partial t} + \mathbf{e}_i \cdot \nabla g_i = -\frac{g_i - g_i^{eq}}{\lambda} + (\mathbf{e}_i - \mathbf{u}) \cdot [\Gamma_i(\mathbf{u}) \cdot \mathbf{F} + \Gamma_i(0) \cdot \nabla\zeta(\rho)] \tag{5-5}$$

$$p = \sum g_i \tag{5-6}$$

$$\rho \mathbf{u} c_s^2 = \sum g_i \mathbf{e}_i \tag{5-7}$$

$$g_i^{eq} = t_i\left[p + \rho c_s^2\left(\frac{\mathbf{e}_i \cdot \mathbf{u}}{c_s^2} + \frac{(\mathbf{e}_i \cdot \mathbf{u})^2}{2c_s^4} - \frac{\mathbf{u} \cdot \mathbf{u}}{2c_s^2}\right)\right] \tag{5-8}$$

In order to track the evolution of the interface, a second distribution function is introduced:

$$h_i = \frac{C}{\rho} f_i \tag{5-9}$$

$$h_i^{eq} = \frac{C}{\rho} f_i^{eq} = t_i C\left[1 + \frac{\mathbf{e}_i \cdot \mathbf{u}}{c_s^2} + \frac{(\mathbf{e}_i \cdot \mathbf{u})^2}{2c_s^4} - \frac{\mathbf{u} \cdot \mathbf{u}}{2c_s^2}\right] \tag{5-10}$$

We can derive the evolution equation for h_i using Eqs. (2-6), (2-7), (2-15), (2-21), (5-9), and (5-10):

$$\frac{\partial h_i}{\partial t} + \mathbf{e}_i \cdot \nabla h_i = \frac{Dh_i}{Dt} = \frac{C}{\rho}\frac{Df_i}{Dt} + f_i \frac{D}{Dt}\left(\frac{C}{\rho}\right) \tag{5-11}$$

where

$$\frac{Df_i}{Dt} = \frac{\partial f_i}{\partial t} + \mathbf{e}_i \cdot \nabla f_i = -\frac{f_i - f_i^{eq}}{\lambda} + \frac{\mathbf{F} \cdot (\mathbf{e}_i - \mathbf{u})}{\rho c_s^2} f_i^{eq} \tag{5-12}$$

$$\frac{D}{Dt}\left(\frac{C}{\rho}\right) = \frac{1}{\rho}\left(\frac{\partial C}{\partial t} + \mathbf{e}_i \cdot \nabla C\right) - \frac{C}{\rho^2}\left(\frac{\partial \rho}{\partial t} + \mathbf{e}_i \cdot \nabla \rho\right) \tag{5-13}$$

Here we have chosen the same governing equation – the Cahn-Hilliard equation (Eq. (4-3)) for the evolution of composition C as in the phase-field model, therefore, we can replace the first term on the right-hand side of Eq. (5-13) with:

$$\frac{\partial C}{\partial t} + \mathbf{e}_i \cdot \nabla C = (\mathbf{e}_i - \mathbf{u}) \cdot \nabla C + \nabla \cdot M \nabla \mu \tag{5-14}$$

In addition, for an incompressible fluid, we have:

$$\frac{\partial \rho}{\partial t} + \mathbf{u} \cdot \nabla \rho = 0 \tag{5-15}$$

and then the second term on the right-hand side of Eq. (5-13) can be replaced with:

$$\frac{\partial \rho}{\partial t} + \mathbf{e}_i \cdot \nabla \rho = (\mathbf{e}_i - \mathbf{u}) \cdot \nabla \rho \tag{5-16}$$

Plugging Eqs. (5-13), (5-14), and (5-16) into Eq. (5-11) leads to the governing equation for h_i:

$$\frac{\partial h_i}{\partial t} + \mathbf{e}_i \cdot \nabla h_i = -\frac{h_i - h_i^{eq}}{\lambda} + (\mathbf{e}_i - \mathbf{u}) \cdot \left(\frac{C}{\rho c_s^2}\mathbf{F} + \nabla C - \frac{C}{\rho}\nabla \rho\right) \Gamma_i(\mathbf{u}) + \Gamma_i(\mathbf{u}) \nabla \cdot M \nabla \mu \tag{5-17}$$

Note that f_i/ρ is approximated as f_i^{eq}/ρ for the convenience of calculation as He et al. did in Eq. (2-14). From Eqs. (2-6), (2-7), (5-9), and (5-10), we can obtain:

$$\sum h_i = C \tag{5-18}$$

$$\sum h_i \mathbf{e}_i = C\mathbf{u} \tag{5-19}$$

5.2.2 Derivation of the forcing term

A multiscale analysis on the evolution equations of the two sets of distribution functions (Eqs. (5-5) and (5-17)) is performed to help relate the microscopic quantities to the macroscopic terms. The particle distribution functions g_i and h_i can be expanded around the particle equilibrium state as:

$$g_i = g_i^{eq} + \epsilon g_i^{(1)} + \epsilon^2 g_i^{(2)} + O(\epsilon^3) \tag{5-20}$$

$$h_i = h_i^{eq} + \epsilon h_i^{(1)} + \epsilon^2 h_i^{(2)} + O(\epsilon^3) \tag{5-21}$$

where ϵ is identified as the Knudsen number. The time and spatial derivatives are expanded as in Eqs. (2-27) and (2-28). Therefore, we can perform the Chapman-Enskog multiscale analysis on Eqs. (5-5) and (5-17) respectively. Collecting terms for the order ϵ and ϵ^2, respectively, and neglecting the higher order terms yield:

$$\epsilon: \left(\frac{\partial}{\partial t_1} + \mathbf{e}_i \cdot \nabla\right) g_i^{eq} = -\frac{1}{\lambda} g_i^{(1)} \tag{5-22}$$

$$\epsilon^2: \frac{\partial}{\partial t_2} g_i^{eq} + \left(\frac{\partial}{\partial t_1} + \mathbf{e}_i \cdot \nabla\right) g_i^{(1)} \tag{5-23}$$

$$= -\frac{1}{\lambda} g_i^{(2)} + (\mathbf{e}_i - \mathbf{u}) \cdot [\Gamma_i(\mathbf{u}) \cdot \mathbf{F} + \Gamma_i(0) \cdot \nabla\zeta(\rho)]$$

$$\epsilon: \left(\frac{\partial}{\partial t_1} + \mathbf{e}_i \cdot \nabla\right) h_i^{eq} = -\frac{1}{\lambda} h_i^{(1)} \tag{5-24}$$

$$\epsilon^2: \frac{\partial}{\partial t_2} h_i^{eq} + \left(\frac{\partial}{\partial t_1} + \mathbf{e}_i \cdot \nabla\right) h_i^{(1)} \tag{5-25}$$

$$= -\frac{1}{\lambda} h_i^{(2)} + (\mathbf{e}_i - \mathbf{u}) \cdot \left(\frac{C}{\rho c_s^2}\mathbf{F} + \nabla C - \frac{C}{\rho}\nabla\rho\right) \Gamma_i(\mathbf{u})$$

$$+ \Gamma_i(\mathbf{u}) \nabla \cdot M \nabla\mu$$

Note that the second term on the right side of Eq. (5-5) represents the interaction force between particles and should be counted as a second order term because the 0th order represents the equilibrium state, the first order accounts for the particle collision, and the

particle interaction force is assumed to be on a larger spatial scale and a longer time scale than particle collision. With Eqs. (2-21) and (5-2), we can obtain:

$$\sum g_i^{eq} = p \tag{5-26}$$

$$\sum g_i^{eq} \mathbf{e}_i = \rho \mathbf{u} c_s^2 \tag{5-27}$$

Comparing to Eqs. (5-6) and (5-7) using Eq. (5-20), we can get:

$$\sum g_i^{(1)} = 0; \sum g_i^{(2)} = 0 \tag{5-28}$$

$$\sum g_i^{(1)} \mathbf{e}_i = 0; \sum g_i^{(2)} \mathbf{e}_i = 0 \tag{5-29}$$

In the same way, we can obtain:

$$\sum h_i^{eq} = C \tag{5-30}$$

$$\sum h_i^{eq} \boldsymbol{e}_i = C\mathbf{u} \tag{5-31}$$

$$\sum h_i^{(1)} = 0; \sum h_i^{(2)} = 0 \tag{5-32}$$

$$\sum h_i^{(1)} \mathbf{e}_i = 0; \sum h_i^{(2)} \mathbf{e}_i = 0 \tag{5-33}$$

Summing Eqs. (5-22) and (5-23) using Eqs. (5-26), (5-27), (5-28), and (5-29), we can obtain:

$$\frac{\partial p}{\partial t_1} + \nabla^{(1)} \cdot (\rho \mathbf{u} c_s^2) = 0 \tag{5-34}$$

$$\frac{\partial p}{\partial t_2} = -\mathbf{u} \cdot \nabla^{(1)} (p - \rho c_s^2) \tag{5-35}$$

Combining Eqs (5-34) and (5-35) leads to:

$$\frac{\partial p}{\partial t} + \mathbf{u} \cdot \nabla p + \rho c_s^2 \nabla \cdot \mathbf{u} = 0 \tag{5-36}$$

Since p is a function of ρ for isothermal fluid, the material derivative of p is negligible under incompressible limit, and Eq. (5-36) is thus equivalent to the mass conservation equation for incompressible fluids at constant temperature. Multiplying (5-22) and (5-23) by $\mathbf{e}_i$ and summing them up over i using Eqs. (5-26), (5-27), (5-28), and (5-29), we obtain:

$$\frac{\partial}{\partial t_1}(\rho \mathbf{u} c_s^2) + \nabla^{(1)} \cdot \left(\boldsymbol{\Pi}_g^{(0)}\right) = 0 \tag{5-37}$$

$$\frac{\partial}{\partial t_2}(\rho \mathbf{u} c_s^2) + \nabla^{(1)} \cdot \left(\boldsymbol{\Pi}_g^{(1)}\right) = c_s^2 \mathbf{F} + c_s^2 \nabla^{(1)} \zeta(\rho) \tag{5-38}$$

where

$$\boldsymbol{\Pi}_g = \sum g_i \mathbf{e}_i \mathbf{e}_i \tag{5-39}$$

Combining Eqs (5-37) and (5-38) leads to:

$$\frac{\partial}{\partial t}(\rho \mathbf{u}) + \frac{1}{c_s^2} \nabla \cdot \left(\boldsymbol{\Pi}_g^{(0)} + \boldsymbol{\Pi}_g^{(1)}\right) = \mathbf{F} + \nabla \zeta(\rho) \tag{5-40}$$

With Eqs. (2-21), (5-2), and (5-39), we can have:

$$\boldsymbol{\Pi}_g^{(0)} = \sum g_i^{eq} \mathbf{e}_i \mathbf{e}_i = c_s^2 p \mathbf{I} + \rho c_s^2 \mathbf{u}\mathbf{u} \tag{5-41}$$

where $\mathbf{I}$ is the identity matrix. From Eqs. (5-2) and (5-22), we can have,

$$g_i^{(1)} = -t_i \lambda \Big[\mathbf{Q}_i : \nabla \rho \mathbf{u} + \mathbf{e}_i \cdot \nabla \zeta(\rho) - \mathbf{e}_i \nabla : \rho \mathbf{u}\mathbf{u} + \frac{1}{2c_s^2}\left((\mathbf{e}_i \cdot \nabla)(\mathbf{Q}_i : \rho \mathbf{u}\mathbf{u})\right) \Big] \tag{5-42}$$

where $\mathbf{Q}_i = \mathbf{e}_i \mathbf{e}_i - c_s^2 \mathbf{I}$. Therefore,

$$\boldsymbol{\Pi}_g^{(1)} = \sum g_i^{(1)} \mathbf{e}_i \mathbf{e}_i = -\lambda c_s^4 (\nabla \rho \mathbf{u} + (\nabla \rho \mathbf{u})^T) \tag{5-43}$$

It is interesting to point out that $\mathbf{\Pi}_g^{(1)}$ is recovered from the O(ϵ^1) order component of g_i and dependent on velocity gradients, which is consistent with the microscopic view of $g_i^{(1)}$. Plugging Eqs. (5-41) and (5-43) back into (5-40) leads to:

$$\frac{\partial}{\partial t}(\rho\mathbf{u}) + \nabla\cdot(\rho\mathbf{u}\mathbf{u}) = -\nabla p + \nabla\cdot\left(\lambda c_s^2(\nabla\rho\mathbf{u} + (\nabla\rho\mathbf{u})^T)\right) + \mathbf{F} + \nabla\zeta(\rho) \tag{5-44}$$

Comparing with the momentum equation of the phase-field model used in COMSOL (Eq. (4-2)), we can then derive:

$$\nu = \lambda c_s^2 \tag{5-45}$$

$$\mathbf{F} = -\nabla\zeta(\rho) + \mu\nabla C + \rho\mathbf{g} \tag{5-46}$$

where ν is identified as the kinematic viscosity, C is the phase composition of the fluid, $\mathbf{g}$ is the gravity, and μ is the chemical potential that is the derivative of Gibbs free energy with respect to C at constant temperature and pressure as defined in Eq. (4-5). Because there is a large difference of C but little difference of μ across the interface under equilibrium, we replace the surface tension term $\mu\nabla C$ in $\mathbf{F}$ (Eq. (5-46)) with $-C\nabla\mu$ using the identity $\mu\nabla C = -C\nabla\mu$ [99] to reduce numerical errors around the interface. Therefore, $\mathbf{F}$ becomes:

$$\mathbf{F} = \nabla\rho c_s^2 - \nabla p - C\nabla\mu + \rho\mathbf{g} \tag{5-47}$$

Note that this forcing term has been used by Lee et al. [172], but we have shown it can be directly derived from the phase-field model. This completes our first contribution in the derivation of the forcing term from the phase-field model.

In the same way, we can sum Eqs. (5-24) and (5-25) over i using Eqs. (5-30), (5-31), (5-32), and (5-33) and obtain:

$$\frac{\partial C}{\partial t_1} + \nabla \cdot (C\mathbf{u}) = 0 \tag{5-48}$$

$$\frac{\partial C}{\partial t_2} = \nabla \cdot M \nabla \mu \tag{5-49}$$

Combining Eqs. (5-48) and (5-49) recovers the Cahn-Hilliard equation as in Eq. (4-3). Two points should be noted: first, the diffusion process driven by the chemical potential difference is assumed to occur on a longer time scale than the particle collision; second, to recover the Cahn-Hilliard equation only the 0^{th} and 1^{st} order velocity moments of the distribution function h_i (i.e., Eqs. (5-18) and (5-19)) are used to link the microscopic description of the particle motion to the macroscopic fluid motion, while to recover the mass and momentum conservation equations (Eqs. (5-36) and (5-44)) the 0^{th}, 1^{st}, and 2^{nd} order velocity moments of the distribution function g_i (Eqs. (5-6), (5-7), and (5-39)) are used, which has important implications for boundary conditions. That is, the boundary conditions for the distribution functions need to maintain the same relationships between the distribution functions and the macroscopic quantities in the velocity moments.

5.2.3 Solving Lattice Boltzmann equations

The objective of this section is to develop an explicit scheme for solving the particle evolution equations and determine the best way of computing the relaxation time that plays a central role in the particle evolution dynamics.

To solve the evolution equations for g_i (Eq. (5-5)) and h_i (Eq. (5-17)), we can apply the trapezoidal rule to integrate over one time step δt along the characteristic direction given by $\mathbf{e}_i$:

$$g_i(\mathbf{x}+\mathbf{e}_i\delta t, t+\delta t) - g_i(\mathbf{x}, t) \tag{5-50}$$

$$= -\frac{1}{2\tau}\left[\left(g_i - g_i^{eq}\right)\big|_{\mathbf{x}+\mathbf{e}_i\delta t, t+\delta t} - \left(g_i - g_i^{eq}\right)\big|_{\mathbf{x},t}\right]$$

$$+ \frac{\delta t}{2}\left[gt_i\big|_{\mathbf{x}+\mathbf{e}_i\delta t, t+\delta t} + gt_i\big|_{\mathbf{x},t}\right]$$

$$h_i(\mathbf{x}+\mathbf{e}_i\delta t, t+\delta t) - h_i(\mathbf{x}, t) \tag{5-51}$$

$$= -\frac{1}{2\tau}\left[\left(h_i - h_i^{eq}\right)\big|_{\mathbf{x}+\mathbf{e}_i\delta t, t+\delta t} - \left(h_i - h_i^{eq}\right)\big|_{\mathbf{x},t}\right]$$

$$+ \frac{\delta t}{2}\left[ht_i\big|_{\mathbf{x}+\mathbf{e}_i\delta t, t+\delta t} + ht_i\big|_{\mathbf{x},t}\right]$$

where $\tau = \lambda/\delta t$ is the dimensionless relaxation time,

$$gt_i = (\mathbf{e}_i - \mathbf{u}) \cdot [\Gamma_i(\mathbf{u}) \cdot \mathbf{F} + \Gamma_i(0) \cdot \nabla\zeta(\rho)] \tag{5-52}$$

$$ht_i = (\mathbf{e}_i - \mathbf{u}) \cdot \left(\frac{C}{\rho c_s^2}\mathbf{F} + \nabla C - \frac{C}{\rho}\nabla\rho\right)\Gamma_i(\mathbf{u}) + \Gamma_i(\mathbf{u})\nabla \cdot M\nabla\mu \tag{5-53}$$

To maintain an explicit scheme, we introduce the modified distribution functions:

$$\bar{g}_i = g_i + \frac{1}{2\tau}\left(g_i - g_i^{eq}\right) - \frac{\delta t}{2}gt_i \tag{5-54}$$

$$\bar{g}_i^{eq} = g_i^{eq} - \frac{\delta t}{2}gt_i \tag{5-55}$$

$$\bar{h}_i = h_i + \frac{1}{2\tau}\left(h_i - h_i^{eq}\right) - \frac{\delta t}{2}ht_i \tag{5-56}$$

$$\bar{h}_i^{eq} = h_i^{eq} - \frac{\delta t}{2}ht_i \tag{5-57}$$

Then the evolution equations (5-50) and (5-51) become:

$$\bar{g}_i(\mathbf{x}+\mathbf{e}_i\delta t, t+\delta t) - \bar{g}_i(\mathbf{x}, t) = -\frac{1}{\tau+0.5}\left(\bar{g}_i - \bar{g}_i^{eq}\right)\big|_{\mathbf{x},t} + \delta t gt_i\big|_{\mathbf{x},t} \tag{5-58}$$

$$\bar{h}_i(\mathbf{x}+\mathbf{e}_i\delta t, t+\delta t) - \bar{h}_i(\mathbf{x}, t) = -\frac{1}{\tau+0.5}\left(\bar{h}_i - \bar{h}_i^{eq}\right)\big|_{\mathbf{x},t} + \delta t ht_i\big|_{\mathbf{x},t} \tag{5-59}$$

With Eqs. (5-6), (5-7), (5-18), (5-19), (5-54), and (5-56), we can obtain:

$$C = \sum \bar{h}_i + \frac{\delta t}{2} \nabla \cdot M \nabla \mu \tag{5-60}$$

$$p = \sum \bar{g}_i - \frac{\delta t}{2} \mathbf{u} \cdot \nabla \zeta(\rho) \tag{5-61}$$

$$\rho \mathbf{u} = \frac{1}{c_s^2} \sum \bar{g}_i \mathbf{e}_i - \frac{\delta t}{2} C \nabla \mu \tag{5-62}$$

Note that in Eqs. (5-60) and (5-61) we use μ and p from the previous time step to avoid implicitness, which still gives a second order accuracy in time [176]. The density is taken as a linear function of the composition C across the interface:

$$\rho = \frac{C - C_l}{C_h - C_l} (\rho_h - \rho_l) + \rho_l \tag{5-63}$$

where the subscripts h and l stand for the two different phases, C_l and C_h are two constants representing two different phases (here we choose C_l = 0 for surrounding air and C_h = 1 for liquid).

So far we have shown the derivation of the LB evolution equations of the distribution functions and the forcing term **F** from the phase-field model. Although the similar LB evolution equations have been used in the literature before (e.g., [172]), we have shown a different approach of deriving the LB evolution equations and identified the physical meanings of different components of the distribution functions, especially for the explicit expression of $g_i^{(1)}$, which represents the momentum flux from the neighboring region due to the velocity gradients. We have also learned that the formulation of g_i^{eq}, and h_i^{eq} are responsible for the local conservation of mass and momentum, and the composition C respectively, while $h_i^{(1)}$ does not play any role in the evolution because there is no corresponding term in the recovered macroscopic equations. The second and higher order of the distribution functions g_i and h_i do not affect the macroscopic fluid dynamics either

because there are no corresponding terms in the macroscopic equations, that is, the macroscopic Navier-Stokes equations only contain the information of the evolution dynamics of the 0^{th} and 1^{st} order of the distribution functions. The implication is that the LB evolution equations of the distribution functions have the capacity of describing more complicated dynamics (higher order non-linear dynamics) beyond the Navier-Stokes equations by properly formulating corresponding macroscopic terms for higher order components of the distribution functions in a similar fashion although the focus of the current work is only to recover the dynamics described by the phase-field model. The physical meanings of different components of the distribution functions from the above derivation have shown consistency between the microscopic description and the macroscopic description of the fluids and this understanding can also help us formulate the boundary conditions without messing up the fluid dynamics.

5.2.4 Relaxation time and boundary conditions

In order to apply the LBM to simulate droplet impingement dynamics, we need to address three additional issues that were insufficiently addressed in the literature, including the treatment of the relaxation time τ across the liquid-air interface, the wetting boundary condition, and the velocity boundary for the solid wall.

5.2.4.1 Modeling of relaxation time across the interface

One popular treatment for the relaxation time across the interface is to take the same linear form as for density:

$$\tau = \frac{C - C_l}{C_h - C_l}(\tau_h - \tau_l) + \tau_l \tag{5-64}$$

Lee and Liu [172] proposed an inverse linear form arguing that the collision frequency should be linearly proportional to C:

$$\frac{1}{\tau} = \frac{C - C_l}{C_h - C_l}\left(\frac{1}{\tau_h} - \frac{1}{\tau_l}\right) + \frac{1}{\tau_l} \tag{5-65}$$

However, we have found inconsistencies between the treatments in the existing LB schemes and in the phase-field model and many other well-established traditional CFD algorithms. In the phase-field model, the dynamic viscosity η ($\eta = \rho\tau c_s^2 \delta t$) is treated to be proportional to C, which leads to:

$$\tau = \frac{\frac{C - C_l}{C_h - C_l}(\rho_h\tau_h - \rho_l\tau_l) + \rho_l\tau_l}{\frac{C - C_l}{C_h - C_l}(\rho_h - \rho_l) + \rho_l} \tag{5-66}$$

The profiles of relaxation time and dynamic viscosity calculated from these three different approaches are plotted in Figure 5-1 through Figure 5-4 for two different situations (low liquid viscosity: $\tau_l > \tau_h$ and high liquid viscosity: $\tau_l < \tau_h$). As we can see, there are clear differences between the relaxation profiles calculated using the three different approaches.

Lee and Liu [172] reported a much slower droplet spreading, not matching experimental data, for low liquid viscosity with the adoption of the linear form (Eq. (5-64)) than the inverse linear form (Eq. (5-65)). As Figure 5-1 shows, the inverse linear form (Eq. (5-65)) yields relaxation time behavior qualitatively similar to that produced using the linear dynamic viscosity form (Eq. (5-66)) when $\tau_l > \tau_h$. On the other hand, the inverse linear form agrees poorly with calculations using the linear dynamic viscosity form, even in the trend of dependence on composition C, when $\tau_l < \tau_h$ as shown in Figure 5-3. The simplest linear from (Eq. (5-64)) shows predictions which deviate substantially both in trend and

magnitude from those by other two models for both viscosity limits as shown in Figure 5-1 and Figure 5-3.

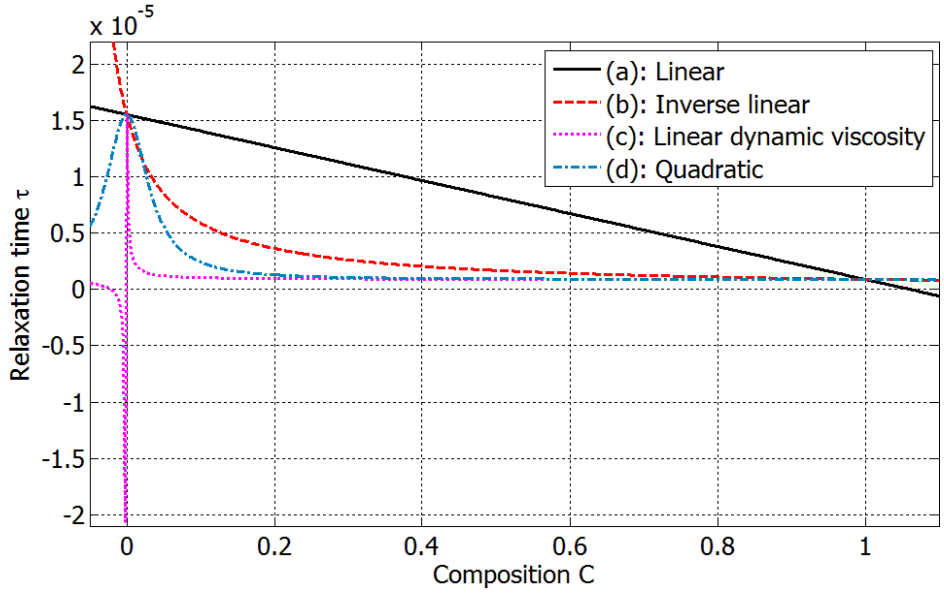

Figure 5-1. Relaxation time as a function of C for low viscosity liquid ($\tau_l > \tau_h$) calculated from different equations: (a). Eq. (5-64); (b). Eq. (5-65); (c). Eq. (5-66); (d). Eq. (5-67).

It is compelling to use Eq. (5-66) because of its fundamental consistency with the continuous formulation of transport equations; however, as shown in Figure 5-1 and Figure 5-3, the relaxation time exhibits drastic change due to high density variation when C is around 0. Not only non-physical negative τ values are observed at low fluid viscosities, but also severe numerical instabilities in solving the LBM equations occur when C is slightly changing near 0 during the transient simulation. The numerical instability has been confirmed by our numerical tests under a wide range of conditions.

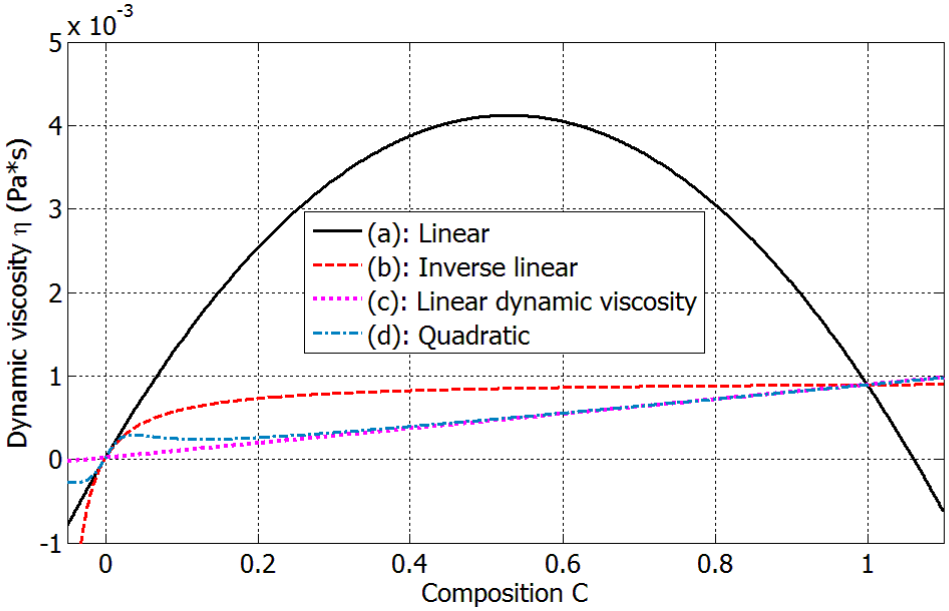

Figure 5-2. Dynamic viscosity as a function of C for low viscosity liquid ($\tau_l > \tau_h$) calculated from different equations: (a). Eq. (5-64); (b). Eq. (5-65); (c). Eq. (5-66); (d). Eq. (5-67).

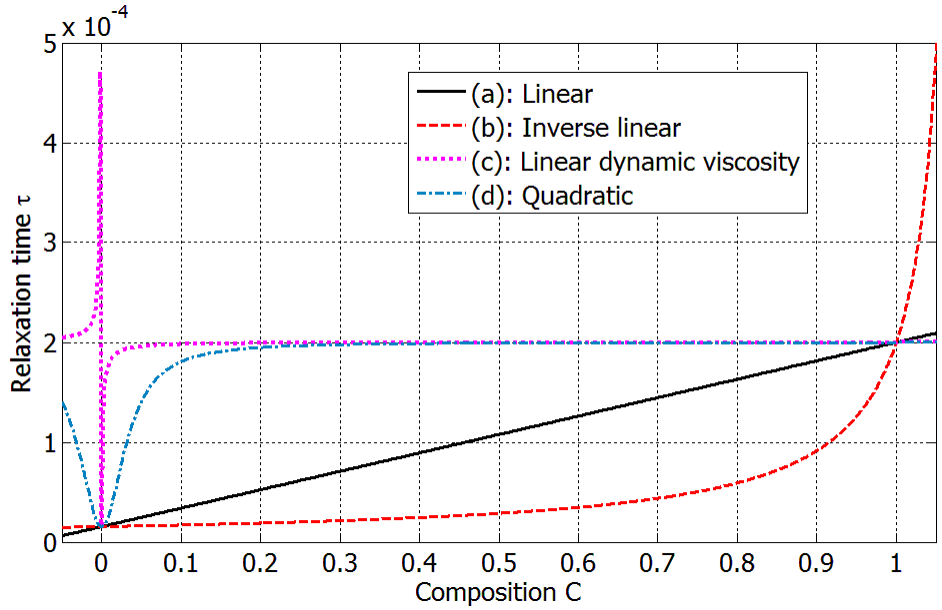

Figure 5-3. Relaxation time as a function of C for high viscosity liquid ($\tau_l < \tau_h$) calculated from different equations: (a). Eq. (5-64); (b). Eq. (5-65); (c). Eq. (5-66); (d). Eq. (5-67).

Therefore, as an approach justified on the basis of improving robustness for numerical computations, yet without a significant deviation from the fundamental form inspired by the continuous form of governing transport equations, we propose a quadratic form to alleviate the stability issue associated with oscillations and to negative values with Eq. (5-66):

$$\tau = \frac{\left(\frac{C - C_l}{C_h - C_l}\right)^2 (\rho_h \tau_h - \rho_l \tau_l) + \rho_l \tau_l}{\left(\frac{C - C_l}{C_h - C_l}\right)^2 (\rho_h - \rho_l) + \rho_l} \tag{5-67}$$

The unique construction of the function form will ensure the calculated relaxation profile always remains close to that calculated with the phase-field approach (i.e., Eq. (5-66)) because both $((C - C_l)/(C_h - C_l))^2$ and $(C - C_l)/(C_h - C_l)$ vary from 0 to 1 with slightly different changing speed. The predictions of the relaxation time using Eq. (5-67) for both situations ($\tau_l > \tau_h$ or $\tau_l < \tau_h$) are shown in Figure 5-1 and Figure 5-3, respectively, to demonstrate that the quadratic form generally follows the results of Eq. (5-66) in the off-zero range of composition C values, yet avoids the oscillation and negative values in the vicinity of $C = 0$.

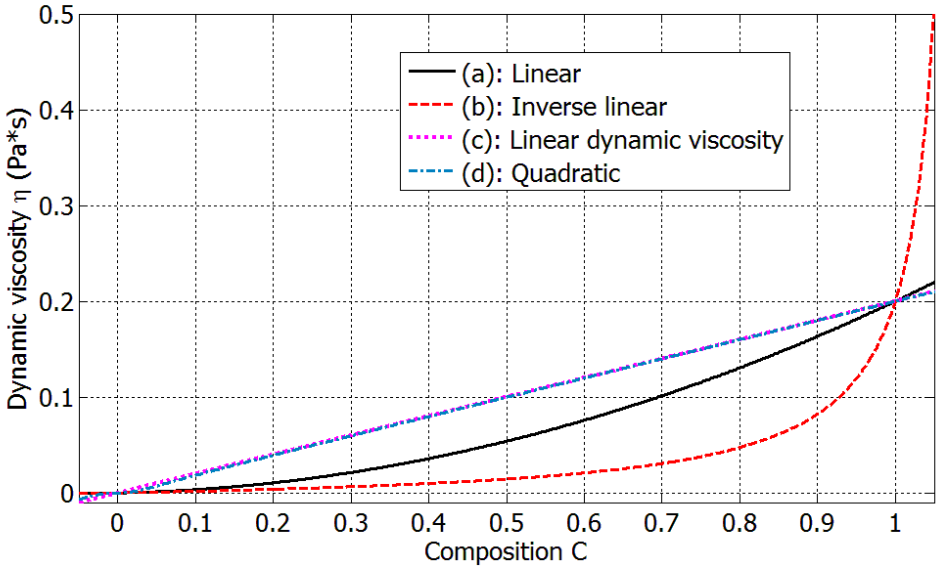

Figure 5-4. Dynamic viscosity as a function of C for high viscosity liquid ($\tau_l < \tau_h$) calculated from different equations: (a). Eq. (5-64); (b). Eq. (5-65); (c). Eq. (5-66); (d). Eq. (5-67).

5.2.4.2 Partial wetting boundary conditions

For most previous studies, a surface energy formulation for computation of the contact angle is employed by taking into account the wall free energy through linear, quadratic, or cubic approximations [170, 172]. A geometric formulation for the wetting condition is mathematically equivalent to the surface energy formulation, but computationally more efficient and more accurate in numerical discretization because the surface energy formulation usually causes a discrepancy between the prescribed contact angle and the computed contact angle [177]. Inspired by the adoption of the geometric formulation in the phase-field model, we also adopt the geometric formulation for the proposed LB formulation in order to be consistent with COMSOL implementation of the contact angle treatment. The geometric relationships are illustrated in Figure 5-5.

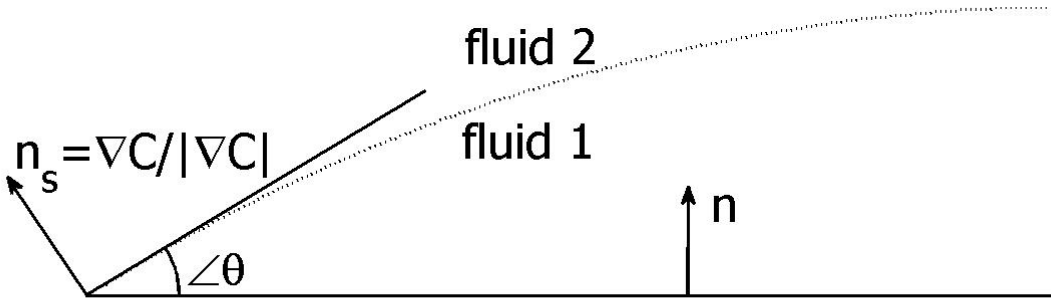

Figure 5-5. Illustration of the geometric relationships of a contact angle.

$$\mathbf{n}_s = \frac{\nabla C}{|\nabla C|} \tag{5-68}$$

where $\mathbf{n}_s$ is the outer normal to the interface.

$$\tan\left(\frac{\pi}{2} - \theta\right) = \frac{\mathbf{n}_s \cdot \mathbf{n}}{|\mathbf{n}_s - (\mathbf{n}_s \cdot \mathbf{n})\mathbf{n}|} = \frac{\mathbf{n} \cdot \nabla C}{|\nabla C - (\mathbf{n} \cdot \nabla C)\mathbf{n}|} \tag{5-69}$$

where θ is the equilibrium contact angle, and $\mathbf{n}$ is the normal to the wall. A second boundary condition is required to ensure there is no mass flux across the non-permeable wall:

$$\mathbf{n} \cdot \nabla \mu|_{wall} = 0 \tag{5-70}$$

For a given direction of the wall (i.e., n), Eqs. (5-69) and (5-70) specify the Neumann boundary conditions for C and μ respectively. In order to test its impact on the numerical accuracy, we compared the proposed geometric formulation and the existing surface energy formulation [172] for both static and dynamic wetting.

In static wetting, a static droplet is generated sitting on a solid wall with different prescribed contact angles ranging from 15° to 150°. The relevant simulation parameters are:$\rho_h = 1$, $\rho_l = 0.0237$, $\tau_l = 0.205$, $\tau_h = 0.075$, $\sigma = 0.00156$, and $M = 0.02/\beta$. It is assumed that the droplet reaches equilibrium when the kinematic energy per unit volume converges to zero. The equilibrium contact angle is then measured at the contact line

using the geometry of the droplet profile (C = 0.5) obtained from the simulation. We tested the difference between the proposed geometric formulation and the existing surface energy formulation on enforcing the prescribed contact angle as shown in Figure 5-6. As we can tell, the proposed geometric formulation enforces the prescribed contact angle better than the surface energy formulation in most of the cases. They both show zero numerical error when the prescribed contact angle is 90°.

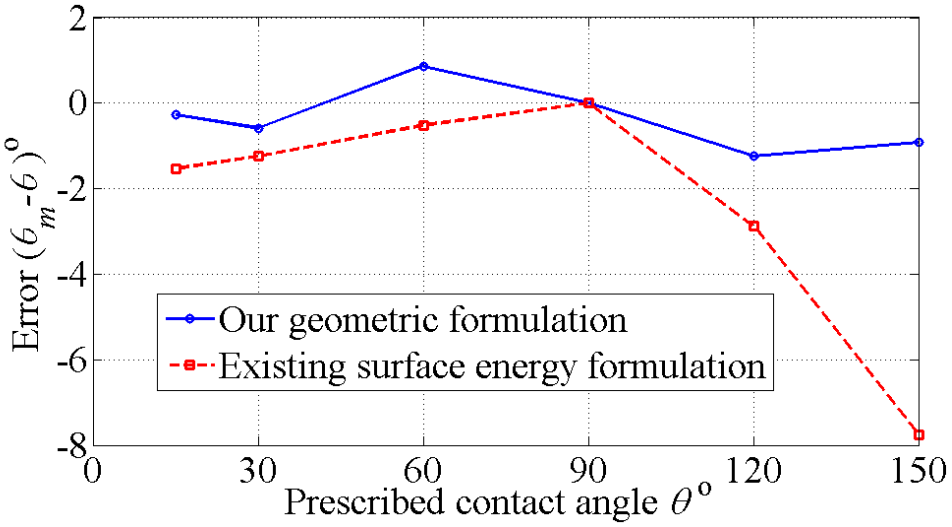

Figure 5-6. Difference between the proposed geometric formulation and the existing surface energy formulation on enforcing prescribed contact angle in static wetting (θ_m: measured contact angle; θ: prescribed contact angle).

In dynamic wetting, a droplet is generated with an initial velocity impinging on a solid surface with a prescribed contact angle of 107°. The Weber number and the Reynolds number are set to be 12.8 and 238 respectively. The contact angle is measured at the contact line using the droplet profile at every time step during the impinging process. As we can observe from Figure 5-7, the measured contact angle from simulations with the surface energy formulation gradually relaxes to the prescribed contact angle during the

droplet impinging process while the proposed geometric formulation can enforce the prescribed contact angle consistently during the entire dynamic wetting process.

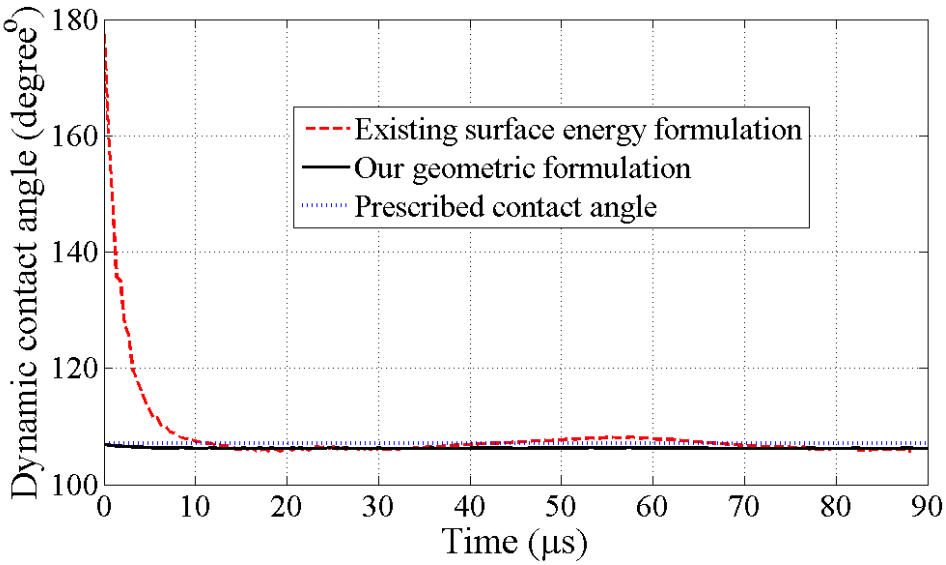

Figure 5-7. Difference between the proposed geometric formulation and the existing surface energy formulation on enforcing prescribed contact angle during the dynamic wetting process.

5.2.4.3 Velocity boundary conditions

It is straightforward to apply a Dirichlet velocity boundary condition for incompressible Navier-Stokes equations because Navier-Stokes equations explicitly solve for the velocity field. On the other hand, LBM solves the evolution of particle populations that have more degrees of freedom than what can be imposed by the constraints of the velocity boundary condition. Therefore, it can be complicated to translate the velocity boundary conditions in the continuous formulation into the equivalent boundary conditions for the particle populations. Many previous studies chose the popular bounced-back scheme for the non-slip wall boundary conditions due to its simplicity [169-170], which did not conserve momentum on the boundary [140]. Therefore, it will

not get the hydrodynamics right at the boundary with the bounced-back scheme. In LBM computations, the boundary conditions are implemented by finding the appropriate particle population distribution at each computational node near the wall after the streaming step, as illustrated by the dashed vectors in Figure 5-8, such that the constraints imposed by the specified velocity at the boundary are enforced.

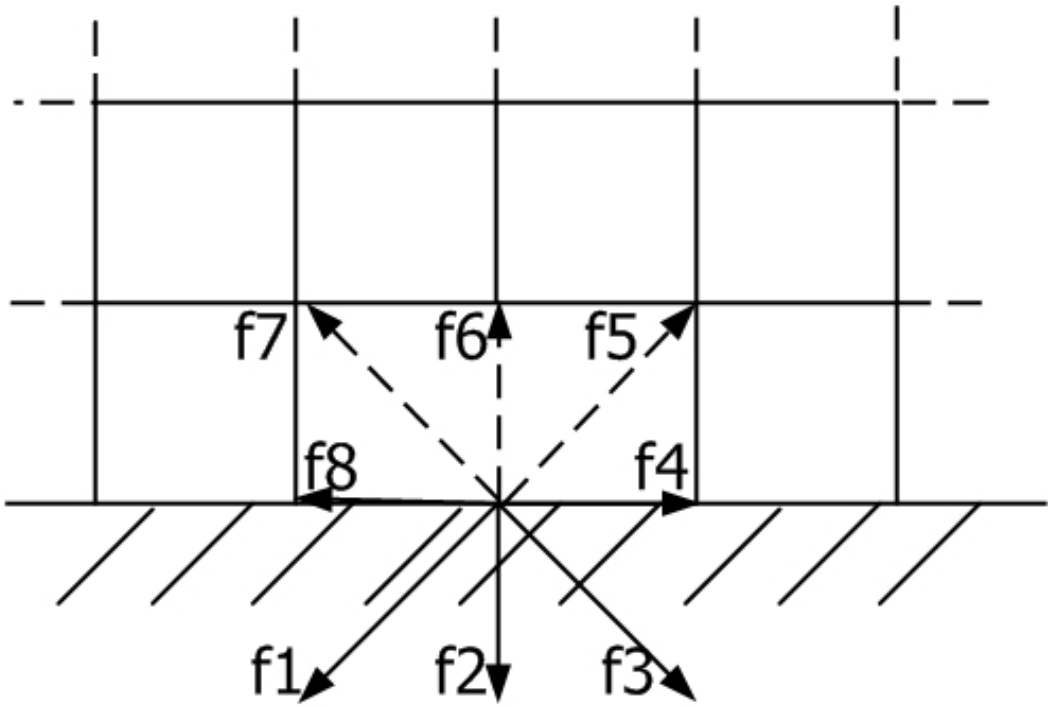

Figure 5-8. Illustration of particle populations on the wall boundary. The dashed vectors stand for incoming unknown particle populations after streaming step.

It should be noted that the proposed LBM formulation solves for evolution of the modified distribution functions $\bar{g}_i$ and $\bar{h}_i$, which only serve for convenience of calculations and do not have clear physical meanings. However, all the constraints from boundary conditions only apply to the original distribution functions g_i and h_i.Therefore, to implement the boundary conditions in our LBM simulations, we need to first obtain g_i and h_i from $\bar{g}_i$ and $\bar{h}_i$, apply all the constraints to find out the unknown g_i and h_i, and

then calculate the unknown $\bar{g}_i$ and $\bar{h}_i$ with Eqs. (5-54), (5-55), (5-56), and (5-57). We will explain how to determine the unknown g_i and h_i in the following.

First, we can find out the macroscopic quantity *C* with known particle populations and Eqs. (5-18) and (5-19):

$$C = \sum h_i = h_+ + h_0 + h_- \tag{5-71}$$

$$C\mathbf{u}_n = \sum h_i \mathbf{e}_i = h_+ - h_- \tag{5-72}$$

where $\mathbf{u}_n$ is the velocity normal to the wall. Therefore we can obtain:

$$C = \frac{1}{1 + \mathbf{u}_n}(2h_+ + h_0) \tag{5-73}$$

Then the density ρ on the boundary can be obtained from Eq. (5-63), and pressure p can be found from Eqs. (5-6) and (5-7) in a same procedure that we used to find out *C*. With the macroscopic quantities *C*, ρ, p, and $\mathbf{u}$ known on the boundary, one needs to find a set of particle populations g_i and h_i that satisfy Eqs. (5-6), (5-7), (5-18), (5-19), and (5-39). Therefore, we can reconstruct g_i and h_i as:

$$g_i = g_i^{eq}(p, \rho, \mathbf{u}) + g_i^{(1)} \tag{5-74}$$

$$h_i = h_i^{eq}(C, \rho, \boldsymbol{u}) \tag{5-75}$$

where $g_i^{(1)}$ can be obtained from Eq. (5-42), which can be approximated by:

$$g_i^{(1)} = -t_i \rho \lambda (\mathbf{Q}_i : \nabla \mathbf{u}) \tag{5-76}$$

This reconstruction of g_i and h_i will make sure the constraints Eqs. (5-6), (5-7), (5-18), (5-19), and (5-39) are satisfied and thus the macroscopic equations recovered on the boundary will be the same as those recovered in the bulk (i.e., Eq. (5-40)). However, the existing equilibrium bounce-back boundary [172] only takes into consideration the local

momentum conservation, that is, the 0th order of the distribution functions g_i^{eq} and h_i^{eq}. The 1st order of the distribution function $g_i^{(1)}$ is missing, which represents the momentum flux due to velocity gradient and viscosity effects. Therefore, the recovered macroscopic momentum equation will be missing the term $\mathbf{\Pi}_g^{(1)}$ in Eq. (5-40) and thus the momentum will not be conserved on the boundary. We have tested the effects of the term $g_i^{(1)}$ on droplet spreading as shown in Figure 5-9. The Weber number and the Reynolds number are set to be 12.8 and 238 respectively for the simulation with a prescribed contact angle of 107°. The experimental data are obtained from [162]. We can see clearly that the droplet spreads more slowly with the equilibrium bounce-back boundary than with our proposed velocity boundary due to the loss of momentum.

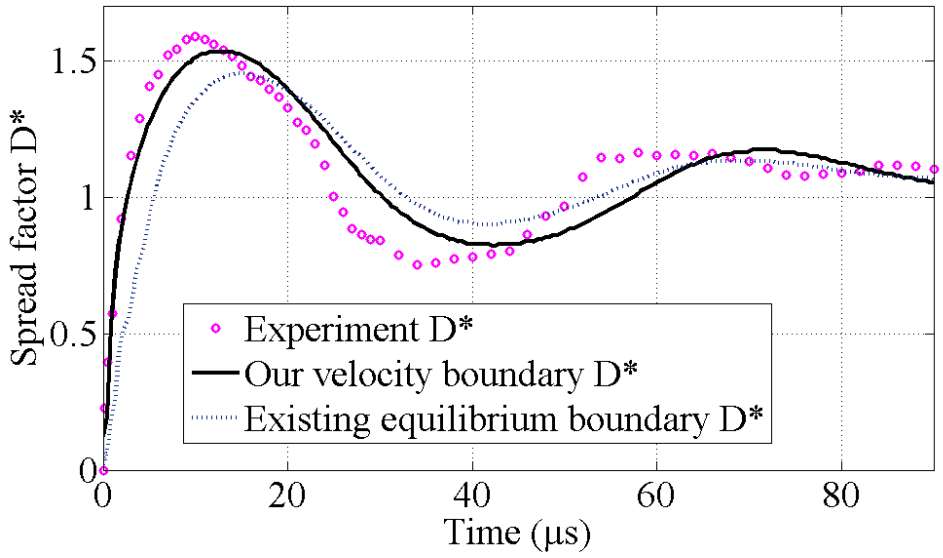

Figure 5-9. Difference between our proposed velocity boundary condition and the existing equilibrium bounce-back boundary condition.

5.3 Validation

We have implemented a 3D numerical solver based on our proposed LBM scheme with a D3Q19 lattice model to simulate droplet impingement on a solid surface This solver has shown a significant speed improvement over traditional CFD algorithms based on the continuous phase-field model, as implemented for example by the commercial software COMSOL. In order to choose appropriate simulation parameters and compare the LB simulation results with experimental data, we need to first address the relationship between the "lattice Boltzmann units" and the physical units.

5.3.1 Lattice Boltzmann units

There are two constraints for choosing appropriate lattice Boltzmann units: first, the simulation is supposed to be equivalent to the physical system; second, the spatial and time step should be small enough to well resolve the simulating physics. In section 4.1.1, we have conducted a dimensionless analysis to convert the physical system into a dimensionless system, which can be readily linked to a LB system. Let the length, time, and mass units in a LB system be δx, δt, and δm respectively, we can have the following relationships between the LB and the dimensionless systems:

$$u^{lb}\left(\frac{\delta x}{\delta t}\right) = u^{d}\left(\frac{L^{d}}{t^{d}}\right) \tag{5-77}$$

$$\nu^{lb}\left(\frac{(\delta x)^2}{\delta t}\right) = \nu^{d}\left(\frac{(L^{d})^2}{t^{d}}\right) \tag{5-78}$$

$$\rho^{lb}\left(\frac{\delta m}{\delta x^3}\right) = \rho^{d}\left(\frac{m^{d}}{(L^{d})^3}\right) \tag{5-79}$$

where the superscripts "*lb*" and "*d*" represent the LB and dimensionless systems respectively, the terms in the brackets are units for corresponding physical quantities, L^d, t^d, and m^d are dimensionless length, time, and mass units in the dimensionless systems

respectively and are all equal to 1, *u, v,* and ρ denote velocity, kinematic viscosity and density respectively. u^d and ρ^d are typically chosen as the reference velocity and density in the dimensionless system and are therefore equal to 1, while ν^d is the dimensionless kinematic viscosity and equal to 1/*Re*. Hence, we can solve Eqs. (5-77), (5-78), and (5-79) to obtain δx, δt, and δm:

$$\delta x = \frac{u^{lb}}{\nu^{lb} Re} \tag{5-80}$$

$$\delta t = \frac{(u^{lb})^2}{\nu^{lb} Re} \tag{5-81}$$

$$\delta m = \frac{\delta x^3}{\rho^{lb}} \tag{5-82}$$

With the three basic units, it is straightforward to calculate other physical quantities in LB units, such as surface tension and gravity:

$$\sigma^{lb} = \frac{\rho^{lb} \delta t^2}{\delta x^3 We} \tag{5-83}$$

$$g^{lb} = \frac{\delta t^2}{\delta x Fr} \tag{5-84}$$

To discretize the LB system, we can divide the reference length into *N* cells and reference time into *Nt* steps, which leads to:

$$N = \frac{1}{\delta x} = \frac{\nu^{lb} Re}{u^{lb}} \tag{5-85}$$

$$Nt = \frac{1}{\delta t} = \frac{\nu^{lb} Re}{(u^{lb})^2} \tag{5-86}$$

Therefore, the spatial and time resolutions for LB simulations are determined by choosing appropriate numerical values for ν^{lb} and u^{lb} for a given physical system (i.e., for a given *Re*). Since the proposed LB formulation is derived based on the

incompressible assumption, u^{lb} needs to be much smaller than the lattice "sound speed" c_s.

5.3.2 Experimental validation

With the implemented numerical solver based on the proposed LB formulation, we have tested five different cases for a single droplet impingement to compare with COMSOL simulation results and experimental data from [162]. The impingement conditions are listed in Table 5-1 and are taken from experimental studies, which will be used for validation of simulations. The fluid properties of the liquid droplet and the surrounding gas are taken as the properties of water and air at 1 atm and 25°C. For all the LBM simulations, the computational domain is set to be 100×100×70, and the droplet radius is set to be 25 LB units. Although the LBM has the advantage for massive parallelization due to the locality of the computations, all reported simulations are run on a single thread on a laptop PC with a memory requirement slightly over 1GB for each simulation and are completed within 20 hours for each case. For a similar mesh density (i.e., spatial resolution of computations), it would roughly take over 1 month for COMSOL to run the same 3D simulation on a 16-core cluster with over 100GB memory requirement based on our experience. Therefore, all the COMSOL simulations presented here were performed with a 2D axi-symmetrical model [109, 178].

The dimensionless spreading factor D^*, droplet height H^*, and the shape coefficient as predicted by our LBM and COMSOL simulations, as well as the LBM simulations by Lee et al. reported in literature [172], are compared against the experimental data as shown in Figure 5-10 through Figure 5-19 for combinations of parameters summarized in Table 5-1. The spreading factor is defined as the ratio of the diameter of the wetted area

to the droplet diameter, the dimensionless droplet height is defined as the ratio of the height of the droplet above the substrate to the droplet diameter, and the shape coefficient is a novel metric that we developed to quantify the droplet shape in section 3.1 [109, 179]. Note that in Lee et al.'s results [172], the spreading factor is defined as the ratio of the spreading diameter to the droplet diameter where the spreading diameter is the blob diameter when the droplet spreads and the diameter of the wetted area when droplet retracts, which is different from the definition of the spreading factor in the experiments.

We can see that overall the results agree very well in all five cases. There is an excellent agreement in time evolution of the spreading factor between our LBM simulations and COMSOL simulations, while the COMSOL simulations and the literature LBM simulations fail to capture the details of the droplet height change, which is particularly evident in Cases 2, 3, and 5 as shown in Figure 5-12, Figure 5-14, and Figure 5-18, respectively, for the later times after 10μs to 20μs, which leads to a discrepancy in the shape coefficient as well, as shown in Figure 5-11 through Figure 5-19. But overall the evolutions of the shape coefficient that characterizes the overall droplet shape match well between our LBM simulations and COMSOL, which establishes the consistency of our LBM formulation with the phase-field model in COMSOL. We can also see that for Cases 1 and 2, as shown in Figure 5-10 and Figure 5-12, respectively, both the LBM and COMSOL simulations fail to capture the oscillations of the droplet height. One possible reason is that the contact line pinning due to possible surface contamination could cause the discrepancy of the final equilibrium spreading factor as shown in Figure 5-10 and Figure 5-12 and affect the overall interface dynamics that is responsible for the droplet height oscillation.

Table 5-1. List of droplet impingement conditions.

	Case 1	Case 2	Case 3	Case 4	Case 5
Impact speed	4.36m/s	4.36m/s	4.36m/s	12.2m/s	12.2m/s
Droplet diameter	48.8μm	48.8μm	48.8μm	50.5μm	50.5μm
Weber number	12.8	12.8	12.8	103	103
Ohnesorge number	0.0151	0.0151	0.0151	0.0148	0.0148
Reynolds number	238	238	238	689	689
Equilibrium	31°	90°	107°	31°	107°

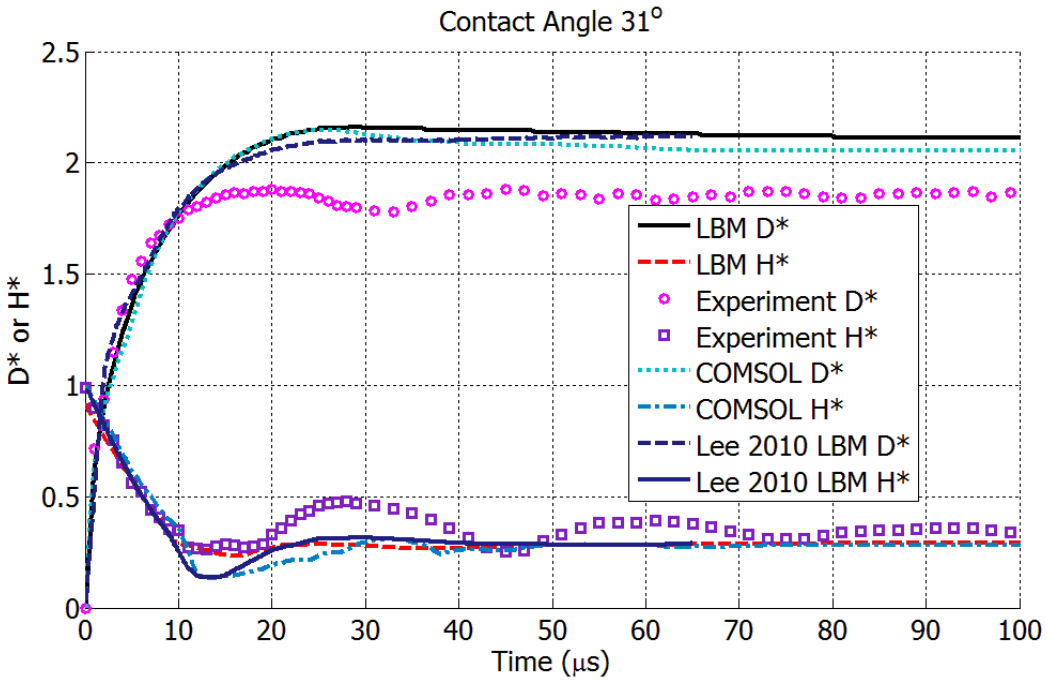

Figure 5-10. Validation of spreading factor D^* and dimensionless droplet height H^* for Case 1.

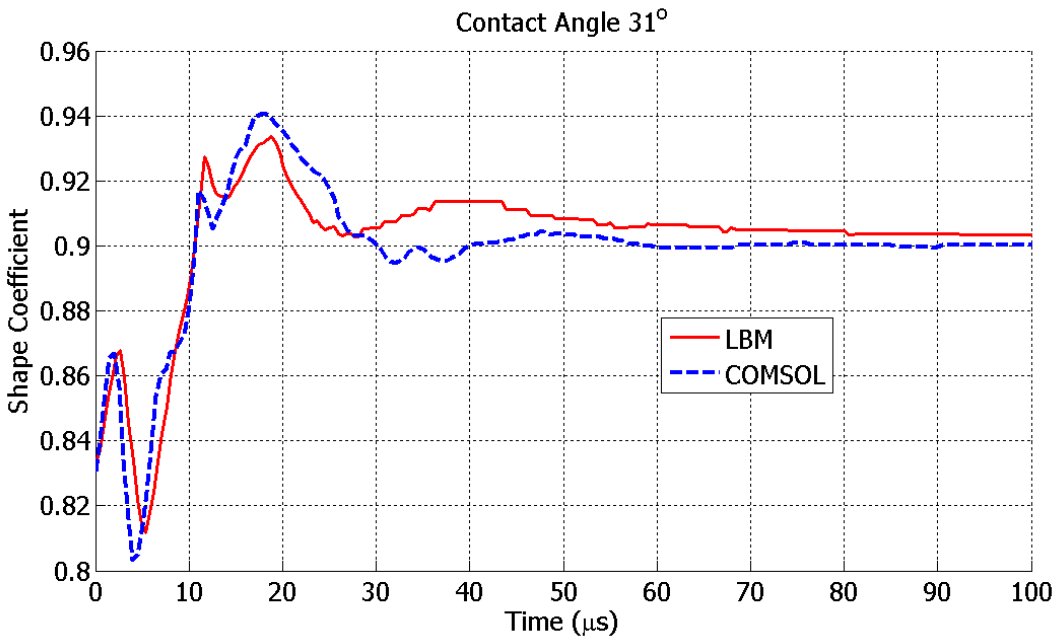

Figure 5-11. Comparison of shape coefficient change between LBM and COMSOL simulations for Case 1.

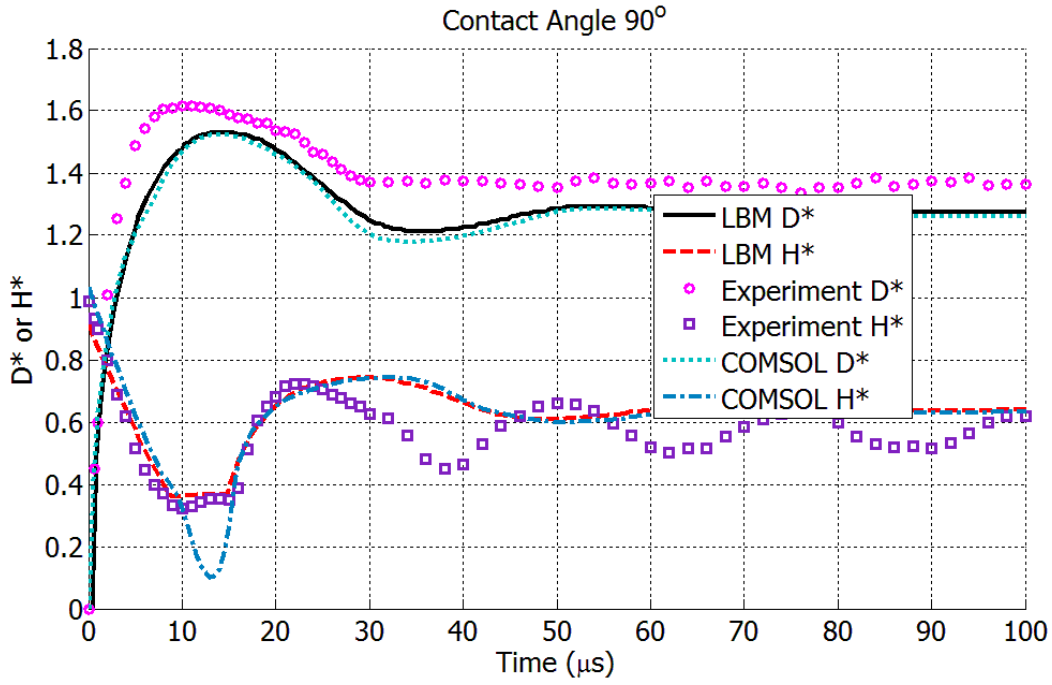

Figure 5-12. Validation of spreading factor D^* and dimensionless droplet height H^* for Case 2.

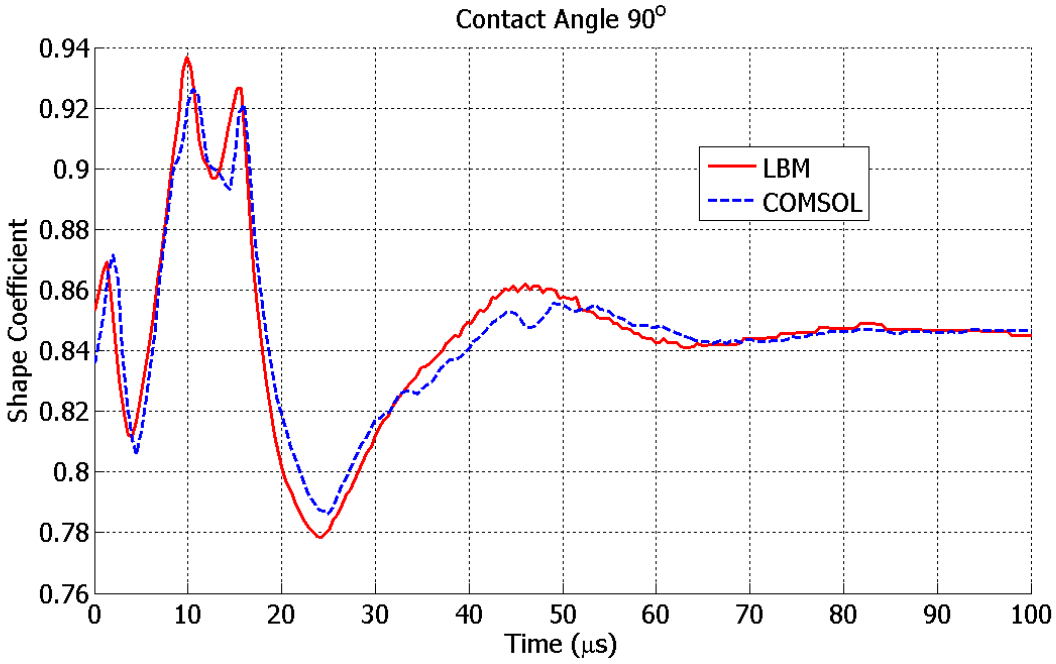

Figure 5-13. Comparison of shape coefficient change between LBM and COMSOL simulations for Case 2.

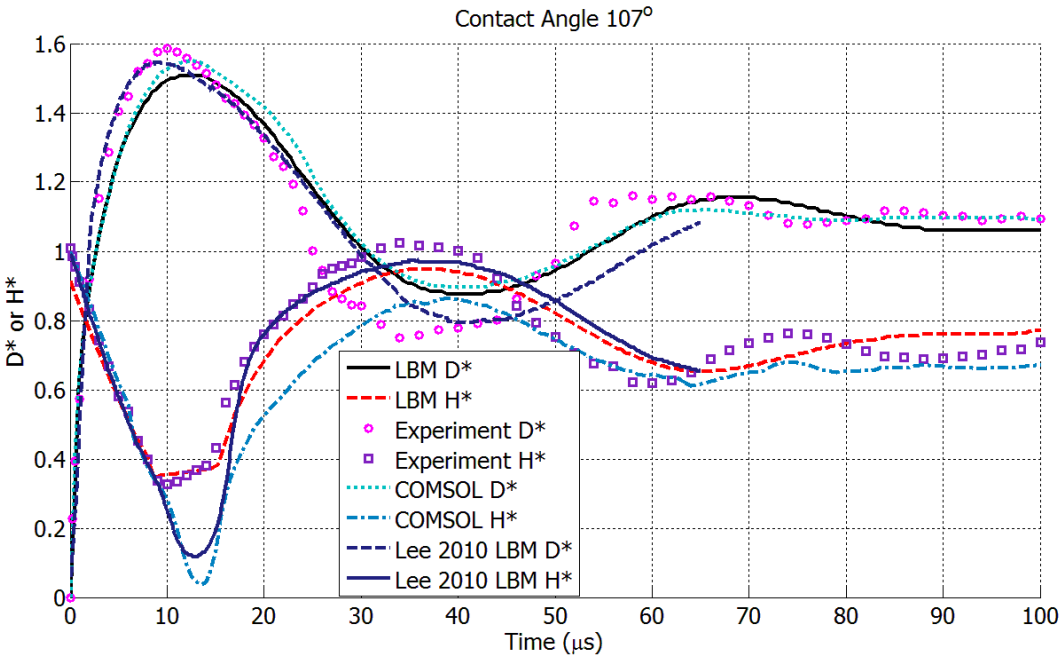

Figure 5-14. Validation of spreading factor D^* and dimensionless droplet height H^* for Case 3.

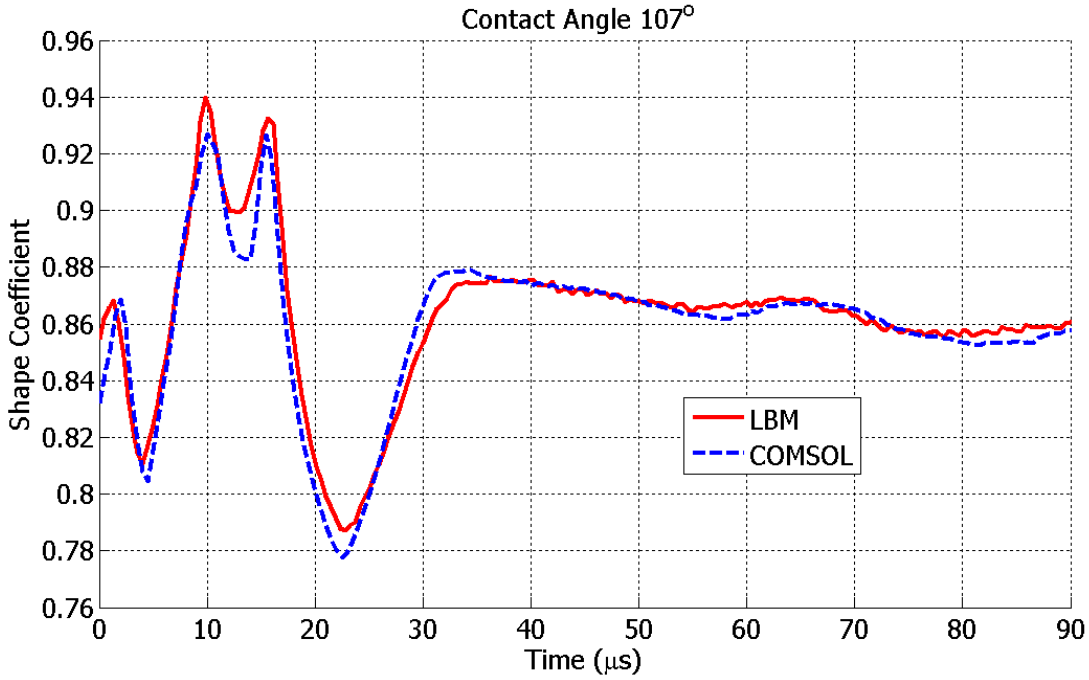

Figure 5-15. Comparison of shape coefficient change between LBM and COMSOL simulations for Case 3.

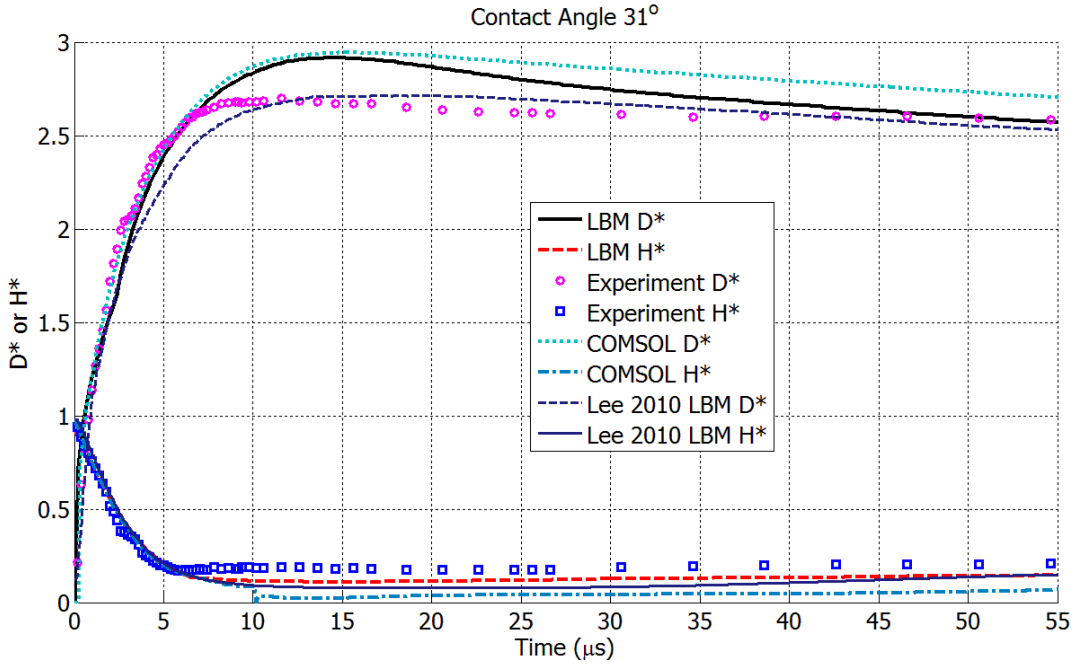

Figure 5-16. Validation of spreading factor D^* and dimensionless droplet height H^* for Case 4.

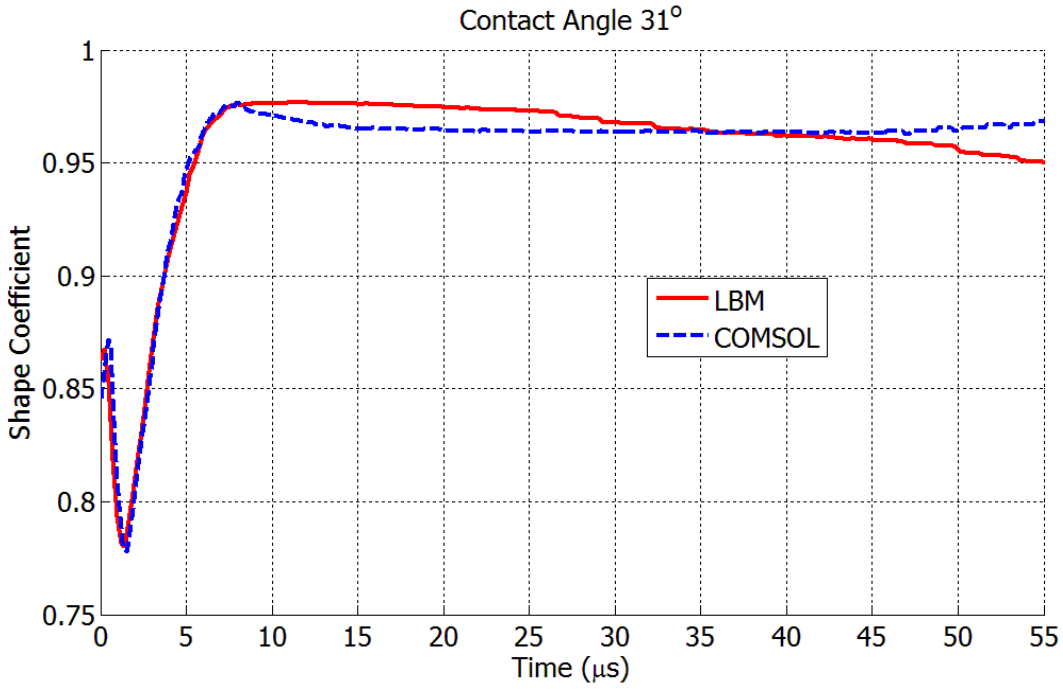

Figure 5-17. Comparison of shape coefficient change between LBM and COMSOL simulations for Case 4.

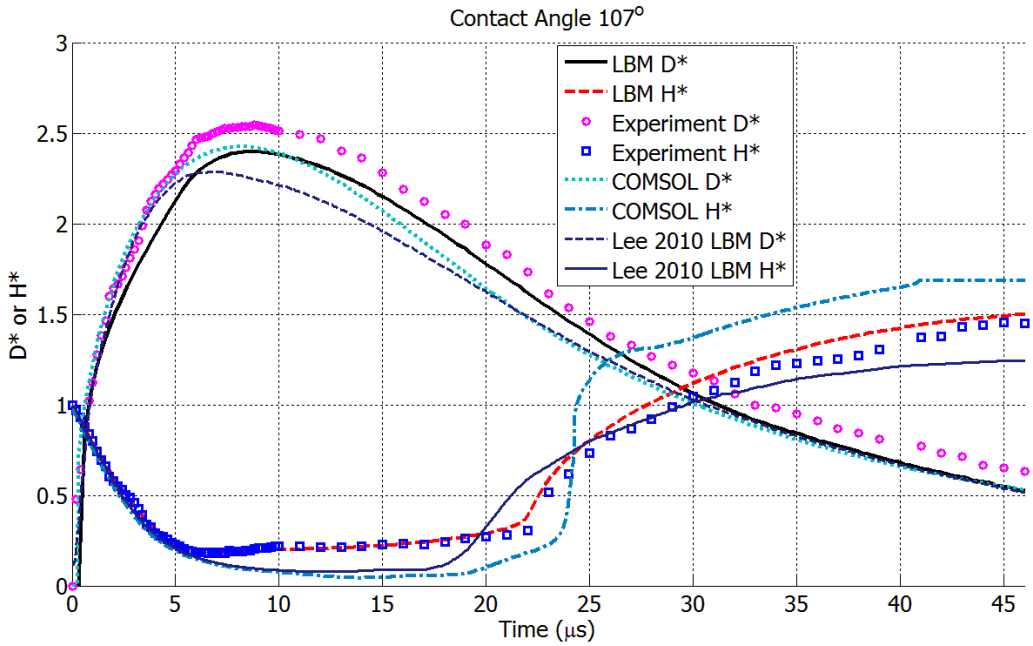

Figure 5-18. Validation of spreading factor D^* and dimensionless droplet height H^* for Case 5.

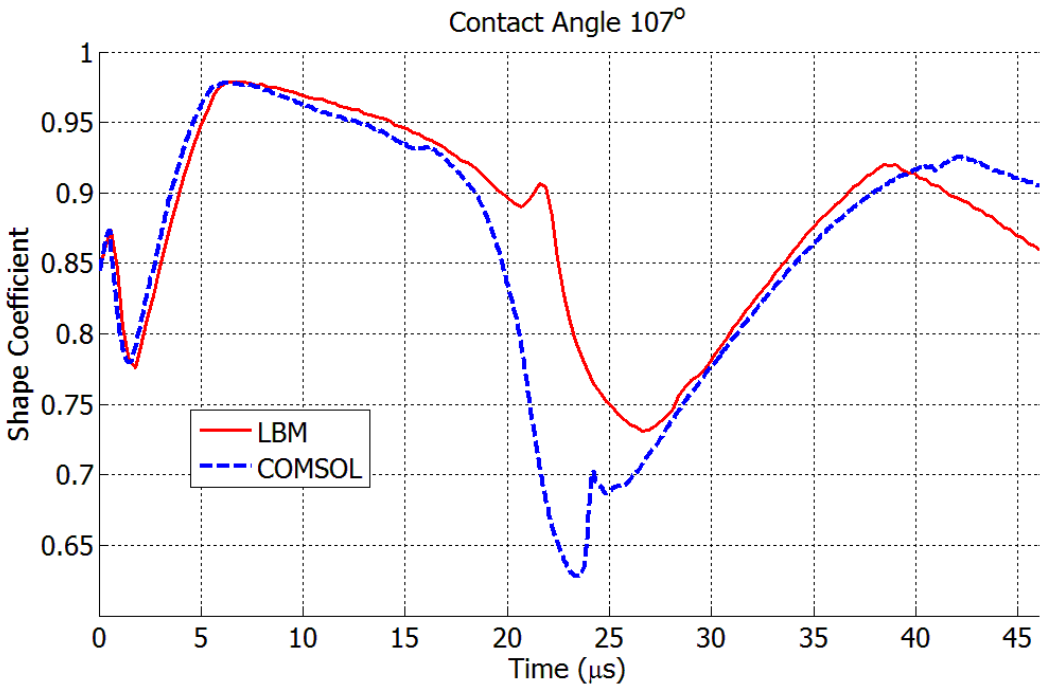

Figure 5-19. Comparison of shape coefficient change between LBM and COMSOL simulations for Case 5.

5.3.3 Demonstration of multiple droplet interaction

Computational efficiency of the implemented LBM solver, based on an improved algorithm described and validated in previous sections, in simulating an individual droplet impingement in 3-D opens up the possibility for studying multiple-droplet interactions. We exemplify this capability with three different simulation cases, including: 1) an impingement of two interacting droplets with a droplet spacing of 80 μm, as shown in Figure 5-20; 2) a-line-of-droplet impingement with a droplet spacing of 65 μm, as shown in Figure 5-21; and 3) a-square-array-of-droplet impingement with droplet spacing of 65 μm, 80 μm, 90 μm, and 100 μm, as shown from Figure 5-22 to Figure 5-25, respectively. The droplet spacing is defined as the distance between the centroids of the droplets. The droplet diameter is set to 50μm, the impact velocity is 10m/s, and the

contact angle is 90º for all cases. The Weber number is 100 and Ohnesorge number is 0.04, so the simulations are focusing on inertia dominated hydrodynamics, with more important effect of surface tension on the droplet shape evolution as compared to viscous forces.

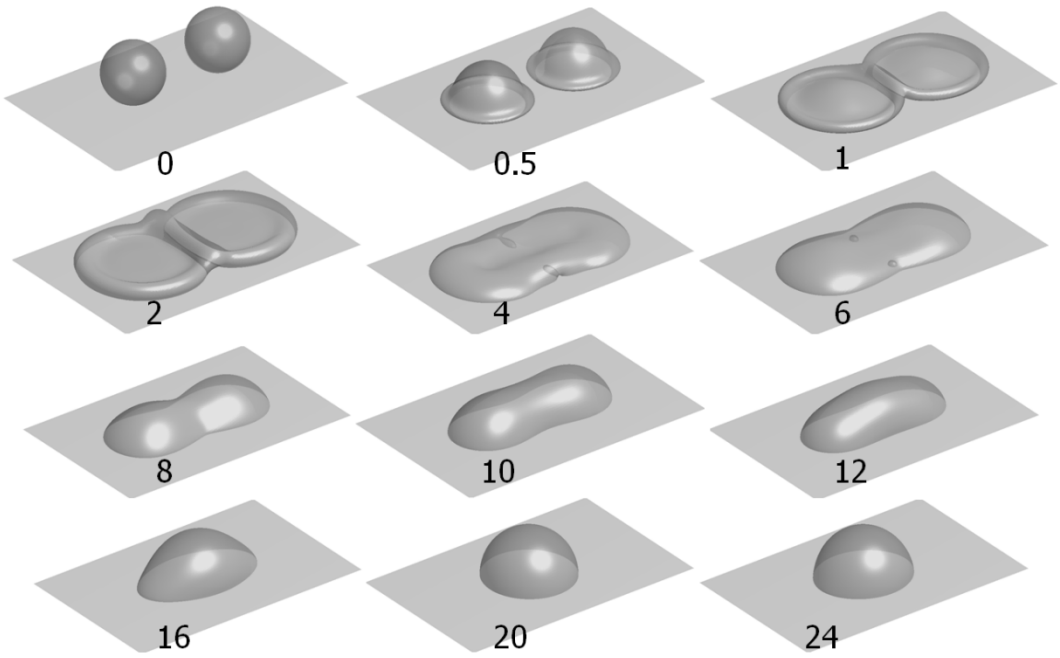

Figure 5-20. Demonstration of two-droplet impingement in the unit of dimensionless time (We = 100; Oh = 0.04; droplet spacing= 80μm).

In the two-droplet interaction case, as shown in Figure 5-20, upon impingement on the substrate, the droplets initially behave independently from each other; the dynamics start to change compared to single droplet impingement when the spreading droplets contact each other. As studied in Chapter 4 and [109], there are three competing forces that drive the shape evolution of a droplet upon impingement on substrate, including the inertial force from kinetic energy, surface tension from interface energy, and viscous force from viscosity effects. Upon contact and merging of two or more droplets, a total interfacial area of the droplet ensemble is reduced, and resulting release of an excess surface energy

is converted mainly into kinetic energy of spreading with minimal viscous energy dissipation (in the case of high We and low Oh numbers). On a longer time scale after the coalescence of the droplets, the kinetic energy of evolving droplet ensemble is dissipated by viscous forces, and the shape of the droplet relaxes back to the equilibrium shape (i.e., a spherical cap sitting on the substrate) of a single large droplet driven by the surface tension.

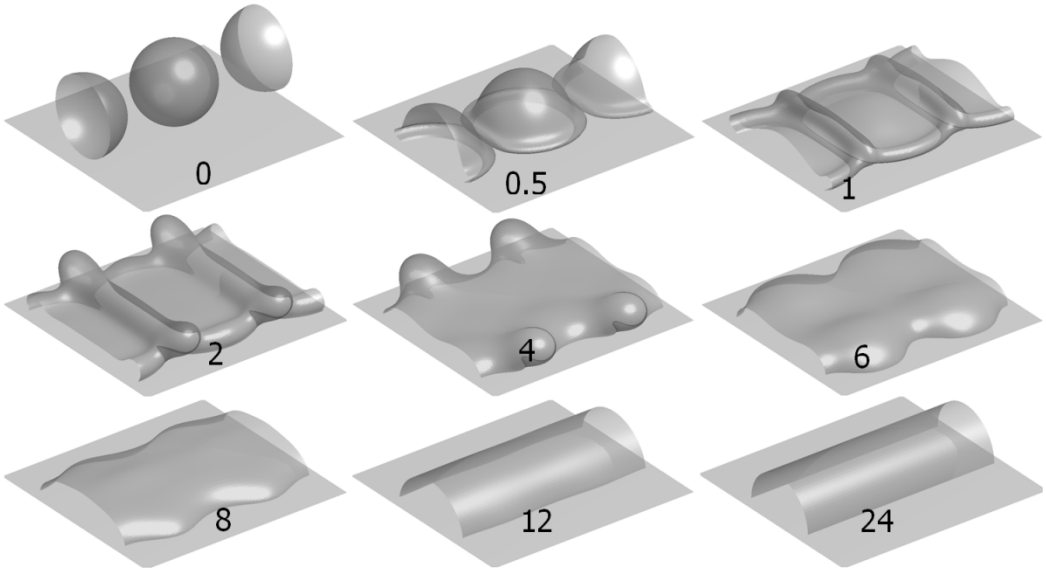

Figure 5-21. Demonstration of a-line-of-droplet impingement in the unit of dimensionless time (We = 100; Oh = 0.04; droplet spacing = 65μm).

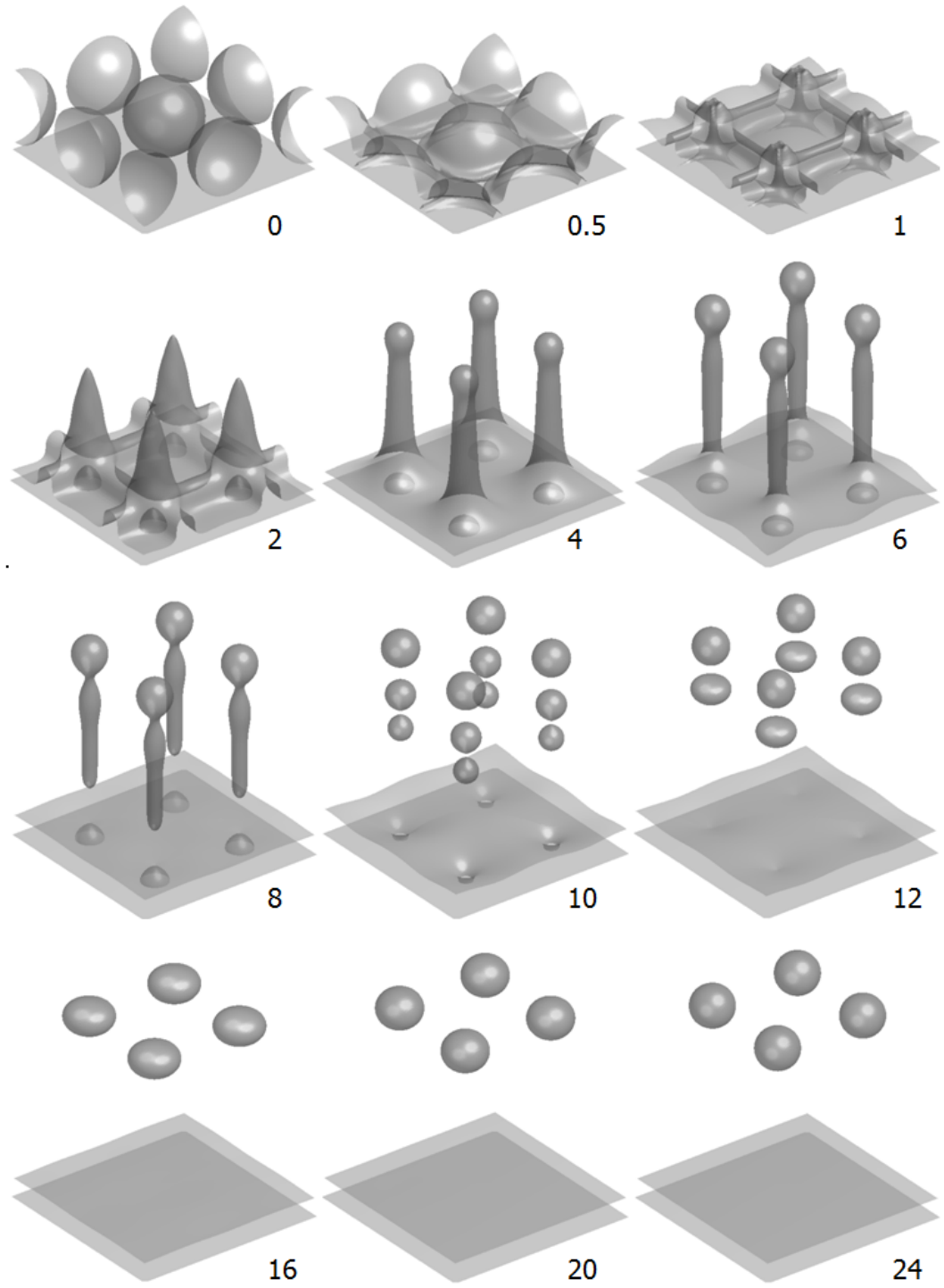

Figure 5-22. Demonstration of an-array-of-droplet impingement in the unit of dimensionless time (We = 100; Oh = 0.04; droplet spacing = 65μm).

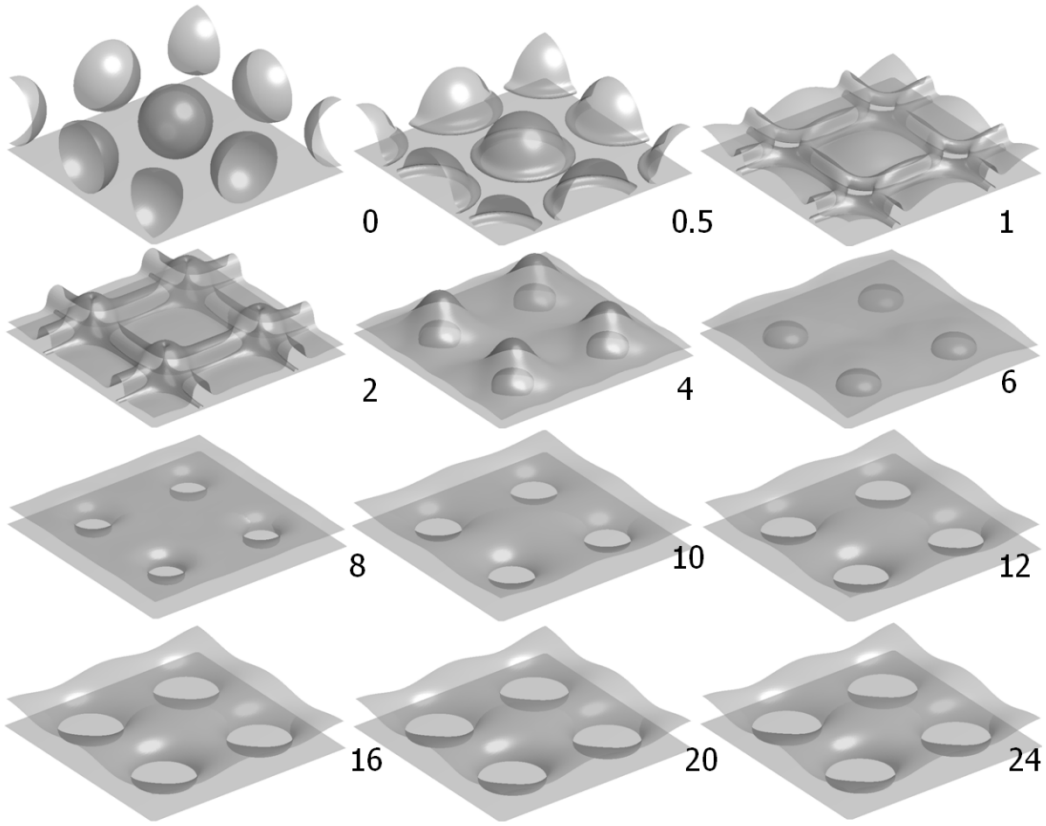

Figure 5-23. Demonstration of an-array-of-droplet impingement in the unit of dimensionless time (We = 100; Oh = 0.04; droplet spacing = 80μm).

For the case of the line-droplet interactions as shown in Figure 5-21, each droplet is neighbored by two droplets along a line with symmetric boundary conditions on the two ends, which effectively simulates the interaction dynamics of an infinitely long linear array of droplets. One notable observation is that the final equilibrium shape is very different from the case of two isolated droplet interaction (Figure 5-20) due to the constraint on the lateral spreading imposed by the presence of an additional neighboring droplet in an infinite line array. However, similar to the case of two-droplet interactions, conversion of surface to kinetic energy upon initial coalescence of droplets is the most critical event that determines the outcome of the interaction dynamics, which is mainly

determined by the droplet spacing under given impingement conditions. Since the droplet spacing in this case (65 μm) is smaller than that in the two-droplet impingement case (80 μm), the droplets contact each other at an earlier time and thus have greater kinetic energy at a merger of interfaces. Therefore, the shape of the droplet deforms greatly with emergence of fluid ridges and fingers during coalescence, as with significant difference between the shapes of the droplets in Figure 5-20 and Figure 5-21 as the droplet ensembles evolve in time towards their equilibrium states.

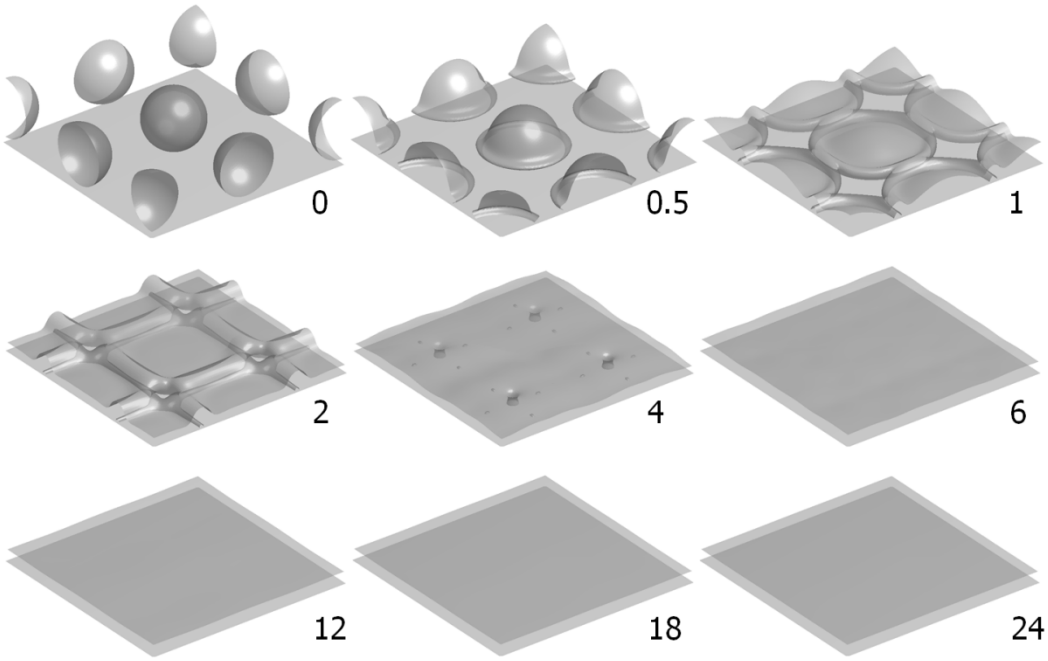

Figure 5-24. Demonstration of an-array-of-droplet impingement in the unit of dimensionless time (We = 100; Oh = 0.04; droplet spacing = 90μm).

In the array-droplet interaction, each droplet is surrounded by eight droplets, which are arranged into a square array with symmetric boundary conditions on all the edges, as shown in Figure 5-22 through Figure 5-25. Therefore, an infinitely large two-dimensional array of droplets is effectively simulated. Due to the additional neighboring droplets, the interaction dynamics become much more complex than in the previous cases and the final

equilibrium shape is different for arrangements with different droplet spacing (65, 80, 90, and 100 μm), as illustrated in Figure 5-22 through Figure 5-25. Unlike in the previous two cases considered, in which only two droplets coalesce at one location, four droplets meet at the same location in this case. Therefore, during the droplets coalescence, even more interface energy is converted into kinetic energy that drives dramatic deformation of coalescing droplet shapes, including splash and bounce-back phenomena, as evident in comparing Figure 5-21 and Figure 5-22. Indeed, as shown in Figure 5-22, the kinetic energy gained from the coalescence of the droplets is so large that it drives the droplet shape to deform to such an extent that the droplets break up and generate a stream of satellite droplets. If the droplet spacing is increased to 80 μm as shown in Figure 5-23, periodic depressions in the liquid film are formed at the locations where the droplets meet due to trapping of air bubbles during the droplet coalescence. If the droplet distance is further increased to 90 μm as shown in Figure 5-24, the droplets get in contact with each other at the time instant when the kinetic energy is already fairly small and coalescence of the droplets is largely driven by the surface tension. As a result, a uniform film is formed as the final equilibrium shape. If the droplet distance is further increased to 100 μm, the droplets meet with each other at a time when the droplets almost start to retract and the retracting kinetic energy is large enough to overcome an energetic advantage of reduced surface energy associated with coalescence of the droplets, and eventually break them up into individual droplets at equilibrium, as shown in Figure 5-25. These results further illustrate the importance of the droplet spacing and impingement velocity in multiple-droplet interaction dynamics. Of course, the dynamics will change in the case of fluids with different properties, which will be studied in Chapter 6.

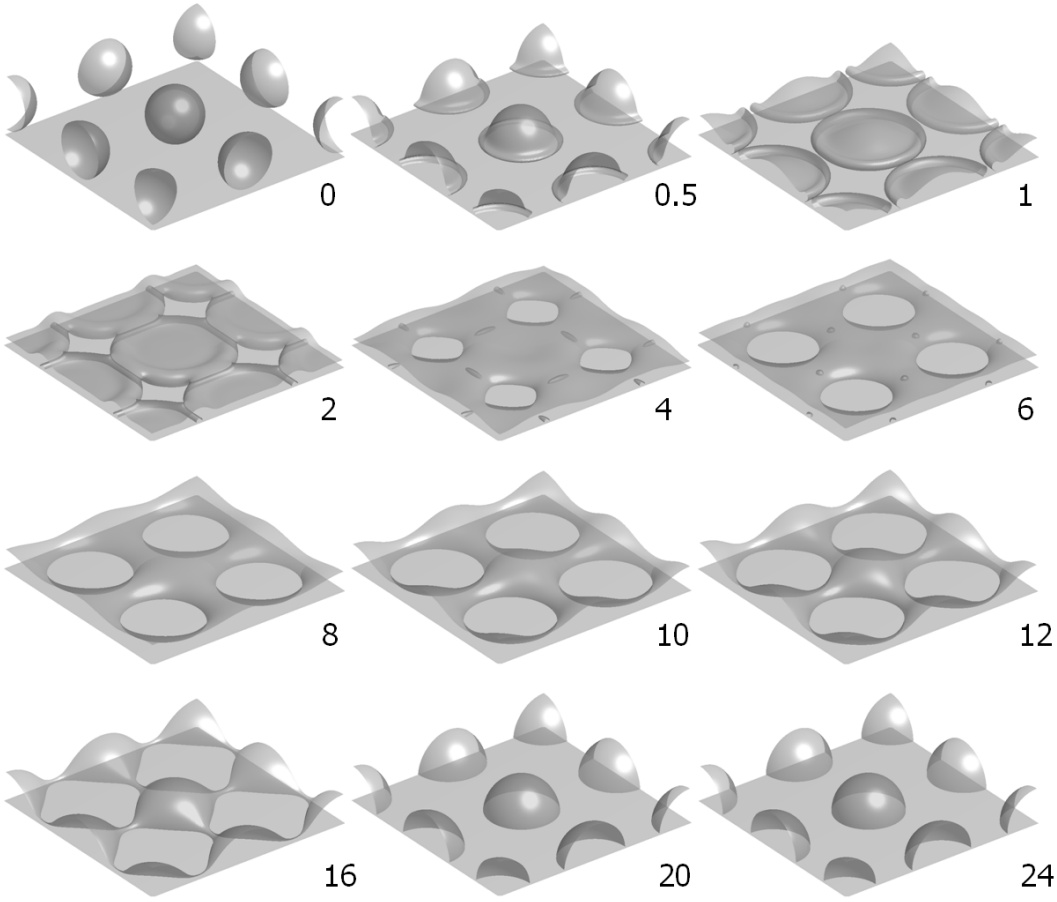

Figure 5-25. Demonstration of an-array-of-droplet impingement in the unit of dimensionless time (We = 100; Oh = 0.04; droplet spacing = 100μm).

As it can be seen from evolution of droplet shapes presented in Figure 5-20 through Figure 5-25, which capture the events of droplet coalescence and breakup, the interface topology and dynamics are highly complex, especially with an increase in the number of interacting droplets. Importantly, the proposed numerical LBM solver with described improvements in implementation of the inter-particle interaction force and interfacial/boundary conditions effectively captures the computational complexity of the physical problem and preserves some inherent symmetries of each simulation case even though the simulations were performed in general 3D format. These results demonstrated

the LBM capability for handling highly complicated interface dynamics with a potential to become a powerful simulation tool to deepen our understanding of interfacial phenomena and, when implemented in massively parallel fashion, become a "digital design tool" for dynamic fluid interfaces of interest to many practical applications. The ability to handle complicated interfacial features can be utilized to optimize the manufacturing process for designs of complex geometrical features. The printing conditions and droplet distance (i.e., distance between nozzles) can also be optimized for targeted printing applications, such as printed electronics and thin-film patterning. As seen in Figure 5-21, lines can be formed readily under these material and interface conditions. The half-cylindrical shape may be sufficient for a conductive line, but if it is meant to be one layer in a tall thin wall, the shape may cause difficulties when depositing subsequent layers. Referring to Figure 5-23, an interesting phenomenon is observed, where the droplet impact locations actually become voids in the thin film that forms from multiple droplets. Different material properties and different impingement conditions will yield films of different shapes, as illustrated in Figure 5-20 through Figure 5-25 and will be further illustrated in Chapter 6, so the capability of simulating multiple conditions should prove beneficial when designing inkjet printing processes.

5.4 Summary

The third research question was studied in this chapter and the hypothesis is validated that a lattice Boltzmann model based on explicit particle evolution can be used to simulate droplet impingement dynamics in 3-D more efficiently than the commercial software packages with even better accuracy.

A novel approach of solving the Navier-Stokes-based phase-field equations was proposed based on the lattice Boltzmann method. We first derived an inter-particle forcing term from the phase-field model and found inconsistency between the existing LB schemes and the phase-field model in calculating the relaxation time around the phase interface. We proposed a new quadratic scheme to ensure consistency with the phase-field model. In addition, we proposed a geometric wetting boundary condition and demonstrated that it was numerically more robust and accurate than the popular surface energy formulation used in the literature. Moreover, a careful examination of the velocity boundary condition revealed that the existing equilibrium bounce-back boundary for the proposed LB formulation for two-phase flow did not conserve momentum on the boundary and we proposed a new velocity boundary condition that ensured momentum conservation on the boundary. A numerical solver was implemented based on the proposed LB formulation for simulating droplet impingement dynamics and the simulation results were validated against COMSOL simulations, the LBM simulations reported in the literature, and experimental data. It was found that the proposed LBM formulation not only had significant improvement on computational efficiency but also produced better accuracy of predictions than COMSOL and the previous reported LBM models. The capability of the proposed LBM solver in handling highly complicated interface dynamics in 3D provides an approach of conducting "virtual experiments" for various interface phenomena involved in the inkjet deposition process, such as interface coalescence and interface breakup. Its computational efficiency in simulating multiple-droplet impingement provides a foundation for its utility in optimizing design of inkjet printers and printing processes for a variety of printing applications.

CHAPTER SIX

INTERFACE EVOLUTION OF MULTIPLE DROPLETS

Studying material interface evolution in the course of multiple-droplet interactions is critical for understanding the material joining process in inkjet deposition. It is possible to optimize the deposition process by examining the interface evolution of multiple-droplet interaction under different printing conditions. In this chapter, we will investigate the interface evolution of multiple-droplet interaction with a solid substrate. We will use the proposed 3-D shape coefficient with a cuboid desired shape and the developed efficient numerical solver to study three different cases, including two-droplet, a-line-of-droplet, and an-array-of-droplet interaction.

6.1 Simulation Conditions

Based on the driving force and resisting force of the droplet impingement [163], droplet impingement behavior can be divided into four different regimes as shown in Figure 4-7 in section 4.1.4. The four regimes characterize the general droplet impact behavior based on driving and resisting forces. For all the following simulations of multiple-droplet interaction dynamics, the droplet diameter and density are set to be 50μm and 1000 kg/m^3 respectively. The fluid properties for the surrounding gas are taken to be those of air at standard temperature and pressure (20°C at 1atm). The contact angle at the solid surface is set to be $\pi/2$ for all the simulations. The fluid properties of the droplet and the droplet impact velocity are varied to change the droplet impact conditions for different regimes. In regime I, the fluid properties of the droplet are 0.05 N/m and 2 cP (0.002 Pa·s) for surface tension and viscosity respectively. The droplet impact velocity is 10 m/s. These

impact conditions correspond to a Weber number of 100 and an Ohnesorge number of 0.04 respectively. In regime II, the fluid properties of the droplet keep the same as those in regime I while the droplet impact velocity is set to be 0.1 m/s. The corresponding Weber and Ohnesorge numbers are 0.01 and 0.04 respectively. In regime III, the viscosity of the droplet is changed to 200 cP and the surface tension is kept at 0.05 N/m. The droplet impact velocity is set to be 0.5 m/s. The resulting Weber and Ohnesorge numbers are 0.25 and 4 respectively. In regime IV, the fluid properties of the droplet are kept as the same as those in regime III while the impact velocity is changed to 20 m/s, which lead to a Weber number of 400 and an Ohnesorge number of 4 respectively.

6.2 Two-Droplet Interaction

Simulations of two-droplet interaction upon impinging on a solid surface have been performed using the validated LBM solver in the four different regimes with the conditions specified in the previous section.

In regime I, the Weber and Ohnesorge numbers are set to be 100 and 0.04 respectively. For multiple-droplet interaction, an additional important parameter that affects the interaction dynamics is the droplet distance, which is defined as the distance between the centroids of the neighbouring droplets minus the droplet diameter. The equilibrium and maximum spread factors that can be calculated from Eqs. (4-21) and (4-22) are 1.2599 and 2.2874 respectively for the impingement conditions in regime I. We have conducted simulations with droplet distance of $0.3D_0$ (15μm), $0.6D_0$ (30μm), $0.8D_0$ (40μm), and D_0 (50μm) respectively. The results of the shape evolution are plotted in Figure 6-1 using the defined shape coefficient in section 3.2.2.

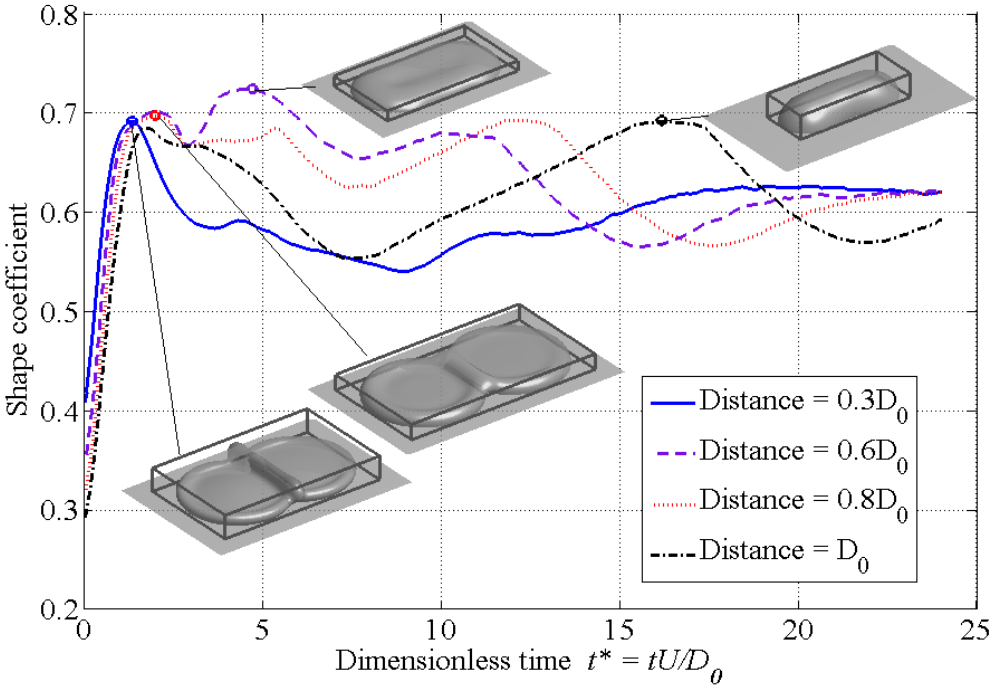

Figure 6-1. Shape evolution of two-droplet interaction in regime I (We = 100; Oh = 0.04).

The inset graphs represent the shape of droplets at the instant when the shape coefficient is maximum for different droplet distances, and the gray boxes represent the desired shape. As we can see, the shape coefficient is smaller with larger droplet distance at the starting point of the shape evolution, which is an effective characterization of the similarity between the droplet shape and the desired shape. In order to explain the physics underlying the shape evolution, we can calculate the characteristic timescales for different driving forces from Eq. (4-33). The characteristic timescales for inertial force, surface tension, and viscous force are 1, 10, and 250 in dimensionless time units respectively.

As we can see in Figure 6-1, the shape evolution is mainly driven by inertial force when $t^* < 1$. During this period, the shape of the droplets is under dramatic change driven by

inertial force, which leads to a sharp increase of the shape coefficient, because inertial force favors a large shape coefficient (i.e., a uniform thin film), and the kinetic energy is converted into surface energy by deviating the droplet shape away from its lowest surface energy form (i.e., a sphere or spherical cap). The shape of the two individual droplets evolves in a very similar way as single droplet impingement until they meet, the moment of which is mainly determined by the droplet distance. Typically the smaller the droplet distances compared to the maximum spread factor, the more kinetic energy the droplet will have when they meet with each other.

The meeting event will lead to the coalescence of the droplet interface, which will release interface energy and convert to kinetic energy at the intersection. The leftover and converted kinetic energy will drive the coalescence of the interface and further deform the interface, which does not necessarily increase the shape coefficient, because the deformation can only go laterally or into a third dimension (i.e., increase the height of the interface) at the intersection of the droplets. If the droplet distance is small compared to the maximum spread factor, the leftover and converted kinetic energy will be very large and will deform the droplet interface, thus decreasing the shape coefficient as shown in Figure 6-1 when droplet distance is $0.3D_0$.

In the retracting stage, the region where the interface is deformed most (the region where the droplets meet each other in this case) will retract faster than other regions by converting the interface energy back into kinetic energy. If the droplet distance is very large, the leftover kinetic energy will not be sufficient to drive the coalescence of the droplet interface as shown in Figure 6-1 when droplet distance is $0.8D_0$ and D_0. In the retracting stage, the lateral retraction in the region where the droplets meet will be slower

than in other regions. The further coalescence of the interface in these two cases is driven by surface tension at a later stage.

When droplet distance is $0.6D_0$, the leftover and converted kinetic energy is large enough to drive the coalescence of the interface but not enough to drive further deformation of the interface laterally or into the third dimension as when droplet distance is $0.3D_0$. An additional complication is the time instant when the droplets meet compared to the characteristic timescales of the inertial force and surface tension. The meeting time instants are 0.40, 0.64, 0.88, and 1.36 for droplet distances of $0.3D_0$, $0.6D_0$, $0.8D_0$, and D_0 respectively. If the meeting occurs when $t^* > 1$ as in the case of a droplet distance of D_0, the surface tension kicks in and starts to influence the shape evolution, which will typically decrease the maximum achievable shape coefficient driven by the kinetic energy, because surface tension favors smaller shape coefficient. As a result, the maximum shape coefficient when droplet distance is D_0 is not achieved until a later stage of shape evolution that is dominated by surface tension as shown in Figure 6-1.

In all of the cases, the surface tension takes over when $t^* > 10$, and the two droplets completely coalesce and eventually reach equilibrium to become a single spherical cap sitting on the solid surface as shown by the converging curves in Figure 6-1.

In regime II, the Weber and Ohnesorge numbers are set to be 0.01 and 0.04 respectively and the maximum spread factor is calculated to be 1.4702. Three different droplet distances are chosen for the simulations, which are $0.3D_0$ (15μm), $0.4D_0$ (20μm), and $0.6D_0$ (30μm) respectively. The simulation results of the shape evolution are plotted in Figure 6-2. In the same way, we can calculate the characteristic timescales for inertial force, surface tension, and viscous force to be 1, 0.1, and 2.5 in dimensionless time units

respectively. Therefore, the shape evolution of the droplets is dominated by the surface tension when $t^* < 1$.

As shown in Figure 6-2, the shape of the droplets first stays nearly unchanged before they touch the solid surface. Once the droplets touch the surface, the competition of the surface tension forces at three different interfaces (i.e., droplet-air, droplet-solid, and air-solid as shown in Figure 1-1), which is determined by the contact angle, will drive the droplet shape change from a sphere to a spherical cap, which is represented by the steady increase of shape coefficient when t^* is between 0.1 and 0.2. What is remarkable is that the rate of the shape coefficient change is almost constant when the shape change is driven dominantly by constant surface tension, which further verifies the effectiveness of our proposed shape coefficient in representing the droplet shapes.

Before the two droplets meet, the shape evolution is very similar to single droplet impingement and we can see some shape oscillation when droplet distance is $0.6D_0$, in which case the two droplets never meet because the maximum spread factor is less than 1.6. The meeting event of the droplets is what differentiates the shape evolution of single droplet impingement and multiple-droplet interaction, thus the timing of the meeting event can significantly alter the course of the shape evolution. The meeting time in this case are 0.256, 0.418, and infinity for droplet distance of $0.3D_0$, $0.4D_0$, and $0.6D_0$ respectively. The meeting of the droplets leads to the coalescence of the interface. As we can see from the inset graph, when the droplet distance is $0.3D_0$, the meeting occurs after the individual droplet almost achieves equilibrium and triggers another round of shape change driven also by surface tension. It is noteworthy that the rates of the shape coefficient change, including both increase and decrease of the shape coefficient ($0.25 <$

$t^* < 0.4$), are very close to the rate of the shape coefficient change in the first round of shape evolution before the droplets meet, which is driven by the same surface tension force. The shape evolution curves for different droplet distances are almost parallel to each other. The droplets finally merge together and become a single droplet driven by the surface tension, which is indicated by the converging shape evolution curves.

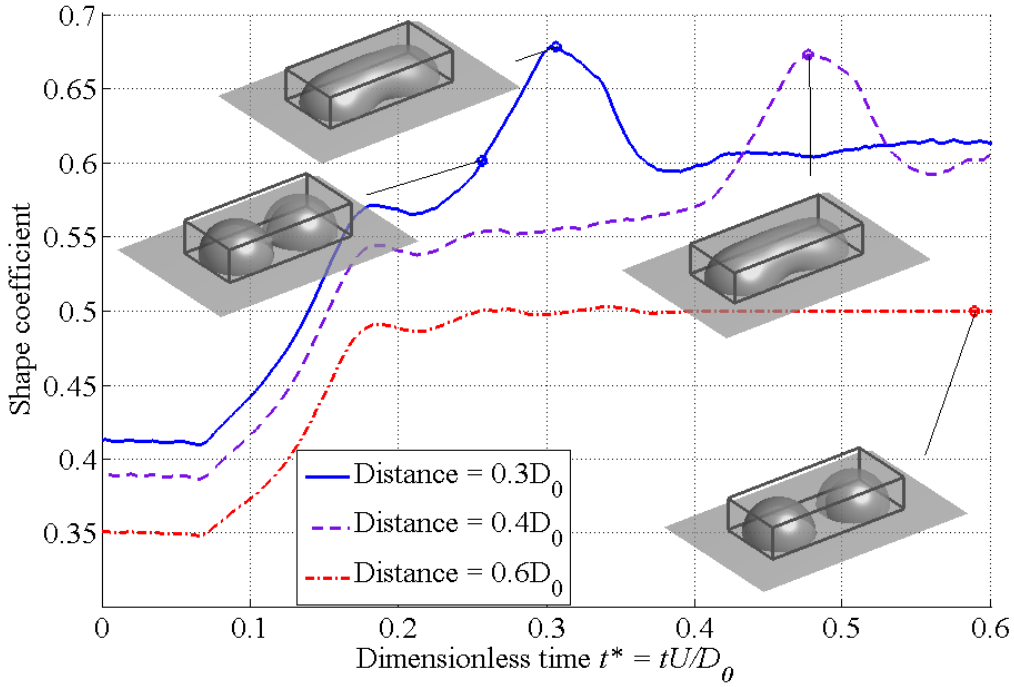

Figure 6-2. Shape evolution of two-droplet interaction in regime II (We = 0.01; Oh = 0.04).

In regime III, the Weber and Ohnesorge numbers are set to be 0.25 and 4 respectively. The same droplet distances are chosen as in regime II, and the simulation results of the shape evolution are plotted in Figure 6-3. The characteristic timescales for inertial force, surface tension, and viscous force are calculated to be 1, 0.5, and 0.125 in dimensionless time units respectively.

As shown in Figure 6-3, the droplets first come down to the solid surface with their

shapes maintained by surface tension, as indicated by the short, nearly horizontal curve in the beginning of the shape evolution. Once the droplets touch the surface, the surface tension forces at the contact line drive the contact line to move to the equilibrium contact angle. Then the surface tension drives the entire droplet shape into equilibrium shape, which is strongly resisted by the viscous force. Note that although the timescale for surface tension to act on the entire droplet is larger than that of the viscous force, the timescale for the surface tension to act only on the contact line (i.e., a small portion of the entire droplet) could be much smaller. This explains the difference of the rate of the shape coefficient change. In the contact line moving stage, the shape coefficient increases at a relatively large rate. While in the following stage, the shape evolution is dominated by the viscous force, which largely decreases the rate of the shape coefficient change.

The meeting event of the droplets for the different droplet distance of $0.3D_0$, $0.4D_0$, and $0.6D_0$ occurs at 8.4, 14.7, and infinity respectively. The meeting of the droplets results in the coalescence of the interface which brings another round of rapid change of shape coefficient. It is worthwhile to point out that the rate of the shape coefficient change during the interface coalescence is close to the rate during the contact line moving stage. The droplet distance merely delays the meeting time and the shape evolution curves strongly resemble each other for the droplet distance of $0.3D_0$ and $0.4D_0$. As before, the two coalescing droplets will merge together and achieve equilibrium as a single droplet, as indicated by the converging shape evolution curves.

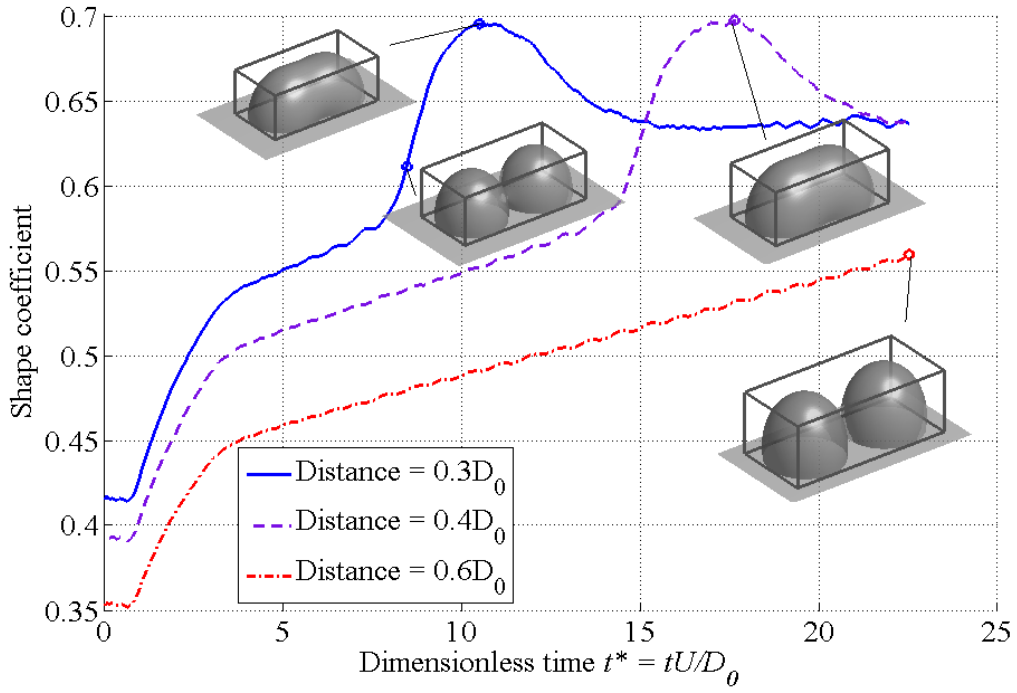

Figure 6-3. Shape evolution of two-droplet interaction in regime III (We = 0.25; Oh = 4).

In regime IV, the Weber and Ohnesorge numbers are set to be 400 and 4 respectively and the maximum spread factor is calculated to be 1.4016. The same droplet distances are therefore chosen for the simulations, which are $0.3D_0$ (15μm), $0.4D_0$ (20μm), and $0.6D_0$ (30μm) respectively. The simulation results of the shape evolution are plotted in Figure 6-4. The characteristic timescales for inertial force, surface tension, and viscous force can be calculated to be 1, 20, and 5 in dimensionless time units respectively. Therefore, the shape evolution of the droplets is dominated by the inertial force when $t^* < 1$.

As shown in Figure 6-4, we can see a rapid increase of shape coefficient due to the deformation of the droplet shape caused by the high speed impact of droplets on the solid surface. During this process, the kinetic energy is converted into surface energy and thus the inertial force is largely reduced. Shortly after, the viscous force kicks in and starts to

dominate the shape evolution when t^* is around 5 because the inertial force becomes much smaller than the beginning, and the surface tension is not comparable to the viscous force. In the following stage, the droplet shape slowly relaxes back to the equilibrium shape driven by surface tension but strongly resisted by the viscous force, during which the surface energy is converted into kinetic energy but dissipated by the viscous force right away. Therefore, the shape coefficient varies very slowly and nothing exciting occurs during this period until the two droplets meet.

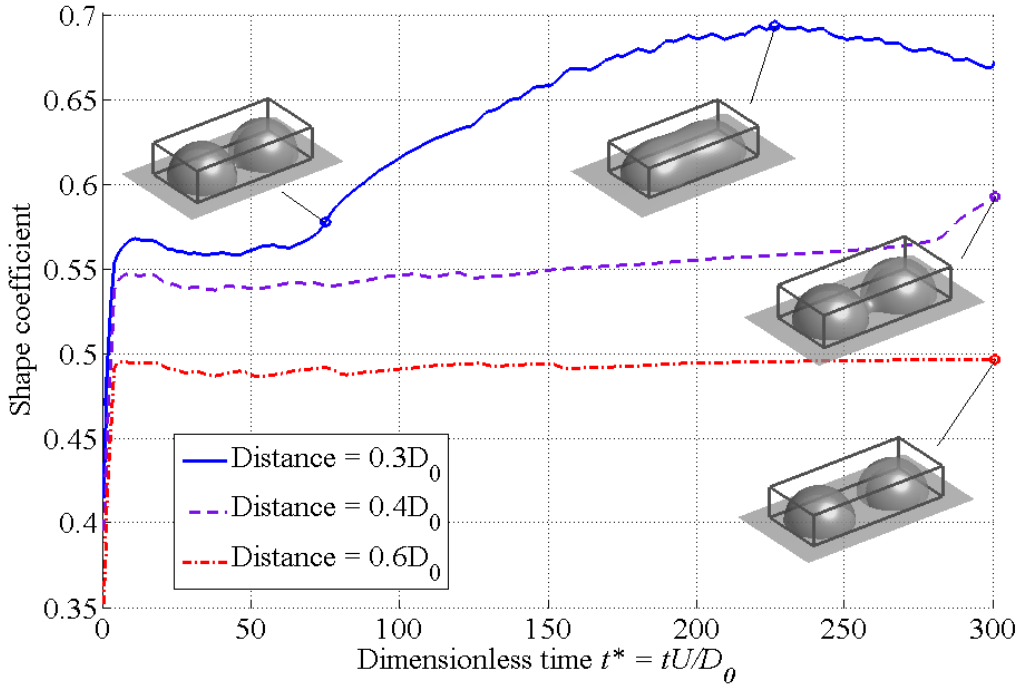

Figure 6-4. Shape evolution of two-droplet interaction in regime IV (We = 400; Oh = 4).

The meeting of the droplets gives rise to a second round of shape change as shown in Figure 6-4. The meeting time instants of the droplets for the different droplet distances of $0.3D_0$, $0.4D_0$, and $0.6D_0$ are 75, 284, and infinity respectively. The rate of the shape coefficient change becomes larger, and the surface tension starts to drive the coalescence

of the interface. It should be noted that the surface tension only acts on a very tiny portion of the interface (i.e., the area the two droplets touch each other) in the beginning and slowly spreads over to other portions of the interface. Therefore, the rate of shape coefficient change is larger than the previous stage, which is also driven by surface tension that acts on the entire droplet. As in regime III, the increase of the droplet distance only delays the meeting of the droplets and the shape evolution curves are very similar to each other for droplet distances of $0.3D_0$ and $0.4D_0$. When the droplet distance is too large, the final equilibrium shape is two individual droplets sitting on the solid surface as shown by the red dotted-line curve in Figure 6-4.

6.3 A-Line-of-Droplet Interaction

Since line printing is a common application for inkjet deposition, it makes practical sense to study the interaction of a line of droplets upon impinging on the substrate. One complication that arises immediately is how many droplets need to be considered. To avoid such complication, we consider an ideal situation with an infinite number of droplets aligned on the same line using symmetric boundaries at the two ends of the line as shown in Figure 5-21. To get an idea of how the impingement conditions affect the droplet interaction behavior for a line of droplets, we can study the droplet interaction dynamics in the four different regimes. The droplet size and density, the properties of the surrounding gas, and the contact angle all take the same value as in two-droplet interaction.

In regime I, the Weber and Ohnesorge numbers are also set to be 100 and 0.04 respectively. The maximum spread factor is 2.2874, and the characteristic timescales for

inertial force, surface tension, and viscous force are 1, 10, and 250 respectively. The droplet distances of $0.3D_0$, $0.6D_0$, $0.8D_0$, and D_0 are simulated, and the results are plotted in Figure 6-5. As we can see, the overall shape evolution path is very similar to the two-droplet interaction under the same conditions in regime I. The difference is that each droplet is neighboured by two droplets symmetrically, which can affect the fluid dynamics of the surrounding air and the droplet itself. One observation is that the time instants when the droplets meet are influenced. The meeting times are 0.4, 0.64, 0.88, and 1.28 for droplet distances of $0.3D_0$, $0.6D_0$, $0.8D_0$, and D_0 respectively, which are slightly earlier than those in two-droplet interaction. The difference becomes more obviously in other regimes as will be shown in the following. Another important observation is that in the retracting stage the two ends of each droplet along the line are pulled by the neighbouring droplets such that the droplet can only retract laterally. When surface tension takes over, it will shape the droplet into a half cylinder to minimize the surface energy under equilibrium.

The equilibrium half cylinder shape is closer to the desired shape than most of the transient shapes during the shape evolution process. Pursuing the equilibrium shape rather than the best transient shape makes the printing process become more predictable and easier to control. The final equilibrium shape can also be controlled by modifying the contact angle of the substrate. If we plan to pursue the equilibrium shape, the time required to achieve the equilibrium shape will become important as we want to minimize the manufacturing time, which still requires a good understanding of the dynamics of the shape evolution. Since the equilibrium shape is driven by the surface tension, the characteristic timescale for the surface tension is therefore very important for determining

the time required to achieve equilibrium, which can, however, still be influenced by other impingement conditions. As shown in Figure 6-5, the shape evolution curve with droplet distance of 0.6 D_0 achieves equilibrium faster than the other conditions. The observation is that the closer the droplet shape is to the equilibrium shape before surface tension takes control, the less time it requires for the droplet to achieve equilibrium after the surface tension takes control.

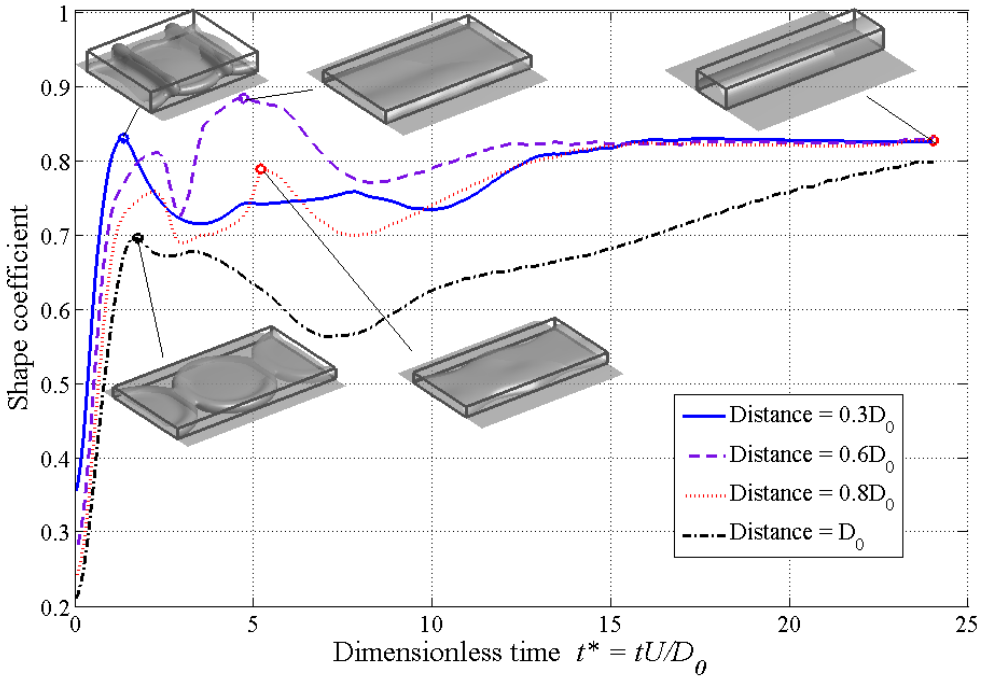

Figure 6-5. Shape evolution of a-line-of-droplet interaction in regime I (We = 100; Oh = 0.04).

In regime II, the Weber and Ohnesorge numbers are set to be 0.01 and 0.04 respectively and the maximum spread factor is calculated to be 1.4702. We have chosen the droplet distances of 0.3D_0, 0.4D_0, and 0.6D_0 for simulations, and the results are plotted in Figure 6-6. The characteristic timescales for inertial force, surface tension, and viscous force are calculated to be 1, 0.1, and 2.5 in dimensionless time units respectively.

The droplet interaction goes through a similar process as explained in two-droplet interaction. Due to the additional neighboring droplet compared to two-droplet interaction, the meeting times for the droplet distances of $0.3D_0$, $0.4D_0$, and $0.6D_0$ are 0.244, 0.35, and infinity respectively, which are clearly earlier than the meeting times for two-droplet interaction in regime II. Since the equilibrium shape in this case is closer to the desired shape than that in the case of two-droplet interaction, the shape coefficient increases monotonically all the way up to the equilibrium shape coefficient during the shape evolution. The increase of the droplet distance merely delays the meeting time, which also increases the time required to achieve the equilibrium shape and thus is unfavorable to reduce the manufacturing time.

It is interesting to compare the results in regimes I and II, which only have a difference of droplet impact velocity. Therefore, the characteristic timescales for the surface tension are the same in physical time unit. Both are 50μs. For the droplet distance of $0.3D_0$, we can compare the time needed to achieve the equilibrium shape in the physical time unit, which is around 75μs (~15 in dimensionless unit as shown in Figure 6-5) in regime I and 165μs (~0.33 in dimensionless unit as shown in Figure 6-6) in regime II. This comparison shows that the droplet impact velocity, one of the most important process parameters, does have a big influence on the time required the achieve equilibrium. The droplet distance, however, needs to be carefully selected to match the impact velocity, neither too small such that the kinetic energy does not deviate the droplet shape too far away from its equilibrium shape (a half cylinder) when the droplets meet, nor too large such that the droplets do not meet as shown in Figure 6-6 when the droplet distance is $0.6D_0$, or it requires the surface tension to help coalesce the interface as shown in Figure 6-5, when

the droplet distance is D_0. Therefore, the implications of these results need to be taken into account for inkjet print head design and printing process control.

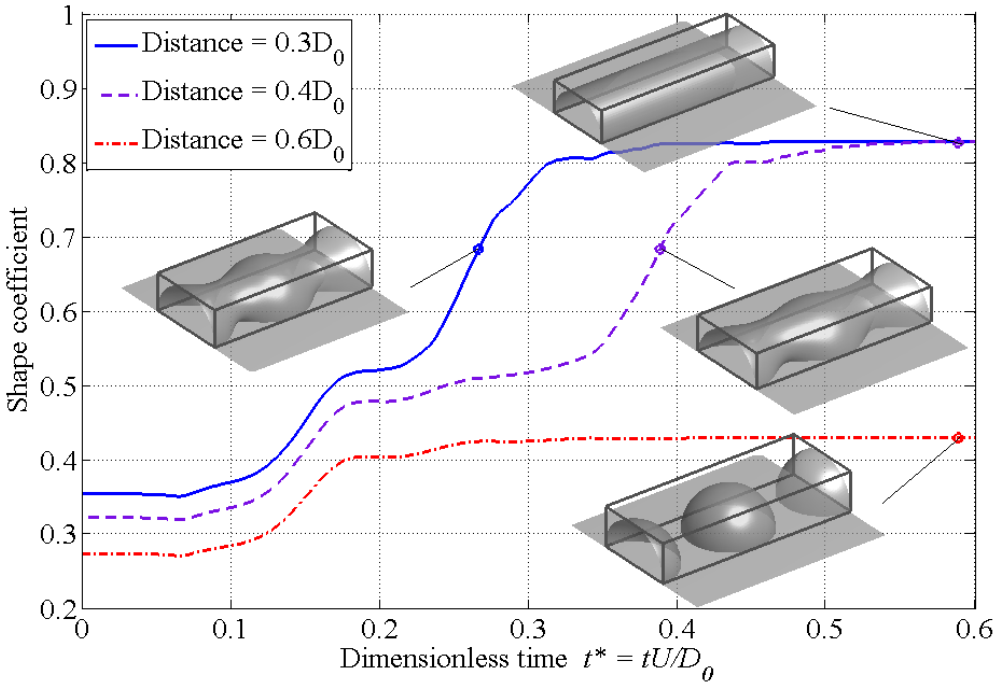

Figure 6-6. Shape evolution of a-line-of-droplet interaction in regime II (We = 0.01; Oh = 0.04).

In regime III, the Weber and Ohnesorge numbers are set to be 0.25 and 4 respectively. The droplet distances of $0.3D_0$, $0.4D_0$, and $0.6D_0$ are simulated, and the results are shown in Figure 6-7. The characteristic timescales for inertial force, surface tension, and viscous force are 1, 0.5, and 0.125 in dimensionless time units respectively. The droplet meeting occurs when the rate of the shape coefficient change suddenly increases as shown in Figure 6-7.

Compared to the two-droplet interaction under the same conditions in regime III, the droplets meet slightly later, and the meeting times for droplet distances of $0.3D_0$, $0.4D_0$, and $0.6D_0$ are 8.625, 15, and infinity respectively. The increase of the droplet distance

delays both the meeting time of the droplets and the time needed to achieve the equilibrium shape. It is noteworthy that for droplet distances of $0.3D_0$ and $0.4D_0$ it takes about the same amount of time from the time when the droplets meet to the time when the equilibrium shape is achieved, as indicated by the transition curves with circle markers in the middle in Figure 6-7, which is driven by the surface tension.

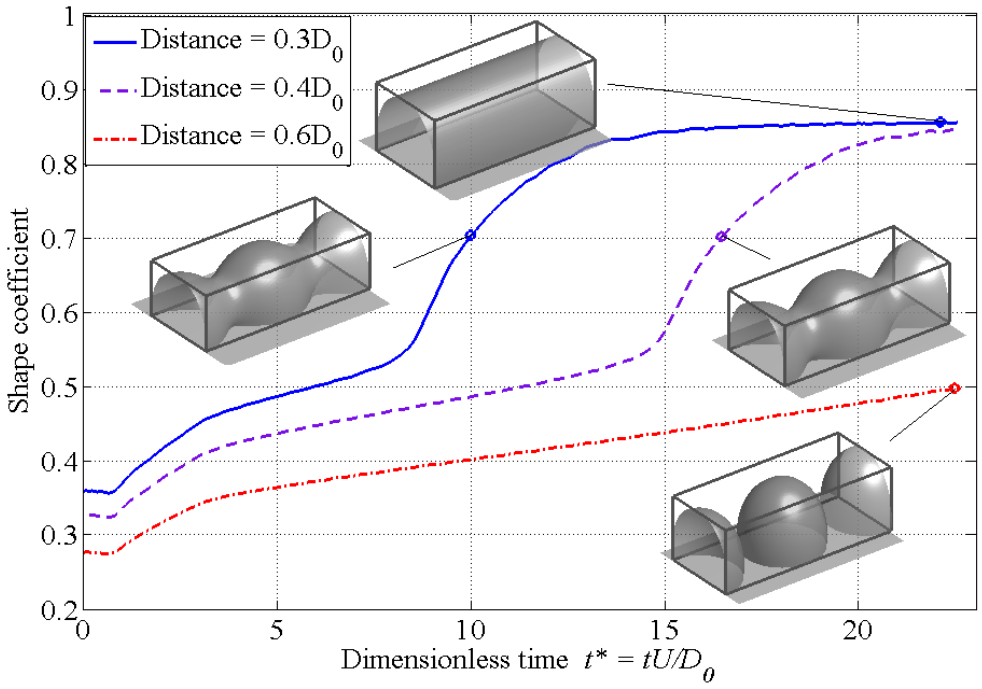

Figure 6-7. Shape evolution of a-line-of-droplet interaction in regime III (We = 0.25; Oh = 4).

Compared to regimes I and II, the characteristic timescale for the surface tension is the same in physical time unit while the viscosity is much higher. As we can see from Figure 6-7, the time needed to achieve equilibrium shape for the droplet distance of $0.3D_0$ is around 15 in dimensionless time units and 1500μs in physical time units, which is much larger than that in regimes I and II. This means the viscosity also has a strong influence on the time needed to achieve equilibrium. In this case, although the characteristic

timescale for surface tension is only 50μs, the viscous force dominates over surface tension and therefore the time needed to achieve equilibrium is mainly determined by the viscosity effects.

In regime IV, the Weber and Ohnesorge numbers are 400 and 4 respectively and the maximum spread factor is 1.4016. Simulations are performed with droplet distances of $0.3D_0$, $0.4D_0$, and $0.6D_0$ and the results are plotted in Figure 6-8. The characteristic timescales for inertial force, surface tension, and viscous force are 1, 20, and 5 in dimensionless time units respectively. The droplets meet at the time when the rate of the shape coefficient change starts to increase as shown in Figure 6-8.

The meeting occurs clearly earlier than in two-droplet interaction due to the additional neighboring droplet and the meeting times are 59, 197, and infinity in dimensionless time units. The increase of the droplet distance delays the droplet meeting as well as the time for achieving the equilibrium shape. Compared to regime III, the characteristic timescales for the surface tension and viscous force are the same in physical time units, which are 50μs and 12.5μs respectively, while the impact velocity is much higher (20m/s VS 0.5m/s). The time needed to achieve equilibrium is around 300 (750μs) for the droplet distance of $0.3D_0$ as shown in Figure 6-8, which is much smaller than that in regime III. This means increasing impact velocity can also speed up the process of achieving equilibrium with high viscosity fluids.

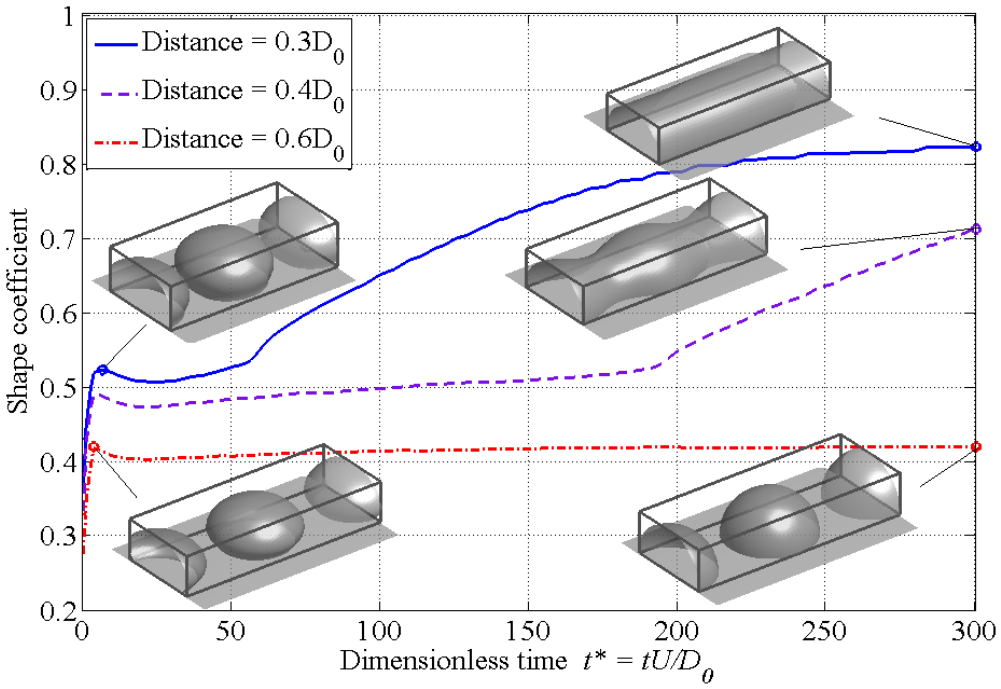

Figure 6-8. Shape evolution of a-line-of-droplet interaction in regime IV (We = 400; Oh = 4).

However, the timescales for achieving equilibrium in regimes III and IV are nowhere close to the characteristic timescale for the surface tension. The reason is that when the Ohnesorge number is larger than 1, the viscous force will dominate the shape evolution, and the timescale for achieving equilibrium will be mainly determined by the viscosity effects. It appears that increasing the impact velocity can only speed up the process in a very limited fashion because achieving equilibrium is driven by the surface tension and increasing the inertial force can only help to a certain extent. One way to speed up the process of achieving equilibrium with high viscosity fluids is to increase the surface tension as well, which will effectively decrease the Ohnesorge number.

6.4 An-Array-of-Droplet Interaction

One of the biggest advantages for inkjet deposition is that it can speed up the manufacturing process and thus reduce the manufacturing time and cost utilizing a scalable array of nozzles. Therefore, it is critical to understand the interaction dynamics of an array of droplets upon impinging on the substrate. To avoid the consideration of the number of droplets, we here study an infinitely large array of droplets using symmetric boundary conditions such that each droplet is surrounded by 8 neighboring droplets as shown in Figure 5-22. The interaction dynamics are investigated in the four different regimes characterized by the driving force and resistance force. The droplet size and density, the properties of the surrounding gas, and the contact angle take the same values as were used in two-droplet interaction.

In regime I, the Weber and Ohnesorge numbers are taken to be 100 and 0.04 respectively. The maximum spread factor is 2.2874 and the characteristic timescales for inertial force, surface tension, and viscous force are 1, 10, and 250 respectively. The droplet distances of $0.3D_0$, $0.6D_0$, $0.8D_0$, and D_0 are simulated and the results are plotted in Figure 6-9. Compared to two-droplet interaction, the interaction dynamics for an array of droplets are more complicated due to the additional neighbouring droplets. One difference is that the coalescence of the interface of multiple droplets releases more interface energy which is converted into kinetic energy. For example, the extra kinetic energy converted from the coalescence of additional droplets causes much larger deformation of the interface than two-droplet interaction and eventually leads to splash for the droplet distance of $0.3D_0$ as shown in Figure 6-9. Due to the additional neighboring droplets, the time instants when the droplets meet are also influenced. The droplet meeting times are 0.4, 0.64, 0.88, and

1.28 for droplet distances of $0.3D_0$, $0.6D_0$, $0.8D_0$, and D_0 respectively, which are slightly earlier than seen in two-droplet interaction.

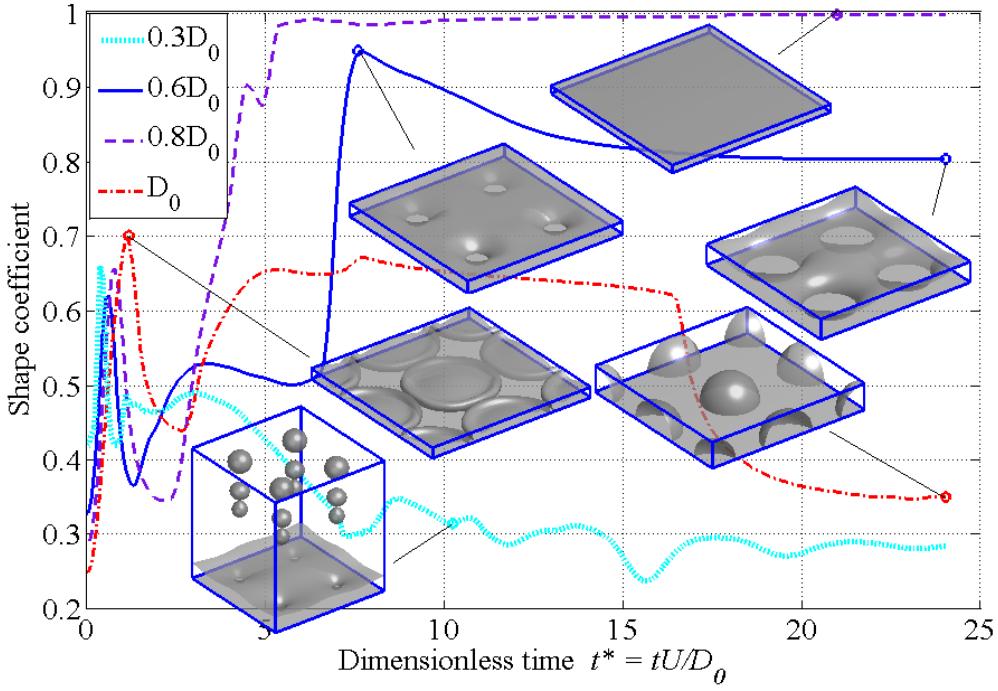

Figure 6-9. Shape evolution of an-array-of-droplet interaction in regime I (We = 100; Oh = 0.04).

Another important phenomenon we need to take note is the formation of air bubbles during the droplet interaction. In the droplet spreading stage for single droplet impact, a liquid thin film (often referred as lamella) is formed that spreads radially over the surface and the diameter of the rim of the lamella is typically larger than the diameter of the wetted area due to the stationary wall boundary that holds back the spreading of the liquid on the surface. For multiple droplet interaction, the rims of the lamella will meet each other first. Therefore, the air under the lamella rim will be trapped when the droplets are fully coalesced and an air bubble will be formed at the location where the droplets meet.

Air bubbles are undesirable for inkjet deposition. The size of the air bubbles is dependent on the difference between the diameters of the lamella rim and the wetted area at the time when the droplets meet and the time it takes for the lamella rims to be fully merged together. Hence, two different approaches can be taken to reduce the bubble size. One is to reduce the difference between the diameters of the lamella rim and the wetted area, which can be influenced by the impact conditions and the time of the droplet meeting. The other is to increase the time required for the lamella rims to be fully coalesced so that the spreading film on the solid surface (that is the increasing diameter of the wetted area during the spreading) has time to drive the air out. If the spreading films on the solid surface can meet before the lamella rims are fully merged, the air bubbles are likely to be eliminated. We can change these relevant timescales by adjusting the droplet distance to eliminate the air bubbles although a solution is not guaranteed for all the impact conditions.

In addition, the final equilibrium shape can take more different forms than two-droplet or line-of-droplet interaction, and the interaction dynamics are more sensitive to the droplet distance and impact conditions. When the droplet distance is $0.3D_0$, the fast moving droplets first coalesce together and trap a large air bubble inside the meeting zone. The kinetic energy gained from the coalescence of the interface leads to the break-off of a large chunk of liquid which then break into droplets due to Rayleigh instability. Due to the size of the air bubble compared to the thickness of the formed thin film, the trapped air bubble then touches the surface of the thin film, which opens up a channel for the air bubble and forms a new liquid-air interface. Then the surface tension drives to minimize

the new interface and forms a uniform thin film. The splashed droplets may come down due to gravity and interact with the thin film again.

When the droplet distance is $0.6D_0$, the coalescence of the interface leads to a much smaller deformation of the interface and there is no splash because the leftover kinetic energy is much smaller when the droplets meet. Air bubbles are also trapped at the locations where the droplets meet. Then the trapped air bubbles become untrapped when they touch the surface of the formed thin film. The air bubbles then become holes due to the interaction with the thin film as shown in Figure 6-9. What is surprising is that these holes do not diminish as in the case when the droplet distance is $0.3D_0$ but increase under surface tension and form a stable equilibrium shape as shown in Figure 6-9. When the droplet distance is $0.8D_0$, the full coalescence of the lamella rims occurs much later than in the previous cases, which gives plenty of time for the spreading film on the solid surface to drive out the air. Therefore, a uniform film is formed under equilibrium as shown in Figure 6-9, which suggests it is possible to completely eliminate the bubbles by fine tuning the droplet distance and impact conditions. When the droplet distance is D_0, the lamella rims of the droplets are never fully coalesced due to the lack of kinetic energy to drive the coalescence. The retracting kinetic energy converted from the deformed interface during the spreading, however, is enough to break up the semi-coalesced interface and form individual droplets sitting on the substrate as shown in Figure 6-9.

In regime II, the Weber and Ohnesorge numbers are set to be 0.01 and 0.04 respectively and the shape evolution is dominated by the surface tension. Simulations with droplet distances of $0.3D_0$, $0.4D_0$, and $0.6D_0$ are performed and the results are plotted in Figure 6-10. The meeting times of the droplets are slightly influenced by the additional

neighboring droplets, which are 0.2440, 0.3500, and infinity for the droplet distances of $0.3D_0$, $0.4D_0$, and $0.6D_0$ respectively.

The shape evolution resembles that in two-droplet interaction in the sense that the shape of the droplets first changes individually until they meet and the maximum shape coefficient occurs during the interface coalescence. The forming of the air bubbles during the interface coalescence causes the decrease of the shape coefficient after the maximum shape coefficient is reached because the definition of the shape coefficient does not favor a discontinuous interface. The size of the air bubbles, as shown in Figure 6-10 when the droplet distance is $0.3D_0$, however, is much smaller than that in regime I at the same droplet distance. The reason is that the interface coalescence is driven by surface tension in this case and thus the difference between the diameters of the lamella rim and the wetted area is smaller and the coalescence occurs at a much slower rate such that the trapped air has more time to escape. One can also tell that increasing the droplet distance not only delays the meeting of the droplets but also produces a very different shape evolution curve as shown in Figure 6-10 when the droplet distance is $0.4D_0$. After a rapid increase of shape coefficient during the interface coalescence (one can also tell when the droplets start to coalesce by looking at the rate of shape coefficient change), the shape coefficient keeps increasing at a slower rate to reduce the size of the holes formed at the locations where the droplets meet. In the case when the droplet distance is $0.6D_0$, the droplets never meet and the shape evolution is very similar to that in two-droplet interaction.

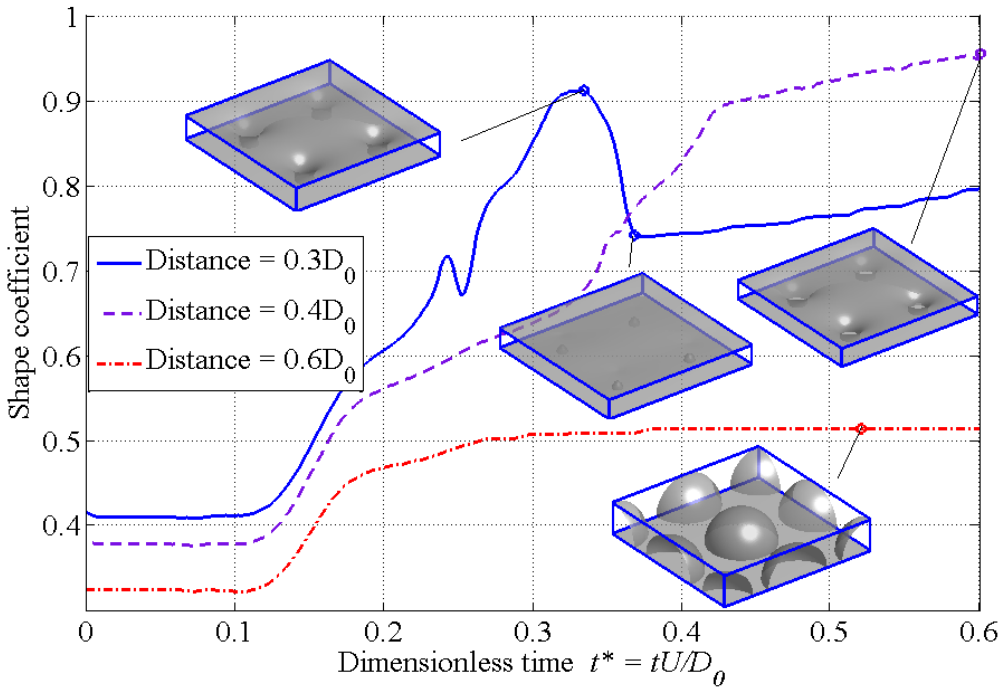

Figure 6-10. Shape evolution of an-array-of-droplet interaction in regime II (We = 0.01; Oh = 0.04).

In regime III, the Weber and Ohnesorge numbers are set to be 0.25 and 4 respectively and the shape evolution is dominated by the viscous force. The meeting times for the droplets are 8.85, 15.15, and infinity for the droplet distances of $0.3D_0$, $0.4D_0$, and $0.6D_0$ respectively as shown in Figure 6-11, which are later than in two-droplet interaction.

Due to the dominance of the viscous force, the extra kinetic energy converted from the coalescence of the interface of additional droplets does not make a big difference in the shape evolution. The shape evolution curves are therefore very similar to those in two-droplet interaction. One difference is that the decrease of the shape coefficient after reaching maximum is because of the coalescence into a single droplet for two-droplet interaction but due to the formation of bubbles in this case. Unlike in regime II, the increase of the droplet distance does not help much with reducing the bubble size but

only delay the droplet meeting.

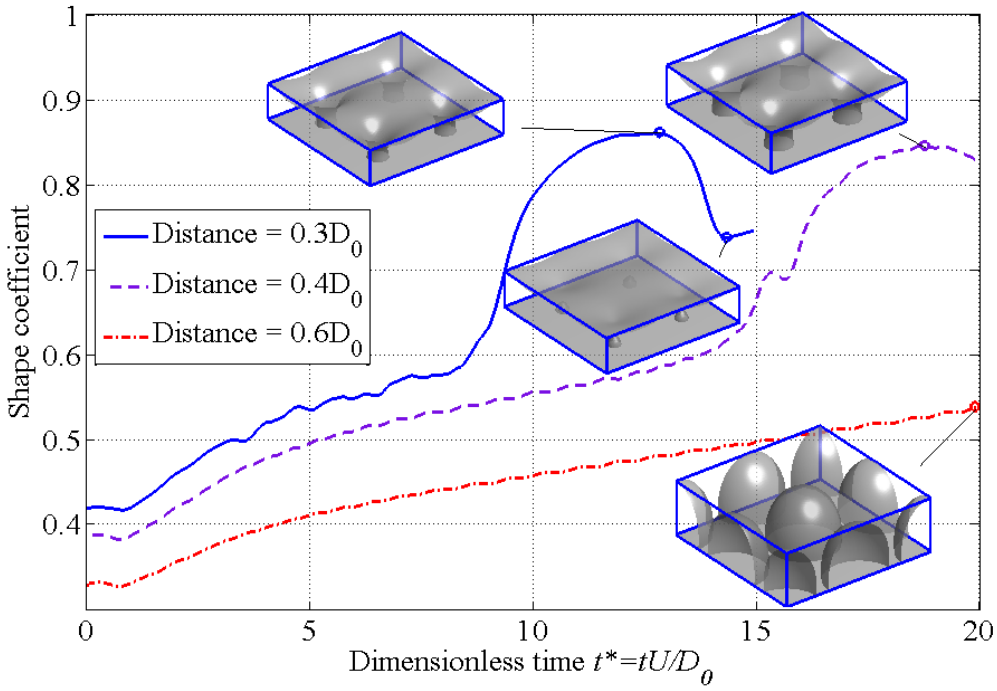

Figure 6-11. Shape evolution of an-array-of-droplet interaction in regime III (We = 0.25; Oh = 4).

In regime IV, the Weber and Ohnesorge numbers are 400 and 4 respectively and the shape evolution is firstly dominated by the inertial force and then by the viscous force after the kinetic energy is dissipated in the early stage. The droplet meeting times are 55, 164, and infinity for the droplet distances of $0.3D_0$, $0.4D_0$, and $0.6D_0$ respectively as shown in Figure 6-12, which are earlier than those in two-droplet interaction. As in two-droplet interaction, the droplet shape is largely deformed individually by the dominating inertial force in the very early stage far before the contact line reaches the maximum spread factor. Therefore, the contact line is still moving forward when the droplets start to retract to convert the interface energy from the deformed interface back to kinetic energy. During this droplet retracting stage, the diameter of the wetted area is larger than any

other portion of the droplet (the lamella rim disappears).

When the droplet distance is larger than the diameter of the largest region of the initially deformed droplet but smaller than the maximum spread diameter, the droplets will meet each other at the contact line on the solid surface, which means no air will be trapped in the meeting zone. All the air in the meeting zone will be driven out during the coalescence of the interface. Therefore, a uniform thin film can be formed due to surface tension after the interface is completely coalesced as shown in Figure 6-12.

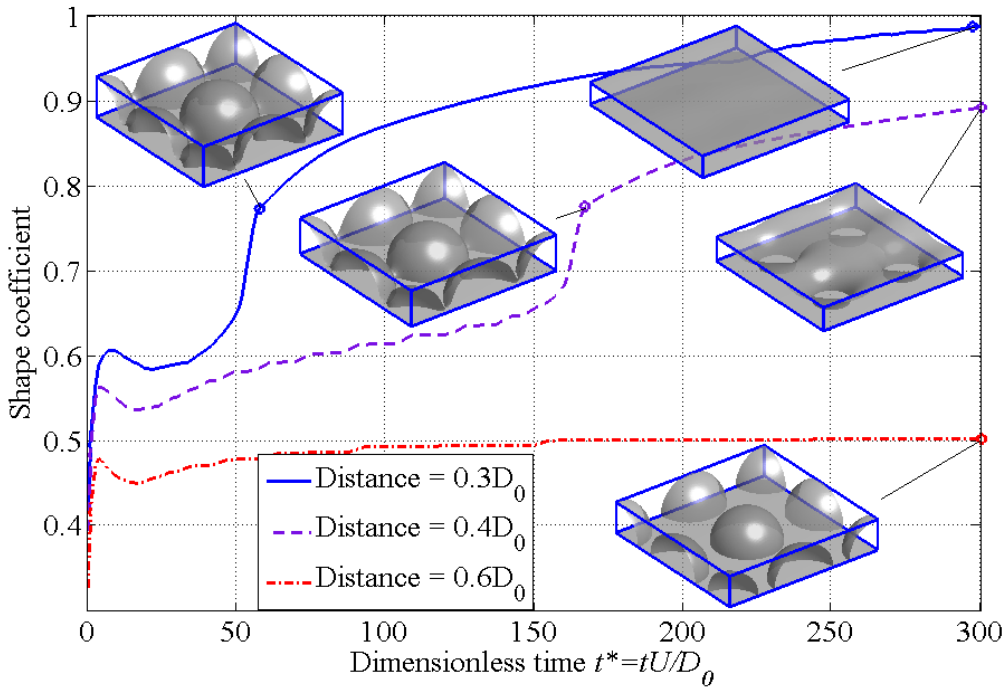

Figure 6-12. Shape evolution of an-array-of-droplet interaction in regime IV (We = 400; Oh = 4).

As we can see, for droplet distances of $0.3D_0$ and $0.4D_0$, the droplets meet after the initial deformation indicated by the steep increase of shape coefficient in the first several dimensionless time units. The inset graphs show that the droplets indeed meet at the contact line. Unlike the line-droplet interaction, the main concern of which is how to

achieve the equilibrium shape in the shortest time, we need to be concerned about both how to achieve the desired equilibrium shape (i.e., a uniform film) and how to achieve faster for array-droplet interaction. The study of the interaction dynamics in regime IV points us in a direction to achieve a uniform thin film for high viscosity fluids, which is to optimize the impact conditions and droplet distance such that the droplets meet at the contact line rather than the lamella rim.

6.5 Summary

Following the development of the powerful numerical solver for simulating droplet impingement dynamics in 3-D in chapter 5, the multiple-droplet interaction dynamics are examined in depth using the developed solver in this chapter in the context of inkjet deposition. The results have further validated the hypothesis for the third research question that the developed numerical solver based on the lattice Boltzmann method makes it possible to study the multiple-droplet interaction dynamics.

An extensive study has been conducted on multiple-droplet interaction dynamics, including two-droplet, a-line-of-droplet, and an-array-of-droplet under a wide range of impact conditions and droplet distances. In two-droplet interaction, the shape evolution during the droplet interaction is carefully studied with the help of our proposed shape coefficient. The underlying physics of the interaction dynamics are carefully examined and analyzed. The interaction between the characteristic timescales of various driving forces during the droplet impingement and the time instant when the droplets meet has proven to be a crucial factor that affects the multiple-droplet interaction dynamics. The shape evolution curves have been used to interpret various events during the interaction

dynamics. The rate of the shape coefficient change is a good indicator for various events. Line-droplet interaction, which is important for various line printing applications, has also been studied under the same framework. It is concluded that the equilibrium shape is an appropriate objective to pursue. Although the characteristic timescale for the surface tension is very important, to achieve the equilibrium shape in the shortest time, however, is still largely determined by the interaction dynamics as shown by our analysis. Array-droplet interaction, which is critical for utilizing inkjet deposition as a scalable manufacturing method, has also been studied. Unlike two-droplet and line-droplet interaction, however, many different equilibrium shapes exist for array-droplet interaction due to the increased complexity caused by the additional droplets. One of the most important threats to manufacturing is the formation of air bubbles during the interaction because of the nature of the droplet impingement dynamics. The process of the air bubble formation is analyzed and suggestions have been proposed to eliminate the air bubbles based on our study.

CHAPTER SEVEN

CONCLUSIONS AND RECOMENDATIONS

Inkjet deposition is an elegant solution to reorganizing materials in a parallel and scalable manner by first dividing materials into small units of droplets and rejoining them back together in an intended order. This effective and efficient approach to material reorganization with a resolution only limited by the droplet size holds the potential to significantly advance manufacturing technology and the great promise of an era of personal fabrication, in which we will be able to not just digitalize information but also real physical products. However, this technology is still at a young stage of development and numerous research questions about the two fundamental processes involved—material division (i.e., droplet formation and ejection) and material joining (i.e., droplet deposition and interaction)—remain open. Material division and material joining are reciprocal processes in the sense that material division is a process of creating new material interface while material joining is a process of reducing material interface. This thesis investigates several aspects of the interface dynamics during the material joining process. This chapter is to bring together the research activities and findings presented throughout the thesis. Therefore, the research activities and findings are first summarized in the next section. Then the hypotheses posed in the first chapter are revisited and evaluated. The specific achievements and contributions of this research are presented next, followed by the limitations of this work and recommendations for future work. The chapter concludes with a few closing remarks on the relevance of this research to the science in a larger scope.

7.1 Thesis summary

The long term vision of this research is to understand the interface dynamics during the droplet deposition process so that we can control the material joining process in inkjet deposition. However, a large gap exists between the current understanding and the long term goal. This thesis provides a series of steps to reduce the gap and advance the frontier toward the goal.

In the first chapter, an extensive background search is conducted in order to evaluate the current state of the art of inkjet deposition in the context of manufacturing and to identify the critical problems. A problem formulation is presented about the droplet deposition process, which is broken down into two coupling sub-processes: droplet impingement and droplet hardening. Although droplet impingement has been studied extensively over a century, little research is reported on the droplet interface evolution and most of the previous research is concerned about single droplet impingement. In order to study the interface evolution during droplet impingement, we are set to accomplish three tasks in this research: to quantify the geometry of the interface effectively, to understand the underlying physics of interface evolution for single droplet impingement, and to develop an efficient numerical tool to enable the study of multiple droplet interaction upon impinging on the substrate. In order to accomplish these three tasks, an extensive literature survey is performed in the second chapter on geometrical characterization, numerical methods for modeling droplet impingement dynamics, and the lattice Boltzmann method.

In the third chapter, a novel metric (the shape coefficient) is developed to quantify the geometry of the interface by measuring the similarity between the geometry of the

evolving interface during the droplet impingement and a desired geometry in both 2-D and 3-D. The ability of the proposed metric to effectively capture the similarity between the evolving geometry and the desired geometry is also verified.

In the following chapter, the proposed geometric metric is used to study the evolution of the geometry of the interface of a single droplet upon impinging on a solid surface. A dimensionless analysis is conducted to reduce the number of parameters, which reveals that three dimensionless numbers are important to the interface dynamics of single droplet impingement: the Weber number, the Reynolds number, and the Froude number. The Ohnesorge number, which is a function of the Weber and Reynolds numbers, is introduced as a dimensionless number for characterizing fluid properties. The Froude number is found to have negligible influence for the droplet size of interest. With a careful examination of the underlying physics of the interface evolution during droplet impingement, the effects of the Weber, Ohnesorge, and Reynolds numbers on the maximum achievable shape coefficient and the timing of the maximum shape coefficient during the interface evolution are investigated. Results show that the Weber number determines the maximum achievable shape coefficient and its timing when Ohnesorge number is smaller than 1 while the Reynolds number is the determining factor when Ohnesorge number is larger than 1. A regime map is constructed with the results and an empirical splash criterion to guide the choice of process parameters for given fluid properties in order to achieve the maximum shape coefficient without splash.

Chapter 5 is motivated by the need for an efficient numerical solver for simulating multiple-droplet interaction which is computationally prohibitive with current commercial software packages. An efficient numerical model is developed based on the

lattice Boltzmann method. A new LB formulation equivalent to the phase-field model is developed with consistent boundary conditions through a multiscale analysis. The numerical model is validated by comparing its simulation results with that of commercial software COMSOL and experimental data. Results show our numerical model not only has significantly improvement of computational speed over COMSOL but also is more accurate.

In chapter 6, the developed numerical solver is used to study the interface evolution of multiple droplet interaction with the aid of the 3-D shape metric proposed in chapter 3. Simulations are performed on a wide range of impingement conditions for two-droplet, a-line-of-droplet, and an-array-of-droplet interactions. The underlying physics of the interface coalescence and breakup coupling with the impingement dynamics are examined. For line-droplet interaction, the strategy for achieving the equilibrium shape in the shortest time is studied. An important issue is discovered for array-droplet interaction, which is the air bubble formation during the droplet interaction. The mechanism for the air bubble formation is investigated and the strategy to avoid this undesirable effect is also suggested.

7.2 Hypotheses evaluation

Three research questions aimed to reduce the gap between the current state of the art and the understanding of the interface dynamics of droplet deposition are posed in the first chapter of this thesis and corresponding hypotheses are proposed, which are investigated throughout the thesis and are now revisited and evaluated in the following.

RQ1: How to characterize and quantify the droplet shape to enable the shape optimization of the droplet deposition process?

Hypothesis: A shape coefficient that is defined to measure the similarity between the droplet shape and the desired shape (a uniform film) can be used to characterize and quantify the droplet shape.

Evaluation: In chapter 3, a shape signature function which contains all the information required to recover the shape is used to characterize the evolving shapes of the droplet and the corresponding desired shape. The approach of defining the shape coefficient by measuring the distance between the shape signature functions theoretically sound because the distance between shape signature functions can represent the similarity between two shapes and have been extensively tested in the literature as surveyed in chapter 2. The effectiveness of the proposed shape coefficient is backed by the results throughout the entire thesis, including the verification in chapter 3, the shape evolution results in chapter 4 for single droplet in 2-D, and the results for multiple-droplet interaction in 3-D in chapter 6. All the results confirm the capability of the defined shape coefficient in capturing the moments when the evolving shape is closest to the desired shape. Studies of droplet shape evolution using the shape coefficient in chapter 4 and 6 also illustrate it is possible to characterize and quantify the droplet shape using the shape coefficient to enable the shape optimization of the droplet deposition process. Therefore, the hypothesis has been fully validated and the research question has been answered.

RQ2: How do the relevant dimensionless numbers affect the best-achievable shape (i.e., closest to a uniform film) and the timing of it for single-droplet impingement on an ideal flat surface?

Hypothesis: A larger Weber number can achieve a more uniform film when the viscous effects are small and a larger Reynolds number leads to a better best-achievable shape when the viscous effects are large. The Froude number does not influence much of the shape evolution when the droplet size is sub-millimeter.

Evaluation: A dimensionless analysis shows that the Weber, Reynolds, and Froude numbers are relevant dimensionless numbers that control the interface evolution for single droplet impingement. The Ohnesorge number is a function of the Weber and Reynolds numbers. The influence of the Froude number on the droplet impingement dynamics is first examined for the droplet size of interest using an experimentally validated numerical model. Results show the Froude number has negligible influence on the impingement dynamics, which is consistent with our theoretical analysis.

The interface dynamics of single droplet impingement are then investigated under a wide range of impingement conditions in different regimes characterized by the Weber and Ohnesorge numbers, which improves our understanding of the underlying physics of the interface dynamics. The understanding of the underlying physics directs us to study the effects of the Weber and Reynolds numbers when the Ohnesorge number is smaller or larger than 1, respectively. Results show that the maximum shape coefficient and its timing are mainly determined by the Weber number when the Ohnesorge number is smaller than 1, while the Reynolds number is the determining factor when the Ohnesorge number is larger than 1, which echoes our theoretical analysis and intuitive understanding. Therefore, our hypothesis is fully supported by theoretical analysis, underlying physics, intuitive understanding, and the simulation results. The research question is also answered.

RQ3: How to build a numerical model that can simulate the droplet impingement dynamics more efficiently than the traditional commercial software packages with certain accuracy to enable 3-D simulation of the droplet impingement dynamics and make it possible to study the multiple-droplet interaction dynamics?

Hypothesis: A lattice Boltzmann model can be used to simulate 3-D droplet impingement dynamics more efficiently than the commercial software packages that use the traditional macroscopic methods within certain range of accuracy and reliability.

Evaluation: In chapter 5, a lattice Boltzmann formulation equivalent to the phase-field model used in COMSOL with consistent boundary conditions is developed based on rigorous mathematical derivation through a multiscale analysis. A numerical solver is then developed based on the model. The simulation results are then compared with those of COMSOL simulations and experimental data. The comparison confirms the significantly improved computational efficiency of our LB model in simulating droplet impingement in 3-D and the consistency with the COMSOL phase field model. The comparison of the results of both LB simulation and COMSOL simulation with the experimental data further validates both numerical models and also shows our LB model has a better accuracy. The examples of multiple droplet interaction simulations in chapter 5 and the simulation results of multiple droplet interaction under a wide range of impingement conditions in chapter 6 demonstrate the capability of the developed LB model. Therefore, our hypothesis is well validated and the research question is answered.

7.3 Contributions

Although droplet impingement is a century-old problem that has been extensively studied during the past century, there is still a large gap between the basic understanding of the droplet impingement dynamics and the understanding of the droplet deposition process in inkjet deposition. Many research questions remain open and unexplored. The primary contribution of this thesis is that we have reduced this gap and gotten much closer than where we were before. The gap is laid out as shown in Figure 1-3. Most previous research has focused on understanding the impingement dynamics for single droplet, while we are determined to understand the interface dynamics relevant to inkjet deposition. Our contribution is listed as below:

1. We proposed a novel metric for quantifying a changing geometry, which enables the study of the evolving geometry of the droplet interface. While there have been numerous efforts to characterize complex geometries, little has been reported on quantifying a changing geometry. In addition, few researchers have studied the dynamics of changing geometries. While numerous natural phenomena involve changing geometries, very little research has been done in this respect due to the lack of a metric to quantify changing geometry. Our original contribution here is that we have developed a novel metric for quantifying a changing geometry, which proves to be useful in studying the dynamics of the changing geometry.

2. We initiated the study of the dynamics of the interface evolution for single droplet impingement and developed a regime map indicating the conditions for achieving the best shape. Although extensive research has been done on the impingement dynamics of single droplet, the dynamics of its interface evolution were not explored. With the help of

our proposed shape metric, we conducted a systematic study on the dynamics of the interface evolution. We were able to assign physical meaning to the developed shape metric by linking different shapes to the preferences of the physical forces on shapes, which improved our understanding of the underlying physics of the interface evolution. The regime map we constructed from the results of the systematic study also proved to be useful and relevant to inkjet deposition.

3. We have developed a numerical model that proves to be more accurate and significantly more efficient than the commercial software packages. This model enables the study of the interface dynamics of multiple droplet interaction, which is important for inkjet deposition. Due to the prohibitive computational cost, multiple droplet interaction was rarely studied. The ability of our numerical model to enable simulation of multiple droplet interaction represented an important contribution to the research community and equipped us with a powerful tool to advance the research frontier on inkjet deposition.

4. We initiated the study of the interface evolution of multiple droplet interaction with the validated numerical tool we developed. We improved the understanding of the interface dynamics under a wide range of conditions with different numbers of droplets and different configurations. Results show important conclusions for improving the inkjet deposition technology, including how to speed up the manufacturing process and how to eliminate the air bubbles/voids in the manufactured parts.

7.4 Significance on inkjet deposition

Inkjet AM machines can typically deliver very high resolution and very good surface finish among other commercial AM machines on the market. Through this study,

however, we have revealed with our simulations that voids or other internal material interfaces can be created during the multiple-droplet interaction, which can significantly reduce the material strength and other material properties. We have also gained a preliminary understanding on how to eliminate the voids during multiple-droplet interaction by optimizing the impingement conditions. Further investigation is also made possible with our developed powerful simulation tool. In addition, this work also has important implications on the inkjet print head design and the printing process control. The effects of the spacing between nozzles in the print head have been studied and shown to be very important on the outcomes of the multiple-droplet interaction dynamics as well as the final equilibrium shapes. The study shows it is possible to optimizing the nozzle spacing with our developed approach and simulation tool. Other than the issue of the voids and internal material interface, we have found the manufacturing time can be shortened and thus the manufacturing cost can be reduced by optimizing the impingement conditions as well. For a line-of-droplet interaction, we are determined from our simulations that the equilibrium shape is a suitable goal for us to pursue in the sense of manufacturing and we have demonstrated that the time required to achieve the equilibrium shape can be optimized with our developed understanding and tools. Therefore, this work has contributed to the two most important aspects of inkjet deposition: product quality and manufacturing time/cost. Further improvements of inkjet deposition technology are also made possible with our developed approach and tools. This work has reduced the gap between the basic science in studying droplet impingement dynamics and the development of inkjet deposition technology.

7.5 Future work recommendations

As with any other research, this work has its limitations. Outlined here are some of the future work that are worth exploring further.

1. Exploration of the effects of contact angle.

The contact angle in most of this research is fixed at 90°. One reason is that the substrates of our interests are mostly polymers (flexible substrates for printed electronics), which typically are hydrophobic (i.e., large contact angle). Another reason is that we find from our analysis and some preliminary results that the contact angle does not have a big influence on the interface dynamics in the early stage of impingement for single droplet. However, we do believe the contact angle plays a more important role in multiple droplet interaction as the dynamics become more complicated. Therefore, an investigation of the effects of the contact angle for multiple droplet interaction is recommended.

2. Incorporation of the droplet hardening mechanism in the model.

The numerical models used in this research only describe the fluid dynamics of the droplet impingement under isothermal conditions. In order to predict the microstructure from the inkjet deposition process, a droplet hardening mechanism needs to be included in the model. As shown in Figure 1-3, there are three different approaches that can make the droplet become solid for different materials, which correspond to three different research directions: 1) for easy-melt metals, incorporating a model for the phase transformation and solidification process into the existing fluid model can enable the study of the coupling effects between the impingement dynamics and the solidification process and the prediction of the geometry of the microstructures; 2) for ceramics or hard-melt metals, a mass transfer model for the evaporation of the solution and the

interaction between the fluid and the solid nano-particles (made from the ceramics or hard-melt metals) need to be included in the existing fluid model such that the motion of the nano-particles and the final microstructure can be predicted; 3) for polymers, a reaction-diffusion polymerization model needs to be incorporated to couple with the current fluid model in order to predict the final microstructures.

3. Parallelization of the LB solver for high performance computing

Due to the locality of the computations in the LB model, a much higher performance can be expected by parallelization of the solver. GPU computing has been gaining lots of momentum in high performance computing. Therefore, it is worth investigating how to implement the existing LB model on GPUs to significantly reduce the computing time. Reducing the computing time will be very beneficial for design and optimization of the complicated inkjet deposition process.

4. Investigation of the multiscale effects

One interesting phenomenon for additive manufacturing is that the manufactured parts are typically on a much larger scale than the scale of the local material joining process. It would be interesting to develop a model to enable the simulation of hundreds of thousands of droplets interacting and hardening so that we can study the phenomenon on different scales to improve our understanding of the multiscale effects and better control the part quality and accuracy on the scale of the manufactured parts.

7.6 Closing remarks

Droplet deposition is a highly complicated process that involves lots of phenomena that has baffled generations of scientists, such as the interface dynamics between multiple

phases or multiple materials, transfer of mass (e.g., evaporation), momentum, and heat (e.g., solidification) in different processes, reaction-diffusion process for polymers, gas-liquid-solid interactions, and multiscale interactions (e.g., diffusion and fluid convection occur on different scale, the local material joining process and the global part structure are on different scale, etc.). Since these processes are common to many science and engineering problems, a complete model of the droplet deposition process will lead to breakthroughs in many other science and engineering disciplines. What is more interesting is to realize that what we are trying to do with droplet deposition is to build organized structures by creating external conditions so that the material can self-organize and evolve to our desired structure, which is battling against the second law of thermodynamics that tends to doom our universe with chaos. Self-organization is a very common phenomenon, such as chemical clock and bio-organism (e.g., cell is a self-organized entity). An understanding of self-organization may hold the key to end the debate on the direction of time (i.e., from order to disorder as common in heat science, or from disorder to order as common in bio-science.) and may help us to understand the nature of the irreversibility. One major branch of science is to search for the elementary particles and to understand their behaviors, but self-organization may completely change the behavior of the elementary particles on a different scale. The self-organized structure on one scale may serve as the "elementary particle" to self-organize into a completely different structure on a larger scale (e.g., molecule → protein → cell → human → community → society). In addition, Ilya Prigogine [180] believes self-organization is due to the nonlinearity of the interaction dynamics that is common under far-from-equilibrium conditions, which makes long-range interaction (or communication between

particles) possible since linear interaction is typically local. By viewing droplet deposition from the perspective of self-organization, we can improve our understanding about the nonlinear nature of the universe and about how to control and utilize the nonlinearity. Therefore, studying the droplet deposition process for inkjet deposition in the perspective of self-organization provides an opportunity to understand the very nature of the universe without getting into the overwhelmingly complexity in bio-organisms.

APPENDIX A

LATTICE STRUCTURES

Some commonly used lattice models are provided below:

D1Q3 [181]	$\mathbf{c_s^2} = \mathbf{\frac{1}{3}}$ $\boldsymbol{t_i} = \begin{cases} \mathbf{2/3} & \boldsymbol{i = 0} \\ \mathbf{1/6} & \boldsymbol{i = 1, 2} \end{cases}$ $\mathbf{e}_{\boldsymbol{i}} = \begin{cases} (\mathbf{0}) & \boldsymbol{i = 0} \\ (\mathbf{\pm 1}) & \boldsymbol{i = 1, 2} \end{cases}$
D1Q5 [181]	$c_s^2 = 1$ $t_i = \begin{cases} 1/2 & i = 0 \\ 1/6 & i = 1, 2 \\ 1/12 & i = 3, 4 \end{cases}$ $\mathbf{e}_i = \begin{cases} (0) & i = 0 \\ (\pm 1) & i = 1, 2 \\ (\pm 3) & i = 3, 4 \end{cases}$
D2Q7 [182]	$c_s^2 = \frac{1}{4}$ $t_i = \begin{cases} 1/2 & i = 0 \\ 1/12 & i = 1, 2,3,4,5,6 \end{cases}$ $\mathbf{e}_i = \begin{cases} (0,0) & i = 0 \\ (\pm 1,0), \left(\pm 1/2 , \pm\sqrt{3}/2\right) & i = 1, 2,3,4,5,6 \end{cases}$
D2Q9 [182]	$c_s^2 = 1/3$ $t_i = \begin{cases} 4/9 & i = 0 \\ 1/9 & i = 1, 2, 3, 4 \\ 1/36 & i = 5, 6, 7, 8 \end{cases}$ $\mathbf{e}_i = \begin{cases} (0,0) & i = 0 \\ (\pm 1,0), (0, \pm 1) & i = 1, 2, 3, 4 \\ (\pm 1, \pm 1) & i = 5, 6, 7, 8 \end{cases}$

D2Q13 [183]

$$c_s^2 = 2/5$$

$$t_i = \begin{cases} 2/5 & i = 0 \\ 8/75 & i = 1,2,3,4 \\ 1/25 & i = 5,6,7,8 \\ 1/300 & i = 9,10,11,12 \end{cases}$$

$$\mathbf{e}_i = \begin{cases} (0,0) & i = 0 \\ (\pm 1,0),(0,\pm 1) & i = 1,2,3,4 \\ (\pm 1,\pm 1) & i = 5,6,7,8 \\ (\pm 2,0),(0,\pm 2) & i = 9,10,11,12 \end{cases}$$

D3Q15 [139]

$$c_s^2 = 1/3$$

$$t_i = \begin{cases} 2/9 & i = 0 \\ 1/9 & i = 1,2,..6 \\ 1/72 & i = 7,8,..14 \end{cases}$$

$$\mathbf{e}_i = \begin{cases} (0,0,0) & i = 0 \\ (\pm 1,0,0),(0,\pm 1,0),(0,0,\pm 1) & i = 1,2,..6 \\ (\pm 1,\pm 1,\pm 1) & i = 7,8,..14 \end{cases}$$

D3Q19 [139]

$$c_s^2 = 1/3$$

$$t_i = \begin{cases} 1/3 & i = 0 \\ 1/18 & i = 1,2,..6 \\ 1/36 & i = 7,8,..18 \end{cases}$$

$$\mathbf{e}_i = \begin{cases} (0,0,0) & i = 0 \\ (\pm 1,0,0),(0,\pm 1,0),(0,0,\pm 1) & i = 1,2,..6 \\ (\pm 1,\pm 1,0),(0,\pm 1,\pm 1),(\pm 1,0,\pm 1) & i = 7,8,..18 \end{cases}$$

D3Q27 [139]

$$c_s^2 = 1/3$$

$$t_i = \begin{cases} 8/27 & i = 0 \\ 2/27 & i = 1,2,..6 \\ 1/54 & i = 7,8..18 \\ 1/216 & i = 19,20..27 \end{cases}$$

$$\mathbf{e}_i = \begin{cases} (0,0,0) & i = 0 \\ (\pm 1,0,0),(0,\pm 1,0),(0,0,\pm 1) & i = 1,2,..6 \\ (\pm 1,\pm 1,0),(0,\pm 1,\pm 1),(\pm 1,0,\pm 1) & i = 7,8..18 \\ (\pm 1,\pm 1,\pm 1) & i = 19,20..27 \end{cases}$$

REFERENCES

1. S. Kalpakjian and S.R. Schmid, *Manufacturing processes for engineering materials*. 2010: Pearson education.

2. J.T. Black and R.A. Kohser, *DeGarmo's materials and processes in manufacturing*. 2011: Wiley.

3. F. Sauter, et al., *Studies in organic archaeometry I: identification of the prehistoric adhesive used by the "Tyrolean Iceman" to fix his weapons.* ARKIVOC, 2000. **735**: p. 747.

4. C.W. Hull, *Apparatus for production of three-dimensional objects by stereolithography*. 11 Mar. 1986: U.S. Patent No. 4,575,330.

5. I. Gibson, D.W. Rosen, and B. Stucker, *Additive manufacturing technologies: rapid prototyping to direct digital manufacturing*. 2010: Springer.

6. O. Hilton, *Scientific examination of questioned documents*. 1982: CRC Press.

7. E.R. Lee, *Microdrop generation*. Vol. 5. 2010: CRC press.

8. J.D. Meyer. *Thermal ink jet: current status and future prospects*. in *Proceedings of SPIE*. 1994.

9. E.L. Kyser, L.F. Collins, and N. Herbert, *Design of an impulse ink jet.* Journal of Applied Photographic Engineering, 1981. **7**(3): p. 73-79.

10. S.A. Elrod, B.T. Khuri-Yakub, and C.F. Quate, *Acoustic lens arrays for ink printing*. 1988, Google Patents.

11. J. Meacham, et al., *Micromachined ultrasonic droplet generator based on a liquid horn structure.* Review of Scientific Instruments, 2004. **75**(5): p. 1347-1352.

12. B. Tay, J. Evans, and M. Edirisinghe, *Solid freeform fabrication of ceramics.* International Materials Reviews, 2003. **48**(6): p. 341-370.

13. Y. Wang and J. Bokor, *Ultra-high-resolution monolithic thermal bubble inkjet print head.* Journal of Micro/Nanolithography, MEMS, and MOEMS, 2007. **6**(4): p. 043009.

14. P.-G. De Gennes, F. Brochard-Wyart, and D. Quéré, *Capillarity and wetting phenomena: drops, bubbles, pearls, waves*. 2004: Springer.

15. E. Dussan, *On the spreading of liquids on solid surfaces: static and dynamic contact lines.* Annual Review of Fluid Mechanics, 1979. **11**(1): p. 371-400.

16. J.C. Berg, *Wettability*. Vol. 49. 1993: CRC Press.

17. V. Carey, *Liquid-Vapor Phase-Change Phenomena: An Introduction to the Themophysics of Vaporization and Condensation Processes in Heat Transfer Equipment*. 1992, Taylor and Francis.

18. R. Rioboo, M. Marengo, and C. Tropea, *Time evolution of liquid drop impact onto solid, dry surfaces.* Experiments in Fluids, 2002. **33**(1): p. 112-124.

19. A.M. Worthington, *On the forms assumed by drops of liquids falling vertically on a horizontal plate.* Proceedings of the royal society of London, 1876. **25**: p. 261-271.

20. L. Xu, W.W. Zhang, and S.R. Nagel, *Drop splashing on a dry smooth surface.* Phys. Rev. Lett., 2005. **94**: p. 184505.

21. L. Xu, L. Barcos, and S.R. Nagel, *Splashing of liquids: Interplay of surface roughness with surrounding gas.* PHYSICAL REVIEW E, 2007. **76**: p. 066311.

22. C.D. Stow and M.G. Hadfield. *An experimental investigation of fluid-flow resulting from the impact of a water drop with an unyielding dry surface*. in *Proceedings of the Royal Society, Series A*. 1981. London.

23. K. Range and F. Feuillebois, *Influence of surface roughness on liquid drop impact.* J. Colloid Interface Sci., 1998. **203**: p. 16-30.

24. R.E. Pepper, L. Courbin, and H.A. Stone, *Splashing on elastic membranes: the importance of early-time dynamics.* Phys. Fluids, 2008. **20**: p. 082103.

25. C. Mundo, M. Sommerfeld, and C. Tropea, *Droplet-Wall Collisions - Experimental Studies of the Deformation and Breakup Process.* Int. J. Multiphas. Flow, 1995. **21**: p. 151-173.

26. B. Kang, Z. Zhao, and D. PouLikakos, *Solidification of liquid metal droplets impacting sequentially on a solid surface.* ASME Journal of Heat Transfer, 1994. **116**: p. 436-445.

27. S. Inada, *Transient heat transfer from a free-falling molten drop of Iead to a cold plate.* J. of Chernical Engineering of Japan, 1988. **21**: p. 582-588.

28. M. Francois, *Computations of drop dynamics with heat transfer*. 2002, University of Florida. p. 214.

29. H. Cheong, G. Jeffreys, and C. Mumford, *A receding interface model for the drying of slurry droplets.* AIChE Journal, 1986. **32**(8): p. 1334-1346.

30. A. Zadražil, F. Stepanek, and O. Matar, *Droplet spreading, imbibition and solidification on porous media.* Journal of Fluid Mechanics, 2006. **562**(1): p. 1-33.

31. R.D. Deegan, et al., *Capillary flow as the cause of ring stains from dried liquid drops.* Nature, 1997. **389**(6653): p. 827-829.

32. D. Kim, et al., *Ink-jet printing of silver conductive tracks on flexible substrates.* Molecular Crystals and Liquid Crystals, 2006. **459**(1): p. 45-55.

33. B.K. Park, et al., *Direct writing of copper conductive patterns by ink-jet printing.* Thin Solid Films, 2007. **515**(19): p. 7706-7711.

34. E. Tekin, P.J. Smith, and U.S. Schubert, *Inkjet printing as a deposition and patterning tool for polymers and inorganic particles.* Soft Matter, 2008. **4**(4): p. 703-713.

35. A.B. Scranton, C.N. Bowman, and R.W. Peiffer, *Photopolymerization: Fundamentals and Applications*. 1997: American Chemical Society.

36. *The Grand Challenges for Engineering* 2008 [cited 2012 Nov. 27th]; Available from: http://www.engineeringchallenges.org/cms/challenges.aspx.

37. J.S. Kang, et al., *Inkjet printed electronics using copper nanoparticle ink.* Journal of Materials Science: Materials in Electronics, 2010. **21**(11): p. 1213-1220.

38. S.H. Ko, et al., *All-inkjet-printed flexible electronics fabrication on a polymer substrate by low-temperature high-resolution selective laser sintering of metal nanoparticles.* Nanotechnology, 2007. **18**(34): p. 345202.

39. T. Kawase, et al., *Inkjet printing of polymer thin film transistors.* Thin Solid Films, 2003. **438**: p. 279-287.

40. H. Minemawari, et al., *Inkjet printing of single-crystal films.* Nature, 2011. **475**(7356): p. 364-367.

41. F.C. Krebs, *Fabrication and processing of polymer solar cells: a review of printing and coating techniques.* Solar Energy Materials and Solar Cells, 2009. **93**(4): p. 394-412.

42. T. Boland, et al., *Application of inkjet printing to tissue engineering.* Biotechnology journal, 2006. **1**(9): p. 910-917.

43. V. Fakhfouri, et al. *Inkjet printing of SU-8 for polymer-based MEMS a case study for microlenses*. in *Micro Electro Mechanical Systems, 2008. MEMS 2008. IEEE 21st International Conference on*. 2008: IEEE.

44. E.A. Roth, et al., *Inkjet printing for high-throughput cell patterning.* Biomaterials, 2004. **25**(17): p. 3707-3715.

45. W.-Y. Yeong, et al., *Rapid prototyping in tissue engineering: challenges and potential.* TRENDS in Biotechnology, 2004. **22**(12): p. 643-652.

46. F. Gao and A.A. Sonin, *Precise Deposition of Molten Microdrops: The Physics of Digital Microfabrication.* Proceedings: Mathematical and Physical Sciences, 1994. **444**(1922): p. 533-554.

47. M. Orme and R.F. Smith, *Enhanced Aluminum Properties by Means of Precise Droplet Deposition.* Journal of Manufacturing Science and Engineering, 2000. **122**(3): p. 484-493.

48. Q. Liu and M. Orme, *High precision solder droplet printing technology and the state-of-the-art.* Journal of Materials Processing Technology, 2001. **115**(3): p. 271-283.

49. H. Sirringhaus, et al., *High-Resolution Inkjet Printing of All-Polymer Transistor Circuits.* Science, 2000. **290**(5499): p. 2123-2126.

50. B. Chen, et al., *All-polymer RC filter circuits fabricated with inkjet printing technology.* Solid-State Electronics, 2003. **47**(5): p. 841-847.

51. T. Cuk, et al., *Using convective flow splitting for the direct printing of fine copper lines.* Applied Physics Letters, 2000. **77**(13): p. 2063-2065.

52. G.G. Rozenberg, et al., *Patterned low temperature copper-rich deposits using inkjet printing.* Applied Physics Letters, 2002. **81**(27): p. 5249.

53. Z. Liu, Y. Su, and K. Varahramyan, *Inkjet-printed silver conductors using silver nitrate ink and their electrical contacts with conducting polymers.* Thin Solid Films, 2005. **478**(1–2): p. 275-279.

54. H.-H. Lee, K.-S. Chou, and K.-C. Huang, *Inkjet printing of nanosized silver colloids.* Nanotechnology, 2005. **16**: p. 2436–2441.

55. T.H.J. van Osch, et al., *Inkjet Printing of Narrow Conductive Tracks on Untreated Polymeric Substrates.* Advanced Materials, 2008. **20**(2): p. 343-345.

56. S.B. Fuller, E.J. Wilhelm, and J.M. Jacobson, *Ink-jet printed nanoparticle microelectromechanical systems.* Microelectromechanical Systems, Journal of, 2002. **11**(1): p. 54-60.

57. J. Perelaer, B.J. de Gans, and U.S. Schubert, *Ink-jet Printing and Microwave Sintering of Conductive Silver Tracks.* Advanced Materials, 2006. **18**(16): p. 2101-2104.

58. N.R. Bieri, et al., *An experimental investigation of microresistor laser printing with gold nanoparticle-laden inks.* Applied Physics A: Materials Science & Processing, 2005. **80**(7): p. 1485-1495.

59. J.B. Szczech, et al., *Fine-line conductor manufacturing using drop-on demand PZT printing technology.* Electronics Packaging Manufacturing, IEEE Transactions on, 2002. **25**(1): p. 26-33.

60. N.R. Bieri, et al., *Microstructuring by printing and laser curing of nanoparticle solutions.* Applied Physics Letters, 2003. **82**(20): p. 3529.

61. N.R. Bieri, et al., *Manufacturing of nanoscale thickness gold lines by laser curing of a discretely deposited nanoparticle suspension.* Superlattices and Microstructures, 2004. **35**(3–6): p. 437-444.

62. C. Jaewon, et al., *Conductor microstructures by laser curing of printed gold nanoparticle ink.* Applied Physics Letters, 2004. **84**(5): p. 801-803.

63. J. Szczech, et al., *Inkjet Processing of Meltallic Nanoparticle Suspensions For Electronic Circuitry Fabrication.* Microscale Thermophysical Engineering, 2004. **8**(4): p. 327-339.

64. K. Arbter, et al., *Application of Affine-Invariant Fourier Descriptors to Recognition of 3-D Objects.* IEEE Trans Pattern Anal Mach Intell, 1990. **12**(7): p. 640 - 647

65. D. Zhang and G. Lu, *A Comparative Study on Shape Retrieval Using Fourier Descriptors with Different Shape Signatures.* J Vis Commun Image Represent., 2003. **14**(1): p. 41-60.

66. E.R. Davies, *Machine Vision: Theory, Algorithms, Practicalities*. 2005: Elsevier.

67. C. Faloutsos, *Searching multimedia databases by content*. Vol. 3. 1996: Springer.

68. E. Paquet, et al., *Description of shape information for 2-D and 3-D objects.* Signal Processing: Image Communication, 2000. **16**(1): p. 103-122.

69. M. Peura and J. Iivarinen. *Efficiency of simple shape descriptors*. in *Proceedings of the third international workshop on visual form*. 1997: Citeseer.

70. R. Ohbuchi, et al. *Shape-similarity search of three-dimensional models using parameterized statistics*. in *Computer Graphics and Applications, 2002. Proceedings. 10th Pacific Conference on*. 2002: IEEE.

71. D. Saupe and D.V. Vranić, *3D model retrieval with spherical harmonics and moments*, in *Pattern Recognition*. 2001, Springer. p. 392-397.

72. R. Osada, et al., *Shape distributions.* ACM Transactions on Graphics (TOG), 2002. **21**(4): p. 807-832.

73. P.J. Van Otterloo, *A contour-oriented approach to shape analysis*. 1991: Prentice Hall International (UK) Ltd.

74. R. Chellappa and R. Bagdazian, *Fourier coding of image boundaries.* Pattern Analysis and Machine Intelligence, IEEE Transactions on, 1984(1): p. 102-105.

75. Q.M. Tieng and W. Boles, *Recognition of 2D object contours using the wavelet transform zero-crossing representation.* Pattern Analysis and Machine Intelligence, IEEE Transactions on, 1997. **19**(8): p. 910-916.

76. D.V. Vranic. *An improvement of rotation invariant 3D-shape based on functions on concentric spheres*. in *Image Processing, 2003. ICIP 2003. Proceedings. 2003 International Conference on*. 2003: IEEE.

77. H. Asada and M. Brady, *The curvature primal sketch.* Pattern Analysis and Machine Intelligence, IEEE Transactions on, 1986(1): p. 2-14.

78. A. Del Bimbo and P. Pala, *Visual image retrieval by elastic matching of user sketches.* Pattern Analysis and Machine Intelligence, IEEE Transactions on, 1997. **19**(2): p. 121-132.

79. G. Lu and A. Sajjanhar, *Region-based shape representation and similarity measure suitable for content-based image retrieval.* Multimedia Systems, 1999. **7**(2): p. 165-174.

80. A. Goshtasby, *Description and discrimination of planar shapes using shape matrices.* Pattern Analysis and Machine Intelligence, IEEE Transactions on, 1985(6): p. 738-743.

81. M. Novotni and R. Klein. *3D Zernike descriptors for content based shape retrieval*. in *Proceedings of the eighth ACM symposium on Solid modeling and applications*. 2003: ACM.

82. M. Ankerst, et al. *3D shape histograms for similarity search and classification in spatial databases*. in *Advances in Spatial Databases*. 1999: Springer.

83. B. Bustos, et al., *Feature-Based Similarity Search in 3D object Databases.* ACM Computing Surveys, 2005. **37**(4): p. 345-387.

84. T. Pavlidis, *Algorithms for graphics and image processing*. 1982: Computer science press.

85. H. Freeman, *On the encoding of arbitrary geometric configurations.* Electronic Computers, IRE Transactions on, 1961(2): p. 260-268.

86. W.I. Grosky and R. Mehrotra, *Index-based object recognition in pictorial data management.* Computer Vision, Graphics, and Image Processing, 1990. **52**(3): p. 416-436.

87. S. Berretti, A. Del Bimbo, and P. Pala, *Retrieval by shape similarity with perceptual distance and effective indexing.* Multimedia, IEEE Transactions on, 2000. **2**(4): p. 225-239.

88. M. Hilaga, et al. *Topology matching for fully automatic similarity estimation of 3D shapes*. in *Proceedings of the 28th annual conference on Computer graphics and interactive techniques*. 2001: ACM.

89. H. Sundar, et al. *Skeleton based shape matching and retrieval*. in *Shape Modeling International, 2003*. 2003: IEEE.

90. M. Manninen, V. Taivassalo, and S. Kallio, *On the mixture model for multiphase flow*. 1996: Technical Research Centre of Finland Finland.

91. M. Ishii and N. Zuber, *Drag coefficient and relative velocity in bubbly, droplet or particulate flows.* AIChE Journal, 1979. **25**(5): p. 843-855.

92. M. Ishii and K. Mishima, *Two-fluid model and hydrodynamic constitutive relations.* Nuclear Engineering and Design, 1984. **82**(2–3): p. 107-126.

93. J. Sanyal, et al., *Numerical simulation of gas–liquid dynamics in cylindrical bubble column reactors.* Chemical Engineering Science, 1999. **54**(21): p. 5071-5083.

94. N. Yang, et al., *Simulation of heterogeneous structure in a circulating fluidized-bed riser by combining the two-fluid model with the EMMS approach.* Industrial & engineering chemistry research, 2004. **43**(18): p. 5548-5561.

95. A. Sokolichin, et al., *Dynamic numerical simulation of gas-liquid two-phase flows Euler/Euler versus Euler/Lagrange.* Chemical Engineering Science, 1997. **52**(4): p. 611-626.

96. F.H. Harlow and J.E. Welch, *Numerical Calculation of Time‐Dependent Viscous Incompressible Flow of Fluid with Free Surface.* Physics of fluids, 1965. **8**: p. 2182.

97. C.W. Hirt and B.D. Nichols, *Volume of fluid (VOF) method for the dynamics of free boundaries.* Journal of computational physics, 1981. **39**(1): p. 201-225.

98. S. Osher and J.A. Sethian, *Fronts propagating with curvature-dependent speed: algorithms based on Hamilton-Jacobi formulations.* Journal of computational physics, 1988. **79**(1): p. 12-49.

99. D. Jacqmin, *Calculation of Two-Phase Navier–Stokes Flows Using Phase-Field Modeling.* Journal of Computational Physics, 1999. **155**(1): p. 96-127.

100. S.O. Unverdi and G. Tryggvason, *A front-tracking method for viscous, incompressible, multi-fluid flows.* Journal of computational physics, 1992. **100**(1): p. 25-37.

101. Y. Renardy and M. Renardy, *PROST: a parabolic reconstruction of surface tension for the volume-of-fluid method.* Journal of computational physics, 2002. **183**(2): p. 400-421.

102. M. Bussmann, J. Mostaghimi, and S. Chandra, *On a three-dimensional volume tracking model of droplet impact.* Physics of fluids, 1999. **11**: p. 1406-1417.

103. M. Pasandideh-Fard, et al., *Capillary effects during droplet impact on a solid surface.* Phys. Fluids, 1996. **8**: p. 1344.

104. W.J. Rider and D.B. Kothe. *Stretching and tearing interface tracking methods*. in *AIAA Computational Fluid Dynamics Conference, 12 th, and Open Forum, San Diego, CA*. 1995.

105. M. Sussman and E.G. Puckett, *A coupled level set and volume-of-fluid method for computing 3D and axisymmetric incompressible two-phase flows.* Journal of computational physics, 2000. **162**(2): p. 301-337.

106. R.P. Fedkiw, et al., *A non-oscillatory Eulerian approach to interfaces in multimaterial flows (the ghost fluid method).* Journal of computational physics, 1999. **152**(2): p. 457-492.

107. S. Osher and R.P. Fedkiw, *Level set methods: an overview and some recent results.* Journal of computational physics, 2001. **169**(2): p. 463-502.

108. D. Anderson, G.B. McFadden, and A. Wheeler, *Diffuse-interface methods in fluid mechanics.* Annual Review of Fluid Mechanics, 1998. **30**(1): p. 139-165.

109. W. Zhou, et al., *What controls dynamics of droplet shape evolution upon impingement on a solid surface?* AIChE Journal, 2013: p. 3071-3082.

110. W. Boettinger, et al., *Phase-Field Simulation of Solidification 1.* Annual review of materials research, 2002. **32**(1): p. 163-194.

111. R. Folch, et al., *Phase-field model for Hele-Shaw flows with arbitrary viscosity contrast. II. Numerical study.* Physical Review E, 1999. **60**(2): p. 1734-1740.

112. B. Alder and T. Wainwright, *Studies in molecular dynamics. I. General method.* The Journal of Chemical Physics, 1959. **31**: p. 459.

113. J.M. Hammersley, D.C. Handscomb, and G. Weiss, *Monte carlo methods.* Physics Today, 1965. **18**: p. 55.

114. J. Koplik, J.R. Banavar, and J.F. Willemsen, *Molecular dynamics of Poiseuille flow and moving contact lines.* Physical Review Letters, 1988. **60**(13): p. 1282-1285.

115. P.A. Thompson and M.O. Robbins, *Simulations of contact-line motion: Slip and the dynamic contact angle.* Physical Review Letters, 1989. **63**(7): p. 766-769.

116. N. Metropolis, et al., *Equation of state calculations by fast computing machines.* The Journal of Chemical Physics, 1953. **21**: p. 1087.

117. W. Young and E. Elcock, *Monte Carlo studies of vacancy migration in binary ordered alloys: I.* Proceedings of the Physical Society, 1966. **89**(3): p. 735.

118. A. Milchev and K. Binder, *Droplet spreading: A Monte Carlo test of Tanner's law.* The Journal of Chemical Physics, 2002. **116**: p. 7691.

119. U. Frisch, B. Hasslacher, and Y. Pomeau, *Lattice-gas automata for the Navier-Stokes equation.* Physical Review Letters, 1986. **56**(14): p. 1505-1508.

120. S. Chen and G.D. Doolen, *Lattice Boltzmann method for fluid flows.* Annual Review of Fluid Mechanics, 1998. **30**(1): p. 329-364.

121. P. Espanol and P. Warren, *Statistical mechanics of dissipative particle dynamics.* EPL (Europhysics Letters), 1995. **30**(4): p. 191.

122. R.A. Gingold and J.J. Monaghan, *Smoothed particle hydrodynamics-theory and application to non-spherical stars.* Monthly notices of the royal astronomical society, 1977. **181**: p. 375-389.

123. P. Espanol, *Fluid particle model.* Physical Review E, 1998. **57**(3): p. 2930.

124. G. Winckelmans and A. Leonard, *Contributions to vortex particle methods for the computation of three-dimensional incompressible unsteady flows.* Journal of computational physics, 1993. **109**(2): p. 247-273.

125. S. Trofimov, E. Nies, and M. Michels, *Thermodynamic consistency in dissipative particle dynamics simulations of strongly nonideal liquids and liquid mixtures.* The Journal of Chemical Physics, 2002. **117**: p. 9383.

126. P. Meakin and A.M. Tartakovsky, *Modeling and simulation of pore‐scale multiphase fluid flow and reactive transport in fractured and porous media.* Reviews of Geophysics, 2009. **47**(3).

127. J.J. Monaghan, *Smoothed particle hydrodynamics.* Reports on progress in physics, 2005. **68**(8): p. 1703.

128. G.R. McNamara and G. Zanetti, *Use of the Boltzmann Equation to Simulate Lattice-Gas Automata.* Physical Review Letters, 1988. **61**(20): p. 2332-2335.

129. S. Wolfram, *Statistical mechanics of cellular automata.* Reviews of modern physics, 1983. **55**(3): p. 601.

130. S. Succi, *The Lattice Boltzmann Equation for Fluid Dynamics and Beyond, Clarendon*. 2001, Oxford.

131. P.L. Bhatnagar, E.P. Gross, and M. Krook, *A Model for Collision Processes in Gases. I. Small Amplitude Processes in Charged and Neutral One-Component Systems.* Physical Review, 1954. **94**(3): p. 511-525.

132. H. Chen, S. Chen, and W.H. Matthaeus, *Recovery of the Navier-Stokes equations using a lattice-gas Boltzmann method.* Physical Review A, 1992. **45**(8): p. R5339-R5342.

133. Y. Qian, D. d'Humieres, and P. Lallemand, *Lattice BGK models for Navier-Stokes equation.* EPL (Europhysics Letters), 1992. **17**(6): p. 479.

134. D. d'Humières, *Multiple–relaxation–time lattice Boltzmann models in three dimensions.* Philosophical Transactions of the Royal Society of London. Series A: Mathematical, Physical and Engineering Sciences, 2002. **360**(1792): p. 437-451.

135. X. He, X. Shan, and G.D. Doolen, *Discrete Boltzmann equation model for nonideal gases.* Physical Review E, 1998. **57**(1): p. R13-R16.

136. Q. Zou and X. He, *On pressure and velocity boundary conditions for the lattice Boltzmann BGK model.* Physics of fluids, 1997. **9**: p. 1591.

137. M.h. Bouzidi, M. Firdaouss, and P. Lallemand, *Momentum transfer of a Boltzmann-lattice fluid with boundaries.* Physics of fluids, 2001. **13**: p. 3452.

138. T. Inamuro, M. Yoshino, and F. Ogino, *A non-slip boundary condition for lattice Boltzmann simulations.* arXiv preprint comp-gas/9508002, 1995.

139. J. Latt, *Hydrodynamic limit of lattice Boltzmann equations*. 2007, University of Geneva.

140. J. Latt, et al., *Straight velocity boundaries in the lattice Boltzmann method.* Physical Review E, 2008. **77**(5): p. 056703.

141. X. Shan and H. Chen, *Lattice Boltzmann model for simulating flows with multiple phases and components.* Physical Review E, 1993. **47**(3): p. 1815-1819.

142. X. Shan and H. Chen, *Simulation of nonideal gases and liquid-gas phase transitions by the lattice Boltzmann equation.* Physical Review E, 1994. **49**(4): p. 2941-2948.

143. M.R. Swift, et al., *Lattice Boltzmann simulations of liquid-gas and binary fluid systems.* Physical Review E, 1996. **54**(5): p. 5041-5052.

144. M.R. Swift, W.R. Osborn, and J.M. Yeomans, *Lattice Boltzmann Simulation of Nonideal Fluids.* Physical Review Letters, 1995. **75**(5): p. 830-833.

145. X. He, S. Chen, and R. Zhang, *A Lattice Boltzmann Scheme for Incompressible Multiphase Flow and Its Application in Simulation of Rayleigh–Taylor Instability.* Journal of computational physics, 1999. **152**(2): p. 642-663.

146. A.J. Wagner, *The origin of spurious velocities in lattice Boltzmann.* International Journal of Modern Physics B, 2003. **17**(01n02): p. 193-196.

147. D. Zhang and G. Lu, *Review of shape representation andd escription techniques.* Patt Recog, 2004. **37**(1): p. 1-19.

148. W. Zhou, et al., *Droplet impingement dynamics in ink-jet deposition.* Virtual and Physical Prototyping, 2012. **7**(1): p. 49-64.

149. H.R. Pruppacher and K.V. Beard, *A wind tunnel investigation of the internal circulation and shape of water drops falling at terminal velocity in air.* Quarterly Journal of the Royal Meteorological Society, 1970. **96**(408): p. 247-256.

150. J.W. Cahn and J.E. Hilliard, *Free Energy of a Nonuniform System. I. Interfacial Free Energy.* J. Chem. Phys, 1958. **28**(2).

151. P. Yue, et al., *Phase-field simulations of interfacial dynamics in viscoelastic fluids using finite elements with adaptive meshing.* Journal of computational physics, 2006. **219**(1): p. 47-67.

152. D. Jacqmin, *Contact-line dynamics of a diffuse fluid interface.* Journal of Fluid Mechanics, 2000. **402**: p. 57-88.

153. P. Attané, F. Girard and V. Morin, *An energy balance approach of the dynamics of drop impact on a solid surface.* Physics of Fluids, 2007. **19**: p. 012101.

154. B.L. Scheller, and D.W. Bousfield, *Newtonian drop impact with a solid surface.* AIChE J. , 1995. **41**: p. 1357.

155. A. Asai, M. Shioya, S. Hirasawa, and T. Okazaki, *Impact of an ink drop on paper.* J. Imaging Sci. Technol., 1993. **37**: p. 205.

156. M. Pasandideh-Fard, Y. M. Qiao, S. Chandra, and J. Mostaghimi, *Capillary effects during droplet impact on a solid surface.* Phys. Fluids, 1996. **8**: p. 1344.

157. S. Chandra, and C.T. Avedisian. *On the collision of a droplet with a solid surface*. in *Proceedings of the Royal Society, Series A*. 1991. London.

158. T. Mao, D. C. S. Kuhn, and H. Tran, *Spread and rebound of liquid droplets upon impact on flat surfaces.* AIChE J., 1997. **43**: p. 2169.

159. S. E. Bechtel, D. B. Bogy, and F. E. Talke, *Impact of a liquid drop against a flat surface.* IBM J. Res. Dev., 1981. **25**: p. 963.

160. H.-Y. Kim, and J.-H. Chun, *The recoiling of liquid droplets upon collision with solid surface.* Physics of Fluids, 2001. **13**: p. 643-659.

161. G. McHale, S. M. Rowan, and M. I. Newton, *Frenkel's method and the spreading of small sperical droplets.* J. Phys. D, 1994. **27**: p. 2619.

162. H. Dong, et al., *Temporally-resolved inkjet drop impaction on surfaces.* AIChE Journal, 2007. **53**(10): p. 2606-2617.

163. S. Schiaffino and A.A. Sonin, *Molten droplet deposition and solidification at low Weber numbers.* Phys. Fluids, 1997. **9**(11): p. 3172-3187.

164. Sartomer. *Sartomer Product Detail*. [cited 2011; Available from: http://www.sartomer.com/prodselectdetail.asp?apid=1&plid=1&sgid=4&prid=SR351.

165. S. Sikalo, et al., *Analysis of impact of droplets on horizontal surfaces.* Experimental Thermal and Fluid Science, 2002. **25**: p. 503-510.

166. L. Xu, L. Barcos, and S.R. Nagel, *Splashing of liquids: Interplay of surface roughness with surrounding gas.* Phys. Rev. E, 2007. **76**: p. 066311.

167. T. Inamuro, et al., *A lattice Boltzmann method for incompressible two-phase flows with large density differences.* Journal of Computational Physics, 2004. **198**(2): p. 628-644.

168. T. Lee and C.-L. Lin, *A stable discretization of the lattice Boltzmann equation for simulation of incompressible two-phase flows at high density ratio.* Journal of Computational Physics, 2005. **206**(1): p. 16-47.

169. Y.Y. Yan and Y.Q. Zu, *A lattice Boltzmann method for incompressible two-phase flows on partial wetting surface with large density ratio.* Journal of Computational Physics, 2007. **227**(1): p. 763-775.

170. A.J. Briant, A.J. Wagner, and J.M. Yeomans, *Lattice Boltzmann simulations of contact line motion. I. Liquid-gas systems.* PHYSICAL REVIEW E, 2004. **69**(3): p. 031602.

171. A.J. Briant and J.M. Yeomans, *Lattice Boltzmann simulations of contact line motion. II. Binary fluids.* PHYSICAL REVIEW E, 2004. **69**(3): p. 031603.

172. T. Lee and L. Liu, *Lattice Boltzmann simulations of micron-scale drop impact on dry surfaces.* Journal of Computational Physics, 2010. **229**(20): p. 8045-8063.

173. S. Chapman and T.G. Cowling, *The mathematical theory of non-uniform gases: an account of the kinetic theory of viscosity, thermal conduction and diffusion in gases*. 1991: Cambridge university press.

174. C. Zhou, P. Yue, and J.J. Feng, *Deformation of a compound drop through a contraction in a pressure-driven pipe flow.* International journal of multiphase flow, 2008. **34**(1): p. 102-109.

175. H. Kusumaatmaja and J. Yeomans, *Lattice Boltzmann Simulations of Wetting and Drop Dynamics*, in *Simulating Complex Systems by Cellular Automata*, J. Kroc, P.M.A. Sloot, and A.G. Hoekstra, Editors. 2010, Springer Berlin Heidelberg. p. 241-274.

176. T. Lee, C.-L. Lin, and L.-D. Chen, *A lattice Boltzmann algorithm for calculation of the laminar jet diffusion flame.* Journal of Computational Physics, 2006. **215**(1): p. 133-152.

177. H. Ding and P.D.M. Spelt, *Wetting condition in diffuse interface simulations of contact line motion.* PHYSICAL REVIEW E, 2007. **75**(4): p. 046708.

178. W. Zhou, et al. *Impact of polyurethane droplets on a rigid surface for ink-jet printing manufacturing*. in *Solid Freeform Fabrication Symposium 2010*. 2010. Austin, TX.

179. W. Zhou, et al. *Shape Characterization for Droplet Impingement Dynamics in Ink-jet Deposition*. in *ASME 2012 International Design Engineering Technical Conference & Computers and Information in Engineering Conference*. 2012 Chicago, Illinois, USA.

180. I. Prigogine, I. Stengers, and A. Toffler, *Order out of chaos*. Order out of chaos.. I. Prigogine, I. Stengers, with a foreword by A. Toffler. Bantam Books, Toronto-New York-London-Sydney. 349 pp. . Vol. 1. 1984.

181. S.S. Chikatamarla and I.V. Karlin, *Lattices for the lattice Boltzmann method.* Physical Review E, 2009. **79**(4): p. 046701.

182. P. Asinari, *Multi-Scale Analysis of Heat and Mass Transfer in Mini/Micro-Structures*. 2005, Ph. D dissertation at the Department.

183. G. O'Brien, T. Nissen‐Meyer, and C. Bean, *A Lattice Boltzmann Method for Elastic Wave Propagation in a Poisson Solid.* Bulletin of the Seismological Society of America, 2012. **102**(3): p. 1224-1234.